

**PROCEEDING
OF 1ST INTERNATIONAL CONFERENCE
ON ENVIRONMENTAL PROTECTION
AND DISASTER RISKS**

PART ONE

Az-buki National Publishing House
Sofia 2020

PROCEEDING
OF 1ST INTERNATIONAL CONFERENCE
ON ENVIRONMENTAL PROTECTION
AND DISASTER RISKS

PART ONE

АЗБУКИ

Az-buki National Publishing House

Sofia 2020

Part One of the proceeding book presents texts on the following topics: *Air Pollution, Climate and Health; Biodiversity; Informatics, Remote Sensing, High Performance Computing and GIS for Environmental Monitoring and Management.*

In Part Two of the proceeding book will be presented texts on the following topics: *Natural Hazards and Risks; Water Resources, Human Activities and Management.*

Proceeding of 1st International Conference on Environmental Protection and disaster RISKS – Part One

Editors:

Georgi Gadzhev
Nina Dobrinkova

Cover Design: Ivo Hristov

Stylist-corrector: Anelia Vracheva

Preprint: Az-buki National Publishing House, www.azbuki.bg

Print: Alliance Print

Size: 70/100/16

Printed Quires: 18,5

ISBN 978-619-7065-38-1

e-ISBN 978-619-7065-39-8

**National research program
Environmental protection and minimization of unfavorable events
and natural disasters hazards**

The general Program objectives are carrying out fundamental and applied studies aiming at ensuring sustainable, favorable and safe living environment for the population of the Republic of Bulgaria

The specific Program objectives are Fundamental studies. Development and/or adoption of methods and carrying out of reliable, comprehensive and detailed studies of:

1. Spatial/temporal variability of the parameters and characteristics of the atmosphere and their impact on quality of life, health risks and ecosystem status;
2. Quality of waters atmosphere and their impact on quality of life, health risks and ecosystem status;
3. Quality of urban environment (buildings, transport and technical infrastructure, green areas, public and open areas) and their impact on quality of life, health risks and ecosystem status;
4. Recurrence and spatial distribution of extreme, unfavorable and catastrophic natural phenomena (droughts, storms, hail, floods, fires, sea waves, soil erosion, etc.) and their connection with atmospheric processes and climate changes; risk assessment and evaluation of the possibilities for forecast, early warning and prevention;
5. Geological environment and geological hazards - recurrence and spatial distribution; risk assessment and evaluation of the possibilities for forecast, early warning and prevention;
6. Hazards for biodiversity and ecosystems functions as a component of sustainable and favorable living environment;
7. Reaction and adaptation of ecosystems to unfavorable and catastrophic events in the geological past (global warming and cooling, collisions with space objects) – a key to understanding the current and predicting the future changes.

Other specific Program objectives are applied studies – elaboration, on the bases of the knowledge, generated by the fundamental studies of:

1. Systems for forecasting of unfavorable and catastrophic natural phenomena;
2. Early warning systems

3. Systems assisting the actions during catastrophic events and disasters;
4. Long-term strategies and measures for preventing and overcoming of unfavorable and catastrophic phenomena;
5. Enriching the knowledge about mechanisms of biodiversity losses in Bulgaria and the Black Sea in climate change conditions, their connections with local human activities, possible pathways for mitigation and adaptation to negative consequences.

Enhancing the qualification of the scientists and developing of up-to date research infrastructure, Dissemination of the scientific results, Transfer of knowledge to the decision making bodies (elaboration of scientifically robust strategies and programs for sustainable government) and Promoting multi-disciplinary partnership between research teams from different scientific fields are also part of the general Program objectives.

Expected results

Fundamental results:

1. Generation of new knowledge about the processes in the atmosphere, hydrosphere, lithosphere and biosphere in regional and local scales, about their interactions and their impact on quality of life, health and ecosystem status.
2. Accounting for the multi-scale nature of the processes.
3. Tracking of the main mechanisms and pathways for forming the characteristics the atmosphere, hydrosphere, lithosphere and biosphere and respectively their impact on quality of life, health and ecosystem status and the genesis of different natural disasters.

4. Applied results:

5. Evaluation of the spatial/temporal variability (mapping) of the unfavorable events risk: extreme seismic events with a big recurrence period, extreme temperatures, bad air and water quality, draughts, floods, storms, hail, icing, fires, geological disasters, biodiversity losses, etc.
6. Systems for forecasting of unfavorable and catastrophic natural phenomena;
7. Early warning systems;
8. Early warning systems for ecosystem changes with elements of worsening of the living environment or bio resource or other ecosystem services loss;
9. Systems assisting the actions during catastrophic events and disasters;
10. Long-term strategies and measures for preventing of unfavorable and catastrophic phenomena, worsening of the living environment or bio resource or other ecosystem services loss;
11. Strategic measures for emission reduction aiming at reduction of the health risks and impact on ecosystems.
12. Elaboration of comments and recommendations for the National action plan for adaptation to climate changes.



NATIONAL GEOINFORMATION CENTER

The NATIONAL GEOINFORMATION CENTER (NGIC) is a newly established scientific infrastructure for cooperation and integration of human resources and informational products and data on the geo-environment, their complex analysis and creation of mathematical models. It is part of the National road map for scientific infrastructure (2017-2023), adopted by the Council of Ministers of Bulgaria. The partners joined in the research consortium are four institutes working in the field of Earth observation: the National Institute of Geophysics, Geodesy and Geography (NIGGG-BAS), the National Institute of Meteorology and Hydrology (NIMH), the Institute of Oceanology (IO-BAS), the Geological Institute (GI-BAS), and two institutes competent in ICT: the Institute of Mathematics and Informatics (IMI-BAS) and the Institute of Information and Communication Technologies (IICT-BAS).

NGIC is a distributed scientific infrastructure with national territorial coverage and integrates monitoring networks, observatories, observation stations, laboratories, computing centers and other specialized equipment of the participating partners. Existing technical resources include unique facilities, scientific equipment and computer networks.

The creation of single, dynamic ICT-based network will ensure the development of multidisciplinary, broad-spectrum of geo products to serve a wide range of users - government, local authorities, business and the public, to solve important national tasks for forecasting and prevention of natural and anthropogenic risks and disasters.

The impact and benefits expected from the implementation of the project include:

- Response to natural and anthropogenic disasters and accidents and creation of prevention plans, including dangerous meteorological conditions and related health problems;
- Sustainable urban development; land use; design and implementation of large infrastructure projects (gas pipelines, highways, water supply, etc.);
- Improved management of water resources through a better understanding of the water cycle, improving the management and protection of terrestrial, coastal and marine ecosystems;
- Analysis of environmental factors affecting human health and well-being, as well as assessing, forecasting, mitigating and adapting to climate change;
- Raised public awareness of natural disasters and industrial accidents through new interactive products;
- Support to the transfer of scientific results in operational technologies by encouraging cooperation and collaboration between research communities.
- Support to the research and development in key areas of Earth sciences, contributing to advances in science and technology.

CONTENTS

- AIR POLLUTION, CLIMATE AND HEALTH
- 8 Winter and Summer Variability and Trends of Modis Derived Sea Surface Temperatures for the Western Black Sea / *Nadezhda Valcheva, Violeta Slabakova*
- 21 Variations of Temperature over Bulgaria and their Connection with Solar Cycles / *Yavor Chapanov*
- 33 Study of One Month High Polluted Pm Event for Sofia Region / *Margret Velizarova, Reneta Dimitrova*
- 44 Satellite Data Assimilation of Air Quality Parameters in Bulgaria / *Dimiter Syrakov, Maria Prodanova, Emilia Georgieva*
- 53 Preliminary Results for the Recurrence of Air Quality Index for the City of Sofia from 2008 to 2019 / *Georgi Gadzhev*
- 65 Particulate Matter Characteristics and Atmospheric Boundary Layer Height over Sofia / *Plamen Savov, Nikolay Kolev, Ekaterina Batchvarova, Hristina Kirova, Maria Kolarova*
- 79 Sensitivity to the Wrf Model Configuration of the Wind Chill Index for Sofia Region – Preliminary Results / *Vladimir Ivanov, Reneta Dimitrova*
- 90 Modelling of the Sulphur and Nitrogen Depositions over the Balkan Peninsula by CMAQ and EMEP-MS-C-W – Preliminary Results / *Georgi Gadzhev, Vladimir Ivanov*
- 101 How Well Do the Air Quality Models EMEP and CAMS Reproduce Particulate Matter Surface Concentrations in Bulgaria / *Hristina Kirova, Nadya Neykova, Emilia Georgieva*
- 112 Cloud and Rain Water Chemical Composition at Peak Cherni Vrah, Bulgaria / *Elena Hristova, Blagorodka Veleva, Krum Velchev, Emilia Georgieva*
- 123 Characteristics of Ultrafine PM Emitted During Gazification of Biomass / *Iliyana Naydenova, Tsvetelina Petrova, Ognyan Sandov, Ricardo Ferreira, Rositsa Velichkova, Mario Costa*
- 134 Black Sea Freezing and Winter Severity: Relation to the Temperature / *Mirna Matov, Elisaveta Peneva, Greta Georgieva*
- 144 Assessment of the Future Climate over Southeast Europe Based on CMIP5 Ensemble of Climate Indices – Part One: Concept and Methods / *Hristo Chervenkov, Vladimir Ivanov, Georgi Gadzhev, Kostadin Ganev*

- 157 Assessment of the Future Climate over Southeast Europe Based on CMIP5 Ensemble of Climate Indices – Part Two: Results and Discussion / *Hristo Chervenkov, Vladimir Ivanov, Georgi Gadzhev, Kostadin Ganey*
- 170 Application of Backward Trajectories and Cluster Analyses for Study of Variations in PM₁₀ Concentrations / *Rozeta Neykova, Elena Hristova*
- 180 Relationship between Particulate Matter and Health Indicators for Acute Morbidity in Sofia / *Petar Zhivkov, Aleksandar Simidchiev*
- 194 Nocturnal Boundary-Layer Characteristic in a Costal Site Using Long-Term Sodar Data / *Damyam Barantiev, Ekaterina Batchvarova*
- 205 Environmental Impact of Quarry Activities: the Case Study of a Gneiss Deposit in the Region of Blagoevgrad / *Radostina Angelova, Rositsa Velichkova, Sylvia Alexandrova*

BIODIVERSITY

- 216 *Peniophora Proxima* (Peniophoraceae, Basidiomycota): Newly Recorded for the Bulgarian Mycota / *Aneta Lambevskya-Hristova, Svetlana Bancheva*
- 221 Applicability of Control Region of Mitochondrial DNA for Assessment of Turbot Populations Along the Bulgarian Black Sea Coast / *Petya Ivanova, Nina Dzhebekova, Ivan Atanassov, Krasimir Rusanov, Violin Raykov, Ivelina Zlateva, Maria Yankova*

INFORMATICS, REMOTE SENSING, HIGH PERFORMANCE COMPUTING AND GIS FOR ENVIRONMENTAL MONITORING AND MANAGEMENT

- 231 Open Source GIS Decision Support Tools for Wildfire and Flood Natural Hazards with Embedded Interactive Training Resources / *Stefan Stefanov, Nina Dobrinkova, Emilia Tosheva*
- 241 Methodology for Calculating the Parameters of Radio Paths with Ionospheric Reflection / *Rumiana Bojilova, Plamen Mukhtarov*
- 249 GIS in Crises Management Use of Smart Phone GIS Application in the Event of Natural Disaster / *Aleksandar Petrovski, Nenad Taneski, Jugoslav Ackoski*
- 259 Framework for Wildfire Danger Prediction System / *Nina Dobrinkova, Maria Asenova*
- 271 Evaluation of Sentinel-3a OLCI Ocean Color Products in the Western Black Sea / *Violeta Slabakova, Snejana Moncheva, Natalyia Slabakova, Nina Dzhebekova*
- 282 A Modelling System for Numerical Weather Prediction in the Bulgarian Antarctic Base Area / *Boriana Chtirkova, Elisaveta Peneva, Gergana Georgieva*

WINTER AND SUMMER VARIABILITY AND TRENDS OF MODIS DERIVED SEA SURFACE TEMPERATURES FOR THE WESTERN BLACK SEA

Nadezhda Valcheva, Violeta Slabakova

Institute of Oceanology – Bulgarian Academy of Sciences (IO-BAS)

Abstract: The study investigates on sea surface temperature (SST) seasonal to interannual variability in the western Black Sea using gridded fields of MODIS derived SST monthly averages of 4 km horizontal resolution. More specifically, winter and summer SSTs products were considered spanning a 17-year period (2003-2019). To this end, seasonal climatic mean fields were obtained and observed features were discussed from a hydrodynamic view point. Furthermore, time series of winter and summer SST means were analysed to reveal the spatial variability pattern. In terms of zonal flow, the winter SST increases eastward, while the summer ones - from northwest to southeast. Both winter and summer SSTs exhibit increasing long-term trends; there is almost uniform increase of the winter SSTs of 0.6-0.7°C per decade for all zonal areas, while the summer ones tend to vary in somewhat wider range – 0.5-0.7°C per decade. Besides, based on the normalized SST anomalies, it was found out that during 2003-2019 SSTs have grown with a lower rate compared to the two preceding decades. Finally, in attempt to link the SST variability to global teleconnection patterns such as North Atlantic Oscillation (NAO), a spectral analysis of seasonal time series was performed, which indicated the existence of quasi-decadal scale of variation that roughly follows the NAO positive and negative cycles.

Keywords: Black Sea, sea surface temperature, remote sensing, seasonal anomaly, decadal variability

INTRODUCTION

Sea surface temperature (SST) is the temperature of the extremely thin interface between the ocean and the overlying atmosphere, which controls heat and gas exchange. SST is also the longest and most widely measured parameter in the ocean (Emery, 2015). In the Black Sea, it influences the water circulation and ecological condition of the basin and has an impact on the temperature of the Cold Intermediate Layer (CIL). The temperature of the surface layer and SST respond most quickly to the atmospheric impacts, which is the reason why SST experiences

a significant spatial and temporal (interannual, seasonal, and synoptic) variability (Ginzburg et al., 2008). Therefore, it is important to investigate about the spatial SST variability on intraannual (seasonal) and inter-annual scales as well as relevant long-term trends.

In the last four decades, Black sea SST variability has become a subject of increased scientific interest. The first studies on interannual variability of temperature started to be published in the 1980s and 1990s after collecting large series of quasi-regular measurements launched back in the 1950s.(Polonsky et al., 2013). Some of the studies are based on hydrologic observations. For example, Polonsky and Lovenkova (2004) analysed the long-term variability and trends in the upper layer temperature during the cold half of the year using contact observation for the period 1960–1990. They report typical cooling values of $1^{\circ}\text{C}/10$ yr is located in the northern part of the studied standard section. The temporal trends and interannual to interdecadal scale SST changes during the 20th century over contrasting shelf and deep sea regions were presented in Shapiro et al. (2010).Analysis of the time series has revealed decoupling between the shelf and deep sea regions in response to climate change. The deep sea experienced general cooling, which was particularly strong from the beginning of the century until the late 1960s. The western shelf did not exhibit a particular trend, except for the last 15-20 years when warming was detected.

However, only the satellite infrared measurements can represent the SST of the $10\ \mu\text{m}$ thick skin layer of the ocean, opposed the bulk SSTs measured by the buoys and ships in the layer 1-5 m (Emery, 2015). Furthermore, due to their larger coverage, satellite datasets give the opportunity to investigate interannual SST variability and to reveal long-term climatic trends not only on the basin wide scale but also for smaller regions of particular dynamics (Ginzburg et al., 2004).For example, night-time weekly AVHRR measurements were used to investigate seasonal and interannual variability of the Black Sea SST during 1982-2000. Analysis of the weekly SST means were used to calculate winter and summer SST anomalies as well as a long-term trend. As a result a positive basin wide trend of about $0.09^{\circ}\text{C}\ \text{yr}^{-1}$ has revealed, which however was different for the western and eastern deep sea regions – about 0.08 and $0.11^{\circ}\text{C}\ \text{yr}^{-1}$, respectively (Ginzburg et al., 2004). Polonsky et al. (2013) discovered a quasi-decadal SST variability with winter and summer fluctuations differing in amplitudes and phases. The difference between the temperature values from satellite and contact measurement data on average for all decades did not exceed 0.3°C . In winter, the large-scale SST spatial distribution was characterized by temperature increase from north to south (in the north-western shelf with high horizontal temperature gradients) and from west to east in the deep water region, while in summer, the increase was observed from northwest to southeast.

Furthermore, the long-term variability of the temperature fields in the Black Sea can serve as a reliable indicator of regional climate change. During the 20th

century, the Black Sea surface temperature had been constantly increasing due to climate change. Sakalii and Başısta (2018) analysed SST data covering the period 1982-2015 and predicted the Black Sea SST until 2100. They found out that SST increased with a rate of 0.64°C per decade thus conforming to the worst climate change scenario. By the end of 21st century, the relative increase of the average SST was predicted to be 5.1°C .

Moreover, SST spatial variations can be used as an indicator for the large- and mesoscale water dynamics. For example, SST data were used to explore the Black Sea heat balance underpinning the relevance of the fundamental oceanographic issue about how close the SST reproduces the air temperature (Esbensen and Reynolds, 1981; Gulev, 1994). Stanev and Staneva (2001) demonstrated that large area-dependent differences could exist between the SST and air temperature, creating an important eddy-dominated component of the ocean-atmospheric heat exchange.

Finally, SST exerts an impact on the ocean primary productivity through both physical effect on water stratification (which in turn affects nutrient availability) and its biological effect on plankton metabolic rates. The rise of global mean SST over the past century is linked with both decreases and increases in primary productivity depending on the time period and the region (Belkin, 2016). Oguz (2005) suggests that climate plays a crucial role in the Black Sea ecosystem state fluctuations. During the 1980s and 1990s, the existing atmospheric and hydrological processes, together with nutrient supply, led to an enhanced plankton productivity, which ultimately resulted in an increased jellyfish production and a longer over-fishing period. On the other hand, a decreasing trend in Chlorophyll a and primary production has been observed worldwide as SST increases, suggesting that reduced phytoplankton biomass in the Black Sea ecosystem, hence its recovery, is not solely a factor of diminished nutrient loading (McQuatters-Gollop et al., 2008).

Therefore, the proposed study aim to assess the spatial SST variability on seasonal and interannual scales as well as relevant long-term trends making use of remote sensing data, and to detect variability cycles possibly related to global tele-connection patterns.

DATA AND METHODS

Study domain encompasses the western Black Sea between $27.5\text{-}30.0^{\circ}\text{E}$ and $42.0\text{-}44.0^{\circ}\text{N}$ (Fig. 1). It includes near-shore (coastal) and shelf (inner and outer), spreading meridionally along the shore curve, and open (deep sea) areas. The SST data used in this study represent monthly global binned MODIS/AQUA Level 3 standard mapped night-time images (Brown & Minnett, 1999) at 4 km horizontal resolution spanning the period 2003-2019. The data were obtained from Ocean Color website provided by National Aeronautics and Space Administration (NASA). For extraction of the fixed region of interest and highest quality data from each monthly composite SST images, the SeaDAS v.7.5 (Fu et al., 1999) software was used.

Previously, Slabakova & Valcheva (2007) have performed validation of MODIS SSTs against in situ (CTD) sea water temperature for the western Black Sea. Match-up data were extracted for a period of four years (2003-2006). A strong correlation (0.953) between the two data types was ascertain, while root-mean square errors and biases for separate datasets (cruises) were found to vary in ranges 0.18-0.30°C and 0.278-0.450°C, respectively. This indicates a good agreement with standards established in EOS Data Product Handbook (2000).



Figure 1. Scheme of the study domain. Location of points, for which seasonal SST time series were derived, are illustrated as coloured rings as follows: coastal stations in blue, inner shelf ones in red, outer shelf in green, open sea in violet

In order to achieve the study aims, mean winter and summer climatic fields are constructed by averaging the monthly gridded fields over the time-span of interest (entire study period or separate years within it). Seasons are defined as three-month periods: winter includes January, February and March, and summer - July, August and September.

Furthermore, the SST normalized anomaly (referred hereafter as anomaly) M_{NA} (°C) is calculated using the following formulation:

$$M_{NA} = \frac{M_Y(i) - CM_{17}}{STD_{17}} \quad (1)$$

where $M_T^{(i)}$ is the seasonal mean for each year, CM_{17} – climatic seasonal mean for the entire 17-year period, STD_{17} – respective standard deviation. The overall anomaly is computed by averaging the seasonal normalized anomaly over appropriate number of years. Spectral analysis was performed applying Fast Fourier Transformation on the mean seasonal SST scalar time series using estimates of spectral density as mean values of periodogram.

RESULTS AND DISCUSSION

Seasonal mean SST climatic fields, presented in Fig. 2, are very similar to those derived from in-situ CTD bulk temperature data spanning the period 1995-2010 (Valcheva, 2014). More specifically, the winter climatic SST distribution reveals the main features of typical seasonal dynamics, namely presence of narrow frontal zone of sharp horizontal gradients between coastal and inner shelf waters, on one hand, and outer shelf and deep basin, on the other, defined between 6.8 and 7.6°C isotherms; colder coastal waters of temperatures lower than 6.2°C; and vast area of quasi uniform open sea waters of temperatures about 8°C. The front is determined by intensification of the large-scale circulation – the Rim current flow is strongly pressed against the basin lateral boundaries – intense mixing of surface waters and restricted water exchange with the northwestern shelf.

In summer, the relatively cooler waters in the northernmost part of the domain are marked by temperatures lower than 24.1°C. Farther within the western shelf, these waters are being transformed while their impact can be traced along the entire shelf curve. The frontal zone is less discernable and considerably wider with respect to winter, which is determined by the weakening and instability of the large scale circulation (lower Rim current velocity) and existence of quasi-stable (recurrent) anticyclonic eddies. With this respect, Burgas eddy is visible on the SST climatic distribution on the coastal side of the Rim current in both seasons marked by temperatures higher than 24.3°C in summer and lower than 6°C in winter, that is being slightly warmer and cooler, respectively, with respect to the surrounding waters. The same is valid for Kaliakra eddy that contains cooler waters in both seasons – less than 6.4°C in winter and 24.0°C in summer. Thus, the summer circulation pattern allows for horizontal water exchange between the periphery of the large-scale gyres and the shelf. The process of entrainment of warmer open sea waters (SST>24.5°C) in the shelf and near-shore zone, which are being spread to the north, is particularly visible in the middle and southern part of the study area. The summer SSTs increase from northwest to southeast as discovered also by Polonsky et al. (2013). Spatial temperature variability ranges in less than 0.7°C, i.e. three to four times smaller compared to the winter (2.6°C).

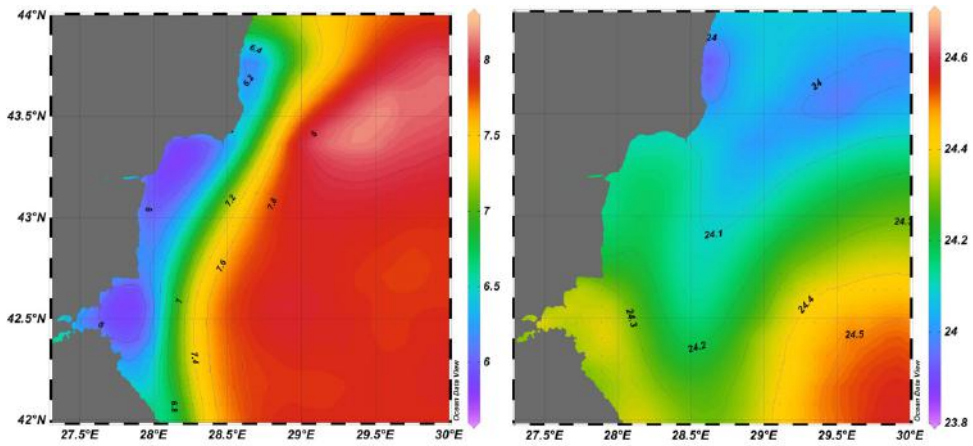


Figure 2. Winter (left) and summer (right) mean SST (°C) climatic spatial distribution over the western Black Sea for 2003-2019

With this respect, the analysis of seasonal time series derived for locations in near-shore (coastal), inner and outer shelf, and open sea can be particularly useful. Therefore, 23 points were selected normal to the general exposure of the shore (Fig. 1). In Table 1 seasonal SST minima and maxima for mentioned areas as well as the maximum and average temperature differences are summarized. This allows for more thorough examination of the SST spatial variability.

Table 1. SST minima / maxima and relevant temperature differences for areas of particular surface dynamics

| Area | SST min (°C) | | SST max (°C) | | SST diff. max (°C) | | SST diff. average (°C) | |
|-------------|--------------|--------|--------------|--------|--------------------|--------|------------------------|--------|
| | winter | summer | winter | summer | winter | summer | winter | summer |
| Coastal | 3.9 | 22.6 | 7.8 | 25.2 | 2.5 | 0.7 | 1.2 | 0.5 |
| Inner shelf | 4.2 | 22.9 | 7.9 | 25.2 | 2.5 | 0.7 | 1.0 | 0.4 |
| Outer shelf | 4.8 | 22.9 | 8.5 | 25.1 | 2.8 | 0.6 | 1.4 | 0.3 |
| Open sea | 6.5 | 22.8 | 9.2 | 25.2 | 0.9 | 0.9 | 0.4 | 0.4 |

In meridional direction, SST increases southward. This increase is more pronounced in coastal and shelf areas, particularly in winter – about 2-3°C (1.0-1.4°C on the average). In summer, this pattern is less discernible and the temperature difference does not exceed 0.7°C (0.3-0.5°C on the average). Deep water SSTs do not differ noticeably between northern and southern regions, in both seasons, as the maximum difference is less than a degree and the average one is 0.4°C (Table 1, Fig. 3). In terms of zonal flow, the winter SST increases eastward, which means that the cooling of coastal waters is the most marked. The temperature differences between near-shore

and open sea regions experience significant fluctuations of 1.5-3.8°C. In summer, the opposite takes place as the coastal waters were heated more than the offshore ones. However, the difference is so minor (less than an order of magnitude compared to the winter one) that it is not greater than a couple of tenths of a degree (Table 1, Fig. 3).

From hydrodynamic point of view, the open sea waters are part of a large scale circulation cell, namely the western gyre, and the small spatial variability can be attributed to the more intense mixing that takes place there. On the other hand, the water flow in shelf and coastal areas is mainly governed by the mesoscale circulation features, which defines the greater spatial variability observed. In winter, it is still more uniform due to the intensified circulation, while in summer the pattern may considerably differ between areas due to circulation instability and presence of eddies. Interannual variability of zonal temperature differences is much

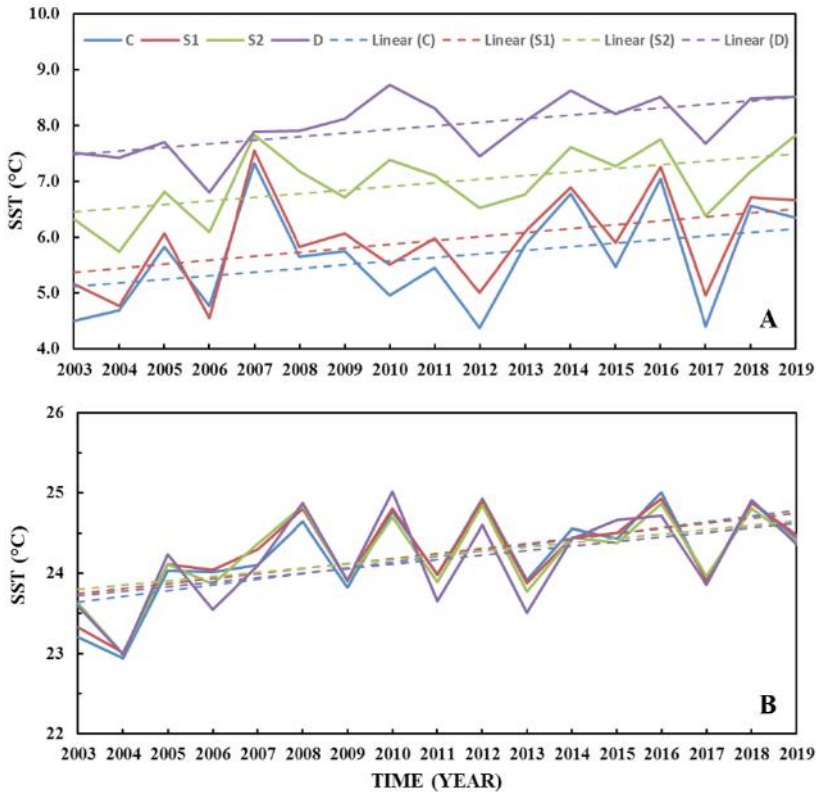


Figure 3. Time series of winter (A) and summer (B) SST climatic means obtained for zonal stretches for 2003-2019: coastal (C), inner shelf (S1), outer shelf (S2) and deep sea (D). Respective linear trends are represented with dashed line

more pronounced than the meridional ones, in winter in particular. For this season, the range is largest in the beginning – 2003-2004 (about 3°C) – and the middle of the study period – 2010-2011 (about 3.5°C) – whereas it is the smallest in 2007 (0.5°C). Thus, 2010-2011 data sustain the hypothesis for decoupling between open sea and periphery. The variability of summer zonal temperature differences appears to be more uniform with a steady decreasing trend.

Several authors (e.g. Oguz et al., 2003; Stanev et al., 2014) suggested that the erosion of the Black Sea upper layer stratification is mainly associated with the atmospheric warming of the sea surface and winter SST can be used as indicator of the cooling intensity (Piotukh et al., 2011). With this respect, the warmest winters were those of 2007, 2014 and 2016 (SST maxima of 7.9-8.6°C), as well as the winters of 2009-2010 for the open sea area with absolute maximum of 8.7°C (Fig. 3A). During such winters, the cooling of surface waters is insufficient leading to limited ventilation of the upper layer and shrinking of cold intermediate layer. Such phenomena were reported in 2011 and 2015-2016 (Stanev et al., 2019; Valcheva et al., 2020). On the other hand, the coolest winters were in 2006, 2012 and 2017 when SSTs in near-shore waters dropped to 4.3-4.8°C and in open sea areas – to 6.8-7.7°C, which assisted the recovery of the vertical stratification. The warmest summers took place in 2010, 2012 and 2016 when SSTs reached 25°C. This suggests that periods of the SST rise and fall alter every 5-6 years. Moreover, the fluctuations are synphase in all areas (especially well pronounced for summer, see Fig. 3B) except for winters of 2008-2010. Besides, the winter SST fluctuations get smoother in offshore direction.

Both winter and summer SSTs exhibit increasing long-term trends (Fig. 3). Linear approximation predicts almost uniform increase of the winter SSTs of 0.06-0.07°C yr⁻¹ for all zonal areas, while the summer ones tend to vary in somewhat wider range – 0.05-0.07°C yr⁻¹ – as the near-shore SSTs rise is more pronounced. These values are in agreement with the findings of Sakalii and Baştusta (2018) and, having in mind those reported by Ginzburg et al. (2004), it seems that during 2003-2019 SSTs have grown with a lower rate compared to the two preceding decades.

Furthermore, spatial distribution of the anomaly calculated using (1) averaged over the study period is presented in Fig. 4. It can be seen that the summer anomalies (ranging within ±0.6°C) are more than ten times greater than the winter ones (roughly ±0.04°C). While the summer anomalies field is smoother and resembles the mean climatic SST distribution, the winter one shows a more varied aspect. Thus, the water flow from the northwestern shelf was marked by negative summer SSTs anomalies at the same time that the warming took place mainly in the open sea area (positive anomalies within the western gyre in particular). Through the process of entrainment, these warmer waters had contributed to the positive anomaly observed on the southern shelf and adjacent coastal waters. Nevertheless, small negative SST anomaly is present within the middle part of the shelf (~- 0.2°C).

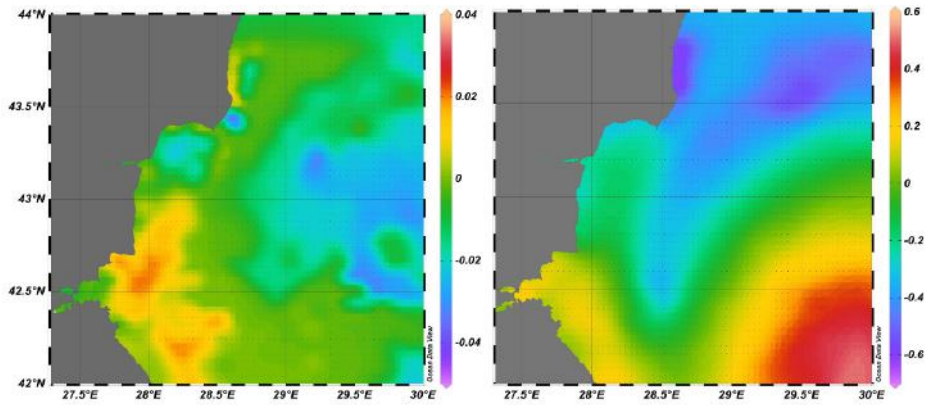


Figure 4. Winter (left) and summer (right) spatial distribution of the average SST normalized anomaly ($^{\circ}\text{C}$) over the western Black Sea for 2003-2019

As for the winter SST anomaly field, the negative anomaly can be observed in deep sea area; there is neutral anomaly over the larger part of the shelf and positive one over certain spans of the middle and mostly southern shelf (especially in front of Burgas Bay). The slight cooling of the open sea surface might have contributed to the reduced SST growth rate during the last 15-20 years. As a whole, the result suggest that the trend of decoupling between the basin periphery and deep sea region, detected by Shapiro et al. (2010) and attributed to the climate change, is still present in first two decades of the 21st century.

The cycle of SST interannual variability suggested above agrees with previous studies (e.g. Oguz et al., 2006; Capet et al., 2012), which imply the existence of teleconnection between Black Sea regional atmospheric condition and large scale atmospheric pattern driven by the North Atlantic Oscillation (NAO). More specifically, this refers to a sequence of cold and mild winter cycles with approximately 5-year duration that roughly follows the NAO positive and negative cycles. Similar fluctuations were detected for mixed layer temperature (Valcheva, 2018) and cold intermediate layer thickness (Valcheva et al., 2020). In attempt to confirm this finding with the SST dataset used in this study, a spectral analysis of seasonal time series was performed. The result revealed that the largest spectral density corresponds to the highest frequency fluctuations of two years. However, the second peak indicates an 8-year cycle of variability, which is more discernable for the winter time series. Such quasi-decadal fluctuations agree with the observed peak in 8-10 year band of the winter mean NAO index power spectrum, which was found to enhance particularly over the second half of the 20th century (Polonsky et al., 2004).

CONCLUSIONS

The study dealt with the spatio-temporal variability and related long-term trends of winter and summer sea surface temperature derived from MODIS remote sensing data. Thus, climatic SST field reveals the main features of typical seasonal hydrodynamics: in winter the temperatures vary between 6.2°C in near-shore zone to about 8°C in the open sea presenting a marked narrow transition zone of strong horizontal gradients, whereas in summer relatively cooler waters coming from the northwestern shelf mixed with warmer ones (SST~24.5°C) as they flow in the domain due to instability of the large scale circulation. It was confirmed existence of quasi-stable anticyclonic mesoscale features, such as Burgas and Kaliakra eddies on the coastal side of the Rim current, as well as the process of entrainment of open sea waters in the shelf and near-shore zone, which are being spread to the north.

In summer, spatial temperature variability ranges in less than 0.7°C, i.e. three to four times smaller compared to winter (2.6°C). In meridional direction, SST increases southward. This increase is more pronounced in coastal and shelf areas, particularly in winter – about 2-3°C. In terms of zonal flow, the winter SST increases eastward, while the summer ones – from northwest to southeast. Interannual variability of zonal temperature differences is much more pronounced than the meridional ones, in winter in particular.

With respect to the increased atmospheric warming of the sea surface and use of winter SST as indicator of the cooling intensity, warmest and coolest winters have been identified –2007, 2014 2009-2010, and 2016 (7.9-8.7°C); and 2006, 2012 and 2017 (4.3-4.8°C). Both winter and summer SSTs exhibit increasing long-term trends; there is almost uniform increase of the winter SSTs of 0.6-0.7°C per decade for all zonal areas, while the summer ones tend to vary in somewhat wider range – 0.5-0.7°C per decade. The results suggest that during 2003-2019 SSTs have grown with a lower rate compared to the two preceding decades.

Furthermore, spatial distribution of the averaged normalized anomalies reveals that the summer anomalies ($\pm 0.6^\circ\text{C}$) are more than ten times greater than the winter ones ($\pm 0.04^\circ\text{C}$). While the summer anomalies field is smoother and resembles the mean climatic SST distribution, the winter one shows a more varied aspect. As a whole, the outcome confirms the trend of decoupling between the basin periphery and deep sea region. Finally, the spectral analysis of seasonal time series confirmed the existence of a quasi-decadal SST variability cycle, which agrees with the observed peak of the winter mean NAO index power spectrum.

ACKNOWLEDGMENTS

This work has been carried out in the framework of the National Science Program "Environmental Protection and Reduction of Risks of Adverse Events and

Natural Disasters", approved by the Resolution of the Council of Ministers № 577/17.08.2018 and supported by the Ministry of Education and Science (MES) of Bulgaria (Agreement № Д01-322/18.12.2019).

REFERENCES

- Belkin, I. (2016). Chapter 5.2: Sea surface temperature trends in large marine ecosystems. In IOC-UNESCO and UNEP (2016). *Large Marine Ecosystems: Status and Trends*, United Nations Environment Programme, Nairobi, 101-109.
- Brown, O. & Minnett, P. J. (1999). Modis Infrared Sea Surface Temperature Algorithm. *Algorithm Theoretical Basis Document, Version 2.0*, modis.gsfc.nasa.gov/data/atbd/atbd_mod25.pdf.
- Capet, A., Barth, A., Beckers, J.-M. & Grégoire, M. (2012). Interannual variability of Black Sea's hydrodynamics and connection to atmospheric patterns. *Deep Sea Research Part II: Topical Studies in Oceanography*, 77–80, 128-142.
- Emery, W. J. (2015). Sea Surface Temperature. *Encyclopedia of Atmospheric Sciences 2nd Edition, Vol. 1*, 136-143.
- EOS Data Product Handbook Volume 2 (2000), Parkinson, C. L. & Greenstone, R. (Eds). *NASA Goddard Space Flight Greenbelt, Maryland*, 256.
- Esbensen, S.K. & Reynolds, R.W. (1981). Estimating monthly averaged air-sea transfers of heat and momentum using the bulk aerodynamic method. *J. Phys. Oceanogr.* 11, 457–465.
- Fu, G., Baith, K. & McClain, C. (1999). The SeaWiFS Data Analysis System. *Proceedings of the 4th Pacific Ocean Remote Sensing Conference*, 73–79.
- Ginzburg, A. I., Kostianoy, A. G. & Sheremet, N. A. (2004). Seasonal and interannual variability of the Black Sea surface temperature as revealed from satellite data (1982-2000). *Journal Marine Systems*. 52, 33–50.
- Ginzburg, A. I., Kostianoy, A. G. & Sheremet, N. A. (2008). Sea surface temperature variability. *The Black Sea Environment. The Handbook of Environmental Chemistry. Vol. 5: Water Pollution, Part 5/Q*, Kostianoy A. G. and Kosarev A. N. (Eds.). *Springer-Verlag Berlin Heidelberg*, 255–276.
- Gulev, S.K. (1994). Influence of space-time averaging on the ocean-atmosphere exchange estimates in the North Atlantic midlatitudes. *J. Phys. Oceanogr.* 24, 1236–1255.
- McQuatters-Gollop, A., Mee, L.D., Raitzos, D.E. & Shapiro, G.I. (2008). Non-linearities, regime shifts and recovery: The recent influence of climate on Black Sea chlorophyll. *Journal of Marine Systems* 74, 649–658.

- Oguz, T. (2005). Black Sea ecosystem response to climatic teleconnections. *Oceanography, Vol. 18(2)*, 122-133.
- Oguz, T., Cokacar, T., Malanotte-Rizzoli, P. & Ducklow, H.W. (2003). Climatic warming and accompanying changes in the ecological regime of the Black Sea during 1990s. *Global Biogeochem. Cycles, 17*, 1088.
- Oguz, T., Dippner, J.W. & Kaymaz, Z. (2006). Climatic regulation of the Black Sea hydrometeorological and ecological properties at interannual to decadal time scales. *J. Mar. Syst., 60*, 235–254.
- Piotukh, V. B., Zatsepin, A. G., Kazmin, A. S. & Yakubenko, V. G. (2011). Impact of the winter cooling on the variability of the thermohaline characteristics of the active layer in the Black Sea. *Oceanology 51*, 221–230.
- Polonsky, A. B. & Lovenkova, E. A. (2004). Temperature and salinity trends in the active layer of the Black Sea in the second half of the 20th century and their possible causes. *Izvestiya, Atmospheric and Oceanic Physics, Vol. 40 (6)*, 747–755.
- Polonsky, A.B., Basharin, D.V., Voskresenskaya, E.N. & Worley, S. (2004). North Atlantic Oscillation: description, mechanisms, and influence on the Eurasian climate. *Phys. Oceanogr., 15 (2)*, 96-113.
- Polonsky, A. B., Shokurova, I. G. & Belokopytov, V. N. (2013). Decadal variability of temperature and salinity in the Black Sea. *Journal of Marine Hydrophysics, 16*, 27-41. (In Russian).
- Sakalii, A. & Baştusta, N. (2018). Sea surface temperature change in the Black Sea under climate change: A simulation of the sea surface temperature up to 2100, *Int. J Climatol.*; 38, 4687-4698.
- Shapiro, G. I., Aleynik, D. L. & Mee, L. D. (2010). Long term trends in the sea surface temperature of the Black Sea. *Ocean Sciences, 6*, 491–501.
- Slabakova, V. & Valcheva, N. (2007). Estimation of feasibility of the Sea Surface Temperature satellite data use through comparison against in situ measurements for the western Black Sea Region. *Proc. of the 3rd Int. Scientific Conf. "Space Ecology Nanotechnology Safety"*, 185-190.
- Stanev, E.V. & Staneva, J.V. (2001). The sensitivity of the heat exchange at sea surface to meso and sub-basin scale eddies: Model study for the Black Sea. *Dynamics of Atmospheres and Oceans 33*, 163–189.
- Stanev, E.V., He, Y., Staneva, J. & Yakushev, E. (2014). Mixing in the Black Sea detected from the temporal and spatial variability of oxygen and sulphide Argo float observations and numerical modelling, *Biogeosciences, 11 (20)*, 5707–5732.
- Stanev, E. V., Peneva, E. & Chtirkova, B. (2019). Climate Change and Regional Ocean Water Mass Disappearance: Case of the Black Sea. *J. Geophys. Res. C: Oceans 124*.

- Valcheva, N. (2014). Climatic distribution of summer and winter temperature and salinity in the Western Black sea. *Proc. of 12th Int. Conf. on "Marine Sciences and Technologies - Black Sea '2014"*, 189-195.
- Valcheva, N. (2018). Interannual variability of the mixed layer summer sea water temperature in the Western Black Sea. *Proc. of 14th Int. Conf. on "Marine Sciences and Technologies - Black Sea '2018"*, 204-209.
- Valcheva, N., Marinova, V., Peneva, E., Lima, L., Celiberti, S. & Masina, S. (2020). Spatio-temporal variability of the Black Sea Cold Intermediate Layer properties derived from in situ data. The Copernicus Marine Environment Monitoring Service Ocean State Report. *J. of Operational Oceanography*, 33-41.

✉ **Nadezhda Valcheva**

<https://orcid.org/0000-0002-7690-8731>
Institute of Oceanology
Bulgarian Academy of Sciences (IO-BAS)
Varna, Bulgaria
E-mail: valcheva@io-bas.bg

✉ **Violeta Slabakova**

<https://orcid.org/0000-0002-3089-0126>
Institute of Oceanology
Bulgarian Academy of Sciences (IO-BAS)
Varna, Bulgaria
E-mail: v.slabakova@io-bas.bg

VARIATIONS OF TEMPERATURE OVER BULGARIA AND THEIR CONNECTION WITH SOLAR CYCLES

Yavor Chapanov

*Climate, Atmosphere and Water Research Institute –
Bulgarian Academy of Sciences (CAWRI-BAS)*

Abstract. The Sun is the main source of energy for all Earth's geosystems, including climate, weather, mean sea level, winds, precipitation, and etc., mainly through Total Solar Irradiance (TSI), whose variations during solar activity cause various changes on the Earth surface. Climate processes, interactions between atmosphere-and ocean system, various local, regional and global hydrological cycles are the main mediator between solar activity and a number of geophysical processes on the Earth surface. The temperature at the Earth surface is widely used climate index, whose variations consist of significant seasonal oscillations, trend and long-term cycles. The variations of temperature over Bulgaria is investigated by means of several long time series of meteorological observations. The changes of seasonal components of temperature and long-term oscillations are analyzed in narrow frequency bands by means of the Partial Fourier Approximation. These temperature variations are compared with the corresponding cycles of solar activity in order to create long-term forecast models.

Keywords: solar activity; temperature; climate variations

INTRODUCTION

The solar activity affects terrestrial systems by means of direct radiation over Earth surface, solar wind, and the solar magnetic field. The TSI cycles are the main source of climate indices variations. The solar wind directly affects Earth magnetic field, ionosphere and atmosphere. The variations of solar magnetic field modulate solar wind and cosmic rays in the frame of the heliosphere. The cosmic rays (CR) near Earth are modulated by Earth magnetic field variations, too. Recently a new mechanism of climate modulation, based on cosmic rays variations, has been proposed (Kilifarska et al., 2005, 2008; Kilifarska 2011; Velinov et al., 2005). This mechanism is based on chain processes near tropopause by ozone production, temperature variations, followed by vertical winds and water content change. The last step of this chain affects surface temperature, because the atmospheric water is one of the most powerful greenhouse gas. This model provides an explanation for

the cascade processes in which CR, whose total energy is relatively small, cause climatic effects with much more energy. The solar activity cycles modulate CR directly by the heliosphere and indirectly by the geomagnetic field changes, whose effect is visible mainly at high latitudes. A significant part of cosmic rays consists of charged solar particles, whose interaction with the Earth atmosphere is preceded by focussing effect of geomagnetic field over polar regions, while the most energetic galactic cosmic rays affect all Earth regions. The cosmic ray intensity exposes antiphase variations to the TSI variations. The TSI is strong during solar activity maximum, when the cosmic ray intensity has minimum and vice versa. So, during TSI maxima, the warming processes occur on Earth surface, and during TSI minima the thermal cycle amplitudes are amplified, due to cooling effects of cosmic rays. The variations of Earth temperature are affected directly by TSI cycles and indirectly by solar wind and solar magnetic field. These solar cycles are presented by the indices of TSI, sunspot numbers (also known as Wolf's number) and North-South (N-S) solar asymmetry.

The knowledge of temperature variations and cycles is important in various fields of human activity. An aspect of this knowledge is assessment of agrometeorological conditions in national agricultural lands. The determination of statistically significant tendency of average annual air temperature is important for spring crop growing (Georgieva, Shopova and Kazandjiev, 2019; Kazandjiev, Shopova, Georgieva, 2018). The climate change and coming with them abiotic stressors, a consequence of extreme weather conditions affect agriculture plant productivity (Slavcheva-Sirakova et al., 2020; Shopova, Alexandrov and Todorova, 2019). The goal of this study is to determine the thermal trends and changes of seasonal and long-term components of temperature at several Bulgarian meteorological stations, their connection with the cycles and harmonics of solar activity in order to improve long term forecasts.

DATA

The used data consist of centennial time series of monthly temperature variations from 4 Bulgarian stations in Vidin, Pleven, Razgrad, Dobrich and Sofia (Fig.1).

The solar data are presented by the Total Solar Irradiance (TSI) variations and N-S solar asymmetry (Fig.2). The estimated TSI for the last 400 years is based on the NRLTSI2 historical TSI reconstruction model (Kopp et al., 2016; Lean, 2010; Coddington et al., 2016). The index S_a of N-S solar asymmetry is calculated by formula

$$S_a = \frac{(A_N - A_S)}{(A_N + A_S)} S_a = \frac{(A_N - A_S)}{(A_N + A_S)}, \quad (1)$$

where A_N is the total area of the sunspots over Northern solar hemisphere and A_S - the total area of the sunspots over Southern solar hemisphere. The data of sunspot area since 1874 are observed by the Royal Greenwich Observatory and merged after

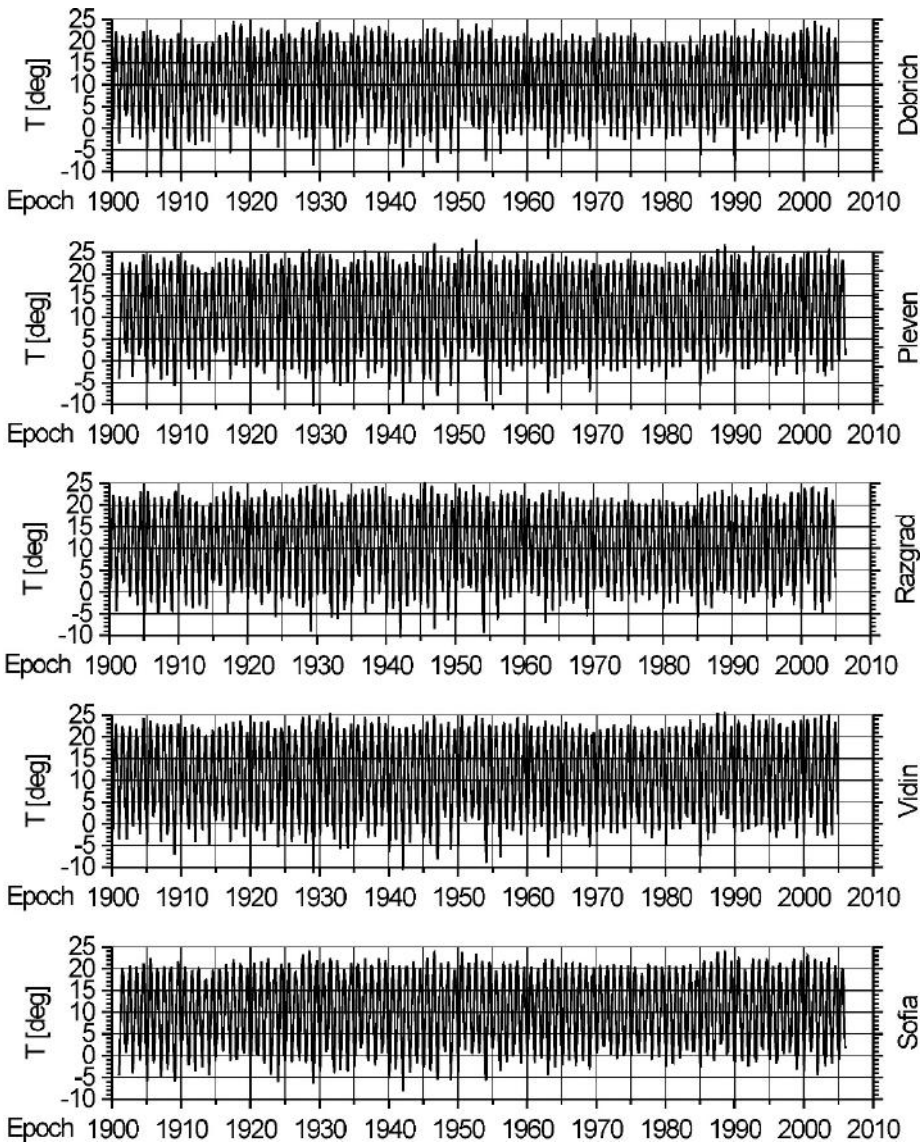


Figure 1. Monthly temperature data from stations Dobrich, Pleven, Razgrad, Vidin and Sofia

1976 with the US Air Force (USAF) and the US National Oceanic and Atmospheric Administration (NOAA) data by D. Hathaway.

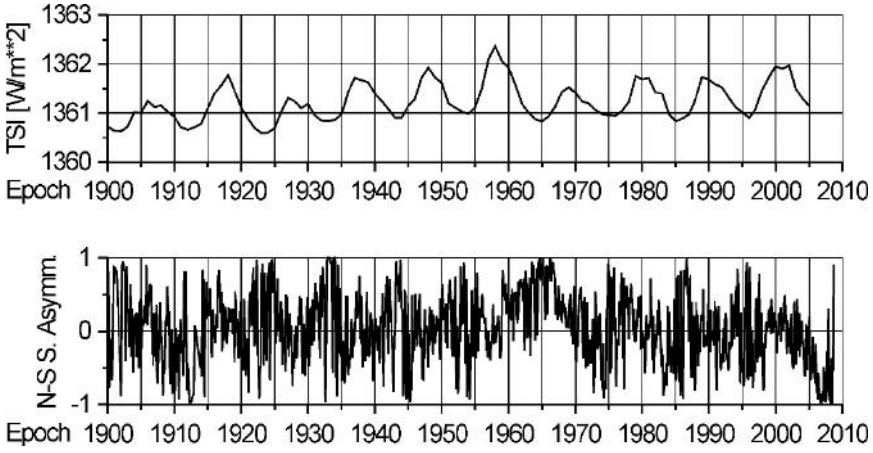


Figure 2. Solar indices TSI and N-S solar asymmetry

METHODS

The time series spectra are determined by the well-known Fast Fourier Transform (FFT). The periodical variations are derived from the data by means of partial Fourier approximation (PFA) based on the Least-Squares (LS) estimation of Fourier coefficients. The Partial Fourier approximation $F(t)$ of time series is given by

$$F(t) = f_0 + f_1(t - t_0) + \sum_{k=1}^n a_k \sin k \frac{2\pi}{P_0} (t - t_0) + b_k \cos k \frac{2\pi}{P_0} (t - t_0), \quad (2)$$

where P_0 is the period of the first harmonic, t_0 - the mean epoch of observations, f_0 , f_1 , a_k and b_k are unknown coefficients and n is the number of harmonics of the partial sum, which covers all oscillations with periods between P_0/n and P_0 . The application of the LS estimation of Fourier coefficients needs at least $2n+2$ observations, so the number of harmonics n is chosen significantly smaller than the number N of sampled data f_i . The small number of harmonics n yields to LS estimation of the coefficient errors. This estimation is the first essential difference with the classical Fourier approximation. The second difference is the arbitrary choice of the period of first harmonic P_0 , instead of the observational time span, so the estimated frequencies may cover the desired set of real oscillations. This method allows a flexible and easy separation of harmonic oscillations into different frequency bands by the formula

$$B(t) = \sum_{k=m_1}^{m_2} a_k \sin k \frac{2\pi}{P_0} (t - t_0) + b_k \cos k \frac{2\pi}{P_0} (t - t_0), \quad (3)$$

where the desired frequencies ω_k are limited by the bandwidth

$$\frac{2\delta m_1}{P_0} \leq \omega_k \leq \frac{2\delta m_2}{P_0} \quad (4)$$

After estimating the Fourier coefficients, it is possible to identify a narrow frequency zone presenting significant amplitude, and defining a given cycle. Then this cycle can be reconstructed in time domain as the partial sum limited to the corresponding frequency bandwidth. Doing this for terrestrial and solar time series, we shall identify their respective cycles, isolate and compare the common ones.

The used time series cover 105-year overlapped time interval for the period 1900.0 – 2005.0. Each time series consist of 1260 monthly data points. The PFA performs estimation of 150 harmonics with the accuracy better than 0.07°C for temperature; 0.02 for N-S solar asymmetry and 0.5mW/m² for TSI.

The seasonal amplitude of temperature variations A_T for each year is calculated by

$$A_T = T_{max} - T_{min}, \quad (5)$$

where the T_{max} is the maximal summer temperature of a given station, and T_{min} – the minimal winter temperature.

RESULTS

The main results of this study are described by analyses of FFT spectra; seasonal and long-term variations of the temperature; thermal trends due to global warming; influence of TSI and N-S solar asymmetry harmonics on temperature oscillations and variations of seasonal components.

FFT spectra

The time series spectra are calculated by the Fast Fourier Transform (FFT) and they are shown in Fig. 3. It is remarkable that the temperature spectra are almost coherent for interannual oscillations, especially for the stations from North Bulgaria. All time series have significant oscillations with periods 2.2, 2.5, 2.8, 3.4, 4.0, 5.2, 7.0 and 10.5 year, so a high correlation between the long-term variations of temperature is expected.

Seasonal and long-term variations of temperature

The amplitudes of seasonal oscillations of the temperature, determined by (5) are shown in Fig. 4. It is visible that these variations consist of a lot identical interannual cycles and the time series are highly correlated. The seasonal components of temperature have common long-term variations and trends. It is remarkable significant positive linear trends after 1975.

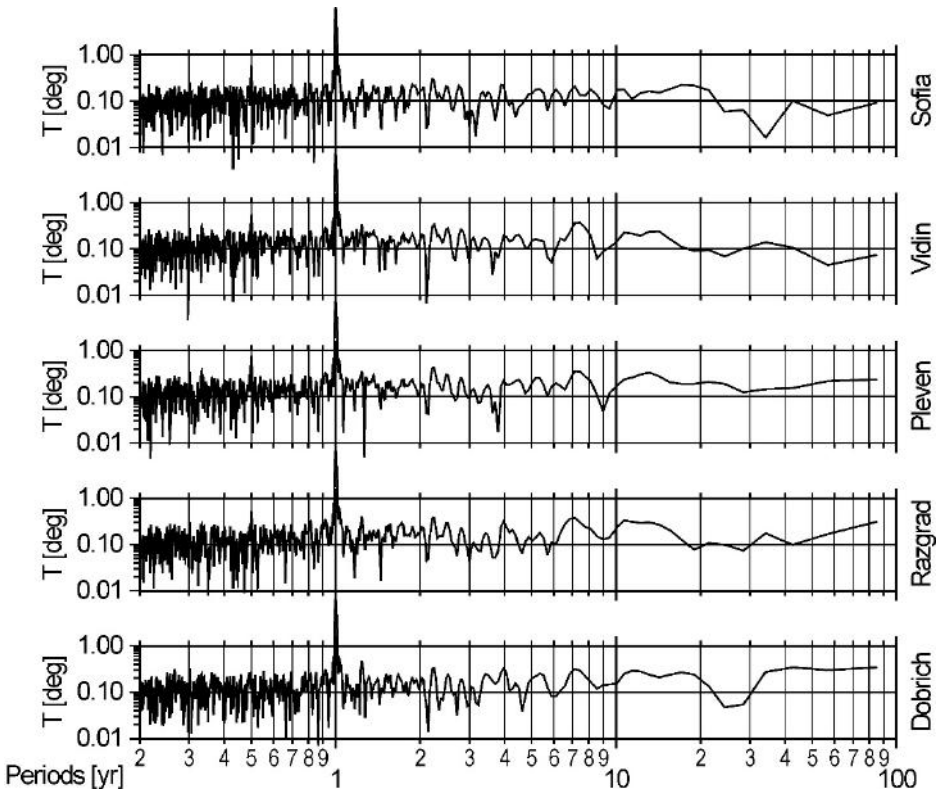


Figure 3. Spectra of temperature variations

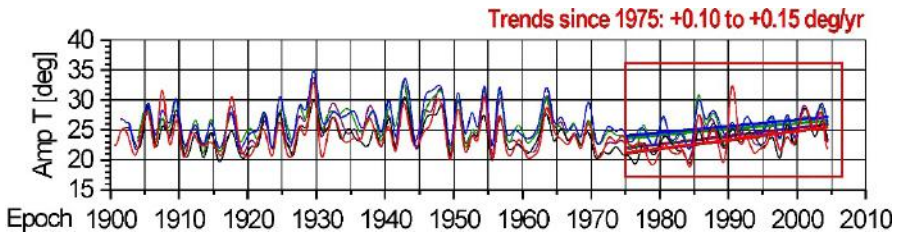


Figure 4. Seasonal amplitudes of temperature at stations Dobrich (red), Pleven (blue), Razgrad (purple), Vidin (green) and Sofia (black)

The long-term oscillations of temperature are separated from the seasonal components as superposition of oscillations with periods 2 – 104yr and 15 – 104yr, determined by the Method of Partial Fourier Approximation (Fig.5). All time series in Fig. 5 are highly correlated with common interannual and decadal cycles. The

common tendency of temperature rise, associated with the global warming, is presented after 1995 for the decadal oscillations with periodicity 15 – 104 years, while in second case (periodicity 2 – 104 years) the positive tendency is after 1980.

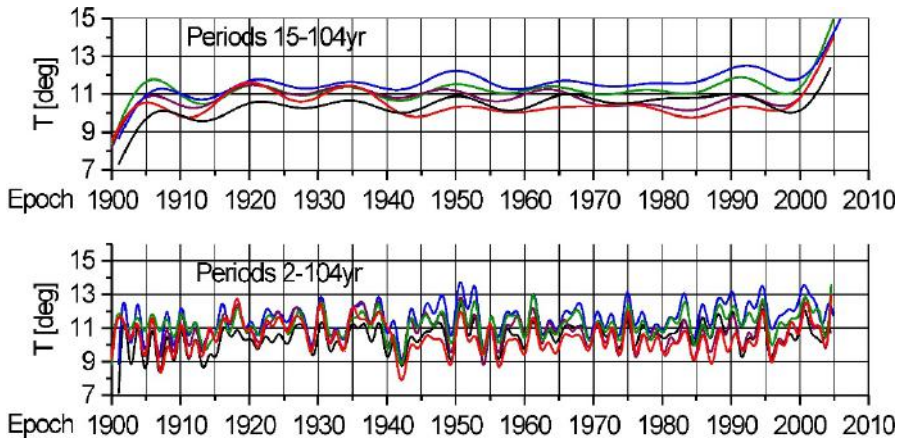


Figure 5. Long-term variations of temperature at stations Dobrich (red), Pleven (blue), Razgrad (purple), Vidin (green) and Sofia (black)

Thermal trends due to global warming

The time series from Fig. 5 are not suitable to determine the response of temperature rise due to global warming, because the time series contain significant interannual and long-term oscillations. The temperature rate from different time series are shown in Table 1.

Table 1. Linear trends of temperature in different time series in [°C/yr]

| Station | Original data | Long-term 2-104yr | Long-term 15-104yr | Seasonal amplitude after 1975 |
|---------|---------------|-------------------|--------------------|-------------------------------|
| Vidin | +0.005 | +0.004 | +0.009 | +0.10 |
| Pleven | +0.011 | +0.010 | +0.015 | +0.11 |
| Razgrad | -0.002 | -0.002 | +0.002 | +0.13 |
| Dobrich | -0.003 | -0.003 | +0.001 | +0.14 |
| Sofia | +0.009 | +0.009 | +0.011 | +0.15 |

The original and long-term time series don't match the temperature rate connected with the global warming. Their rates of linear trends are almost zero or negative. The only exception is the positive rate of seasonal amplitude after 1975, whose value is between +0.010 and +0.15°C/yr (Fig. 4 and Table 1).

Influence of solar harmonics on temperature cycles

The influence of solar harmonics on temperature variations is often hidden, because the major part of solar signals is absorbed by cooling process of evaporation, especially in the case of decadal cycles. Nevertheless, some interannual cycles of the temperature are sensitive to the solar harmonics.

The solar-temperature influence will be demonstrated on data from a single station, because the oscillations are highly correlated with a lot of identical cycles between different stations. The TSI harmonics from period bands 3.6 – 3.7yr; 4.3 – 4.4yr and 5.8 – 6.2yr have excellent agreement with the corresponding oscillation of temperature from station Vidin (Fig.6).

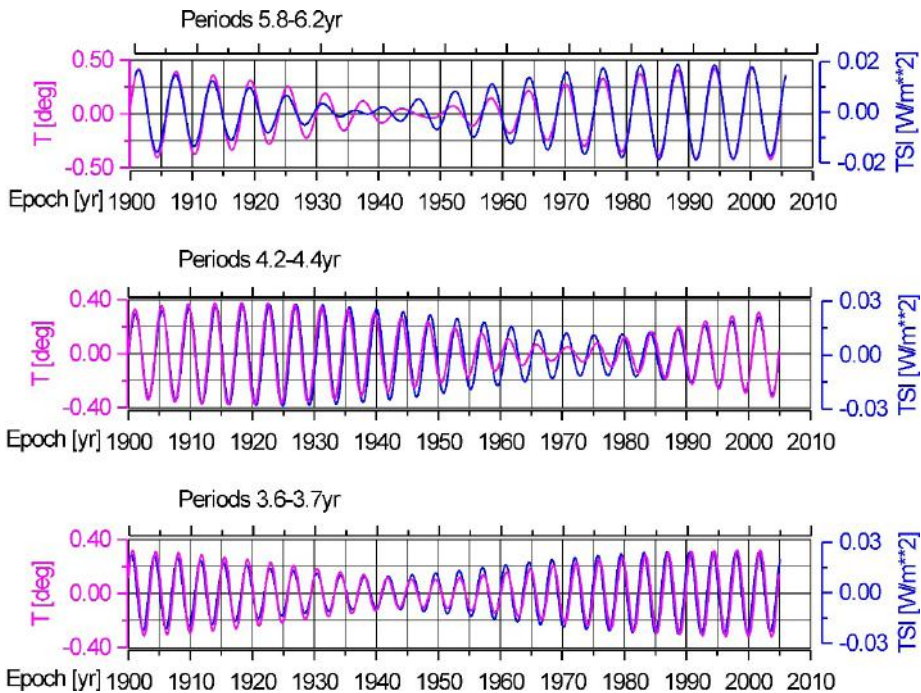


Figure 6. Common interannual cycles of temperature at station Vidin and TSI variations.

The harmonics of N-S solar asymmetry have good agreement with temperature cycles with periods from bands 4.8-5.0yr; 8.7 – 9.5yr and 11.7 – 13.1yr (Fig.7). These solar cycles are connected with the solar magnetic field variations and corresponding influence on the heliosphere and galactic cosmic rays, whose effects on temperature oscillations is explained by the model of Kilifarska.

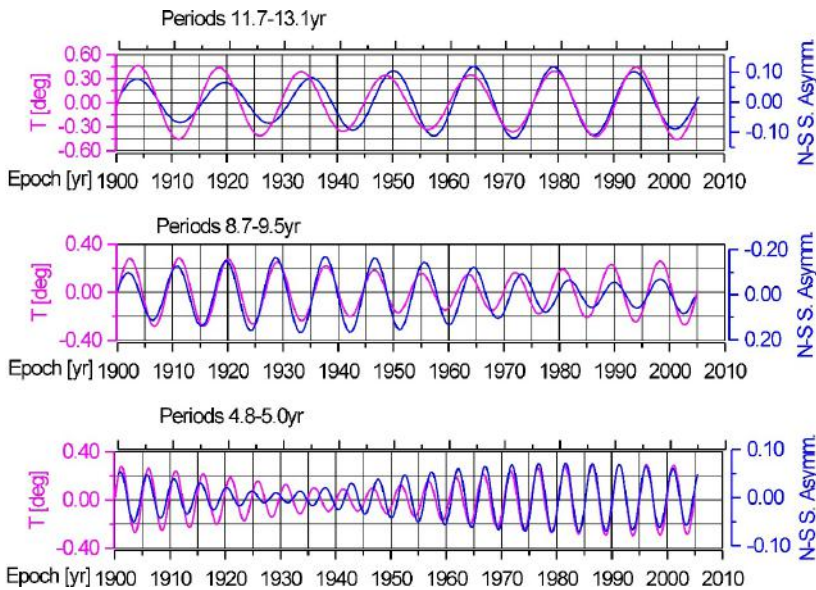


Figure 7. Common cycles of temperature at station Vidin and N-S solar asymmetry variations

Influence of solar harmonics on seasonal variations of the temperature

The seasonal variations are also affected by the solar activity. The amplitudes of seasonal components of temperature have significant interannual and decadal oscillations from the interval $20^{\circ}\text{C} - 30^{\circ}\text{C}$. A part of these oscillations can be explained by the influence of solar harmonics. The TSI harmonics with periods 6.2 – 6.6yr and 7.5 – 81yr have good phase agreement with the amplitudes of seasonal components of temperature at station Sofia (Fig.8). Common cycles with periods 17.2 – 20.6yr of seasonal amplitude of temperature at station Sofia and N-S solar asymmetry with short phase reverse exist (Fig.9). The cumulative effects of these cycles may explain at least 5°C of the observed amplitude of seasonal components.

Temperature variations driven by Schwabe –Wolf and Hale solar cycles

The classical 11-year Schwabe-Wolf and 22-year cycles of solar magnetic field (Hale cycles) also affect temperature variations. The common 10.5-year cycles of temperature and TSI variations are shown in Fig.10. The 10.5-year temperature cycles from all stations have very small phase differences and the solar signal delay is below 3yr. The 21-year cycles of temperature have relatively small phase differences (Fig.11) and the delay of the TSI effects on the temperature is between 0 and 2 years for different stations. The cumulative effects of Schwabe –Wolf and Hale solar cycles on temperature variations is about 0.7°C .

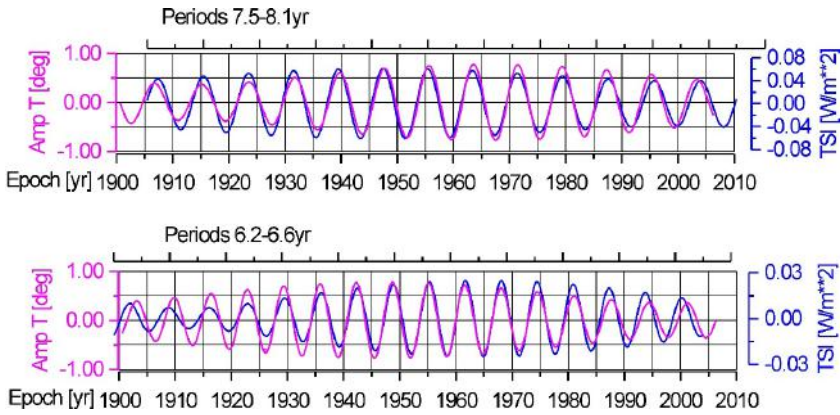


Figure 8. Common cycles of seasonal amplitude of temperature at station Sofia and TSI variations

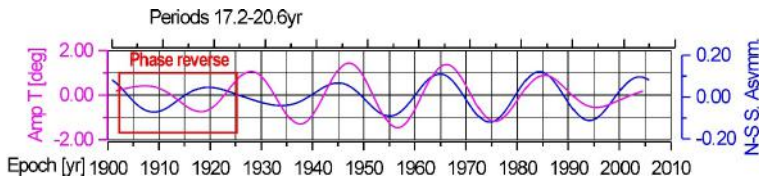


Figure 9. Common cycles of seasonal amplitude of temperature at station Sofia and N-S solar asymmetry variations

CONCLUSIONS

The temperature variations for the period 1900-2005 from 5 Bulgarian stations are analysed and compared with some solar harmonics and cycles. The linear trends, seasonal components and long-term oscillations of the temperature are determined. Almost all of periodic components of observed temperature are highly correlated, including the seasonal variations and long-terms. The linear trends of the centennial time series of temperature don't match the tendency of temperature rise due to the global warming. The global warming signature is discovered in variations of seasonal amplitudes after 1975, where the amplitude rates are between $0.10^{\circ}\text{C}/\text{yr}$ and $0.15^{\circ}\text{C}/\text{yr}$. The 11-year Schwabe-Wolf and 22-year cycles of solar magnetic field (Hale cycles) affect temperature variations with time delay between 0 and 3 years, where the common effect on temperature is about 0.7°C . The TSI and N-S solar asymmetry harmonics have good agreement with the variations of temperature and seasonal amplitudes in narrow frequency bands, whose periods are between 3.6 and 20.6 years. These results may improve climatic models and some long-term forecasts.

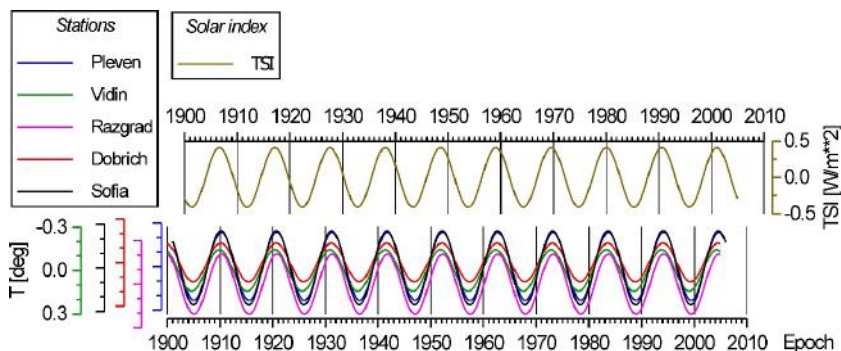


Figure 10. Common 10.5-year cycles of temperature and TSI variations

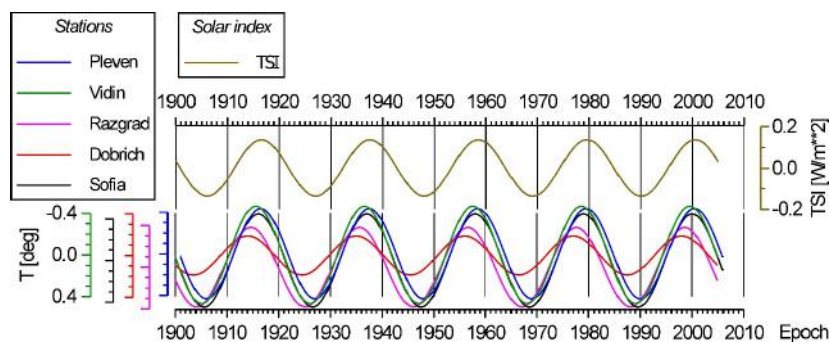


Figure 11. Common 21-year cycles of temperature and TSI variations

ACKNOWLEDGEMENTS

This work has been carried out in the framework of the National Science Program “Environmental Protection and Reduction of Risks of Adverse Events and Natural Disasters”, approved by the Resolution of the Council of Ministers № 577/17.08.2018 and supported by the Ministry of Education and Science (MES) of Bulgaria (Agreement № Д01-322/18.12.2019).

REFERENCES

- Coddington, O., Lean, J.L., Pilewskie, P., Snow, M., Lindholm, D. (2015). A solar irradiance climate data record. *Bull. American Meteorological Soc.* 97(7), 1265 – 1282.
- Georgieva, V., Shopova, N., Kazandjiev, V. (2019). Assessment of conditions in South Bulgaria for spring crop growing using agrometeorological indices. *AIP Conf. Proc.*, Vol. 2075, Iss. 1, id.120014

- Kazandjiev V., Shopova N., Georgieva V. (2018). Hydrothermal conditions during vegetation season and spring crop growing in Plovdiv region. *Journal of Balkan Ecology*, 21, 1, *PublishScieSet-Eco Publisher*, 2018, 23 – 38.
- Kilifarska, N.A. and Haight, J.D. (2005). The impact of solar variability on the middle atmosphere in present day and pre-industrial atmospheres. *J. Atmos. Solar Terr. Phys.*, 67, 3, 241 – 249.
- Kilifarska, N.A., Tassev, Y.K. and Tomova, D.Y. (2008). Cosmic ray showers and their relation to the stratospheric sudden warmings. *Sun and Geosphere*, 3, 1, 10 – 17.
- Kilifarska, N.A. (2011). Long-term variations in the stratospheric winter time ozone variability – 22 year cycle. *Comptes rendus de l'Académie bulgare des Sciences*, 64, 6, 867 – 874.
- Kopp, G., Krivova, N., Lean, J., and Wu, C.J. (2016). The Impact of the Revised Sunspot Record on Solar Irradiance Reconstructions, *Solar Physics*. doi: 10.1007/s11207-016-0853-x
- Lean, J.L. (2010). Cycles and Trends in Solar Irradiance and Climate, Wiley Interdisciplinary Reviews, *Climate Change* 1. doi: 10.1002/wcc.018.
- Shopova, N., Alexandrov V., Todorova G. (2019). Cluster analysis of the highest daily temperature amplitudes in some agricultural regions of Southeastern Bulgaria, *Proc. First Sci. Conf. "Climate, atmosphere and water resources in the face of climate change"* Sofia, 14 – 15 October 2019, 64 – 72.
- Slavcheva-Sirakova, D., Shopova, N., Kostadinov, K., Filipov, S., Velichkova, K. (2020). Climate analysis and effects of abiotic stress on salad grounded in underground greenhouse and outdoor and effects of organic fertilizers in the fight with stress factors. *Proc. Conference "Agriculture for Life, Life for Agriculture"*, Bucharest 4 – 6 June 2020.
- Velinov, P.I.Y., Mateev L. and Kilifarska N.A., (2005). 3-D model for cosmic ray planetary ionisation in the middle atmosphere. *Ann. Geophys.*, 23, 9, 3043 – 3046.

✉ **Yavor Chapanov**

<http://orcid.org/0000-0002-6159-3554>

Climate, Atmosphere and Water Research Institute
Bulgarian Academy of Sciences (CAWRI-BAS)

Sofia, Bulgaria

E-mail: yavor.chapanov@gmail.com

STUDY OF ONE MONTH EVENT OF HIGH PM POLLUTION FOR SOFIA REGION

Margret Velizarova¹, Reneta Dimitrova^{1,2}

¹ *“St. Kliment Ohridski” University of Sofia*

² *National Institute of Geophysics, Geodesy and Geography –
Bulgarian Academy of Sciences (NIGGG –BAS)*

Abstract: The habitants in Bulgarian capital city are unfortunately still exposed to high levels of particulate matter (PM) despite a lot of efforts made by the government and municipality during the last decades. A high resolution modelling using ADMS-Urban system was carried out for prolonged one month (January 2014) event with elevated levels of PM concentration for Sofia region. Four main emission sources (point industrial, domestic heating, roads and non-well defined transport) were taken into account for this study. Although this type of modelling accounts only for the local sources and has some deficiency, it can be very useful tool for estimation of the contribution of each source type to the concentration field and also allows to simulate different scenarios for future emission reduction that can help the authorities in decision making.

Keywords: Air quality modelling, PM pollution in Sofia, ADMS-Urban model.

INTRODUCTION

Air pollution causes great harm to European citizens' health and about 400 000 people die prematurely due to excessive air pollutants such as dust particles, nitrogen dioxide and ozone each year (EU Special Report, 2018). Around one-quarter of Europeans living in urban areas were exposed to air pollutant levels exceeding some EU air quality standards and up to 96% of EU citizens living in urban areas were exposed to levels of air pollutants considered by the WHO as damaging to health (EEA, 2018). Lost years of healthy life in some EU Member States are similar to countries often associated with poor air quality, such as China and India and unfortunately Bulgaria is the leader in this bad statistics with almost 2.5 lost years of healthy life from ambient air pollution per hundred inhabitants (EU Special Report, 2018).

The air quality in big cities is substantially affected by anthropogenic pollutant emissions and weather patterns. Most harmful for the Bulgarian big cities like Sofia and Plovdiv is particulate matter (PM) pollution during the winter according to the national reports on the state and protection of the environment for 2010-2014.

Plenty of work in the field of the regional air quality modelling has been made in Bulgaria in the last two decades (Gadzhev et al., 2014a, b; Georgieva et al., 2015, 2017; Syrakov et al., 2015, 2016), most of the simulations are based on the US EPA WRF (Skamarock et al., 2008) - CMAQ (Byun and Schere, 2006) system. Advantages of these models include the ability to use temporally and spatially varying meteorology and model chemical reactions, but due to used parametrizations of physical processes however, these models have restrictions of grid resolution (finest is usually 1 km). ADMS-Urban system (CERC, 2017) is a city-scale model that resolves concentration fields explicitly representing the near-field features of the dispersion of emissions with very high resolution (meters). Furthermore it can be nested within the regional model CMAQ and this approach accounts for the full range of temporal and spatial scales (Stoker et al., 2012), which will be subject of our future work.

A lot of efforts were made by the government and Sofia municipality during the last decades, but unfortunately the capital city habitants are still exposed to high levels of PM₁₀ (defined according European Union DIRECTIVE 2008/50/EC; EEA, 2008). High resolution modelling is carried out for prolonged one month event with elevated levels of PM concentration for Sofia region. The case study was selected based on observations with persistent elevated levels of PM in January 2014. The main goal is to estimate the abilities of the ADMS-Urban to capture the concentration pattern using available detailed emission inventory developed for Sofia and fill the missing details of concentration of the pollutants.

METHODOLOGY AND MODEL SET-UP

ADMS-Urban system

ADMS-Urban is a comprehensive system for modelling air quality and it is being used across the world for air quality management and assessment studies of complex situations in urban areas, cities, towns and close to motorways, roads and large industrial areas (Stoker et al., 2012; Hood et al., 2018; Biggart et al., 2020). The “local” Gaussian type model with integrated street canyon model is nested within a trajectory model so that significant areas may be considered. ADMS-Urban is significantly more advanced than most of the other air Gaussian type dispersion models in that it incorporates the latest understanding of the boundary layer structure, using advanced algorithms for the height-dependence of wind speed, turbulence and stability to produce improved predictions. The model also takes account of the impacts of street canyons on dispersion, turbulence and mixing induced by traffic, and includes a photochemical model for NO_x and ozone. Predicting pollutant concentrations from an urban area is a complex modelling problem. ADMS-Urban has been developed with a number of features to simplify the modelling process and help users.

Model set-up

The domain in this study covers Sofia city and suburbs, approximately 38 km by 32 km, with grid resolution of 50 m (Figures 1a-d). Spatial data entered into ADMS-Urban should be in a Cartesian coordinate system measured in metres in one of the available geographic projections. Different number of vertical levels can be exploited, but high number increases the computational time significantly. We have used only 2 levels for this study as we consider only surface concentration. All different types of sources – point (industrial stacks), roads, domestic heating and not well-defined transport are mapped into the selected domain. We have used in this study detailed emission inventory developed for Sofia municipality, published and described in details in Sofia municipality reports (2017; 2019). The emissions required very detailed shape description for line and area sources, while point sources are defined by their geographical coordinates transferred in the study domain. All sources were described into details and their locations are presented in Figure 1(a-d).

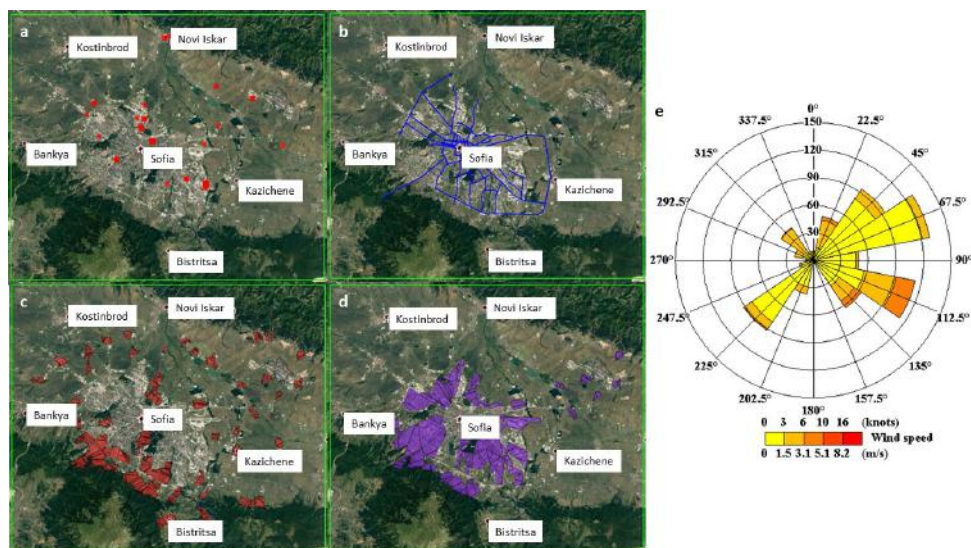


Figure 1. Map for simulations with all types of emission sources included – (a) point (industrial stacks), (b) roads, (c) domestic heating and (d) not well-defined transport; and (e) wind rose at Druzhdza site for January 2014

One month of simulations for January 2014 was selected based on 10-years of record of hourly concentrations of PM_{10} taken from the official air quality network (EEA, <http://eea.government.bg/kav/>), for the stations located in Sofia (Druzhdza, Nadezhda, Pavlovo, Hipodruma, Orlov most). In addition, concentrations of $PM_{2.5}$ at Hipodruma

station were used. The mountain site Kopitoto, located near Sofia, was used as a background station in this study. The meteorological conditions (measured also at each site) were prescribed from Druzhba site, as it consists full record of hourly data with a few missing records only, which were reconstructed based on interpolation method integrated into the model, taking the available values from the nearest hours. The meteorological variables used in this study are hourly data for wind speed (minimum 0.75 ms^{-1} is required) and direction, temperature, relative humidity, incoming solar radiation (when data are missing for cloud cover). The local meteorological conditions for the simulated period were low wind velocity (less than 2 ms^{-1}) and predominant south-eastern and north-eastern flow. Wind rose for January 2014 is shown in Figure 1e. ADMS-Urban was run daily providing 24-h average concentration outputs for the entire domain and prescribed locations, corresponding to the measurement sites.

ADMS-Urban allows a lot of additional options that we applied in this study. Sofia valley has a complex topography that affects the pollution transport and this option was included with the model runs. The effect of complex terrain is modelled by changing the plume trajectory and dispersion to account for disturbances in Monin-Obukhov length. Turbulence is considered using three sets corresponding to unstable (convective), near neutral and stable conditions, based on Monin-Obukhov length and corresponding to different diffusivity coefficients. Loss of the airborne concentration of pollutant occurs by dry and wet deposition. Wet deposition did not apply in this study as there was no precipitation data for this period. The plume rise module predicts the trajectory, enhanced spread and inversion penetration of a buoyant jet or plume, given the conditions at the source and in the external environment. This module was applied to the industrial point sources requiring additional data for the temperature, flow velocity and geometry of the stack (height and diameter). The basic street canyon module was used for the road sources which required additional information such as the coordinates of each road segment and averaged parameters for road width and canyon height. Only primary pollutants were modelled, chemical reactions were not included in this study.

RESULTS AND DISCUSSION

The study period of high polluted PM event for Sofia region covers one month. Maps with the average concentration of PM_{10} and $\text{PM}_{2.5}$ for January 2014 are shown in Figure 2. These maps present contribution of all main sources with added background concentration calculated for each day from the measurements at Kopitoto site. Main polluted areas are located near the busy roads and cover the villages surrounding the city, where the domestic heating emissions are coming from wood and coal burning. Note, that emission inventory for PM_{10} and $\text{PM}_{2.5}$ differ, as for PM_{10} the basic year is 2014 (the modelling year), for the $\text{PM}_{2.5}$ 2017 is taken as a basic year (Sofia municipality report, 2017; 2019). The $\text{PM}_{2.5}$ inventory covers several additional sources in Lozenec, Malinova Dolina, Gorna Bania,

Ovtscha Kupel, Suhodol, Vitosha, Bakston and Manastirski Livadi, which are included for $PM_{2.5}$, but not for PM_{10} simulations.

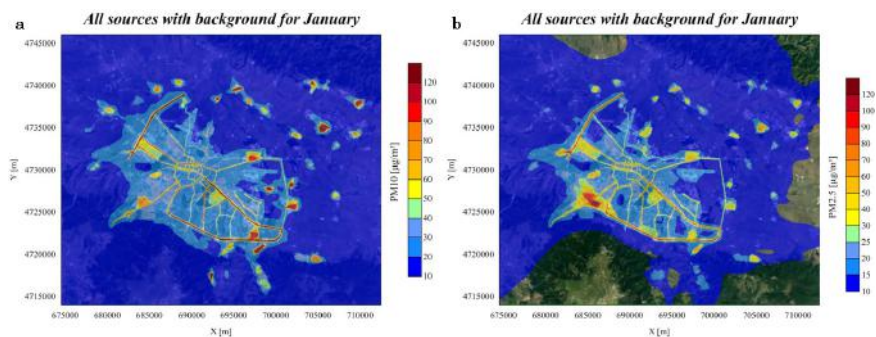


Figure 2. Maps of the average concentration of PM_{10} (a) and $PM_{2.5}$ (b) from all sources with added background concentration for January 2014

Estimated contribution of each separate source to the total concentration field, with the impact (presented in %) are shown for all main four sources (Figures 3 – 6). Two more sources – from construction and repair activities, and landfills and quarries, were included and tested in simulations, but their contribution was less than 1% and they are excluded from the analysis.

Figure 3 shows that the pollution related to domestic heating is higher in the villages around Sofia, especially those, located in the proximity to the mountain slopes north (Stara Planina) and south (Vitosha and Plana mountains), more likely due to the effect of complex topography that affects the local circulation. For these areas the contribution of domestic heating is between 80 to 100 %.

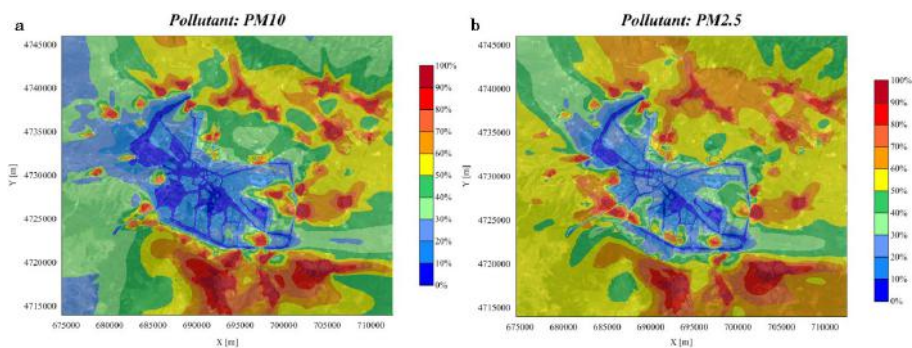


Figure 3. Contribution of domestic heating to averaged concentration fields for PM_{10} (a) and $PM_{2.5}$ (b) from all sources for January 2014

Figure 4 presents the pollution due to the main busy roads with most significant contribution to central city area and ring road around Sofia. Note, that the newly developed north tangent from the ring road is not included into simulations, as the last available developed emission inventory, used in this study, covers previous periods (2014 for PM_{10} and 2017 for $PM_{2.5}$). The most polluted areas with contribution between 80 -100 % due to traffic are nearby boulevards “Tsarigradsko shose”, “Slivnitsa”, “Todor Aleksandrov”, “Botevgradsko shose”, suburbs Gorublene – Pancharevo, the south ring road in proximity of Vitosha mountain, as well as the north-western ring road, which gives connection between big residential areas – Nadezhda, Obelya, Lyulin and “Struma” motorway.

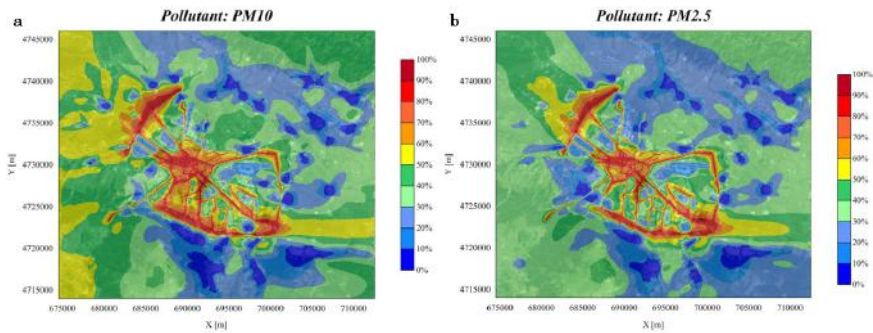


Figure 4. Contribution of main roads to averaged concentration fields for PM_{10} (a) and $PM_{2.5}$ (b) from all sources for January 2014

Figure 5 shows contribution of pollution due to not well-defined transport, considered in this study as a volume source with vertical extension of 1m. These sources correspond to the residential areas and the emission is calculated based on

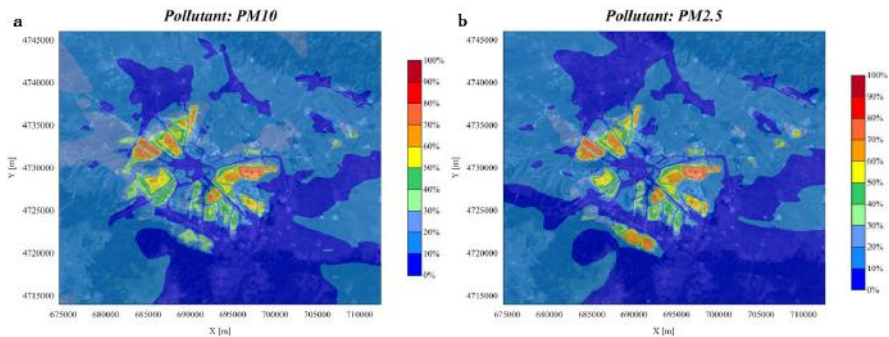


Figure 5. Contribution of not well-defined transport sources to averaged concentration fields for PM_{10} (a) and $PM_{2.5}$ (b) from all sources for January 2014

population living in the area and registered vehicles. This source provides between 50 – 80% of the total concentration in the described big residential regions and the Sofia airport area.

The impact of the industrial point sources is much lower (less than 50%) in comparison to the other sources (Figure 6). The main contribution they have in the northern part of the Sofia valley where a cluster of objects is located in the industrial city area (in proximity to Nadezhda residential area), power plants “Iztok”, “Sofia”, “Lyulin” and big industrial sources in Novi Iskar.

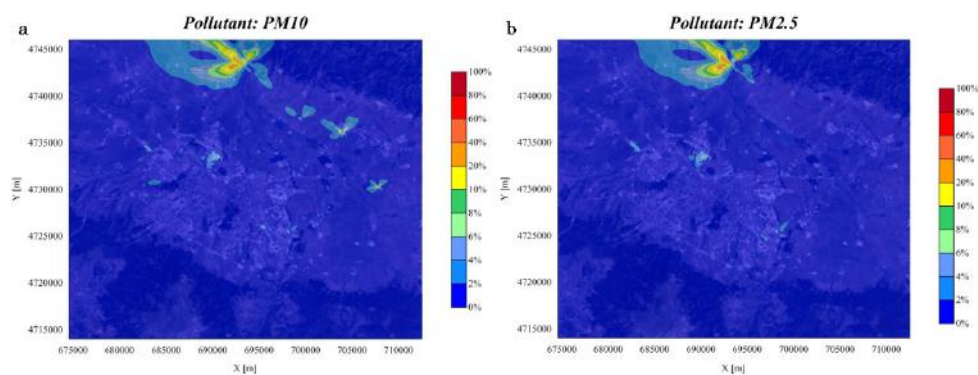


Figure 6. Contribution of point industrial sources to averaged concentration fields for PM_{10} (a) and $PM_{2.5}$ (b) from all sources for January 2014

Direct comparison at selected locations (observational sites) shows that simulated concentrations are much lower than observed for some periods (especially 3-8, 18-19 January 2014), which is not surprising, as the modelling considers only primary pollutants and these periods correspond to very high stable conditions favourable for long living pollution in the atmosphere and possible secondary pollution formation (Figure 7). Also this study do not take into account for possible transport coming from sources located out of the study area. The background concentration, taken at the Kopitoto station, cannot provide information on additional transport due to local circulation and for some cases is not representative enough.

The evaluation of the performance of WRF-CMAQ air quality modelling system in Bulgaria also shows significant underestimation of PM_{10} concentration especially during the winter period (from October to March), when modelled values are 2-4 times lower than observed ones (Georgieva et al., 2015, Syrakov et al., 2015), which is in agreement with the presented study. This deficiency in air quality modelling in regional and local scale pointed out for a possible problem with the emission inventory for the Sofia region and more efforts needed in this direction.



Figure 7. Comparison of simulated 24-h concentration (with and without background concentration taking account) at all available measurement sites for January, 2014

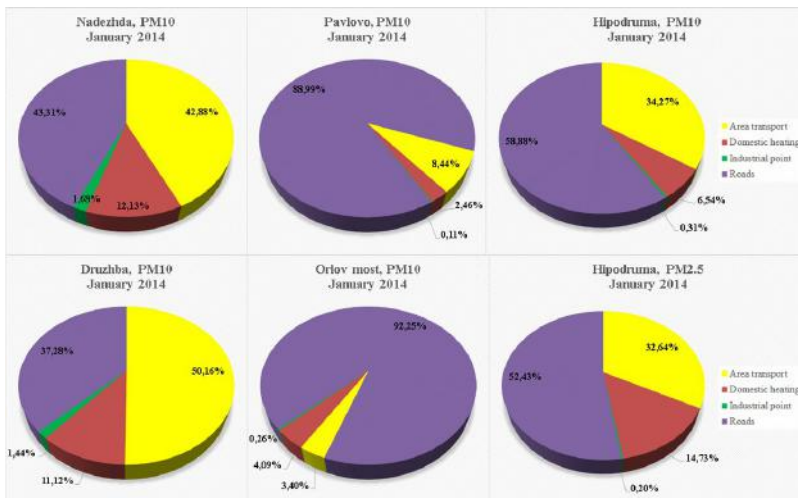


Figure 8. Contribution of different sources to concentration at locations of the air quality stations for January, 2014

In spite of this deficiency, simulations are useful for estimation of the contribution of the local sources at the selected receptors (Figure 8). It is obvious that stations Pavlovo, Hipodruma and Orlov most mostly account for the traffic pollution (more

than 50%). Nadezhda and Druzhba stations are located in a residential areas and high contribution (~50%) have the not well-defined area transport and only less than 2% due to the point industrial sources. The domestic heating produces almost double concentration for $PM_{2.5}$ in comparison with PM_{10} (see Hipodruma site). The contribution of domestic heating to PM_{10} concentration is also visible at all sites, but predominant at Nadezhda and Druzhba, most likely because they are located in the suburbs in proximity to satellite villages around Sofia.

CONCLUSIONS

In spite of efforts made by the Sofia municipality, the air quality is still poor, especially related to PM (Sofia municipality report, 2017; 2019). The most favourable for smog formation are meteorological conditions during the winter, due to formation of prolonged inversions and low turbulence under calm conditions related to non-dynamic (anticyclonic) weather. One month with very high PM pollution registered by the official air quality stations was simulated by ADMS-model. Although this type of modelling account only for the local sources, it can be very useful tool for estimation of the contribution of each source type to the concentration field, and it allows to simulate different scenarios that can help the authorities in the decision making. Only primary pollutants (PM_{10} and $PM_{2.5}$) were modelled (chemical transformations are not included) with meteorological hourly data measured at Druzhba station, which can be comment as a deficiency of the study. But a lot of additional options available with the sophisticated Gaussian model (ADMS-Urban) allow to make advanced estimation of the local pollution, much better than using other models from this type for air quality assessment.

The main findings in this study are:

I) Modelling of PM_{10} and $PM_{2.5}$ concentrations with ADMS-Urban shows very high levels ($200 \mu\text{gm}^{-3}$) at the villages around Sofia, where air quality measurements are not available at present.

II) Contribution of transport (from the main busy roads and area non well-defined transport) is much higher than input from other sources.

III) Domestic heating is significantly important in the suburban satellite villages around Sofia and its contribution to the central city area is low, less than 20% for PM_{10} and less than 30% for $PM_{2.5}$.

IV) Contribution of industrial point sources is very low, less than 5% in the area in close proximity to the main source for the simulated case, but keep in mind that the pattern can be different under strong winds when the pollution can affect areas on larger distances.

V) Direct comparison with the measurement shows that local primary emissions contribute only partly to the measured concentrations and the rest is more likely due to several possible reasons – underestimation of the emissions, secondary pollutants and transport from the sources outside of the domain.

VI) This work has pointed out the need for updated and reliable detailed emission inventory for Sofia, including all different types of sources and pollutants. Developed new atmospheric air quality management program for Sofia municipality and future work on this topic can contribute significantly to improve air quality modelling for the region.

ACKNOWLEDGMENTS

This work has been carried out in the framework of the National Science Program "Environmental Protection and Reduction of Risks of Adverse Events and Natural Disasters", approved by the Resolution of the Council of Ministers № 577/17.08.2018 and supported by the Ministry of Education and Science (MES) of Bulgaria (Agreement № Д01-322/18.12.2019).

We acknowledge the provided access to the e-infrastructure of the NCDSC – part of the Bulgarian National Roadmap on RIs, with the financial support by the Grant No D01-221/03.12.2018.

REFERENCES

- Biggart, M., Stocke, J., Doherty, R.M., et al. (2020). Street-scale air quality modelling for Beijing during a winter 2016 measurement campaign. *Atmos Chem Phys*, 20(5), 2755-2780.
- Byun, D. & Schere, K.L. (2006). Review of the Governing Equations, Computational Algorithms, and Other Components of the Models-3 Community Multiscale Air Quality (CMAQ) Modeling System, *Applied Mechanics Reviews*, 59, 51-77.
- CERC, (2017). *CERC_ADMS-Urban4.1.1_User_Guide.pdf*.
- European Court of Auditors, (2018). *Air pollution: Our health still insufficiently protected. Report N°23*.
- European Environment Agency (2008). Directive 2008/50/EC of the European Parliament and of the Council of 21 May 2008 on ambient air quality and cleaner air for Europe. *OJL 152, 11.6.2008*, 1–44.
- European Environment Agency (2018). *Environmental indicator report 2018*, EEA No 19/2018, Luxembourg.
- Gadzhev, G., Ganey, K., Miloshev, N., Syrakov, D. & Prodanova, M., (2014a). Some basic facts about the atmospheric composition in Bulgaria - Grid computing simulations, *8353 LNCS*, 484-490.
- Gadzhev, G., Ganey, K., Miloshev, N., Syrakov, D. & Prodanova, M., (2014b). Analysis of the processes which form the air pollution pattern over Bulgaria, *8353 LNCS*, 390-396.
- Georgieva, E., Syrakov, D., Prodanova, M., Etropolska, I. & Slavov, K. (2015). Evaluating the performance of WRF-CMAQ air quality modelling system in Bulgaria by means of the DELTA tool. *IJEP*, 57(3-4), DOI: 10.1504/IJEP.2015.074512.

- Georgieva, I., Gadzhev, G., Ganev, K., Melas, D. & Wang, T. (2017). High Performance Computing Simulations of the Atmospheric Composition in Bulgaria and the City of Sofia, *Cybernetics and Information Technologies*, 17(5), DOI: 10.1515/cait-2017-0053.
- Hood, C., MacKenzie, I., Stocker, J., Johnson, K., Carruthers, D., Vieno, M. & Doherty, R. (2018). Air quality simulations for London using a coupled regional-to-local modelling system. *Atmos Chem Phys*, 18, 11221-11245.
- Skamarock, W.C., Klemp, J.B., Dudhia, J., et al. (2008) A Description of the Advanced Research WRF Version 3. *NCAR Technical Note, NCAR/TN-475+STR*
- Sofia municipality, (2017). *Atmospheric air quality management program of capital municipality for the period 2015-2020 – reduction of emissions and reach of the established norms for fine particles PM_{10}* (in Bulgarian).
- Sofia municipality, (2019). *Program for supplementation of the program Atmospheric air quality management program of capital municipality for the period 2015-2020 - reduction of emissions and achievement of the established norms for fine particles PM_{10} , by indicators fine particles with size up to 2.5 microns and polycyclic aromatic hydrocarbons.* (in Bulgarian).
- Stocker, J., Hood, C., Carruthers, D. & McHugh, C. (2012). ADMS-Urban: developments in modelling dispersion from the city scale to the local scale. *IJEP*, 50(1/2/3/4), 308-316.
- Syrakov, D., Prodanova, M. & Georgieva, E. (2015). Performance of the Bulgarian WRF-CMAQ modelling system for three subdomains in Europe. *Física de la Tierra*, 27, 137-153.
- Syrakov, D., Prodanova, M., Georgieva, E., Etropolska & I., Slavov, K. (2016). Simulation of European air quality by WRF-CMAQ models using AQMEII-2 infrastructure. *J Comput Appl Math*, 293, 232-24.

✉ **Margret Velizarova**

Department of Meteorology and Geophysics
Faculty of Physics
“St. Kliment Ohridski” University of Sofia
Sofia, Bulgaria
E-mail: margretv@phys.uni-sofia.bg

✉ **Reneta Dimitrova**

<http://orcid.org/0000-0002-5931-8713>
Department of Meteorology and Geophysics
Faculty of Physics
“St. Kliment Ohridski” University of Sofia
National Institute of Geophysics, Geodesy and Geography
Bulgarian Academy of Sciences
Sofia, Bulgaria
E-mail: r.dimitrova@phys.uni-sofia.bg

SATELLITE DATA ASSIMILATION OF AIR QUALITY PARAMETERS IN BULGARIA

Dimitër Syrakov^{1,2}, Maria Prodanova^{1,2}, Emilia Georgieva¹

¹*National Institute of Meteorology and Hydrology (NIMH)*

²*National Institute of Geophysics, Geodesy and Geography –
Bulgarian Academy of Sciences (NIGGG-BAS)*

Abstract The operational Bulgarian Chemical Weather Forecast System (BgCWFS) was modified and applied for assimilation of satellite retrieved atmospheric chemistry parameters - Aerosol Optical Depth (AOD) and columnar values of NO₂ and SO₂. The work outlines the methodology based on calculation of correction factors between model estimated and satellite derived parameters. Two model simulations for August 2017 and February 2019 are made – Model Run (without satellite data assimilation – *mod-run*) and Satellite Run (with satellite data assimilation – *sat-run*) for all 5 domains of BgCWFS. In the paper the effect of the assimilation is demonstrated stressing mainly on the difference between *sat-* and *mod-*runs. The comparison of *sat-run* results with observations and with third party modelling results are object of other publications.

Keywords: Modelling air quality, satellite retrieve data, GOME-2, MetOP satellites, data assimilation

INTRODUCTION

Satellite derived air pollution data are nowadays increasingly used in combination with comprehensive chemical transport models (CTM) for better description of the atmospheric composition and for improved forecast of pollutants concentrations at ground level (Benedetti et al., 2009, Park et al., 2011, Gadzhev et al., 2015). In the last few decades, major efforts are put on improving modeled aerosol parameters, as aerosols play significant role in the Earth's energy budget and climate. Aerosols in the atmosphere are product of complex interactions between sources and chemical transformations at different scales, determining their high variability in space and time (Boucher, 2015). Satellites provide information for AOD that is a measure of the aerosol loading in the entire atmospheric column. They could provide information for sources, typically not included in the models, such as dust storms and wild fires. Together with aerosol parameters (AOD, AAI etc.) some gaseous parameters are retrieved. In the article

the effects of similar assimilation of two gaseous parameters – columnar values of NO₂ and SO₂ – is presented.

The purpose of this work is to establish a methodology for satellite data assimilation in the current Bulgarian Chemical Weather Forecast System and to discuss some preliminary results from simulations for two one-month periods. Up to now, satellite data are not used in relation to air quality in Bulgaria. This work is the first attempt to benefit from available satellite data for better understanding and simulating air quality parameters in the country.

THE MODELING SYSTEM

The Bulgarian Chemical Weather Forecast System (Syraikov et al., 2013, 2014) is based on the state of the art WRF-CMAQ modelling chain. WRF v3.6 (Skamarock & Klemp, 2008) is used as meteorological pre-processor to the CMAQ model, v4.6 (Byun & Schere, 2006). The nesting capabilities of both models are used; they are run over five nested domains – Europe (EU, 81 km horizontal resolution), Balkan Peninsula (BP, 27 km), Bulgaria (BG, 9 km), Sofia district (SD, 3 km) and Sofia city (SC, 1km). WRF is fed by the forecast/reanalyse production of the US NCEP (National Centres for Environmental Prediction). As far as this data is global, it provides the initial and boundary meteorological conditions for WRF as well. The chemical boundary conditions over the mother domain (Europe) are set according to the climatic profiles, embedded in the CMAQ software. The presumption is that the possible errors decrease inside the domain because of the continuous action of pollution sources. The boundary conditions for each of the other domains are determined from the senior one.

The physical parameterisations selected for WRF are the well-known and widely used Kain-Fritsch scheme for the cumulus parameterization, YSU for PBL, WSM6 for microphysics, RRTM for radiation, Noah for land-surface model, RADM for wet deposition of gases and particulates. The exploited version of CMAQ uses CBIV as gas-phase chemical mechanism and ISORROPIA 1.7 for inorganic aerosol thermodynamics/partitioning. The emissions are based on the inventory, provided by TNO (The Netherlands Organization for Applied Scientific Research) for 2010 for Europe (Kuenen et al., 2014). For Bulgaria, national emission inventories for 2015 are used.

SATELLITE DATA ASSIMILATION DESCRIPTION

AOD calculations

AOD is not routinely calculated in BgCWFS as well as in the most of the CTMs. Different algorithms are described in the literature. Results from testing some of them for calculating AOD at 550 nm are reported in (Syraikov et al., 2019). Finally, the FlexAOD software (Curci, 2012, Curci et al., 2015) is chosen for post-processing of CMAQ estimated profiles of aerosols species. The algorithm is based on the Mie theory and the tool has a version consistent with the CMAQ

output. It is well known that models usually underestimate the particulate matter concentrations. The assimilation of satellite retrieved AOD is supposed to improve this shortcoming.

Assimilation technology

For BgCWFS we consider aerosol data provided by GOME-2 instrument on board of MetOpA, MetOpB and MetOpC satellites. An objective analysis scheme (called further ANALIZ) is used for combining model estimated and satellite retrieved data (AOD and columnar densities of NO₂ and SO₂). The object analysis scheme is original one, based on calculation of autocorrelation functions and application of spline interpolation.

The analyzed data is used to calculate the correction factors between model estimated and satellite assimilated parameters – different factors for AOD, NO₂ and SO₂. The gridded values of the correction factors are then used to correct the concentrations of different pollutants (Fig.1). The correction factor of AOD is applied to all particle variables and is one and the same for all levels. The correction factor of NO₂ and SO₂ is applied to the respective variable profiles. In such a way new fields for the satellite passage hour are produced serving as initial condition for further CMAQ calculations.

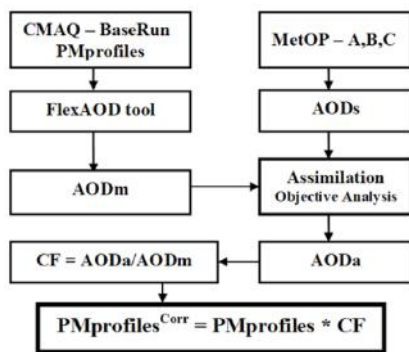


Figure1. Scheme for use of satellite retrieved AOD in BgCWFS for the satellite overpass hour Hs.

BgCWFS is modified in a way to organize pseudo-operational (real time) satellite data assimilation. The main data stream for one day is as follows:

1. Performs full-day CMAQ integration with initial conditions from the previous day. Concentrations for the whole day are obtained – CONC(00÷24)
2. Prepares new initial condition (IC) for satellite passage hour Hs performing:
 - a. Prepares the satellite data as input to ANALIZ (for Hs).

- b. Extracts and saves CONC(00÷Hs-1).
 - c. Extracts and saves CONC(Hs).
 - d. Prepares input for FlexAOD (for the whole day).
 - e. Runs FlexAOD.
 - f. Prepares AOD data as input to ANALIZ (for Hs).
 - g. Prepares NO₂ and SO₂ columnar data as input to ANALIZ (for Hs).
 - h. Runs ANALIZ (for AOD, NO₂ and SO₂ for Hs).
 - i. Calculates Correction Factor (CF) for AOD, NO₂ and SO₂ (for Hs).
 - j. Modifies PM, NO₂ and SO₂ fields by CF - new IC for Hs.
3. Performs a part-day CMAQ integration for $h=Hs\div 24 - \text{CONC}(Hs\div 24)$.
 4. Concatenates CONC(00÷Hs-1) with CONC(Hs÷24:00) – new CONC(00÷24)

The assimilation is taking place in the first three model domains of BgCWFS (EU, BP and BG). The remaining two domains (SD and SC) obtain satellite influence via their boundary conditions, calculated from the senior domains. This is made because of the specific characteristic resolution of GOME-2 data (about 40 km). Such assimilation is made for first time, worldwide. According to the numerous publications, satellite data assimilation has been applied for one domain, only. Another novelty is the simultaneous assimilation of AOD, NO₂ and SO₂.

RESULTS

As far as only limited amount of pollutants are monitored and the measurements are made at the ground, mainly, a post-processing of obtained data is performed consisting in extracting the surface values of several key pollutants as well as producing compositions as PM₁₀, PM_{2.5}, AOD and columnar values of NO₂ (NO_{2_C}) and SO₂ (SO_{2_C}). This is made for both sat- and mod-runs, results saved as so called ARCH-files (ARCHs and ARCHm, respectively).

The detailed investigation of the results of the satellite data assimilation is object of another publication. Here, only effects of the assimilation will be demonstrated exploiting the difference “sat-mod” of several variables, for different days and domains. The main behavior of this difference is as follows:

- In first hours of the day, the differences remaining from the previous day are relatively small, with positive and negative values.
- At hour Hs (satellite overpass fixed to 09:00 UTC) a disturbance appears like a simultaneous area source of pollution (similar to fire or other area accident)
- The shape and the structure of this disturbance are quite irregular and it appears approximately over the territory covered by satellite measurements (but not over the whole area).
- Similarly to pollution distribution, the disturbances evolves with time and move as if due to atmospheric circulation.
- Usually, its maximal values decrease and for some variables become small or disappear by the end of the day.

- Often, the disturbances remain to the next day, especially for the bigger modelling domains.

An example of this behavior is shown on Fig. 2 (satellite overpass hour Hs=9:00 UTC).

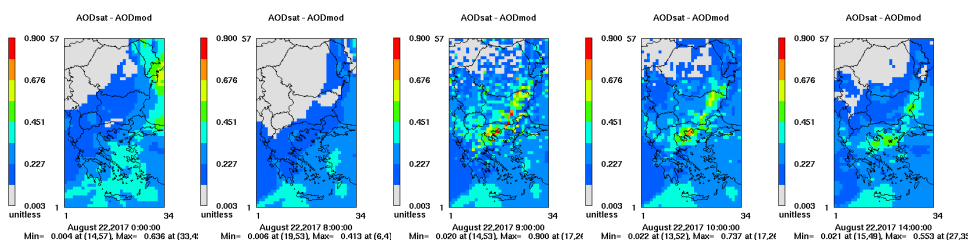


Figure 2. Evolution of the disturbance in the AOD “sat-mod” difference caused by satellite data assimilation over domain BP (Balkan Peninsula), 27 km resolution, h=0, 8, 9(Hs), 10, 14, on 22. August 2017

Of course, the details of this common behavior of the “sat-mod” difference vary very much with the different days, different variables, different domains, and for different seasons, as well.

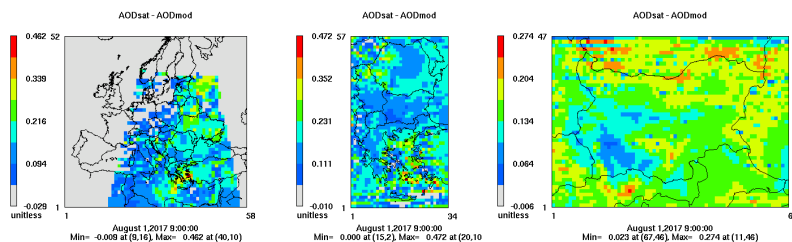


Figure 3. Maps of dAOD fields on 01.08.2017 at time step h=Hs for the first 3 BgCWFS domains

The AOD-differences (dAOD) by the two versions of BgCWFS at the moment Hs more or less follow the satellite data coverage. This can be seen in Fig. 3, where dAOD is shown in the first three BgCWFS domains for 01.08.2017. One can notice that the three fields are quite consistent. More or less similar is the spatial distribution of dPM10. Note that PM10 is directly influenced by the ratio AODsat/AODmod (not the differences but the ratio) at the same hour.

The satellite data for NO2_C cover bigger areas than for the AOD ones. The coverage by SO2_C data is smaller, but it is still bigger than for AOD. The dNO2 behavior is slightly different than dAOD. Up to the moment Hs of a certain day

the differences “sat-mod” are around zero. At Hs, fragmentary spots appear with positive and negative values, predominantly in the first two modelling domains. At $h=H_s+1$, the positive spots practically disappear and the negative ones decrease their maxima. Possible reason for this behavior is the high reactivity of NO₂. Fig. 4 shows the time evolution of the dNO₂ spatial distribution in domain Bulgaria.

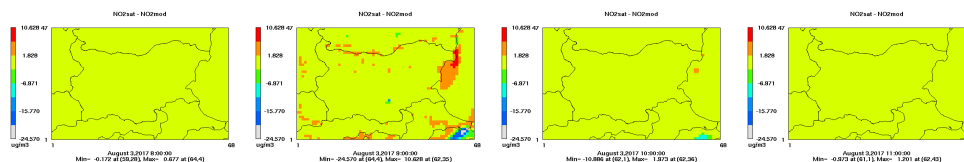


Figure 4. Maps of dNO₂ for the domain BG on 03.08.2017 at different time steps, $h=8, 9$ (Hs), 10, 11

Fig. 5 shows the time evolution of dSO₂ fields for domain Bulgaria on 07.02.2019. The decrease of the differences with the time is smaller than for August 2017; small positive differences remains for the next day.

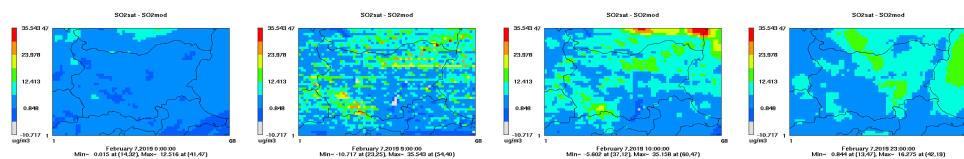


Figure 5. Maps of dSO₂ for domain BG on 07.02.2019 at different time steps, $h=0, 9$ (Hs), 10, 23

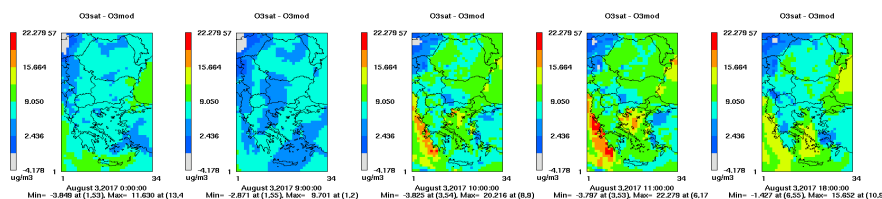


Figure 6. Maps of dO₃ for 3.08.2017 at different time steps: $h=0, 9$ (Hs), 10, 11, 18.

Interesting fact is the appearance of high values of dSO₂ over the upper border of the domain. This is example of influence of the senior domain - satellite data assimilation from domain BP is transferred to domain BG via the boundary conditions. Such an effect is observed for other days and pollutants.

The final example for the effect of satellite data assimilation is the evolution of ozone surface concentrations. Like the other parameters directly influenced by the satellite data assimilation (PM, NO₂, SO₂) the dO₃ behavior is also characterized by “explosion” (higher values with respect to previous hour), but at time H_s+1, i.e. one hour later than satellite passage. This delay is due to the fact that ozone is a secondary pollutant and some time is necessary for reactions (mainly with already changed NO₂) leading to this deviation from the usual daily evolution of the changes “sat-mod”. The spots with differences dO₃ are quite irregular on the maps, mainly positive, and their decrease lasts much longer time, often continuing during the next day. Increase of spot maxima during the following one or two hours after H_s is also possible. In Fig. 6, one can see the time evolution of dO₃ during the first hours of the day (with remains from the previous day), the appearance of a new disturbance at h=H_s+1=10:00 UTC due to assimilation of satellite NO₂ data, the increase of its intensity and further decrease several hours later.

CONCLUSIONS

Satellite retrieved atmospheric chemistry data were assimilated for the first time in the Bulgarian Chemical Weather Forecast System. The off-line version of the modelling system was run over five nested domains for two months (August 2017 and February 2019) in two modes – without satellite data (mod-run), and with satellite data assimilation for AOD and columnar NO₂ and SO₂ (sat-run). The preliminary analysis of the results in this work was focussed mainly on the evolution of the fields of the “sat-mod” differences of several parameters (AOD, PM₁₀, NO₂ and SO₂). The main behaviour of these differences is demonstrated. The deviations are also outlined and commented. Further investigations are required to understand the advantages and the weaknesses of the BgCWFS-sat modelling system, using both comparisons with observations and model inter-comparisons to data from air quality networks.

ACKNOWLEDGMENTS

This study was carried out in the framework of the project SIDUAQ, funded by the European Space Agency (ESA) through contract No. 4000124150/18/NL/SC. Deep gratitude is due to ESA services providing data from GOME-2 instrument on board of MetOp-A, B and C satellites.

REFERENCES

Benedetti A., J.-J. Morcrette, O. Boucher, A. Dethof, R. J. Engelen, M. Fisher, H. Flentjes, N. Huneus, L. Jones, J. W. Kaiser, S. Kinne, A. Man- gold, M. Razinger, A. J. Simmons, M. Suttie, and the GEMS-AER team

- (2009): Aerosol analysis and forecast in the ECMWF Integrated Forecast System. Part II: Data assimilation. *J. Geophys. Res.*, 114, D13205.
- Boucher, O. (2015). Atmospheric Aerosols: Properties and Climate Impacts, Springer, Dordrecht. ISBN 9789401796484.
- Byun, D., & Schere, K. L. (2006) Review of the governing equations, computational algorithms and other components of the Models-3 Community Multiscale Air Quality (CMAQ) modeling system. *Appl. Mech. Rev.*, 59, 51–77
- Curci, G. (2012). FlexAOD: A Chemistry-transport Model Post-processing Tool for A Flexible Calculation of Aerosol Optical Properties. In: *Proceedings of the 9-th International Symposium on Tropospheric Profiling*, L'Aquila, Italy, September 2012, ISBN: 978-90-815839-4-7
- Curci, G., Hogrefe, C., Bianconi, R., Im, U., Balzarini, A., Baró, R., Brunner, D., Forkel, R., Giordano, L., Hirtl, M., Honzak, L., Jiménez-Guerrero, P., Knote, C., Langer, M., Makar, P. A., Pirovano, G., Pérez, J. L., San José, R., Syrakov, D., Tuccella, P., Werhahn, J., Wolke, R., Žabkar, Zhang, R. J., and Galmarini, S. (2015): Uncertainties of simulated aerosol optical properties induced by assumptions on aerosol physical and chemical properties: An AQMEII-2 perspective. *Atmos. Environ.* , 115, 541–552
- Gadzhev, G., Ganey, K., Miloshev, N., (2015) Numerical study of the atmospheric composition climate of Bulgaria - Validation of the computer simulation results, *International Journal of Environment and Pollution*, 57 (3-4), 189-201.
- Kuenen, J.J.P., Visschedijk, A.J.H., Jozwicka, M., Denier van der Gon, H.A.C. (2014). TNO-MACC_II emission inventory; a multi-year (2003–2009) consistent high-resolution European emission inventory for air quality modelling. *Atmos. Chem. Phys.*, 14 (20), 10963–10976.
- Park R. S., Song C. H., Han K. M., Park M. E., Lee S.-S., Kim S.-B., Shimizu A. (2011). A study on the aerosol optical properties over East Asia using a combination of CMAQ-simulated aerosol optical properties and remote-sensing data via a data assimilation technique. *Atmos. Chem. Phys.*, 11 (23), 12275–12296.
- Skamarock, W.C. & Klemp, J.B. (2008): A time-split non-hydrostatic atmospheric model. *J. Comput. Phys.*, 227 (7), 3465–3485.
- Syrakov, D., Prodanova, M., Slavov, K., Etropolska, I., Ganey, K., Miloshev, N., Ljubenov, T. (2013). Bulgarian System for Air Pollution Forecast. *J. Int. Sci. Publ.: Ecol. Saf.*, 7 (1), 325-334.
- Syrakov, D., Prodanova, M., Etropolska, I., Slavov, K., Ganey, K., Miloshev, N., Ljubenov, T. (2014). A Multi- Domain Operational Chemical Weather Forecast System. In: Lirkov I. et al. (eds.) Large-Scale

Scientific Computing, LNCS 8353, 413–420. Springer-Verlag Berlin Heidelberg.

Syrakov D., Prodanova M., Georgieva E., Dimitrova M., Spassova T., Atanassov D., Veleva B., Nedkov R. (2019). Aerosol optical depth calculations using the Bulgarian Chemical Weather Forecast System. *Bulg. J. Meteorol. Hydrol.* 22 (3).

✉ **Dimiter Syrakov**

<https://orcid.org/0000-0001-5057-8490>

National Institute of Meteorology and Hydrology

National Institute of Geophysics, Geodesy and Geography – Bulgarian Academy of Sciences
Sofia, Bulgaria

E-mail: dimeter.syrakov@meteo.bg

✉ **Maria Prodanova**

<https://orcid.org/0000-0002-7395-9314>

National Institute of Meteorology and Hydrology

National Institute of Geophysics, Geodesy and Geography – Bulgarian Academy of Sciences
Sofia, Bulgaria

E-mail: maria.prodanova@meteo.bg

✉ **Emilia Georgieva**

<https://orcid.org/0000-0002-8466-4976>

National Institute of Meteorology and Hydrology

Sofia, Bulgaria

E-mail: emilia.georgieva@meteo.bg

PRELIMINARY RESULTS FOR THE RECURRENCE OF AIR QUALITY INDEX FOR THE CITY OF SOFIA FROM 2008 TO 2019

Georgi Gadzhev

*National Institute of Geophysics, Geodesy and Geography –
Bulgarian Academy of Sciences (NIGGG-BAS)*

Abstract: The living environment of human beings and, obviously, the atmospheric composition has a great impact for the quality of life and human health. Air Quality (AQ) is a key element of European citizens' wellbeing and quality of life. The objectives of the present work are to conduct reliable, comprehensive and detailed studies of the impact of lower atmosphere composition on the quality of life and health risks for the population in the city of Sofia. The performed numerical simulations with the US EPA Models-3 system are for 12 years from 2008-2019 and calculated on five domains: Europe, Balkan Peninsula, Bulgaria, Sofia Municipality and Sofia City with increasing space resolution - from 81 km (Europe) to 1 km (Sofia City). The System is based on the well-known models WRF (Meso-Meteorological Model) and US EPA dispersion model CMAQ (Chemical Transport Model). As emission input the TNO data is used for the two biggest domains. For the 3 Bulgarian domains the current emission inventory prepared by Bulgarian environmental authorities is exploited.

Keywords: Air Quality Indices, air quality, quality of life, health risks.

INTRODUCTION

The Air Quality is a key element for the well-being and quality of life of human beings. According to the World Health Organization, air pollution severely affects the health of European citizens. There is increasing evidence of adverse effects of air pollution on the respiratory and the cardiovascular system as a result of both acute and chronic exposure. In particular, a significant reduction of life expectancy by a year or more is assumed to be linked to long-term exposure to high air concentrations of particulate matter (PM). There is considerable concern about impaired and detrimental air quality conditions over many areas in Europe, especially in urbanized areas, despite 30 years of legislation and emission reductions. Current legislation, e.g. the Ozone daughter directive

2002/3/EC (European Parliament, 2002), requires informing the public on AQ, assessing air pollutant concentrations throughout the whole territory of Member States and indicating exceedances of limit and target values, forecasting potential exceedances and assessing possible emergency measures to abate exceedances. For this purpose, modeling tools must be used in parallel with air pollution measurements. There are also different kind indexes for the well-being and quality of life of the humans, such as UV, Heat and Wind chill -Indexes, but they are not subject of interest in present study (Bojilova, Mukhtarov, Miloshev 2020, Evtimov, Ivanov 2008, Ivanov, Evtimov 2014, Chervenkov, Slavov, Ivanov 2019). The goals of reliable air quality studies are the efficient control and protection of population exposure as well as possible emission abatement measures. In recent years the concept of “chemical weather” arises and in many countries respective forecast systems are being developed along with the usual meteorological weather forecasts (Sofiev at al., 2006, Poupkou et al., 2008, Monteiro et al., 2005, San Jose et al., 2006, Mukhtarov, Bojilova 2017, Bojilova, Mukhtarov 2019). Air pollution easily crosses national borders. It would be cost-effective and beneficial for citizens, society and decision-makers that national chemical weather forecast and information systems were networked across Europe.

MODELING TOOLS

The present study is based on air quality simulations with US EPA Models-3 air quality modeling system, consisting of 3 models:

- **CMAQ v.4.6** - Community Multi-scale Air Quality model, <http://www.cmaq-model.org/>, (Denis et al. 1996, Byun, Ching 1999, Byun, Schere 2006), the Chemical Transport Model (CTM);

- **WRF v.3.2.1** - Weather Research and Forecasting Model, <http://www.wrf-model.org/>, (Skamarock et al. 2007), the meteorological pre-processor to CMAQ. The Weather Research and Forecasting (WRF) Model is a next generation meso-scale numerical weather prediction system designed to serve both operational forecasting and atmospheric research needs. It is an evolutionary successor to the MM5 model. The creation and further development of WRF is due to the collaborative efforts of several US institutions like NCAR, NOAA, NCEP and others. The WRF is a fully compressible and non-hydrostatic model with terrain-following hydrostatic pressure coordinate. The grid staggering is the Arakawa-C type. One can find more info on <http://www.wrf-model.org/index.php>;

- **SMOKE v.2.4** - Sparse Matrix Operator Kernel Emissions Modelling System, <http://www.smoke-model.org/>, (Coats, Houyoux 1996, Houyoux, Vukovich 1999, CEP 2003), the emission pre-processor to CMAQ. CMAQ demands its emission input in specific format reflecting the time evolution of all pollutants accounted for by the chemical mechanism used (CB-IV in this

case). Emission inventories are used as raw data for anthropogenic emission processing. The inventories are made on annual basis for big territories; many pollutants are estimated as groups (VOC and PM_{2.5} for instance). Preparation of emission input to a Chemical Transport Model requires emission processing. Such emission processing component in EPA Models-3 system is SMOKE but it is partly used, here, because it's quite strong relation to US emission sources specifics. In this study SMOKE is used only for calculating biogenic (BgS) emissions and for merging Area sources (AS), Large point sources (LPS) and BgS-files into a CMAQ emission input file. The area source emissions and the large point source emissions are prepared by the interface programs AEmis and PEmis.

In the System, WRF model is driven by the NCEP data in GRIB-2 format with space resolution of $1^{\circ} \times 1^{\circ}$ and 6-hour time resolution. TNO inventory for 2005 (Denier van der Gon et al., 2010) is exploited partly for Bulgaria domain, TNO being the Netherlands's Organization for Applied Scientific Research. For Bulgaria itself and for the other Bulgarian domains, the National inventory for 2010 as provided by Bulgarian Executive Environmental Agency is used. That means TNO inventory is used only for the territories outside Bulgaria in the mother CMAQ's domain.

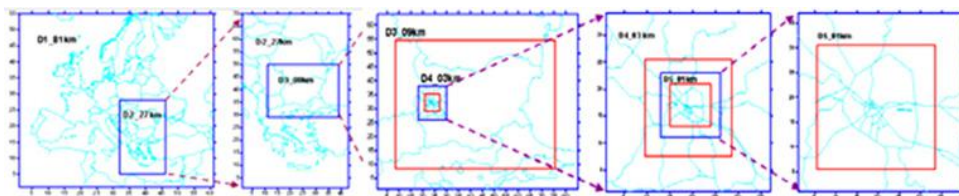


Figure 1. Five computational domains (CMAQ domains are nested in WRF ones)

The nesting capabilities of WRF and CMAQ are used to downscale the simulations from European region to the Sofia city area. The resolution of the mother domain (Europe) is 81 km, big enough as to correspond to met-data space resolution. Four other domains are nested in it and in each other – Balkan Peninsula (27km resolution), Bulgaria (9 km), Sofia municipality (3 km) and Sofia city (1 km) as shown in Fig. 1. The climatic data is used for chemical boundary conditions following the presumption that the errors introduced by this assumption will decrease quickly to the centre of the domain due to the continuous acting of the pollution sources. All other domains receive their boundary conditions from the previous domain in the hierarchy.

The post-processing program XtrCON extracts part of the pollutants for archiving and further handling. Only surface values of the most important pollutants are saved

- 8 gases and 11 aerosols (including PM10 and PM2.5). Part of these pollutants is more or less monitored and they are referred in the European legislation with the respective thresholds. For the moment it presents 4 main pollutants - Ozone, NO₂, SO₂ and PM10 which are used to calculate the Air Quality Indices (AQI). Calculation of the Air Quality (AQ) impact on human health and quality of life in Sofia city is the objective of the present study. The impact is calculated in the terms of the so called AQI – an integral characteristic directly measuring the effects of AQ on human health. The calculations are made on the basis of long term AQ simulations, which make it possible to reveal the climate of AQI spatial/temporal distribution and behaviour.

The AQI is defined as a measure of air pollution seen in the context of its impact on human health. It provides an integrated assessment of the impact of the whole range of pollutants on human health and is calculated based on the concentration of various pollutants obtained from measurements or numerical modeling. The index is defined in several segments (EPA, 2009), each of which is a linear function of the concentration of each considered pollutant:

$$I = ((I_{high} - I_{low}) / (C_{high} - C_{low}))(C - C_{low}) \quad (1)$$

where:

I = the AQI,

C = the pollutant concentration,

C_{low} – the concentration breakpoint that is $\leq C$,

C_{high} – the concentration breakpoint that is $\geq C$.

I_{low} – the index breakpoint corresponding to C_{low}

I_{high} – the index breakpoint corresponding to C_{high} .

In that calculation the index falls in one of the ranges of the dimensionless scale. In each range index values are associated with an intuitive colour code, a linguistic description and a health description.

Pretty often in order to evaluate the air quality situation in European cities, all detailed measurements are transformed into a single relative figure: the Common Air Quality Index (CAQI) and this index have 5 levels using a scale from 0 (very low) to > 100 (very high). The index is based on 3 pollutants of major concern in Europe: PM10, NO₂, O₃ and will be able to take into account to 3 additional pollutants (CO, PM2.5 and SO₂).

One of the most commonly used air quality index is the UK Daily Air Quality Index (Leeuw, F. de, Mol, W., 2005), also used in Bulgaria (Etropolska et al. 2010), (Syrakov et al, 2012, 2013, 2014a, 2014b, 2015), (Georgieva, I., 2014), (Georgieva et al. 2015), (Georgieva, I. and Ivanov, V., 2017, 2018), (Ivanov, V. and Georgieva, I., 2017) and (Gadzhev 2018).

RESULTS

Annual recurrence of AQI in “Low”, “Moderate” and “High” bands over territory of Sofia city from 2015 to 2019 and average recurrence for the whole period 2008-2019 (08-19):

Figure 2 demonstrate the spatial and diurnal variation of the annual recurrence of Low band for the chosen hours 04:00, 12:00 and 18:00UTC for the chosen periods. Here we have to mention that in the Low range the air is most clean, so high recurrence values mean more cases with clean air (red colour) and lower recurrence values mean (blue colour), less cases with clean air (worse AQ status). What can be noticed is: the recurrence in Low range is different for all years at 04:00UTC.

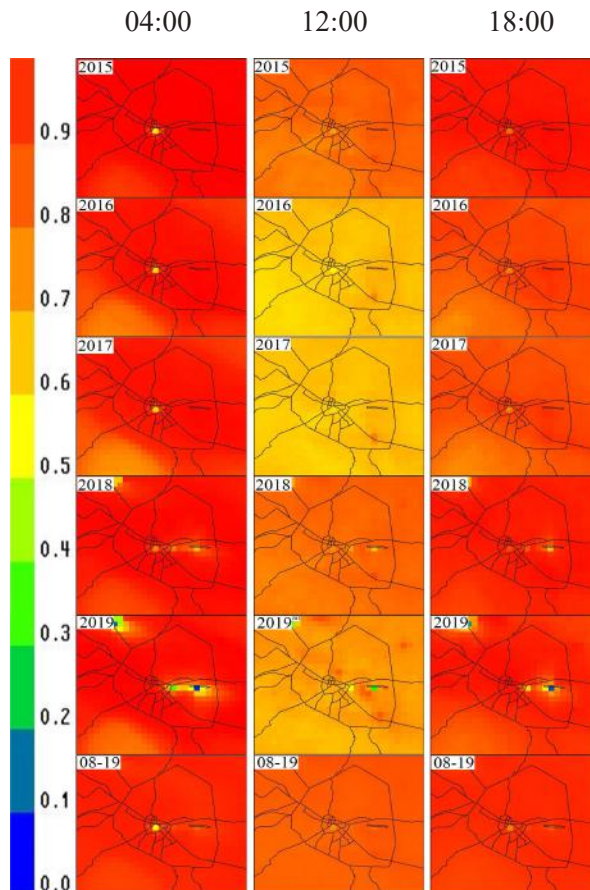


Figure 2. Annual recurrence of AQI in “Low” band over territory of Sofia city from 2015 to 2019 and average recurrence for the whole period 2008-2019 (08-19)

In 2015, 2018 and 08-19 at 12:00 UTC the recurrence in Low band is bigger than this in 2016, 2017 and 2019. While at 18:00 UTC the higher recurrence is in 2015, 2018, 2019 and 08-19. The high polluted areas are the city centre at 04:00 and two spots (Kostinbrod and Sofia airport) in 2019 and they are very well displayed in figure.

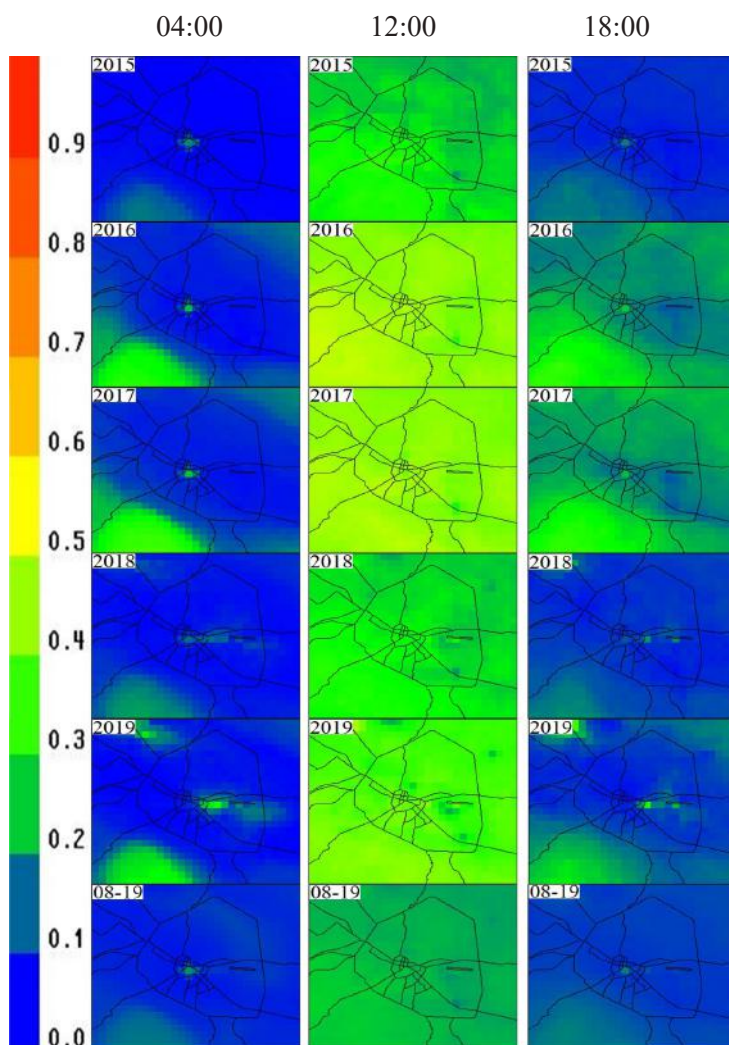


Figure 3. Annual recurrence of AQI in “Moderate” band over territory of Sofia city from 2015 to 2019 and average recurrence for the whole period 2008-2019 (08-19)

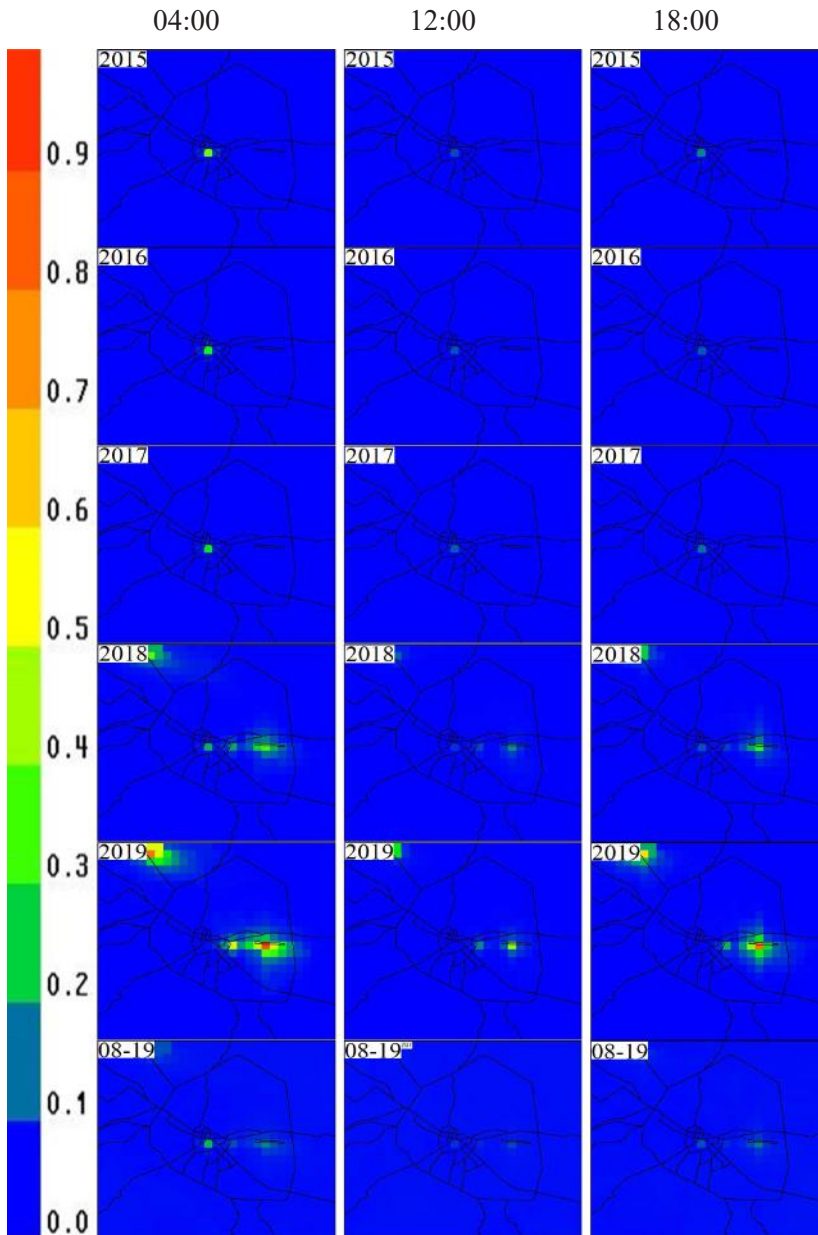


Figure 4. Annual recurrence of AQI in “High” band over territory of Sofia city from 2015 to 2019 and average recurrence for the whole period 2008-2019 (08-19)

In Figure 3 and Figure 4 (Moderate and High ranges) - high recurrence values means less favourable and respectively bad AQ status. It can be seen that most areas with high recurrence of cases with lower AQ status are at noon in the whole domain and mostly over the Vitosha Mountain in other hours. This is due to the intensive O₃ photo-chemistry reactions, the higher NO₂ concentrations lead to production of higher O₃ concentration. The major NO₂ sources in the city are the surface sources (road transport). It can be seen at 18:00 UTC in 2016 and 2017 where over the road network it leads to decreasing of O₃ concentration and with that improving the AQ status. Average for the 2008-2019 in Moderate band at 18:00 UTC it can be also noticed about 10-20% recurrence with not so good AQ status over Vitosha Mountain. Higher values over the Vitosha Mountain in the night and the afternoon are due to the higher concentration of O₃ in mountain areas and intensive ozone transport from higher levels (intensive turbulence during midday). The behavior of the surface ozone is complex. The O₃ in Bulgaria is to a great extent due to transport from abroad and above (Gadzhev et al. 2013 and Kaleyina et al. 2013a, 2013b, 2014). This is the reason why the O₃ concentrations early in the morning are smaller (less intensive transport from higher levels), and higher at noon and afternoon (more turbulent atmosphere (more intensive transport from higher levels) and O₃ photochemistry).

The high recurrence of cases in Figure 4 with most polluted air (High band) appears again in the city centre almost at all hours in all years. In the city centre can be observed more than 20% "High" pollution in the night and 10% at the day.

Bad AQ status from the High band almost never disappears. In 2018 and mostly in 2019 it's make impression that the cases with more worse AQ status are much higher than the other years, as the recurrence around the Kostinbrod, TPP Sofia and Sofia airport can reach about 70% at the different time of the day.

At the plots for average for the 2008-2019 in High band can be seen that at all hours there are places with worst AQ status where the recurrence is almost 20% of all happened cases.

CONCLUSIONS

The simulations for Sofia city show that the air quality status of Sofia is not so good (evaluated with a spatial resolution of 1km).

AQ status falls mostly in Low and Moderate bands, but the recurrence of cases with High pollution is close to 20% mostly at the city center.

The recurrence of cases in Low and Moderate bands has been different for different years.

The pollution in the city is probably due to the surface sources like road transport and also the TPPs in the city and Sofia airport.

Apart from these general features the climatic behavior of the AQI probabilities is rather complex with significant spatial, seasonal and diurnal variability. The

areas with slightly worse AQ status are not necessarily linked to the big pollution sources. Wide rural and even mountain regions can also have significant probability for AQI from the Moderate range.

The hot spot in Sofia city, where index with higher impact (High band) is the city center. The recurrence in High band is relatively high - about 20 % in the morning and 10% in the afternoon.

ACKNOWLEDGMENTS

Bulgarian National Science Fund (grant DN-04/2/13.12.2016).

Special thanks are due to US EPA and US NCEP for providing free-of-charge data and software and to the Netherlands Organization for Applied Scientific research (TNO) for providing the high-resolution European anthropogenic emission inventory.

REFERENCES

- Bojilova R., Mukhtarov P., Miloshev N., (2020) Climatology of the Index of the Biologically Active Ultraviolet Radiation for Sofia. An Empirical Forecast Model for Predicting the UV-Index, *Comptes rendus de l'Acad'emie bulgare des Sciences*, 73, 4, 2020, 531-538
- Bojilova R., Mukhtarov P., (2019) Response of the electron density profiles to geomagnetic disturbances in January 2005, *Stud. Geophys. Geod.*, 63, 3, 436-444
- Byun, D., Ching, J., (1999), *Science Algorithms of the EPA Models-3 Community Multiscale Air Quality (CMAQ) Modeling System*. EPA Report 600/R-99/030, Washington DC.
- Byun, D., Schere, K.L., (2006), Review of the governing equations, computational algorithms, and other components of the models-3 community multiscale air quality (CMAQ) modeling system. *Appl. Mech. Rev.* 59, 51-77
- CEP, (2003), *Sparse Matrix Operator Kernel Emission (SMOKE) Modeling System*, University of North Carolina, Carolina Environmental Programs - CEP, Research Triangle Park, North Carolina.
- Chervenkov H., Slavov K., Ivanov V., (2019) STARDEX and ETCCDI climate indices based on E-OBS and CARPATCLIM: Part one: General description, *Lecture Notes in Computer Science (including subseries Lecture Notes in Artificial Intelligence and Lecture Notes in Bioinformatics)*, 11189 LNCS, pp. 360-367
- Coats, C.J., Jr., and Houyoux, M.R., (1996), *Fast Emissions Modeling With the Sparse Matrix Operator Kernel Emissions Modeling System, The Emissions*

- Inventory: Key to Planning, Permits, Compliance, and Reporting*, Air and Waste Management Association, New Orleans, September
- Denier van der Gon, H., Visschedijk, A., van de Brugh, H., Droge, R., (2010), *A high resolution European emission data base for the year 2005*, TNO-report TNO-034-UT-2010-01895 RPT-ML, Apeldoorn, The Netherlands
- Dennis, R.L., Byun, D.W., Novak, J.H., Galluppi, K.J., Coats, C.J., and Vouk, M.A., (1996), The Next Generation of Integrated Air Quality Modeling: EPA's Models-3, *Atmospheric Environment* 30, 1925–1938.
- EMEP/CORINAIR (2002), *Atmospheric emission inventory guidebook, third edition*, European Environmental Agency.
- EPA (2009). *Technical assistance document for the reporting of daily air quality - the Air Quality Index (AQI)*. EPA-454/B-09-001, US Environmental Protection Agency, Research Triangle Park, North Carolina, Office of Air Quality Planning and Standards, Research Triangle Park, North Carolina 27711.
- EU (2007a).
- Etropolska, I., Prodanova, M., Syrakov, D., Ganev, K., Miloshev, N., Slavov, K., (2010), *Lecture Notes in Computer Science (including subseries Lecture Notes in Artificial Intelligence and Lecture Notes in Bioinformatics)*, 6046 LNCS, 2011, 141-149
- European Parliament (2002), DIRECTIVE 2002/3/EC of 12 February 2002 relating to ozone in ambient air, Official Journal of the European Communities (9.3.2002) L67, 14–30
- Evtimov S., Ivanov V., (2008) Correspondence analysis of the atmospheric phenomena in Bulgaria, *Comptes Rendus de L'Academie Bulgare des Sciences*, 61(4), 443-450
- Gadzhev, G., (2018) Recurrence of air quality for the city of Sofia for 2013 and 2014, *Bulgarian Geophysical Journal*, 2018, 41, 46-58
- Gadzhev, G., Ganev, K., Miloshev, N., Syrakov, D., Prodanova, M., (2013) Numerical Study of the Atmospheric Composition in Bulgaria, *Computers and Mathematics with Applications*, 65, 402-422.
- Georgieva, I., (2014) Study of the air quality index climate for Bulgaria, *Proc. of the international conference on numerical methods for scientific computations and advanced applications*, May 19-22, 2014, Bansko, ISBN978-954-91700-7-8, 39-42.
- Georgieva I., Gadzhev, G., Ganev, K., Prodanova, M., Syrakov, D., Miloshev, N. (2015) Numerical study of the air quality in the city of Sofia – some preliminary results, *International Journal of Environment and pollution*, 57, Nos. 3/4, 162-174.
- Georgieva, I., Ivanov, V., (2017), Impact of the Air Pollution on the Quality of Life and Health Risks in Bulgaria, *HARMO 18 - 18th International*

- Conference on Harmonisation within Atmospheric Dispersion Modelling for Regulatory Purposes, Proceedings*, 647-652
- Georgieva, I., Ivanov, V., (2018), Computer simulations of the impact of air pollution on the quality of life and health risks in Bulgaria, *Int. J. Environment and Pollution*, 64, Nos. 1/3, 2018, 35-46
- Houyoux, M.R., and Vukovich, J.M., (1999), *Updates to the Sparse Matrix Operator Kernel Emission (SMOKE) Modeling System and Integration with Models-3, The Emission Inventory: Regional Strategies for the Future*, Raleigh, NC, Air and Waste Management Association
- Ivanov V., Evtimov S., (2014), Wind chill hazard in Bulgaria during 2003-2012 period, *Comptes Rendus de L'Academie Bulgare des Sciences*, 67(11), pp. 1521-1530
- Ivanov, V. and Georgieva, I., (2017) Air quality index evaluations for Sofia city, *17th IEEE International Conference on Smart Technologies, EUROCON 2017 - Conference Proceedings*, Article number 8011246, Pages 920-925
- Kaleyna P., Pl. Muhtarov, N. Miloshev, (2013a) Condition of The Stratospheric and Mesospheric Ozone Layer over Bulgaria for the Period 1996-2012: Part 1 – Total Ozone Content, Seasonal Variations, *Bulgarian Geophysical Journal*, 39, National Institute Of Geophysics, Geodesy And Geography, Bulgarian Academy Of Sciences
- Kaleyna P., Pl. Muhtarov, N. Miloshev, (2013b) Condition of The Stratospheric and Mesospheric Ozone Layer over Bulgaria for the Period 1996-2012: Part 2 – Total Ozone Content, Short term variations, *Bulgarian Geophysical Journal*, 39, National Institute Of Geophysics, Geodesy And Geography, Bulgarian Academy Of Sciences
- Kaleyna P., Mukhtarov P., Miloshev N., (2014) Seasonal Variations of the Total Column Ozone over Bulgaria in the Period 1996–2012, *Comptes rendus de l'Acad'emie bulgare des Sciences*, 67, 7.
- Leeuw, F. de, Mol, W., (2005), Air Quality and Air Quality Indices: a world apart. ETC/ACC Technical Paper 2005/5
- Monteiro, A., Lopes, M., Miranda, A.I., Borrego, C. and Vautard, R., (2005), Air pollution forecast in Portugal: a demand from the new air quality framework directive, *Internat. J. Environment and Pollution*, 25, 4–15
- Mukhtarov P., Bojilova R., (2019) INFLUENCE OF SOLAR AND GEOMAGNETIC ACTIVITY ON THE IONOSPHERE OVER BULGARIA, *Comptes rendus de l'Acad'emie bulgare des Sciences*, 70, 9, 1289-1296
- Poupkou, A., I. Kioutsioukis, I. Lisaridis, K. Markakis, D. Melas, C. Zerefos and Giannaros, T., (2008b) Air quality forecasting for Europe, the Balkans and Athens, *3rd Environmental conference of Macedonia*, 14-17 March 2008, Thessaloniki, Greece.

- San Jose, R., J. Perez and R. Gonzalez, (2006), *Air Quality Real-Time Operational Forecasting System for Europe: an application of MM5-CMAQ-EMIMO modeling system*, in Brebia, C. (Ed.), “Air Pollution XIV”, WIT Press, Southampton, Boston, 75
- Skamarock et al., (2007), A description of the Advanced Research WRF Version 2.
- Sofiev, M., Siljamo, P., Valkama, I., (2006), A dispersion modeling system SILAM and its evaluation against ETEX data. *Atmos. Environ.* 40, 674–685
- Syrakov, D., Etropolska, I., Prodanova, M., Ganev, K., Miloshev, N., Slavov, K., (2012), Operational Pollution Forecast for the Region of Bulgaria, *American Institute of Physics, Conf. Proc.* 1487.
- Syrakov, D., Etropolska, I., Prodanova, M., Slavov, K., Ganev, K., Miloshev, N., Ljubenov T., (2013), Downscaling of Bulgarian Chemical Weather Forecast from Bulgaria region to Sofia city, *American Institute of Physics, Conf. Proc.* 1561, 120-132.
- Syrakov, D., Prodanova, M., Etropolska, I., Slavov, K., Ganev, K., Miloshev, N., Ljubenov T., (2014a), A multy-domain operational chemical weather forecast system, *Lecture Notes in Computer Science (including subseries Lecture Notes in Artificial Intelligence and Lecture Notes in Bioinformatics)*, 8353 LNCS, 2014, 413-420
- Syrakov, D., Prodanova, M., Georgieva, E., Etropolska, I., Slavov, K., (2014b), Impact of NOx emissions on air quality simulations with the Bulgarian WRF-CMAQ modelling system, *HARMO 2014 - 16th International Conference on Harmonisation within Atmospheric Dispersion Modelling for Regulatory Purposes, Proceedings 2014*, 187-190
- Syrakov, D., Prodanova, M., Georgieva, E., Etropolska, I., Slavov, K., (2015), Impact of NOx emissions on air quality simulations with the Bulgarian WRF-CMAQ modelling system, *International Journal of Environment and Pollution*, 57, Issue 3-4, 2015, 285-296

✉ **Georgi Gadzhev**

<http://orcid.org/0000-0002-6159-3554>

National Institute of Geophysics, Geodesy and Geography
Bulgarian Academy of Sciences
Sofia, Bulgaria

E-mail: ggadzhev@geophys.bas.bg

PARTICULATE MATTER CHARACTERISTICS AND ATMOSPHERIC BOUNDARY LAYER HEIGHT OVER SOFIA

**Plamen Savov¹, Nikolay Kolev^{1,2},
Ekaterina Batchvarova³, Hristina Kirova⁴, Maria Kolarova⁴**

¹ *Department of Physics, University of Mining and Geology "St. Ivan Rilski"*

² *Institute of Electronics – Bulgarian Academy of Sciences (IE-BAS)*

³ *Climate, Atmosphere and Water Research Institute –
Bulgarian Academy of Sciences (CAWRI-BAS)*

⁴ *National Institute of Meteorology and Hydrology (NIMH)*

Abstract: The paper presents results from aerosol experimental campaigns performed in the urban environment of Sofia. Laser Particle Counter (PLC) data of 2 summer days (June, 7 and 8) and 4 winter days (December, 18, 19, 20, 21) of 2019 are discussed. Aerosol particle concentrations (number/l and mass $\mu\text{g}/\text{m}^3$) in channels 0-2.5 μm and 2.5-10 μm are measured at the open green area near Pliska (at 30 m distance from boulevard Tsarigradsko shose). The combined effect of the daily development of atmospheric boundary layer height, meteorological parameters, and hourly variations in the concentrations of the aerosol fractions is discussed. WRF-GDAS and HYSPLIT models are used for determination of the atmospheric boundary layer height and to follow the transport of air masses. BSC-DREAM dust model is used as an additional source of information to assess the long-range intrusion of dust.

Keywords: air quality, aerosol concentration, atmospheric boundary layer (ABL), particle number concentrations, WRF-(GDAS) model, HYSPLIT, BSC-DREAM

INTRODUCTION

The Atmospheric Boundary Layer (ABL) height determines the volume in which different gaseous and aerosol pollutants are mixed due to turbulent processes within the atmosphere. To model the ABL height in urban environments is additional challenge due to the specific physical and chemical characteristics which play important role for pollutant dispersion, climate comfort, and weather forecasting (Chen et al., 2011; Batchvarova and Gryning, 2006; Batchvarova et al., 2006; Batchvarova et al., 2011; Rotach et al., 2005; Avolio et al., 2017). Specific studies on the city of Sofia including remote sensing measurements are presented by Kirova&Batchvarova, 2017; Kolev et al., 2016; Savov et al., 2016; Kolev et al., 2019. The combination of models and particle counter measurements provides comprehensive information on both the

aerosols concentration characteristics in the urban atmosphere as well as about the vertical structure of aerosol layers and meteorological parameters determining the transport of air mass (Ngan et al., 2015; Stein et al., 2015; Lin Su et al., 2015).

METHODOLOGY AND EQUIPMENT

Experimental site and instruments

A two-channel BQ20 (TROTEC, Germany) laser particle counter (LPC) with channel 1 (0 - 2.5 μm) and channel 2 (2.5 - 10 μm) denoted further in the paper as PM_{2.5} and PM₁₀, respectively, was used to measure instantly the number of particles and their mass with time step 10 or 15 minutes. The sampling rate is 0.9 l/min. The accuracy of the devices is in the range of 15-20%. Measurements were performed near bus stop Pliska (in the green area in front of the building of Philosophy Faculty of Sofia University), 30 m North of Blvd. "Tsarigradsko shose", the largest boulevard in Sofia, one of the roads of heaviest traffic. It runs 11 km from west to east connecting the center of city with Trakiya highway (A1). Only cars and busses are allowed with speed limit of 80 km/h.

Meteorological data were obtained from an automatic weather station located at Sofia airport with time resolution 30 minutes.

Experimental days

Measurements were performed during two typical summer days (7-8 June 2019), characterized by relatively calm anticyclone weather, and four winter days of (18 – 21 December 2019) characterised with high level of pollution and occurrence of fog in the morning hours. Particular behaviour of the aerosol concentrations was noted on December 21, a day with foehn wind.

Application of models

The Weather Research and Forecasting Model (WRF) is a numerical weather forecasting and atmospheric simulation system designed for both research and operational applications. The WRF model is used for a wide range of meteorological applications from tens to thousands of kilometres. The purpose of applying the WRF-GDAS model is to produce new atmospheric analyses using historical data (available from 2004 to present) and to analyze current atmospheric conditions by using Global Data Assimilation System (GDAS).

The Hybrid Single-Particle Lagrangian Integrated Trajectory model (HYSPLIT, <http://www.arl.noaa.gov/ready/hysplit4.htm>), a Lagrangian dispersion model, has been coupled (online) to the Weather Research and Forecasting (WRF) meteorological model in such a way that the HYSPLIT calculation is run as part of the WRF-ARW prediction calculation (Ngan et al., 2015; Lin Su et al., 2015). The embedded HYSPLIT includes dispersion, trajectories, deposition (dry and wet), etc. (Chen et al., 2011; Stein et al., 2015).

The updated BSC-DREAM8b and the new NMMB/BSC-Dust models (<https://ess.bsc.es/bsc-dust-daily-forecast>), developed in the Earth Sciences Department to simulate and/or predict the atmospheric cycle of mineral dust at BSC were used to assess the long-range transport of dust over the area of Sofia.

RESULTS AND DISCUSSIONS

Summer 2019

Anticyclone synoptic conditions prevailed on 7 and 8 June 2019 causing sunny weather and development of cumulus clouds in the afternoon mostly on the first day. Measured maximal temperatures were 25-30 °C and minimal - 13 °C.

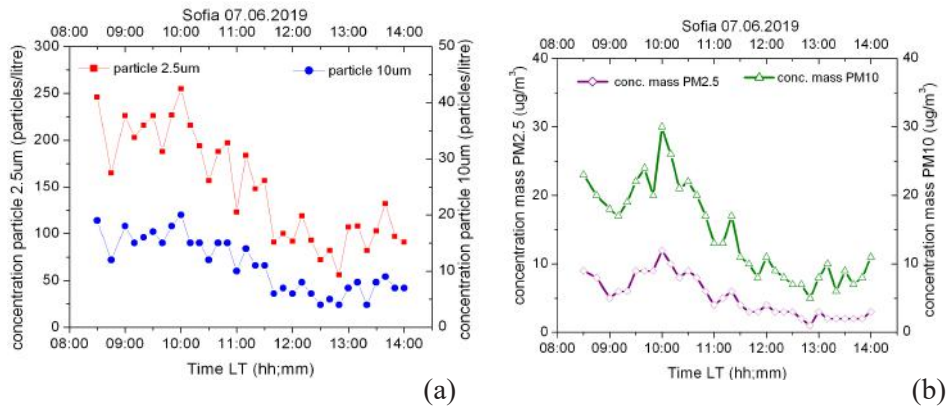


Figure 1. Daily variations in PM_{2.5} and PM₁₀ on 7 June 2019, measured as (a) particles per liter (N/l) and (b) concentration mass ($\mu\text{g}/\text{m}^3$)

The number of PM₁₀ changes from 20 N/l in the morning hours to 10 N/l in the afternoon, and of PM_{2.5} from 250 N/l to 100 N/l (Fig. 1a). The corresponding mass concentrations for PM₁₀ are from 25-30 $\mu\text{g}/\text{m}^3$ to 5 $\mu\text{g}/\text{m}^3$ in the afternoon and for PM_{2.5} from 10-12 $\mu\text{g}/\text{m}^3$ to 5 $\mu\text{g}/\text{m}^3$ (Fig.1b).

WRF-GDAS model forecast for Boundary Layer Depth (Zi) over Sofia is 1200 – 1300 m (Fig. 2a). The model suggests prevailing wind from N (1-4 m/s) from 9 to 15 LT. HYSPLIT Backward trajectories of 1000, 2000 and 3000 m ending in Sofia at 12UTC on June, 7 2019 are shown in Fig. 2b. Transport of air masses from Morocco and Sahara desert at altitude of 3 km can be noted.

Dust concentrations of 20 $\mu\text{g}/\text{m}^3$ forecasted by BSC Dust model at 4 km height do not influenced the level of particulates measured in the urban surface layer. NMMB/BSC Dust (Dust Forecast at 06UTC Friday 07 June) gives a higher concentration of about 20 $\mu\text{g}/\text{m}^3$ in the layer between 3 and 6 km height forecasted over Sofia (Fig. 3a). LON-Height cross-section and LAT-Height cross-section present

Measurements on 8 June show that the number of PM10 is around 20 N/l with max of 25 N/l from 9:30 to 10:30 LT and for PM2.5 the numbers are 220 in the early morning hours and increase to 300-350 N/l from 9:30 to 10:30 LT, then fall to 175 N/l after 12 LT (Fig. 4 a). The corresponding mass concentrations for PM10 are from 15 to 30 $\mu\text{g}/\text{m}^3$. For PM2.5 the concentrations are around 10 $\mu\text{g}/\text{m}^3$ before 12 LT and around 5 $\mu\text{g}/\text{m}^3$ in the early afternoon (Fig. 4 b).

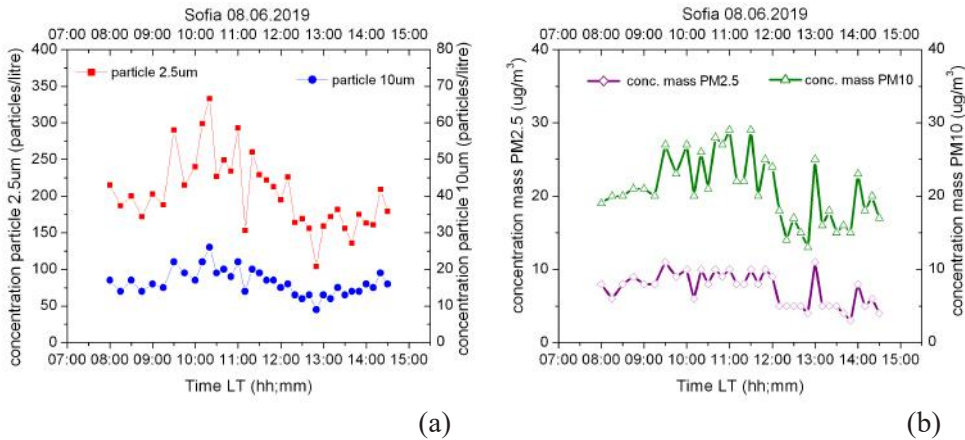


Figure 4. Daily variations in PM2.5 and PM10 on 8 June 2019, measured as (a) particles per liter (N/l) and (b) concentration mass ($\mu\text{g}/\text{m}^3$)

WRF-GDAS model forecast for ABL Height for Sofia is 1800-1900 m. Pasquill Stability Class is from stable (E) in the morning to unstable (B-C) at 12 UTC (Fig. 5a). GDAS wind speed for Sofia on July 8 is 7 m/s in the morning hours and 1-4 m/s after 11 LT from NW. The HYSPLIT Backward trajectories of 1000, 1500 and 2000 m ending in Sofia at 12UTC on June, 8 2019 are shown in Fig. 5b. The transport of air masses at the tree levels is from different areas. The 2000-metre trajectory starts from Algeria. NMMB/BSC Dust (Dust Forecast at 06UTC Sat 08 June) shows a higher concentration of about 20 $\mu\text{g}/\text{m}^3$ in the layer below 2 km, Fig 6a. This suggests that long-range transport of dust may influence the surface PM concentrations in Sofia given the fact that ABL height is about 1900 m. The LON&LAT-Height cross-sections present different distribution of dust concentration compared to the previous day (Fig 6b).

During these summer days, the measured concentrations were lower than the sanitary norms. The height of the convective ABL reached 1350 and 1900 m, on 7 and 8 June respectively. On 7 June (Friday) the morning rush hour concentration peak is at 10 LT and is strongly pronounced (Fig. 1). On 8 June (Saturday), high concentrations remain between 9 and 12 LT. Secondary increase is noted at 13 and

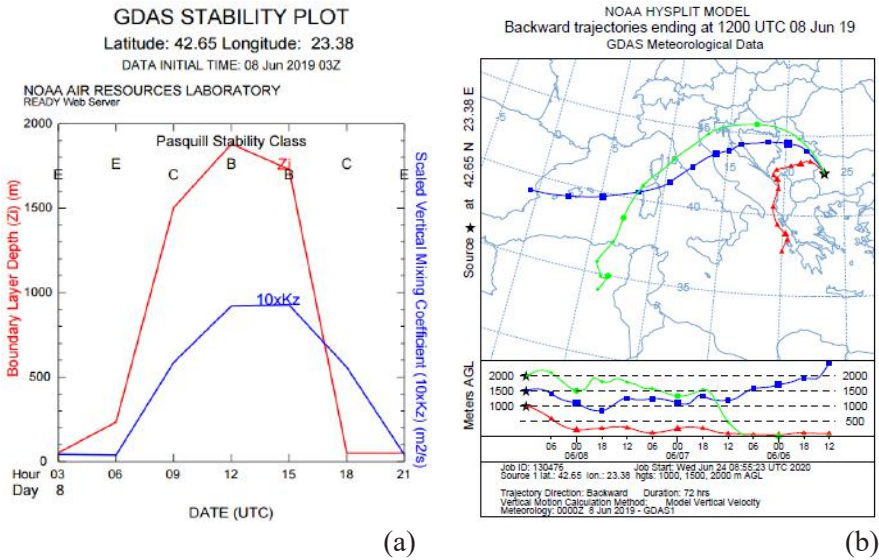


Figure 5. Model results for Sofia on 8 June (a) GDAS Stability plot and (b) HYSPLIT Backward trajectories

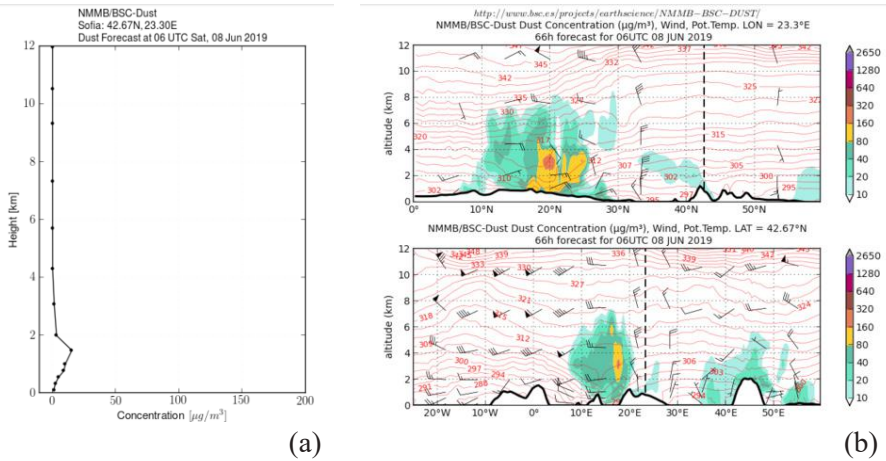


Figure 6. NMMB/BSC Dust Forecast Concentrations ($\mu\text{g}/\text{m}^3$) at 06 UTC on 8 June (a) vertical profile and (b) LON&LAT-Height cross-section

14 LT. Summary of measured and modelled parameters for the summer days is given in Table 1.

Table 1. PM10 and PM2.5 concentrations and meteorological parameters (modelled and observed)

| Day of experiment | PM10 mass min-max ($\mu\text{g}/\text{m}^3$) | PM10 number min-max (N/l) | PM2.5 conc. min-max ($\mu\text{g}/\text{m}^3$) | PM2.5 min-max (N/l) | ABLH min-max (m) | Wind dir/ speed (m/s) (model) | Tmax / Tmin ($^{\circ}\text{C}$) |
|-------------------|------------------------------------------------|---------------------------|--------------------------------------------------|---------------------|------------------|-------------------------------|------------------------------------|
| 7 June | 5-30 | 5-20 | 2-12 | 50-250 | 250-1350 | N / 1-4 | 25-30 / 13 |
| 8 June | 15-30 | 10-30 | 5-10 | 100-350 | 200-1900 | NW / 1-4 | 25-30 / 13 |

It can be noted that the measured particle number is higher on Saturday, 8 June, despite the expected lower traffic contribution. Furthermore, the ratio highest/lowest values is smaller on that day (PM2.5: 350/100 N/l), while on 7 June the ratio is 250/50 N/l. Possible reason for these differences is the long-range transport contribution (Fig. 4 and Fig. 6).

Winter 2019

Anticyclone synoptic circulation prevailed in the period 18-20 December 2019 causing low wind speed from SW-S, morning fog conditions in valleys and low stratus clouds. Measured maximal temperatures were 10 $^{\circ}\text{C}$ and minimal - 0 $^{\circ}\text{C}$. No precipitation and no snow cover were measured in Sofia. Change of weather to cyclone circulation starts from 20 December, leading to feohn wind from S-SW in Sofia reaching 16 m/s, gusts up to 23 m/s and abnormally high temperatures of 15 $^{\circ}\text{C}$.

Measurements on 18 December were performed from 8 to 14 LT under heavy fog (observed relative humidity of 100 %) conditions and show number of PM10 of 200 N/l until 10 LST and lower values (100 N/l) in the afternoon. Registration for PM2.5 shows 4500 N/l in the early morning hours, maximum of 5000-5500 N/l

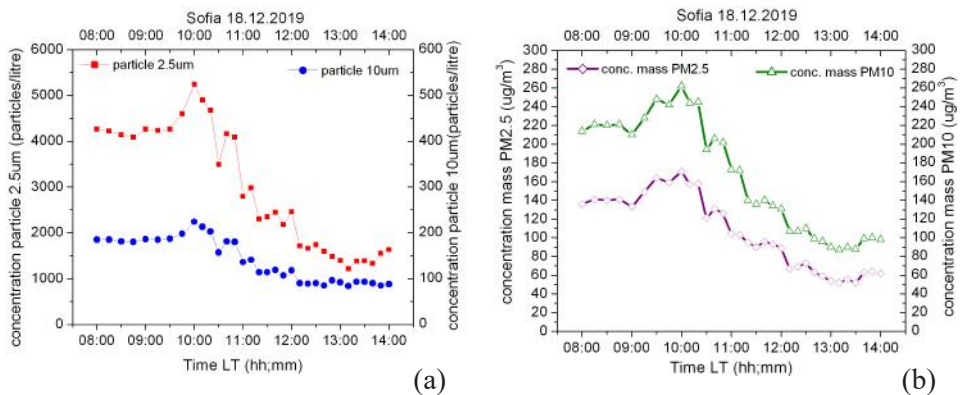


Figure 7. Daily variations in PM2.5 and PM10 on 18 December 2019, measured as (a) particles per liter (N/l) and (b) concentration mass ($\mu\text{g}/\text{m}^3$)

around 10 LT (related to morning rush hours and fog) and gradual decrease to 2500-2000 N/l after 12 LT (Fig. 7a). The corresponding mass concentrations for PM10 (Fig. 7b) is from 220 $\mu\text{g}/\text{m}^3$ at 8 LT, with max of 250-260 $\mu\text{g}/\text{m}^3$ at 9:30-10:30 LT and decrease to 100 $\mu\text{g}/\text{m}^3$ in the early afternoon. The PM2.5 concentrations show similar behavior: around 140 $\mu\text{g}/\text{m}^3$ before 12 LT with, 160-170 $\mu\text{g}/\text{m}^3$ at 10:30 LT and decrease to 60 $\mu\text{g}/\text{m}^3$ in the early afternoon. Summarized information of the winter experimental days is given in Table 2.

GDAS model ABLH of maximum 200 m and stable to neutral stratification over Sofia (Fig. 8a), constant SW-S wind of 1-4 m/s during the day. The 96-hour backward trajectories of height 200, 500 and 1000 m show constant SW flow (Fig. 8b).

Table 2. PM10 and PM2.5 concentrations and meteorological parameters (modelled and observed)

| Day of experiment | PM10 mass min-max ($\mu\text{g}/\text{m}^3$) | PM10 number min-max (N/l) | PM2.5 mass min-max ($\mu\text{g}/\text{m}^3$) | PM2.5 number min-max (N/l) | ABLH min-max (m) | Wind dir/ speed (m/s) (model) | Tmax / Tmin ($^{\circ}\text{C}$) |
|-------------------|------------------------------------------------|---------------------------|-------------------------------------------------|----------------------------|------------------|-------------------------------|------------------------------------|
| 18 Dec. | 80-260 | 100-200 | 50-170 | 2000-5500 | 50-180 / fog | SW-S / 1-4 | 10 / 0 |
| 19 Dec. | 150-600 | 100-400 | 100-375 | 3000-11000 | 50-150 / fog | S-SE / 1-4 | 10 / 0 |
| 20 Dec. | 70-120 | 50-100 | 30-70 | 1100-1700 | 450-150 | S / 1-4 | 10 / 0 |
| 21 Dec. | 10-100 | 20-90 | 10-40 | 300-1400 | Strong wind | S-SW/16 obs | 10-15 / > 0 |

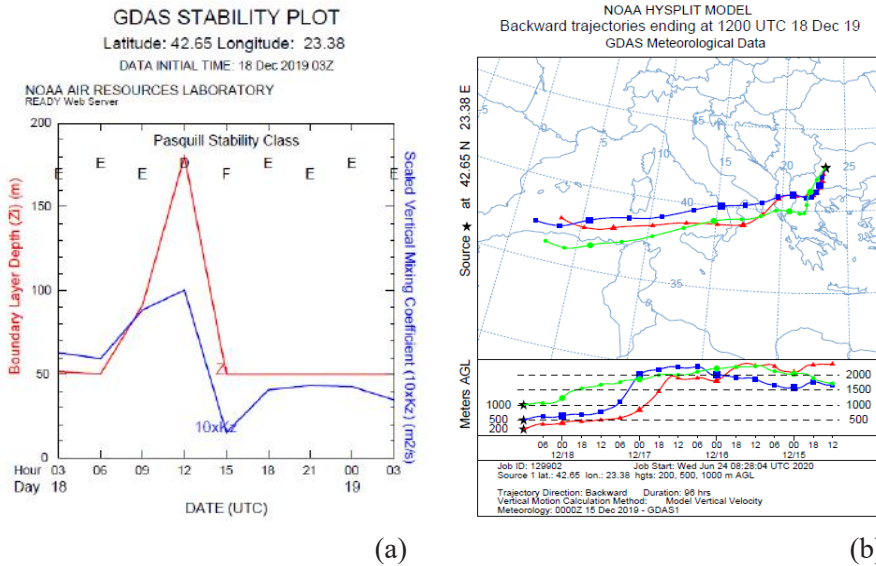


Figure 8. Model results for Sofia on 18 December (a) GDAS Stability plot and (b) HYSPLIT Backward trajectories

Measurements on 19 December were performed from 7 to 12 LT. The stable stratification and fog persisted leading to double increase of all maximal particle number and mass concentrations compared to the previous day (Fig. 9 and Table 2).

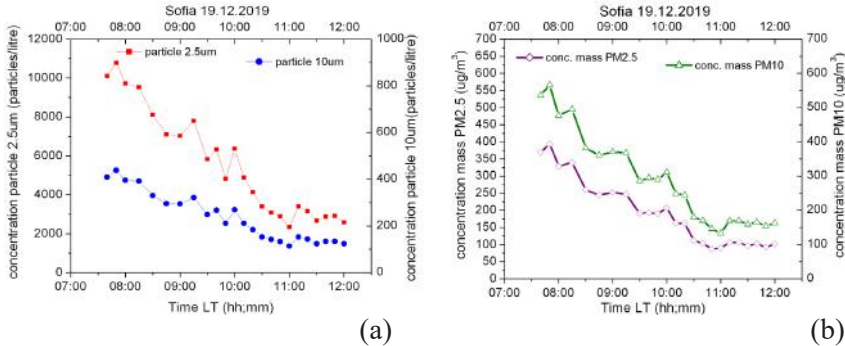


Figure 9. Daily variations in PM2.5 and PM10 on 19 December 2019, measured as (a) particles per liter (N/l) and (b) concentration mass ($\mu\text{g}/\text{m}^3$)

GDAS ABL height over Sofia is below 200 m, stratification is stable to very stable (Fig. 10a), and constant S-SE wind of 1-4 m/s during the day. The 96-hour backward trajectories of height 200, 500 and 1000 m show SW flow from Sicily (Fig. 10b).

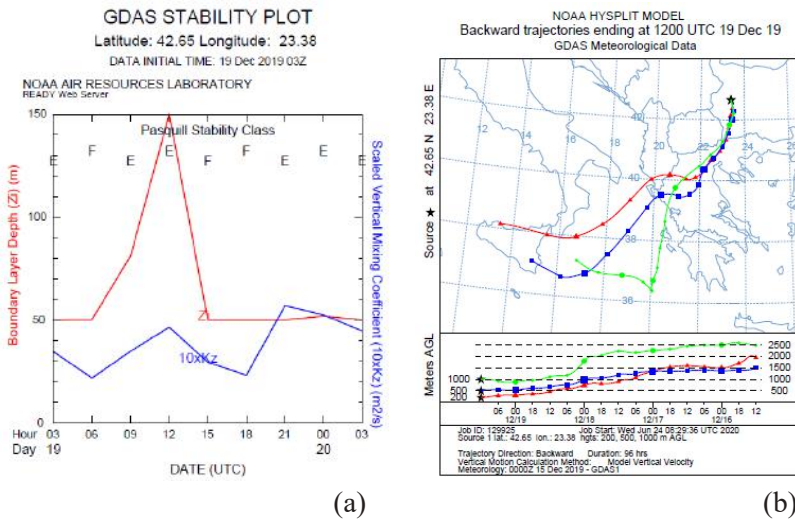


Figure 10. Model results for Sofia on 19 December (a) GDAS Stability plot and (b) HYSPLIT Backward trajectories

On 20 December the meteorological conditions start to change to multi-centered low pressure structure over the Balkan Peninsula. The transport of warm air masses from SW causes increase of temperatures. NMMB/BSC Dust Forecast model indicates dust concentration of $50 \mu\text{g}/\text{m}^3$ at 4000 m, showing long-range transport, which remains far above the ABL (maximal of 450 m) over Sofia.

The number and mass concentration measurements on 20 December show distinct decrease (two times in values) and different from the previous days changes with time. PM_{2.5} mass concentration starts from $70 \mu\text{g}/\text{m}^3$ in the early morning (8:30 LT), a minimum of $30 \mu\text{g}/\text{m}^3$ is recorded between 10 and 11 LT, related to the destruction of the fog. Higher values ($80 \mu\text{g}/\text{m}^3$) are recorded again between 11:30 and 12:30 LT, related with increased traffic of cars leaving the capital for the following 6 days of Christmas. For PM₁₀ the concentrations are with similar behavior to PM_{2.5} but with higher values starting from $100 \mu\text{g}/\text{m}^3$ in the morning (8:30 LT), diminishing to $70 (\mu\text{g}/\text{m}^3)$ and growing again to $120 \mu\text{g}/\text{m}^3$ after 11 LT. After 12:30 LT the concentrations slowly decrease (Fig. 11 and Table 2).

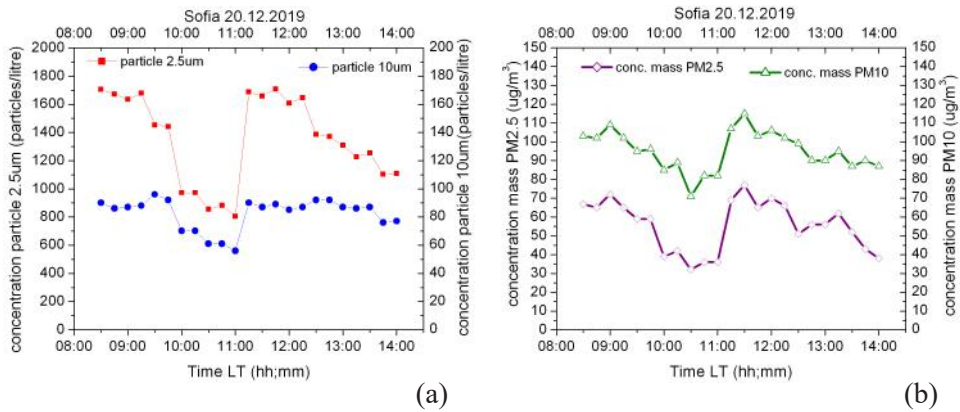


Figure 11. Daily variations in PM_{2.5} and PM₁₀ on 20 December 2019, measured as (a) particles per liter (N/l) and (b) concentration mass ($\mu\text{g}/\text{m}^3$)

On 21 December the cyclone formed over Italy moves to NE above the Hungarian Plane. The southwesterly wind speed increases. Passing over Vitosha Mountain this flow is observed as feohn in Sofia reaching wind speed of 16 m/s at Sofia airport and gusts of 23 m/s.

The measured PM₁₀ and PM_{2.5} concentrations show peculiarities related to the new meteorological situation starting with low morning concentrations from 7 – 10 LT (PM_{2.5}: $10\text{--}20 \mu\text{g}/\text{m}^3$ and for PM₁₀: $30\text{--}40 \mu\text{g}/\text{m}^3$). Very rapidly the

concentrations increase twice to $50 \mu\text{g}/\text{m}^3$ and $90 \mu\text{g}/\text{m}^3$, correspondingly (Fig. 12b). After 10:30 LT the concentrations decrease. This behavior is possibly related to short time wind gust situation during the peak period when large amounts of dust are lifted from surface. It is interesting to note that PM10 number concentration increased twice and PM2.5 three times for the period 10-10:30 LT (Fig. 12a). The peak cannot be explained with high transport traffic, as it is Saturday of a 6-day holiday period.

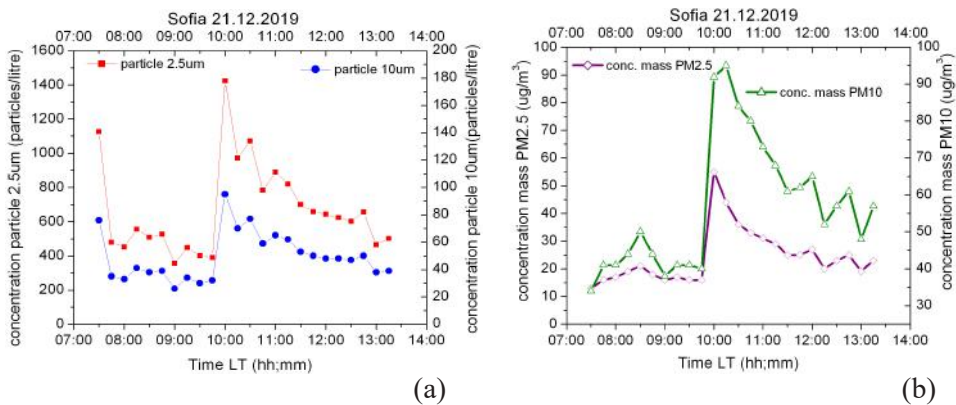


Figure 12. Daily variations in PM2.5 and PM10 on 21 December 2019, measured as (a) particles per liter (N/l) and (b) concentration mass ($\mu\text{g}/\text{m}^3$)

The last 2 days of the winter experimental campaign are peculiar in view of particle concentrations and show the dynamic interplay between meteorology and sources for the air quality in the city.

CONCLUSIONS

This study presents experimental results concerning the daily distribution of the aerosol particles in the urban environment and the correlation to the synoptic situations, meteorological parameters and ABL height. The analysis is based on 2 summer and 4 winter days of aerosol particles (concentration and number) measurements with laser aerosol particle counters.

In summer, the ABL is high and the observed concentration of aerosol particles is under the sanitary norms and changes two times from maximal to minimal values. The maximum is related to intensive transport traffic along the Tsarigradsko shore in the morning hours.

In winter, the ABL height is low the observed concentrations of aerosol particles are higher than the norms for 18 and 19 December. The maximal values are 3 times higher than the minimal and are related to fog conditions and intensive transport

traffic along the Tsarigradsko shose in the morning hours. On 20 and 21 December the concentrations show peculiar changes with time related to Christmas holidays and rare meteorological conditions.

ACKNOWLEDGMENTS

This work is carried out in the framework of the National Science Program "Environmental Protection and Reduction of Risks of Adverse Events and Natural Disasters", approved by the Resolution of the Council of Ministers № 577/17.08.2018 and supported by the Ministry of Education and Science (MES) of Bulgaria (Agreement № D01-230/06.12.2018). The Contributions of Kolarova and Kirova is supported by the project DN4/7 (Study of the PBL structure and dynamics over complex terrain and urban area), funded by the National Science Fund of Bulgaria. The authors gratefully acknowledge the NOAA Air Resources Laboratory (ARL) for the provision of the WRF-GDAS Model used in this publication; the NOAA Air Resources Laboratory (ARL) for the provision of the HYSPLIT transport and dispersion model. Some data and images used in the publication are from the (NMMB/BSC-Dust or BSC-DREAM8b) model, operated by the Barcelona Supercomputing Center (<http://www.bsc.es/ess/bsc-dust-daily-forecast/>).

REFERENCES

- Avolio, E., Federico, S., Miglietta, M., Lo Feudo, T., Calidonna, C., & Sempreviva, A. (2017). Sensitivity analysis of WRF model PBL schemes in simulating boundary layer variables in southern Italy: An experimental campaign. *Atmospheric Research*, 192, 58–71.
- Batchvarova, E. & Gryning, S.-E. (2006). Progress in Urban Dispersion Studies. *Theor. Appl. Climatol.* 84, No. 1-3, 57-67.
- Batchvarova, E., Gryning, S.-E., Rotach, M. & Christen, A. (2006). Comparison of modelled aggregated turbulent fluxes and measured turbulent fluxes at different heights in an urban area. In: *Air pollution modeling and its application XVII*, Borrego, C. and Norman, A. (Eds.), Kluwer Academic/Plenum Publishers (NATO Challenges of Modern Society series) 363-370.
- Batchvarova E., Kolarova M., Veleva B., Neykov N., Neitchev P., Videnov P., Gamanov A., & Barantiev D. (2011). The atmospheric boundary layer – parameterizations, observations and applications. (2011) *Bul. J. Meteo & Hydro*, 16/1, 41-53.
- Chen, F., Kusaka, H., Bornstein, R., Ching, J., Grimmon, C.S.B., Grossman-Clarke, S., Loridan, T., Manning, K.W., Martilli, A.,

- Miao, S., Sailor, D., Salamanca, F.P., Taha, H., Tewari, M., Wang, X., Wyszogrodzki, A.A., & Zhang, C. (2011). The integrated WRF/urban modelling system: development, evaluation, and applications to urban environmental problems. *Int. J.Climatol.* 31 (2), 273–288.
- Kirova, H. & Batchvarova, E. (2017). Mesoscale simulation of meteorological profiles during the Sofia Experiment 2003. *International Journal of Environment and Pollution*, 61, 2, 2017, 134-147. DOI:10.1504/IJEP.10006760
- Kolev, N., Savov, P., Evgenieva, Ts., Miloshev, N., Petkov, D., & Donev, E. (2016). Summer measurements of atmospheric boundary layer (ABL), aerosol optical depth (AOD) and water vapour content (WVC) over Sofia (Bulgaria) 2010–2014. *Compt. rend. Acad. bulg. Sci.*, **69**, 4, 421-429.
- Kolev, N., Savov, P., Evgenieva, Ts., Miloshev, N., Gueorguiev, O., Batchvarova, E., Kolarova, M. Danchovski, V., Ivanov, D. & Petkov, D. (2019). Investigation of the atmospheric boundary layer and optical characteristics of the atmospheric aerosols over Sofia in summer 2016, 10th Jubilee International Conference of the Balkan Physical Union, AIP Conference Proceedings 2075, 120004 (2019) <https://doi.org/10.1063/1.5091262>, Published Online: 26 February 2019.
- Lin Su, Yuan, Z., Hung Fung, J. C., & Hon Lau, A. K. (2015). A comparison of HYSPLIT backward trajectories generated from two GDAS datasets, *Science of the Total Environment*, 506-507, 527-37.
- Ngan, F., Stein, A., & Draxler, R. (2015). Inline coupling of WRF–HYSPLIT: Model development and evaluation using tracer experiments. *J. Appl. Meteor. Climatol.*, 54, 1162–1176
- Rotach, M. W., Vogt, R., Bernhofer, C., Batchvarova, E., Christen, A., Clappier, A., Feddersen, B., Gryning, S.-E., Martucci, G., Mayer, H., Mitev, V., Oke, T. R., Parlow, E., Richner, H., Roth, Roulet, M., Y.-A., Ruffieux, D., Salmond, J. A., Schatzmann, M. & Voogt, J. A. (2005). BUBBLE – an Urban Boundary Layer Meteorology Project, *Theor. Appl. Climatol.* 81, 231–261, DOI 10.1007/s00704-004-0117-9.
- Savov, P., Kolev, N., Evgenieva, Ts., Vatzkitcheva, M., & Danchovski, V. (2016). Correlations between particle number concentrations, boundary layer height, meteorological parameters and urban environments. *Compt. rend. Acad. bulg. Sci.*, 69, 1, 19-24.
- Stein, A., Draxler, R., Rolph, G., Stunder, B., Cohen, M., & Ngan, F. (2015). NOAA’S HYSPLIT Atmospheric transport and dispersion

modeling system. Bulletin of the American Meteorological Society, 96, 12 (DEC. 2015), 2059-2078. Published by: American Meteorological Society.

✉ **Plamen Savov**

Department of Physics
University of Mining and Geology “St. Ivan Rilski”
Sofia, Bulgaria
E-mail: psavov@mgu.bg

✉ **Nikolay Kolev**

Department of Physics
University of Mining and Geology “St. Ivan Rilski”
Institute of Electronics
Bulgarian Academy of Sciences
Sofia, Bulgaria
E-mail: nic_k@abv.bg

✉ **Ekaterina Batchvarova**

Climate, Atmosphere and Water Research Institute
Bulgarian Academy of Sciences
Sofia, Bulgaria
E-mail: ekbatch@gmail.com

✉ **Hristina Kirova**

National Institute of Meteorology and Hydrology
Sofia, Bulgaria
E-mail: hristina.kirova@meteo.bg

✉ **Maria Kolarova**

National Institute of Meteorology and Hydrology
Sofia, Bulgaria
E-mail: maria.kolarova@meteo.bg

SENSITIVITY TO THE WRF MODEL CONFIGURATION OF THE WIND CHILL INDEX FOR SOFIA REGION – PRELIMINARY RESULTS

Vladimir Ivanov¹, Reneta Dimitrova^{1,2}

*¹National Institute of Geophysics, Geodesy and Geography –
Bulgarian Academy of Sciences (NIGGG-BAS)*

*²Faculty of Physics, Department of Meteorology and Geophysics,
“St. Kliment Ohridski” University of Sofia*

Abstract: The thermal comfort is one of the main issues nowadays. The implications from the modelled future climate projections also put a question of the expected thermal environmental conditions. The objective of this paper is a winter human discomfort study for Sofia and its surroundings. Data from numerical simulations with Weather Research and Forecasting (WRF) model were used to calculate a Wind Chill index, which describes the deviation from the winter thermal comfort. This index depends on air temperature and wind, and it is categorized in a 6-grade scale, which describes how far or close are the environmental conditions from the human thermal comfort. Numerical experiments with combination of different parameterization schemes for atmospheric boundary layer and microphysical processes were carried out. Model performance for the temperature and wind speed were used for estimation of the best model options for calculation of the Wind Chill index.

Keywords: Wind chill index modelling, WRF model performance estimation

INTRODUCTION

The thermal comfort is one of the main issues nowadays. The implications from the modelled future climate projections also put a question of the expected thermal environmental conditions (Stocker et al., 2013) and related air pollution (Gadzhev et al., 2014a, Gadzhev et al., 2014b, Gadzhev et al., 2012, Gadzhev et al., 2011). The population of the cities increase more and more nowadays, which entails the growth of the cities through the gradual amplification of urbanizing. That intensify the urban heat island effect (Rizwan, Dennis & Chunho, 2008), change the surroundings environment modifying the local circulations (Hidalgo, Masson, & Gimeno, 2010), lead to implications in the precipitation distribution (Collier, 2006), etc. Therefore, the consequences from the increasing or decreasing of the

air temperatures become of bigger importance. The deviation from the thermal comfort is expressed as a number called Wind Chill index, which depends on air temperature, wind and/or relative humidity, and possibly from other parameters. It is categorized in ordinal scale for deviation of the environmental conditions from the thermal comfort for human beings (Cheng, Niu, & Gao, 2012). The thermal discomfort for the territory of Bulgaria and the Balkan Peninsula is considered in several studies. Some of them deal with observations (Ivanov & Evtimov, 2014a; Ivanov & Evtimov, 2014b). Their results show that the deviations from the thermal comfort in Bulgaria could be significant from the human perspective. Others, estimated by outputs from the regional climate model also show that the Balkan Peninsula is subjected to heat-related illness (Ivanov, Gadzhev, Ganev & Chervenkov, 2020).

The objective of this paper is a winter human discomfort study for Sofia and its surroundings. The Weather Research and Forecasting Model (WRF) model was used for simulation of temperature and wind fields. Different parameterization schemes for atmospheric boundary layer and microphysical processes were used for estimation of the best model options for calculation of the Wind Chill index.

METHODOLOGY

Temperature and wind fields modelling

WRF is a mesoscale numerical simulation system for research and operational forecasting of the atmospheric environment (WRFv3.9; Skamarock et al 2008). Five nested domains in Lambert projection, with D1 at 9 km, D2 at 3 km, and three at 1 km horizontal resolution (D3, D4, D5) and with hourly output, were selected. The map with the modelling domains is shown in Figure 1. The bigger domain D1 covers the north and central parts of the Balkan Peninsula, the inner domain D2 - mainly the territory of Bulgaria, the innermost domains: D3 - the Sofia valley, D4 - Plovdiv region, D5 - Varna region. The study considers only the innermost domain D3, which includes geographically the city of Sofia and its surroundings with complex terrain. The model was implemented with 50 pressure-based terrain-following vertical levels from the surface to 50 hPa. The initial and boundary conditions were derived from the 0.25-degree NCEP Final Operational Model Global Tropospheric Analyses (<http://rda.ucar.edu/datasets/ds083.2/>) datasets available every 6 hours. Data assimilation (fdda model option) was used for the outermost domains D1 for all vertical levels and for domain D2 for the first 10 model levels above the ground.

The atmospheric physics options are responsible for the including of the sub-grid atmospheric and surface processes, which cannot be solved explicitly by the model - the planetary boundary layer (PBL), microphysical processes, convection, shortwave, and longwave radiation processes, land-air interaction. The WRF physics package included: the new version of Radiative Transfer Model - RRTMG parameterization (Iacono et al 2008) - for longwave and shortwave radiation to compute

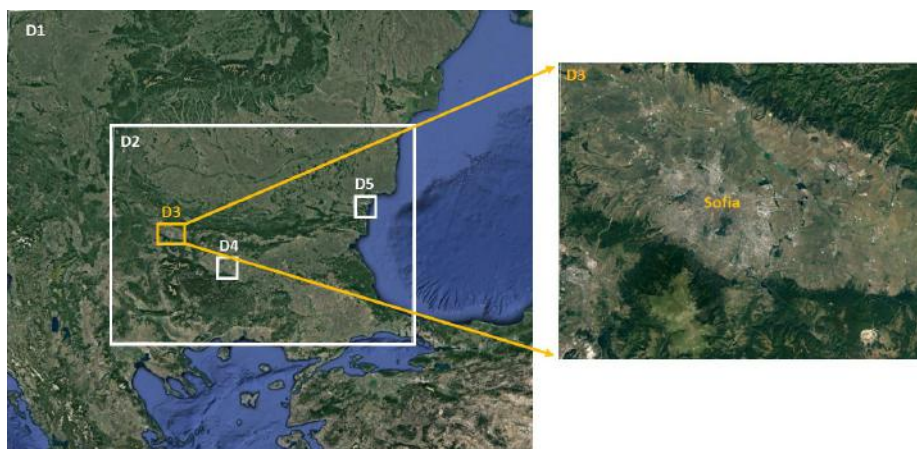


Figure 1. Modelling domains with an enlarged view of the innermost domain D4 and Sofia city

radiation at every 10 minutes; Noah land surface model (Chen, Dudhia 2001); and Kain cumulus parameterization, for D1 domain only (Kain 2004). For this specific study, the most important was to calculate properly surface temperature and wind speed to ensure reliable calculation of the Wind Chill index. The model sensitivity was evaluated using three PBL schemes -Yonsei University scheme (YSU; Hong et al 2006), Mellor-Yamada Nakanishi and Niino Level 2.5 (MYNN2.5; Nakanishi, Niino 2006), the Quasi-Normal Scale Elimination scheme (QNSE; Sukoriansky et al., 2005), and two microphysical schemes – Thompson (Thompson et al 2008), and Lin (Lin et al., 1983). The YSU PBL is a non-local K scheme, first-order; the MYNN2.5 - turbulent kinetic energy, second-order scheme with level 2.5, and QNSE uses a self-consistent, quasi-normal scale elimination algorithm and spectral space representation. The Lin microphysics is a single-moment sophisticated scheme that has ice, snow, and graupel processes, suitable for real-data high-resolution simulations; Thompson also is a single-moment for cloud water, ice, snow, rain, graupel, hail, but calculate also the rain number concentration. The selections were made after laborious inspection process of various schemes in previous studies for the same domain (Egova et al. 2017, Vladimirov et al. 2018). Six experiments were performed in this study with all possible combinations of options, described later by the names of the using schemes.

Wind Chill index calculation

The focus of the study is on the winter bio-meteorological conditions, where the air temperature and the wind speed play the most important role in determining the degree of discomfort. For that purpose, a typical winter month (January 2016) was

selected for simulations. The cold temperatures and bigger wind speeds makes the human body cooling stronger, deteriorating the thermoregulation system, and possibly the tone and the health. For describing the cooling power of the wind in cold weather, we use the Wind Chill index (Osczevski, Bluestein, 2005), given in temperature dimension. It is the temperature that the human individual feel in calm weather, with heat losses from the body equal to ones for the given air temperature and wind speed. The body reacts to different combinations of the air temperature (at 2m) and wind speed (at 10m), which is categorized in a six-grade linguistic scale (Table 1).

Table 1 Wind Chill index severity categorization

| Wind Chill Temperature | Wind Chill category | Environment Risk |
|------------------------|---------------------|--------------------------------------------------------------|
| 0°C ÷ -9°C | Low Risk | Slight increase in discomfort |
| -10°C ÷ -27°C | Moderate Risk | Increased discomfort, with risk of hypothermia and frostbite |
| -28°C ÷ -39°C | High Risk | Exposed skin can freeze in 10 to 30 minutes |
| -40°C ÷ -47°C | Very High Risk | Exposed skin can freeze in 5 to 10 minutes |
| -48°C ÷ -54°C | Severe Risk | Exposed skin can freeze in 2 to 5 minutes |
| < -55°C | Extreme Risk | Exposed skin can freeze in less than 2 minutes |

The wind chill temperature is calculated using simple relation:

$$T_{windChill} = 13.12 + 0.6215T + 11.37V^{0.16} + 0.3965TV^{0.16} \quad (1)$$

The “T” is the air temperature at 2 m in C°. The “V” is wind speed at 10 m in kmh⁻¹. The Wind Chill index has temperature dimension, so we will call it wind chill temperature (WCT).

WRF MODEL VALIDATION

The output from all described above model configurations was validated against observations in winter conditions. Data for air temperature and wind speed from the stations of the National Environment Agency at four locations in the Sofia city (Druzhba, Nadezhda, Pavlovo, Hipodruma) and the mountain site Kopitoto were used. Standard statistics - the Mean Bias (MB) and the Root Mean Square Error (RMSE) were used as criteria for model performance.

The calculated MB are given in Table 2, and the RMSE in Table 3. The MB of the temperature for Druzhba, Hipodruma, and Pavlovo is lower for the MYNN2.5_Thompson configuration. The best model options for simulation of the temperature at Nadezhda is MYNN2.5_Lin, and at Kopitoto is YSU_Thompson. The wind speed MB for Druzhba has minor value for the MYNN2_Lin simulation. The best simulation for the wind speed at Hipodruma is MYNN2.5_Thompson, for Nadezhda it is QNSE_Lin, and for Kopitoto it is the YSU_Thompson. The wind speed at Pavlovo is in the best agreement with observations for the MYNN2.5_Lin sim-

ulation. Overall, the results of the model validation by the MB suggest that the MYNN2.5_Thompson simulates temperature the best. On the other hand, the wind speed is simulated with the lowest MB by the MYNN2.5_Lin configuration.

Table 2 Mean Bias of the model configurations of the temperature at 2 m (T) and wind speed at 10 m (WS)

| Model configuration | Stations | | | | | | | | | |
|---------------------|----------|------|-----------|------|----------|-------|----------|------|---------|------|
| | Druzhba | | Hipodruma | | Kopitoto | | Nadezhda | | Pavlovo | |
| | T | WS | T | WS | T | WS | T | WS | T | WS |
| MYNN2.5_Lin | -0.54 | 0.25 | -0.96 | 1.10 | -4.16 | -5.58 | -0.09 | 1.13 | -1.07 | 0.84 |
| MYNN2.5_Thompson | 0.05 | 0.37 | -0.68 | 1.13 | -3.95 | -5.47 | 0.40 | 1.17 | -0.66 | 0.86 |
| QNSE_Lin | -3.06 | 0.37 | -3.61 | 1.14 | -4.02 | -3.63 | -2.93 | 1.09 | -3.00 | 0.87 |
| QNSE_Thompson | -1.02 | 0.65 | -1.82 | 1.27 | -3.82 | -3.63 | -1.19 | 1.29 | -1.73 | 1.02 |
| YSU_Lin | -0.84 | 0.54 | -1.62 | 1.32 | -3.60 | -2.40 | -0.59 | 1.43 | -1.68 | 0.86 |
| YSU_Thompson | -0.21 | 0.56 | -1.13 | 1.36 | -3.40 | -2.37 | -0.23 | 1.48 | -1.10 | 0.91 |

The smallest model RMSE for the temperature at Druzhba is MYNN2.5_Thompson, at Hipodruma is MYNN2.5_Lin and at Kopitoto is QNSE_Thompson. The model configuration that provides the lowest temperature RMSE at Nadejda is MYNN2.5_Thompson and at Pavlovo is the YSU_Thompson. The smallest RMSE of the wind speed at Druzhba and Hipodruma is the MYNN2_Lin. The QNSE_Thompson provides the smallest RMSE at the Kopitoto site. The model set-up that gives the best results at Nadejda and Pavlovo sites is the MYNN2_Lin. These results of the RMSE lead to the same conclusions as for the MB. Therefore, the MYNN2_Thompson model set-up simulates the air temperature with smaller error, and the MYNN2_Lin set-up simulates in the best way the wind speed. In general, all configurations underestimate the temperature (most significantly at mountain station Kopitoto) and overestimate the wind speed with approximately 1 ms⁻¹ or less.

Table 3. Root Mean Square Error of the model configurations of the temperature at 2 m (T) and wind speed at 10 m (WS)

| Model configuration | Stations | | | | | | | | | |
|---------------------|----------|------|-----------|------|----------|-------|----------|------|---------|------|
| | Druzhba | | Hipodruma | | Kopitoto | | Nadezhda | | Pavlovo | |
| | T | WS | T | WS | T | WS | T | WS | T | WS |
| MYNN2.5_Lin | 3.02 | 1.04 | 3.21 | 1.46 | 4.60 | 12.03 | 3.07 | 1.52 | 3.40 | 1.35 |
| MYNN2.5_Thompson | 2.93 | 1.07 | 3.35 | 1.50 | 4.35 | 12.00 | 2.89 | 1.58 | 3.36 | 1.43 |
| QNSE_Lin | 4.99 | 1.66 | 5.44 | 1.92 | 3.94 | 11.77 | 4.93 | 1.84 | 4.51 | 1.78 |
| QNSE_Thompson | 3.11 | 1.76 | 3.67 | 2.01 | 3.70 | 11.70 | 3.32 | 1.97 | 3.31 | 1.86 |
| YSU_Lin | 3.16 | 1.33 | 3.54 | 1.79 | 3.80 | 12.73 | 3.21 | 1.88 | 3.60 | 1.50 |
| YSU_Thompson | 3.05 | 1.38 | 3.57 | 1.86 | 3.54 | 12.63 | 3.04 | 1.97 | 3.25 | 1.51 |

Overall, the model validation shows that the configurations with MYNN2.5 PBL scheme and Thompson microphysics have better behaviour in comparison to the others, concerning the two meteorological parameters. Their results are superior at Druzhba and Hipodruma stations, while the other model configurations give better results for the other stations. Moreover, the model configuration using the Thompson scheme for microphysical parameterization presents better results than Lin. The Sofia city is located in complex topography with mountain Vitosha nearby, and most likely, these differences result from the local modifications of the large-scale weather. Therefore, reasons could be the roughness and/or topography characteristics surrounding the city, proximity to the mountain areas, terrain height, and the station exposure to the solar radiation. Note that structures are not presented explicitly in these types of models, and shadow as well as the building wake effects can affect the temperature and wind fields significantly.

WIND CHILL MODELLING

The results from the Wind Chill modelling show that different cases belong mainly to the categories – Low Risk, Moderate Risk, and High Risk, and mostly to the first two. The number of Low Risk cases in the different domain locations for the period under consideration is shown in Figure 2. There are between 210 and 360 Low Risk cases in large area of the domain. The different districts of the Sofia city itself are characterized by 210 to 300 cases, except for the areas nearby the Vitosha Mountain. The number of Low Risk cases in the north-western, north-eastern, and south-eastern areas of the domain is higher. There are, however, some differences between the model configurations. The number for the north-eastern near-city areas

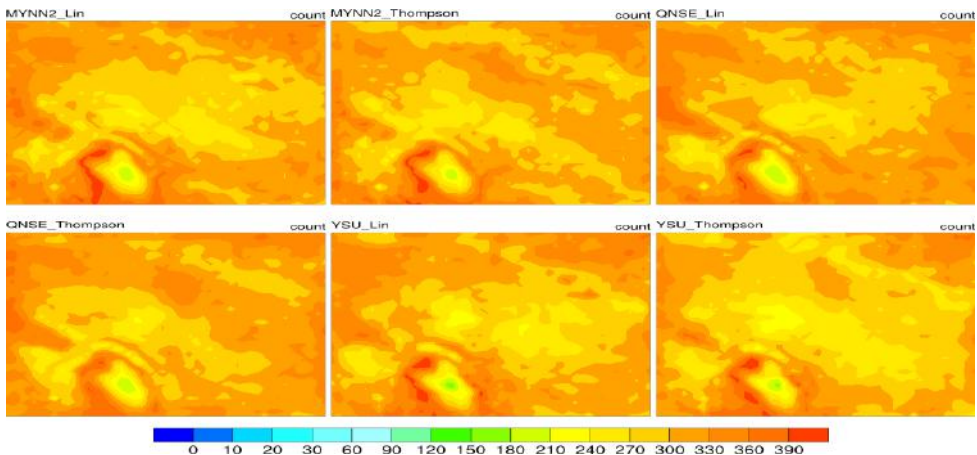


Figure 2. Number of cases for Low Risk conditions from WRF simulations with different model options for January 2016

of the domain for MYNN2.5_Lin, YSU_Lin, and YSU_Thompson, is smaller in comparison with the other model configurations. The QNSE_Thompson has a spot in that area, with about 30 more Low Risk cases than in the surrounding area. The Low Risk count distribution in the Vitosha Mountain is more diverse. It is layered from above 390 in the lowest terrain heights to below 150 cases at the highest ones. The figure shows also, that the north-west and western slopes have more Low Risk cases than the neighbour ones.

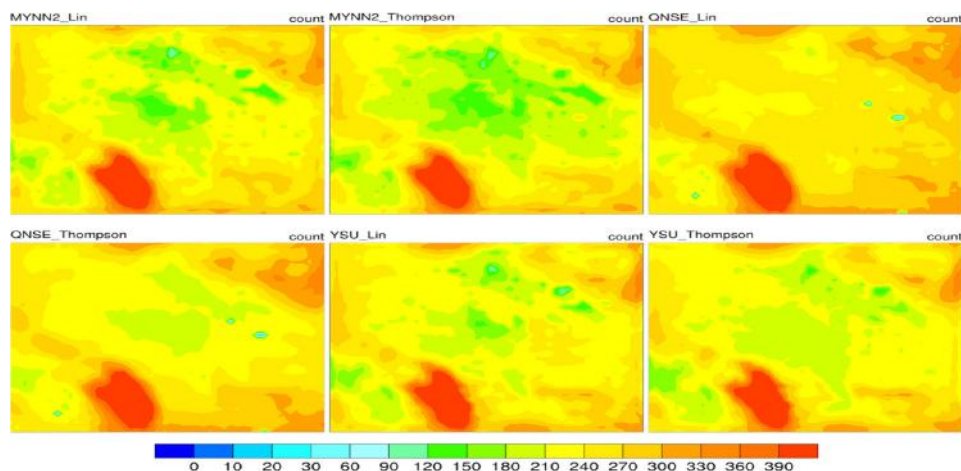


Figure 3. Number of cases for Moderate Risk conditions from WRF simulations with different model options for January 2016

Figure 3 shows the spatial distribution of the Moderate Risk conditions counts in the domain area. Here, the number of cases in the northeastern and the southeastern parts are between 240 and 330. The other areas except Vitosha Mountain have between around 120 and 240 cases with Moderate Risk conditions. There are more than 240 cases in the Vitosha Mountain, and over large area, they are above 390. The Moderate Risk cases spatial distribution has also some distinctive characteristics. The QNSE_Lin model configuration appears to have more Moderate Risk cases than anyone else does. The spatial distribution of that one, QNSE_Thompson and YSU_Thompson is more homogenous than in the other model configurations. The Vitosha Mountain, however, is an exception with above 390 cases for all model configurations.

The plots for the High Risk cases (Figure 4) is very similar for all model configurations, except the QNSE_Lin, which shows some unique spatial features in the eastern northwestern parts of the domain, similar to the Vitosha Mountain. The entire domain area has up to 10 cases. Only for the area of the Vitosha Mountain the number of cases increases from 10 to about 90 at the elevated areas.

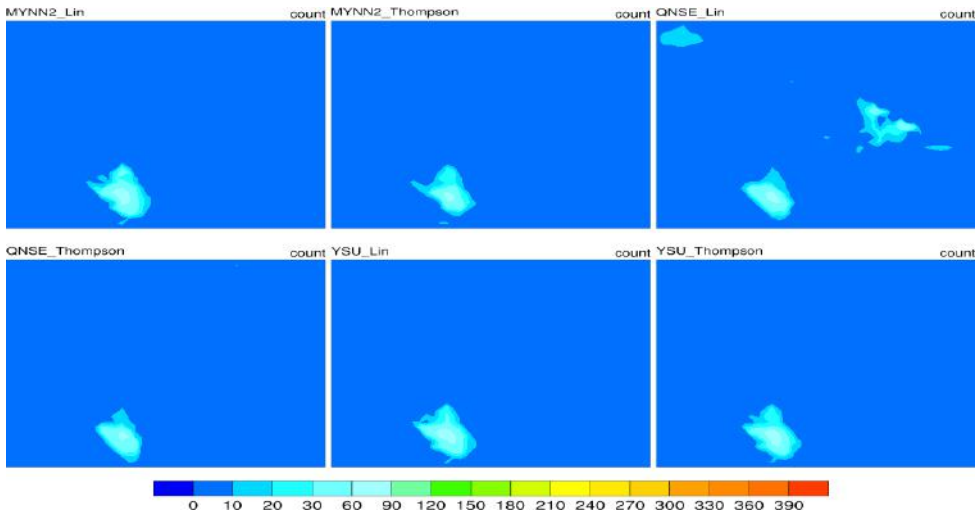


Figure 4. Number of cases for High Risk conditions from WRF simulations with different model options for January 2016

CONCLUSION

As was noted previously, the model configurations with MYNN2.5 show better results than the other (QNSE or YSU) PBL schemes. It is very likely due that Sofia city is located in a valley surrounded by mountains and highland terrain and some PBL schemes do not succeed to simulate the turbulence regime in the low atmospheric levels. The local turbulent kinetic energy scheme MYNN2.5 is more suitable for stable winter conditions. Furthermore, the model configuration with Thompson microphysics gives a little better results than Lin microphysics.

The spatial distribution of the number of Moderate Risk cases of the Wind Chill index calculated from the WRF output for the region of Sofia in the winter depends on the model configuration. Mainly, the type of PBL parameterization scheme ensures that dependency. The model simulations with the MYNN2.5 PBL scheme have a more heterogeneous spatial pattern of the Wind Chill index than the other ones for the Moderate Risk categories. The Low Risk distribution also varies between the model simulations. There are a few High Risk cases, which does not imply significant differences between the model configurations. An exception from the last statement is the Vitosha Mountain, where a high number of High Risk wind chill cases are calculated. This study can recommend using MYNN2.5 PBL and Thompson microphysics for Wind Chill modelling at the Sofia region. However, a more comprehensive study is needed to strengthen these preliminary conclusions.

ACKNOWLEDGMENTS

This work has been carried out in the framework of the National Science Program "Environmental Protection and Reduction of Risks of Adverse Events and Natural Disasters", approved by the Resolution of the Council of Ministers № 577/17.08.2018 and supported by the Ministry of Education and Science (MES) of Bulgaria (Agreement № Д01-322/18.12.2019).

We want to acknowledge the Bulgarian National Science Fund (grant DN-04/2/13.12.2016).

Special thanks to the Faculty of Physics at the University of Sofia "St. Kl. Ohridski" for the access to the supercomputing facilities (NESTUM cluster <http://hpc-lab.sofiatech.bg/home/>, funded by the ERDF Project BG161PO003-1.2.05-0001-C0001) at Sofia Tech Park, Sofia, Bulgaria and to US NCEP for providing free-of-charge data and software.

REFERENCES

- Chen, S. H., Sun W.Y., (2002) A one-dimensional time dependent cloud model. *J. Meteor. Soc. Japan.*, 80(1), 99–118.
- Chen F., Dudhia J (2001) Coupling an advanced land surface–hydrology model with the Penn State–NCAR MM5 modeling system. Part I: Model implementation and sensitivity. *Mon Wea Rev* 129: 569–585
- Cheng, Y., Niu, J., & Gao, N. Thermal comfort models: A review and numerical investigation. (2012) *Building and Environment*, 47(1), 13–22.
- Collier C. G. (2006) The impact of urban areas on weather. *Q. J. R. Meteorol. Soc.*, 132, 1–25.
- Gadzhev, G., Ganev, K., Miloshev, N., Syrakov, D. & Prodanova, M., (2014a) Some basic facts about the atmospheric composition in Bulgaria - Grid computing simulations, *Lecture Notes in Computer Science (including subseries Lecture Notes in Artificial Intelligence and Lecture Notes in Bioinformatics)*, 8353 LNCS, 484-490.
- Gadzhev, G., Ganev, K., Miloshev, N., Syrakov, D. & Prodanova, M., (2014b) Analysis of the processes which form the air pollution pattern over Bulgaria, *Lecture Notes in Computer Science (including subseries Lecture Notes in Artificial Intelligence and Lecture Notes in Bioinformatics)*, 8353 LNCS, 390-396.
- Gadzhev, G., Ganev, K., Syrakov, D., Miloshev, N. & Prodanova, M., (2012) Contribution of biogenic emissions to the atmospheric composition of the Balkan Region and Bulgaria, *International Journal of Environment and Pollution*, 50 (1-4), 130-139.
- Gadzhev, G., Syrakov, D., Ganev, K., Brandiyska, A., Miloshev, N., Georgiev, G. & Prodanova, M., (2011a) Atmospheric composition of the Balkan region and Bulgaria. Study of the contribution of biogenic emissions, *AIP Conference Proceedings*, 1404, 200-209.
- Hidalgo, J., Masson V., & Gimeno, L. (2010) Scaling the Daytime Urban Heat Island and Urban-Breeze Circulation. *J. Appl. Meteor. Climatol.*, 49, 889–901.

- Hong, S., Noh Y. & Dudhia J. (2006), A new vertical diffusion package with an explicit treatment of entrainment processes. *Mon Weather Rev* 134(9):2318–2341.
- Iacono M. J., Delamere J.S., Mlawer E.J., Shephard M.W., Clough S.A. & Collins W.D. (2008) Radiative forcing by long-lived greenhouse gases: Calculations with the AER radiative transfer models. *J Geophys Res Atmos* 113:2-9.
- Ivanov, V., Gadzhev G., Ganev K. & Chervenkov H. (2020) Sensitivity of the Simulated Heat Risk in Southeastern Europe to the RegCM Model Configuration—Preliminary Results. *LNCS*, 11958, 340-347
- Ivanov V., Evtimov, S. (2014a) Wind chill hazard in Bulgaria during 2003-2012 period. *Comptes Rendus de L'Academie Bulgare des Sciences*, 67(11), 1521-1530.
- Ivanov V., Evtimov, S. (2014b) Heat Risks in Bulgaria during 2003-2012 period. *Bulgarian Geophysical Journal*, 40, 3-12.
- Kain J.S. (2004) The Kain–Fritsch convective parameterization: An update. *J Appl Meteorol* 43:170–181
- Lin C, Zhang Z, Pu Z, Wang F (2017) Numerical simulations of an advection fog event over Shanghai Pudong International Airport with the WRF model. *J Meteorol Res* 31(5):874–889.
- Nakanishi, M., Niino, H. (2006) An improved Mellor–Yamada level 3 model: its numerical stability and application to a regional prediction of advecting fog. *Bound. Layer Meteor.*, 119, 397–407.
- Nakanishi, M., Niino, H. (2009) Development of an improved turbulence closure model for the atmospheric boundary layer. **J. Meteor. Soc. Japan**, **87**, 895–912.
- Niu, G.–Y., Yang Z-L., Mitchell K. E., Chen F., Ek, M. B., Barlage M., Kumar A., Manning K, Niyogi D., Rosero E., Tewari M. & Xia Y. (2011) The community Noah land surface model with multiparameterization options (Noah–MP): 1. Model description and evaluation with local–scale measurements. *J. Geophys. Res.*, 116, D12109.
- Olson, J. B., Kenyon, J. S., Angevine, W.M., Brown, J. M., Pagowski, M. & Sušelj K. (2019) A Description of the MYNN-EDMF Scheme and the Coupling to Other Components in WRF–ARW. NOAA Technical Memorandum OAR GSD, 61, 37.
- Osczevski R., Bluestein, M. (2005) The New Wind Chill Equivalent Temperature Chart. *Bull. Amer. Meteor. Soc.*, 86 (10), 1453–1458.
- Rizwan, A. M., Dennis, L. Y., & Chunho, L. I. U. (2008) A review on the generation, determination and mitigation of Urban Heat Island. *Journal of Environmental Sciences*, 20(1), 120-128.
- Skamarock W C, Klemp JB, Dudhia J., et al. (2008) A Description of the Advanced Research WRF Version 3. NCAR Technical Note, NCAR/TN-475+STR.
- Song–You, H., Noh, Y., Dudhia, J. (2006) A new vertical diffusion package with an explicit treatment of entrainment processes. *Mon. Wea. Rev.*, 134, 2318–2341.

- Stocker, T.F., Qin D., Plattner G.-K., Alexander L.V. et al. (2013) Technical Summary. In: Climate Change 2013: The Physical Science Basis. *Contribution of Working Group I to the Fifth Assessment Report of the Intergovernmental Panel on Climate Change* [Stocker, T.F., D. Qin, G.-K. Plattner, M. Tignor, S.K. Allen, J. Boschung, A. Nauels, Y. Xia, V. Bex and P.M. Midgley (eds.)]. United Kingdom and New York: Cambridge University Press, Cambridge.
- Sukoriansky, S., B. Galperin & V. Perov, (2005), Application of a new spectral theory of stably stratified turbulence to the atmospheric boundary layer over sea ice. *Boundary-Layer Meteorol* 117(2):231–257.
- Thompson, G., Field, P. R., Rasmussen, R. M. & Hall, W. D. (2008) Explicit Forecasts of Winter Precipitation Using an Improved Bulk Microphysics Scheme. Part II: Implementation of a New Snow Parameterization. *Mon. Wea. Rev.*, 136, 5095–5115.
- Vladimirov E., Dimitrova R. & Danchevski V., 2018: Sensitivity of WRF model results to topography and land cover: study for the Sofia region, *Annuaire de l'Université de Sofia "St. Kliment Ohridski", Faculté de Physique*, 111:87-101.
- Yang, Z.-L., Niu G.-Y., Mitchell K. E., Chen F., Ek M. B., Barlage M., Longuevergne L., Manning K., Niyogi D., Tewari M., & Xia Y. (2011) The community Noah land surface model with multiparameterization options (Noah-MP): 2. Evaluation over global river basins. *J. Geophys. Res.*, 116, D12110.

✉ **Vladimir Ivanov**

<https://orcid.org/0000-0001-9768-1049>

National Institute of Geophysics, Geodesy and Geography
Bulgarian Academy of Sciences
Sofia, Bulgaria

E-mail: vivanov@geophys.bas.bg

✉ **Reneta Dimitrova**

<http://orcid.org/0000-0002-5931-8713>

National Institute of Geophysics, Geodesy and Geography
Bulgarian Academy of Sciences
Department of Meteorology and Geophysics

Faculty of Physics
"St. Kliment Ohridski" University of Sofia
Sofia, Bulgaria

E-mail: r.dimitrova@phys.uni-sofia.bg

MODELLING OF THE SULPHUR AND NITROGEN DEPOSITIONS OVER THE BALKAN PENINSULA BY CMAQ AND EMEP-MSC-W – PRELIMINARY RESULTS

Georgi Gadzhev, Vladimir Ivanov

*National Institute of Geophysics, Geodesy and Geography –
Bulgarian Academy of Sciences (NIGGG-BAS)*

Abstract. The air quality US EPA models-3 system consisting of SMOKE - emission model and pre-processor, MM5 – meteorological driver, and CMAQ – chemical-transport model, is used in many studies of the air quality in the Balkan Peninsula, and in particular Bulgaria. It runs in different model resolutions, depending on the domain, from European to city scale. The EMEP-MSC-W model is another chemical transport model, widely used in air quality modelling. Two of the processes involved in the concentration change of some pollutant are the dry and wet depositions. The air quality modelling capability depends on many factors, for example, meteorology and emissions. We study the differences in the simulation of the wet and dry depositions for nitrogen and sulphur compounds, between the CMAQ and the EMEP-MSC-W model for a period of 8 years.

Keywords: modelling; CMAQ; EMEP; pollution; composition; air quality

INTRODUCTION

The air pollution nowadays forces many countries to take actions for mitigating its adverse effects on human health. Therefore, we need a lot of information, which is increasing in recent years. There are already more direct and indirect data connected to the air quality from different surface-based and satellite-based observing systems. However, we need to understand the different processes involved in the creation, transportation, and transformation of the air pollutant species, which help us to understand their distribution at different spatial and temporal scales. The research community performs these tasks by air quality models systems, with chemical transport models as the main component. We use one of these systems with the chemical transport model CMAQ, for modeling the air quality in the Balkan Peninsula. Previous results from air pollution modelling for the Balkan Peninsula and Bulgaria are published in a lot of research works (Gadzhev et al. 2014, Georgieva 2014, Syrakov et al. 2015, Kaleyna, Mukhtarov, Miloshev 2013a,

2013b, 2014). The air composition is formed by several processes, which involve dry deposition, wet deposition, horizontal and vertical advection, horizontal and vertical diffusion, emission, chemical transformation, aerosol processes, and aqueous chemistry (Gadzhev, Ganey, Mukhtarov 2020, Gadzhev et al. 2011). They interact in between and determine the air composition at different scales. There are some studies with CMAQ of the dry and wet deposition and their influence on the precipitation for Bulgaria (Syarakov et al. 2019a, 2019b, Georgieva et al. 2017, 2019) for different periods up to two years. Another chemical transport model – EMEP-MSC-W is also widely used for air quality studies in Europe (Simpson et al. 2012). Our aim is to make a preliminary study of the model comparison between long-term high-resolution simulations with the CMAQ and the EMEP-MSC-W simulations of the Nitrogen (N) and Sulphur (S) dry and wet deposition processes in the Balkan Peninsula for a long-term period and high spatial resolution.

METHODOLOGY

The study is based on air quality simulations with two chemical transport models over the Balkan Peninsula from 2000 to the 2007 year. One of these simulations is performed with the US EPA Models-3 system, which includes CMAQ (Community Multiscale Air Quality) model (Denis et al. 1996, Byun, Ching 1999, Byun, Schere 2006), SMOKE (Sparse Matrix Operator Kernel Emissions Modelling System) (Coats, Houyoux 1996, Houyoux, Vukovich 1999, CEP 2003) and the regional mesoscale meteorological model MM5. The CMAQ is a numerical chemical transport model for modelling the different processes and their contribution involved in changing the surface and airborne gases and aerosols. That model needs three kinds of input information – initial and boundary conditions, meteorology, and emissions.

We use the regional mesoscale numerical model MM5 for modelling the weather and climate conditions (Dudhia 1993, Grell, Dudhia, Stauffer) over the Balkan Peninsula. It is a non-hydrostatic high-resolution model, providing the needed raw meteorological output for further processing. We use the nesting capabilities of the MM5, where the output from each outer domain excluding the last one, is used as input for the smaller one. The first and the bigger one (D1) is the European domain with background information, provided from the NCEP Global Analysis Data with $1^\circ \times 1^\circ$ (~81 x 81km) horizontal resolution. Our research work is concentrated on the domain D3 geographically limited to the Balkan Peninsula and some adjacent territories. The output from the MM5 model, need to be reprocessed to the right format for ingesting in the CMAQ. For that purpose, we use the Meteorological – Chemistry Interface Processor – MCIP, which prepares all meteorological input information CMAQ needs.

The emissions from the large source sources and area sources for the whole domain excluding Bulgaria and some adjacent territories are ingested from the TNO

high-resolution emission inventory with spatial resolution $0.25^\circ \times 0.125^\circ$ (Denier van der Gon et al., 2010) in a longitude-latitude grid, reprocessed from the 50-km grid of the EMEP (European Monitoring and Evaluation Programme) database. The emissions for Bulgaria are from the National Emission Inventory. The CMAQ needs also from biogenic emissions. They are provided from the emission pre-processor SMOKE. The input information is provided from the TNO emissions, the MCIP output, and the land-use database.

The CMAQ model accounts for the following processes with a different contribution to the changing of the concentration field for each pollutant: horizontal diffusion (HDIF); horizontal advection (HADV); vertical diffusion (VDIF); vertical advection (VADV); dry deposition (DRYDEP); emissions (EMISS); chemical transformations (CHEM); aerosol processes (AERO); cloud processes (CLOUD). The solution of the transport and transformation equations gives the mean concentration change of i^{th} pollutant in the first model layer from time t to time $t + \Delta t$.

It is presented as a sum of the contribution of the former processes:

$$\Delta c_i^1 = (\Delta c_i^1)_{hdif} + (\Delta c_i^1)_{vdif} + (\Delta c_i^1)_{hadv} + (\Delta c_i^1)_{vadv} + (\Delta c_i^1)_{drydep} + (\Delta c_i^1)_{emiss} + (\Delta c_i^1)_{chem} + (\Delta c_i^1)_{cloud} + (\Delta c_i^1)_{aero}$$

$$\Delta c_i^1 = \frac{1}{h_1} \int_0^{h_1} (c_i(t + \Delta t) - c_i(t)) dz$$

We focus on the dry and wet depositions modelled by the CMAQ in this study. The N deposition contains the contribution from NO_2 (Nitrogen dioxide), NO (Nitrogen oxide), NO_3 (Nitrogen trioxide), N_2O_5 (Dinitrogen pentoxide), HNO_3 (Nitric acid), HONO (Nitrous acid), ANH_{4j} (Accumulation-mode ammonium mass), ANH_{4i} (Aitken-mode ammonium mass), ANO_{3j} (Accumulation-mode nitrate mass), ANO_{3i} (Aitken-mode aerosol nitrate mass) and NH_3 (Ammonia):

$$N_{deposition} = \text{NO}_2 + \text{NO} + \text{NO}_3 + \text{N}_2\text{O}_{25} + \text{HNO}_3 + \text{HONO} + \text{ANH}_{4j} + \text{ANH}_{4i} + \text{ANO}_{3j} + \text{ANO}_{3i}$$

The S deposition contains the contribution from SO_2 (Sulphur dioxide), SULF (Sulphate aerosols), ASO_{4j} (Accumulation-mode aerosol sulphate mass), and ASO_{4i} (Aitken-mode aerosol sulphate mass):

$$S_{deposition} = \text{SO}_2 + \text{SULF} + \text{ASO}_{4j} + \text{ASO}_{4i}$$

The CMAQ deposition output is in 1-hour frequency. Therefore, we sum up the hourly values of the N and S components for every day of the simulation, finding the daily deposition values.

The second model used for comparison with the previous one is with the Meteorological Synthesizing Centre-West (MSC-W) of the European Monitoring and Evaluation Programme (EMEP). It is a chemical transport model (Simpson et al., 2012), a key tool involving in the European air pollution policy assessments. In the beginning, the model covers the whole of Europe with a resolution of about 50 km x 50 km, with vertical levels up to the tropopause (100 hPa). The model has changed over the years, adding different features, and currently, his horizontal resolution ranging from 5 km to 1 degree with 20 vertical levels. In our study, we use a grid size 0.1° x 0.1°. The EMEP-MSC-W model runs with meteorological fields from the numerical weather prediction system ECMWF-IFS Cycle36r1. The model output is with daily frequency, so we do not need to do further post-processing.

For comparison of the models, we use two kind of error characteristics. The first is Normalised Mean Bias noted as (NMB):

$$NMB = \frac{\sum_i M - \sum_i E}{\sum_i E},$$

and the second is the Mean Bias (MB):

$$MB = \frac{1}{n} \sum_i M - \frac{1}{n} \sum_i E$$

The notions in these equations are i - i^{th} value, M - the output form CMAQ, E - the output from EMEP-MSC-W. The results are revealed with the multiyear averaged values of the NMB for each grid point and the annual spatial-averaged values of the bias of the CMAQ output.

RESULTS

The results are given for the N depositions and for the S depositions, separated in dry component, wet component, and total (dry+wet) component. The multiyear average of the S dry, wet, and total depositions (figure 1) reveals the following features. There is a difference between the CMAQ and the EMEP-MSC-W model due to the difference in the emission inventories. We can clearly note the missing of some of the S sources in one model, but not in the other. We can see from the sum of dry and wet deposition shown on the figure, that the TPP Bobov dol, the TPP Pernik, the Sofia city, the town of Devnia, the Bucharest city and the Istanbul city are noticeable in the CMAQ model output, but not in the EMEP-MSC-W output. On the other hand, Zlatna Panega and Southern Italy sources show up in the EMEP output, but not in the CMAQ one. The influence of the input meteorological data and the meteorological driver for the models have a considerable effect mainly on the wet deposition modelling capability. The wet deposition in the EMEP-MSC-W model has smaller spatial gradients, more intensive and local maximums on larger

areas around the corresponding sources. On the other hand, the wet deposition in the CMAQ has smaller values and bigger local spatial gradients.

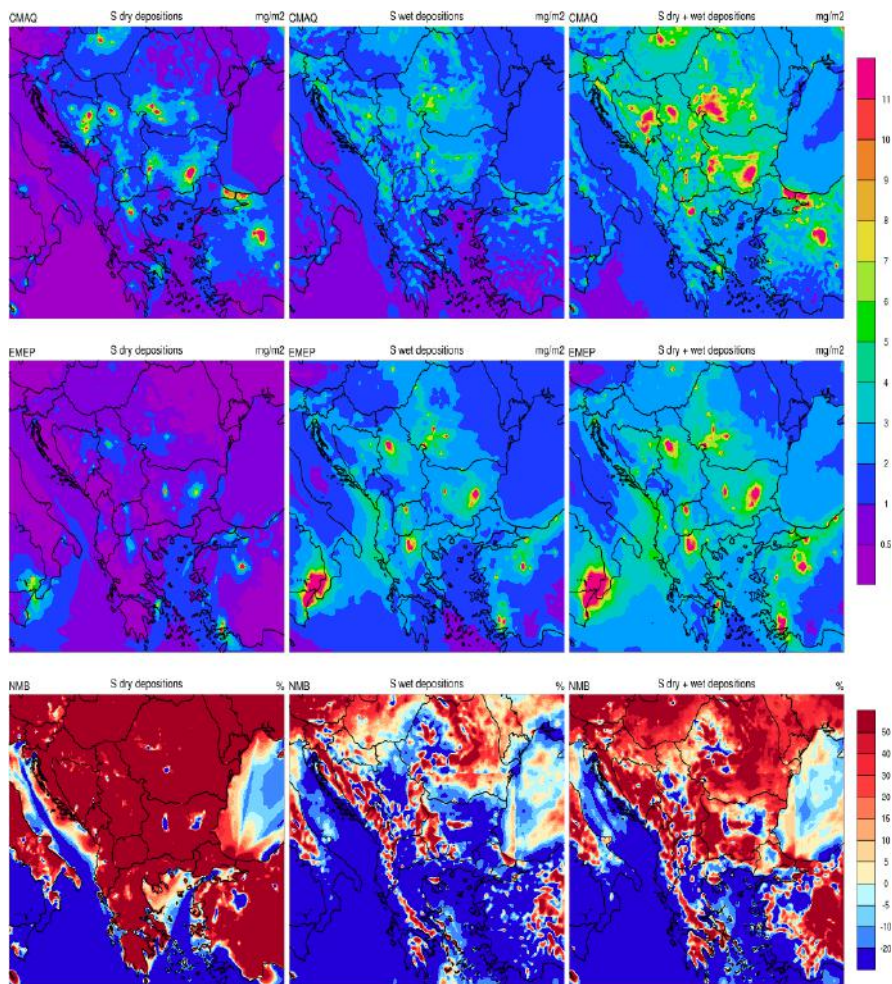


Figure 1. CMAQ (upper row) multiyear average sulphur dry deposition (left plot), wet deposition (middle plot) and dry + wet (right plot). EMEP-MSC-W (middle row) multiyear average Sulphur dry deposition (left plot), wet deposition (middle plot) and dry + wet (right plot). Normalized mean bias [%] of the CMAQ model (lowest row) for sulphur dry deposition (left plot), wet deposition (middle plot) and dry + wet (right plot) in comparison to the EMEP-MSC-W.

The influence of the meteorological conditions and the orography is more notable for figure 1 where the normalized mean biases are shown. The normalized mean bias of the dry deposition over the land areas reaches 50 % and more and only above some of the sources is negative. The normalized mean bias of the sum of the dry and wet depositions has a similar spatial structure with one of the wet depositions for the two models but is more complex. The CMAQ and EMEP-MSC-W simulate the annual area-averaged dry plus wet deposition in a quite similar way from 2000 to 2007, as is shown in table 1. Although more or less different in particular years, they are close. The bias from 2000 to 2003 is negative (figure 2), which is easy to suggest from the area-averaged total depositions and the CMAQ bias for the whole period.

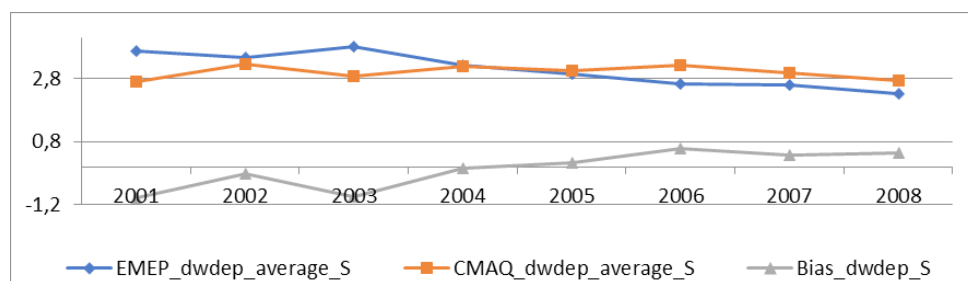


Figure 2. Annual area averaged Sulphur total (dry + wet) depositions and bias of the CMAQ model

Table 1. Annual area averaged and multiyear area averaged (YA) Sulphur total (dry + wet) depositions

| Year | EMEP dry + wet average S (mg/m ²) | CMAQ dry + wet average S (mg/m ²) | Bias of dry+ wet S (mg/m ²) |
|------|-----------------------------------------------|-----------------------------------------------|-----------------------------------------|
| 2000 | 3.6684 | 2.6886 | -0.9798 |
| 2001 | 3.4655 | 3.2473 | -0.2182 |
| 2002 | 3.8176 | 2.8822 | -0.9355 |
| 2003 | 3.2111 | 3.1706 | -0.0405 |
| 2004 | 2.9467 | 3.0579 | 0.1112 |
| 2005 | 2.6357 | 3.2199 | 0.5842 |
| 2006 | 2.5942 | 2.965 | 0.3708 |
| 2007 | 2.3126 | 2.7426 | 0.4299 |
| YA | 2.9426 | 3.0188 | 0.0762 |

The result for the N depositions is shown in figure 3. They have different spatial and temporal features from the S ones. As is seen in figure 3, the model difference

between the dry depositions appears in the almost homogeneous distribution for the CMAQ, in contrast to the clearly outlined sources in the EMEP-MSC-W. The input meteorological data and the meteorological driver for the models exert substantial influence mostly on the wet deposition modelling. The spatial gradient of the mean EMEP-MSC-W wet deposition is smaller than the CMAQ one. However, the CMAQ mean wet deposition is smaller and with bigger local spatial gradients following the orography features. The results for the normalized mean biases of the dry, wet, and sum of the dry and wet depositions (figure 3) suggest a substantial influence of the

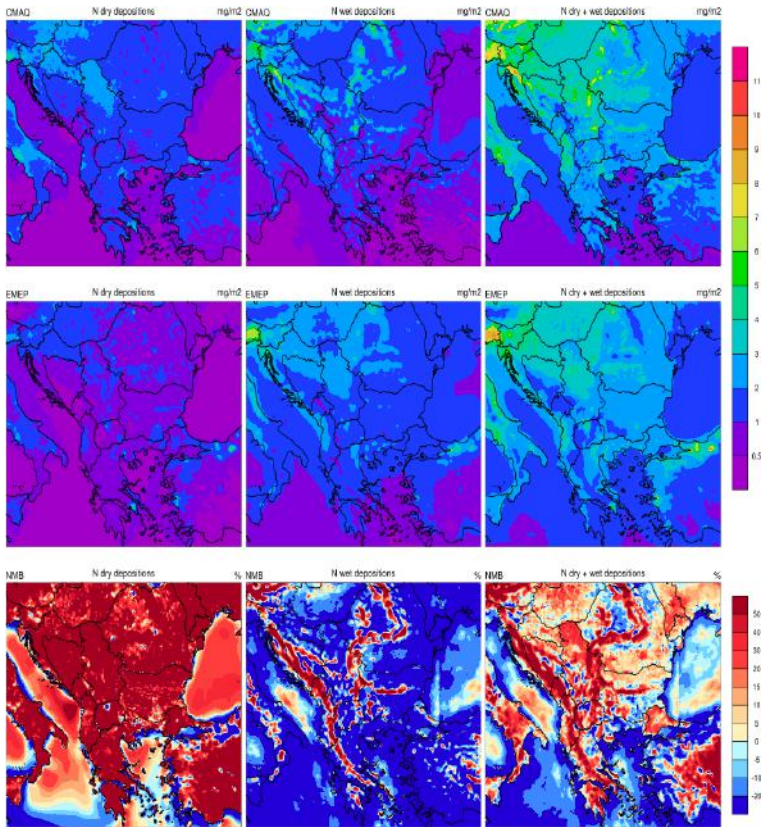


Figure 3. CMAQ (upper row) multiyear average Nitrogen dry deposition (left plot), wet deposition (middle plot) and dry + wet (right plot). EMEP-MSC-W (middle row) multiyear average nitrogen dry deposition (left plot), wet deposition (middle plot) and dry + wet (right plot).). Normalized mean bias [%] of the CMAQ model (lowest row) for nitrogen dry deposition (left plot), wet deposition (middle plot) and dry + wet (right plot) in comparison to the EMEP-MSC-W

meteorological input and the orography on the spatial distribution of the mean wet deposition. The normalized mean bias of the mean dry deposition reaches 50% not only on the land however, is negative in some places. The normalized mean bias of the sum of the dry and wet depositions has a similar, but a more complex structure with the one of the wet deposition, because of the influence of the dry deposition.

The data in table 2 and figure 4 suggest that the simulated annual area-averaged total nitrogen depositions by the CMAQ and EMEP-MS-C-W models pretty much the same, although the CMAQ value is smaller in 2002. The results for the multiyear area-averaged total nitrogen depositions are very similar.

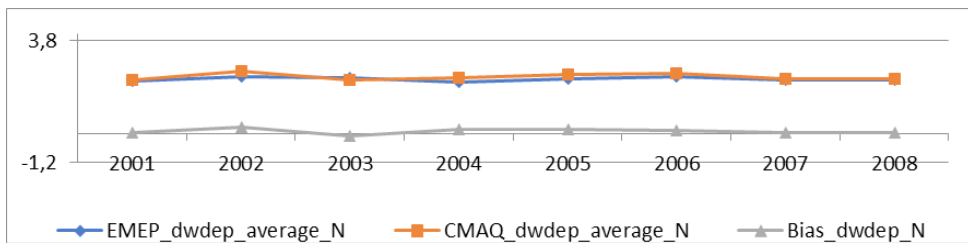


Figure 4. Annual area averaged Nitrogen total (dry + wet) depositions and bias of the CMAQ model.

Table 2. Annual area averaged and multiyear area averaged (YA) Nitrogen total (dry + wet) depositions

| Year | EMEP dry + wet average N (mg/m ²) | CMAQ dry + wet average N (mg/m ²) | Bias of dry+ wet N (mg/m ²) |
|------|-----------------------------------------------|-----------------------------------------------|-----------------------------------------|
| 2000 | 2.1538 | 2.1827 | 0.0289 |
| 2001 | 2.3273 | 2.5671 | 0.2398 |
| 2002 | 2.2701 | 2.1798 | -0.0903 |
| 2003 | 2.1185 | 2.285 | 0.1665 |
| 2004 | 2.2455 | 2.4198 | 0.1743 |
| 2005 | 2.3357 | 2.451 | 0.1153 |
| 2006 | 2.1773 | 2.2341 | 0.0568 |
| 2007 | 2.1989 | 2.2235 | 0.0246 |
| YA | 2.2331 | 2.3286 | 0.0955 |

CONCLUSION

The results suggest that the Nitrogen annual area-averaged total depositions are represented more similarly by the two models, than the Sulphur ones. There is a large orography influence on the sum of dry and wet deposition for both groups of chemical species. The current research suggests that the orography

and meteorology exert substantial influence on the total Nitrogen and Sulphur depositions.

ACKNOWLEDGMENTS

This work has been carried out in the framework of the National Science Program "Environmental Protection and Reduction of Risks of Adverse Events and Natural Disasters", approved by the Resolution of the Council of Ministers № 577/17.08.2018 and supported by the Ministry of Education and Science (MES) of Bulgaria (Agreement № Д01-322/18.12.2019).

Bulgarian National Science Fund (grant DN-04/2/13.12.2016).

Special thanks are due to US EPA and US NCEP for providing free-of-charge data and software and to the Netherlands Organization for Applied Scientific research (TNO) for providing the high-resolution European anthropogenic emission inventory

REFERENCES

- Byun, D., Ching, J., (1999), *Science Algorithms of the EPA Models-3 Community Multiscale Air Quality (CMAQ) Modeling System*. EPA Report 600/R-99/030, Washington DC.
- Byun, D., Schere, K.L., (2006), Review of the governing equations, computational algorithms, and other components of the models-3 community multiscale air quality (CMAQ) modeling system. *Appl. Mech. Rev.* 59, 51 – 77.
- CEP, (2003), *Sparse Matrix Operator Kernel Emission (SMOKE) Modeling System*, University of North Carolina, Carolina Environmental Programs - CEP, Research Triangle Park, North Carolina.
- Coats, C.J., Jr., and Houyoux, M.R., (1996), *Fast Emissions Modeling With the Sparse Matrix Operator Kernel Emissions Modeling System, The Emissions Inventory: Key to Planning, Permits, Compliance, and Reporting, Air and Waste Management Association*, New Orleans, September
- Denier van der Gon, H., Visschedijk, A., van de Brugh, H., Droge, R., (2010), *A high resolution European emission data base for the year 2005*, TNO-report TNO-034-UT-2010-01895 RPT-ML, Apeldoorn, The Netherlands.
- Dennis, R.L., Byun, D.W., Novak, J.H., Galluppi, K.J., Coats, C.J., and Vouk, M.A., (1996), The Next Generation of Integrated Air Quality Modeling: EPA's Models-3, *Atmospheric Environment* 30, 1925 – 1938.
- Dudhia, J. (1993) A nonhydrostatic version of the Penn State-NCAR mesoscale model: validation tests and simulation of an Atlantic cyclone and cold front, *Monthly Weather Review*, 121 (5), 1493 – 1513.

- Gadzhev G., Ganev K., Mukhtarov P., (2020) Statistical Moments of the Vertical Distribution of Air Pollution over Bulgaria, *Lecture Notes in Computer Science (including subseries Lecture Notes in Artificial Intelligence and Lecture Notes in Bioinformatics)*, 11958 LNCS, 213 – 219.
- Gadzhev, G., Ganev, K., Miloshev, N., Syrakov, D., Prodanova, M. (2013) Numerical Study of the Atmospheric Composition in Bulgaria, *Computers and Mathematics with Applications*, 65, 402 – 422.
- Gadzhev G., Syrakov, D., Ganev, K., Brandiyska, A., Miloshev, N., Georgiev, G., Prodanova, M. (2011) Atmospheric composition of the Balkan region and Bulgaria. Study of the contribution of biogenic emissions, *AIP Conference Proceedings*, 1404, 200 – 209.
- Georgieva E., Syrakov D., Hristova E., Prodanova M., Gospodinov I. (2019) Comparison of EMEP and WRF_CMAQ modelling results for deposition estimates in Bulgaria for 2016 and 2017, *19th International Conference on Harmonisation within Atmospheric Dispersion Modelling for Regulatory Purposes, Harmo 2019*.
- Georgieva E., Hristova E., Syrakov D., Prodanova M., Batchvarova E. (2017) Preliminary evaluation of CMAQ modelled wet deposition of sulphur and nitrogen over Bulgaria. *HARMO 2017 – 18th International Conference on Harmonisation within Atmospheric Dispersion Modelling for Regulatory Purposes, Proceedings 2017 – October*, 51 – 55.
- Georgieva, I. (2014) Study of the air quality index climate for Bulgaria, *Proc. of the international conference on numerical methods for scientific computations and advanced applications*, May 19 – 22, 2014, Bansko, ISBN978-954-91700-7-8, 39. – 42.
- Grell, G.A., Dudhia, J., Stauffer, D.R. *A description of the Fifth Generation Penn State/NCAR Mesoscale Model (MM5) NCAR Technical Note*, NCAR TN-398-STR, 138.
- Houyoux, M.R., and Vukovich, J.M. (1999) *Updates to the Sparse Matrix Operator Kernel Emission (SMOKE) Modeling System and Integration with Models-3, The Emission Inventory: Regional Strategies for the Future*, Raleigh, NC, Air and Waste Management Association.
- Kaleyna P., Mukhtarov P., Miloshev N. (2014) Seasonal Variations of the Total Column Ozone over Bulgaria in the Period 1996–2012, *Comptes rendus de l'Acad'emie bulgare des Sciences*, 67, 7.
- Kaleyna P., Pl. Muhtarov, N. Miloshev, (2013a) Condition of The Stratospheric and Mesospheric Ozone Layer over Bulgaria for the Period 1996 – 2012: Part 1 – Total Ozone Content, Seasonal Variations, *Bulgarian Geophysical Journal*, 39, National Institute Of Geophysics, Geodesy And Geography, Bulgarian Academy Of Sciences.

- Kaleyna P., Pl. Muhtarov, N. Miloshev, (2013b) Condition of The Stratospheric and Mesospheric Ozone Layer over Bulgaria for the Period 1996 – 2012: Part 2 – Total Ozone Content, Short term variations, *Bulgarian Geophysical Journal*, 39, National Institute Of Geophysics, Geodesy And Geography, Bulgarian Academy Of Sciences.
- Leeuw, F. de, Mol, W., (2005), Air Quality and Air Quality Indices: a world apart. ETC/ACC Technical Paper 2005/5.
- Simpson, D., Benedictow, A., Berge, H., Bergström, R., Emberson, L. D., Fagerli, H., Flechard, C. R., Hayman G. D., Gauss M., Jonson J. E., Jenkin M. E., Nyíri A., Richter C., Semeena V. S., Tsyro S., Tuovinen J.-P., Valdebenito A & Wind P. (2012). The EMEP MSC-W chemical transport model – technical description. *Atmos. Chem. Phys.*, 12, 7825 – 7865.
- Syrakov D., Prodanova M., Georgieva E., Hristova E., (2019a) Applying WRF-CMAQ models for assessment of sulphur and nitrogen deposition in Bulgaria for the years 2016 and 2017, *International Journal of Environment and Pollution*, 66(1-3), 162-186
- Syrakov D., Georgieva E., Prodanova M., Hristova E., Gospodinov I., Slavov K., Veleva B. (2019b) Application of WRF-CMAQ model system for analysis of sulfur and nitrogen deposition over Bulgaria, *Lecture Notes in Computer Science (including subseries Lecture Notes in Artificial Intelligence and Lecture Notes in Bioinformatics)*, 11189 LNCS, 474 – 482.
- Syrakov, D., Prodanova, M., Georgieva, E., Etropolska, I., Slavov, K. (2015), Impact of NOx emissions on air quality simulations with the Bulgarian WRF-CMAQ modelling system, *International Journal of Environment and Pollution*, 57, Issue 3-4, 2015, 285 – 296.

✉ **Georgi Gadzhev**

<http://orcid.org/0000-0002-6159-3554>

National Institute of Geophysics, Geodesy and Geography
Bulgarian Academy of Sciences
Sofia, Bulgaria

E-mail: ggadzhev@geophys.bas.bg

✉ **Vladimir Ivanov**

<https://orcid.org/0000-0001-9768-1049>

National Institute of Geophysics, Geodesy and Geography
Bulgarian Academy of Sciences
Sofia, Bulgaria

E-mail: vivanov@geophys.bas.bg

HOW WELL DO THE AIR QUALITY MODELS EMEP AND CAMS REPRODUCE PARTICULATE MATTER SURFACE CONCENTRATIONS IN BULGARIA

Hristina Kirova, Nadya Neykova, Emilia Georgieva
National Institute of Meteorology and Hydrology (NIMH)

Abstract: The main objective of this study is to evaluate the performance of some well-known and widely used operational air quality modelling systems (EMEP- MSC-W, and the models at the Copernicus Atmosphere Monitoring Service (CAMS)) for simulations of particulate matter in Bulgaria. The analysis is focussed on a summer month (August 2017) and includes comparison of model to observations from 24 regular air quality background stations, as well as model inter-comparison. Along with statistical indicators various graphs are used - box plots, kernel density estimations, and scatter plots. The spatial distribution is discussed upon maps of monthly mean concentrations and comparison of domain averaged model concentrations. The spatial distribution of PM₁₀ is similar only over the Black sea. The highest domain mean surface concentrations are simulated by CAMS global – by about 12% for PM₁₀ and by about 14% for PM_{2.5} higher than the other models.

Keywords: chemical transport models, PM₁₀, PM_{2.5}, regular air quality observations, model validation, Bulgaria

INTRODUCTION

Particulate matter (PM) are constantly studied because of their effects on the human health and on the environment. While monitoring facilities for surface level concentrations are growing in number and type, the information from observational data is still limited in time and space. Chemical transport models (CTM) has been recognized as valuable tool not only for air quality assessment, but also for policy support in determining abatement measures (McMurry et al., 2004, Miranda et al., 2015). The PM modelling, however, still represents a challenging task, as their concentrations are influenced not only by different emission sources, but also by atmospheric processes and chemical transformation mechanisms taking place over various spatial scales. Some international initiatives for evaluation of CTMs in the last years (e.g. AQMEII (Air Quality Modelling Evaluation International Initiatives), FAIRMODE (Forum for AIR quality MODELing)) have allowed better understanding of the weaknesses and strengths of the models and have contributed

to their improvement and further development. Nowadays, CTMs are the backbone of many comprehensive air quality forecasting systems designed for different scales – from country, to European and global ones (e.g. Schaap et al., 2008, Sofiev et al., 2008, Mailler et al., 2017).

At the National Institute of Meteorology and Hydrology (NIMH) a chemical weather forecasting system has been also set up, BgCWFS (Syrakov et al. 2013, Etropolska et al., 2011). The system was evaluated on European scale in the framework of AQMEII (Brunner et al., 2015, Curci et al., 2015, Im et al., 2015). On national scale, BgCWFS results with 9 km spatial resolution, showed underestimation for PM_{10} (Georgieva et al., 2015). Exceedances of PM limit values are often observed at many sites in Bulgaria (Naydenova et al., 2018, EEA Report, 2019), and there is a public and expert interest in possibilities of operational modelling systems to predict surface PM concentrations.

For this study we have chosen to look at freely available results of three well-known and widely used operational air quality modelling systems for a case study in Bulgaria. The systems differ in their input data, emissions handling, parameterisation schemes, chemical mechanisms etc., but it is believed that they capture the main characteristics of the surface PM distribution. In brief, results from the following systems are used here:

EMEP MSC-W (denoted further as EMEP) – the model of the Meteorological Synthesizing Centre-West (MSC-W) of the European Monitoring and Evaluation Programme) (Simpson et al., 2012). The EMEP model is one of the major instruments which is applied for decision and policy making not only because of its coverage but also because its output includes photooxidants, inorganic and organic aerosols and depositions. This is the model used by the European Environmental Agency for annual reporting on the air quality status in Europe. The model domain covers an extended European region with a horizontal resolution of $0.1^\circ \times 0.1^\circ$ and 20 vertical layers (the lowest with a height of approximately 50 meters). Results for the year 2017 from version rv4_33 are used.

The second system is the regional (European) ensemble air quality forecasting system at the Copernicus Atmosphere Monitoring Service (CAMS) (denoted further as CAMS-ENS). Its main characteristics are: coverage – Europe, spatial and temporal resolution: 0.1° and 1 h, vertical levels up to 5000 m. The Ensemble forecast is the median of the forecasts from 9 different state-of-the-art atmospheric modelling systems (CHIMERE, EMEP, EURAD-IM, DEHM, GEM-AQ, LOTOS-EUROS, MATCH, MOCAGE, SILAM), ECMWF Copernicus Report, 2019. All CTM's use the same emissions data, the same meteorological driver and the same boundary conditions. The regional CAMS system combines model data and in-situ observations to provide air quality forecasts.

The third system is the global CAMS (CAMS-ECMWF). It provides operational forecast for atmospheric chemistry parameters globally with horizontal reso-

lution of 40 km on 60 vertical levels going up to 0.1 hPa, the temporal resolution is 3 h. CAMS – ECMWF assimilates data from satellite observations. Thus means emissions by dust storms and wildfires are taken into account.

The period for the case study is one month - August 2017. This is a typical summer month, characterized by high temperatures and low precipitations. The prevailing weather is of anticyclonic type (except 5 days with weak pressure field and 10 days with cyclonic type). Massive thunderstorms were registered on 4 days. The number of days at NIMH stations with rainfall more than 1 mm was between 1 and 4, and with rainfall above 10 mm was between 0 and 3 (National Institute of Meteorology and Hydrology - Monthly Bulletin). High temperatures and low amount of precipitation are favorable conditions for wildfires which occurred at the beginning of the studied period and in the second part of the month in southern Bulgaria. Saharan dust intrusions towards the country, detected by data from GOME2 instrument on MetOP satellites, were identified in about 14 days throughout the month. As during summer the domestic heating - one of the major emission sources for PM - is missing, the selected month is assumed to be influenced by natural aerosols, which CAMS modelling systems can treat through the data assimilation.

The main goal of this work is to evaluate the performance of EMEP, CAMS-ENS and CAMS-ECMWF for PM₁₀ and PM_{2.5} surface concentrations in Bulgaria during the selected period, comparing model results to observations and performing model intercomparison.

METHODS

To check the performance of the models, two main aspects were considered:

a) Model to observation analysis

The modelled daily PM values are compared to the daily observed ones in each station with available observations of PM₁₀ (24 stations) and PM_{2.5} (8 stations) August 2017. The stations are part of the air quality monitoring network managed by the Bulgarian Executive Environment Agency (ExEA), Fig. 1.

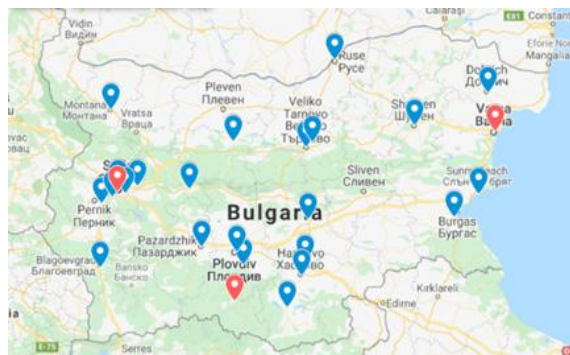


Figure 1. Map of the stations with available observations of PM₁₀ and PM_{2.5} for August 2017. The 3 stations selected for graphs are marked with red color: Sofia Hipodruma, Varna – SOU Angel Kanchev, and Rozhen

The performance of the EMEP and CAMS-EN Smodels is evaluated through box plots, kernel density estimations (kde) of the probability density functions (pdf), scatter plots and statistical indicators. Here we show as example the plots for 3 selected stations located in different environment: one urban - Sofia Hipodruma (BG0050A), one at the Black Sea coast-Varna – SOU Angel Kanchev (BG0075A), and one of rural/mountain type - Rozhen (BG0053R, 1720 m asl), Fig. 1.

The daily values for all stations are grouped and shown on one scatter plot for each model. The statistical indicators, averaged over all stations, include the mean observed and modelled concentrations, the mean bias error (MBE), the root mean square error (RMSE), the correlation coefficient (Corr), the fractional gross error (FGE), and the normalized mean bias (NMB).

b) Model - to - model comparison

For this analysis we use qualitative comparison - maps for mean monthly concentrations of particulate matters (PM_{10} and $PM_{2.5}$). As a quantitative measure the values of the domain mean concentrations, as simulated by the different systems for the month, are calculated.

RESULTS

The comparison of model data from EMEP and CAMS-ENS to observed PM_{10} concentrations is visualized in Fig.2 for the selected three stations. The graphs presenting the kernel density estimations show that PM_{10} concentrations estimated by both models have similar distributions. The box plots indicate that both models have smaller means and dispersions than the observed data, but CAMS-ENS model has smaller dispersion than the EMEP model. For the rural remote station Rozhen the models have better resemblance to the observed data than for the urban stations, as expected because this station is not influenced by local emissions typical for the cities.

Both models underestimate the observed PM_{10} concentrations. This can also be seen from the statistical indicators of modelled versus observed PM_{10} averaged over all 24 stations presented in Table 1 and on the scatter plots for all 24 stations presented in Fig. 3. The statistical indicators show very similar results for the two models with underestimation on average by about 50%. The scatter plot indicates that the EMEP model has more often overestimation of some daily values than CAMS-ENS. Overall we can conclude that EMEP model underestimates the observed PM_{10} concentrations to a lesser extent than CAMS-ENS model, but the correlation is better for CAMS-ENS.

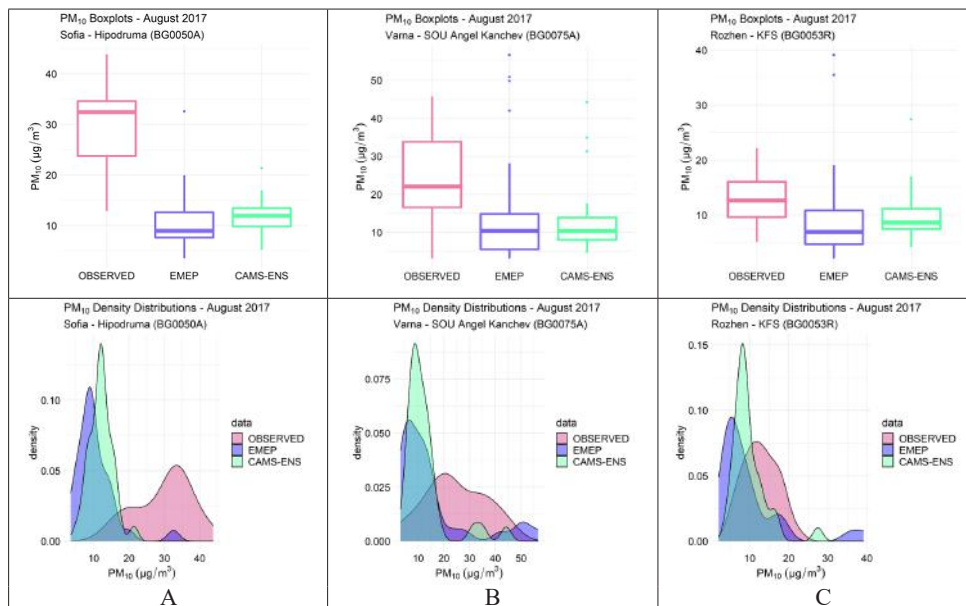


Figure 2. Observed vs modelled PM_{10} in August 2017: a) Sofia – Hipodruma, b) Varna, c) Rozhen: Box plots on 1st row and corresponding kernel density estimations on 2nd row

Table1. Statistical indicators of modelled versus observed PM_{10} concentrations averaged over 24 stations

| PM_{10} (Nstations=24) | Mean_OBS [$\mu g m^{-3}$] | Mean_MOD [$\mu g m^{-3}$] | MBE [$\mu g m^{-3}$] | RMSE [$\mu g m^{-3}$] | Cor | FGE | NMB[%] |
|-----------------------------|--------------------------------|--------------------------------|---------------------------|----------------------------|------|------|--------|
| EMEP | 25.68 | 12.90 | -12.78 | 15.82 | 0.47 | 0.79 | -49.77 |
| CAMS-ENS | 25.68 | 10.99 | -14.69 | 16.11 | 0.56 | 0.80 | -57.22 |

The distributions of the modelled and observed $PM_{2.5}$ concentrations are presented in the box plots and kernel density estimation plots, in Fig. 4. Compared to the results for PM_{10} , the difference between modelled and observed $PM_{2.5}$ concentrations is smaller. The modelled $PM_{2.5}$ concentrations by both models are similarly distributed. Both models have smaller means and dispersion than the observed data but CAMS-ENS model has smaller dispersion than the EMEP model. As with PM_{10} the performance is better for the rural remote station Rozhen.

Both models underestimate the observed $PM_{2.5}$ concentrations, as indicated by the statistical indicators in Table 2 and the scatter plots in Fig. 5. The underestimation,

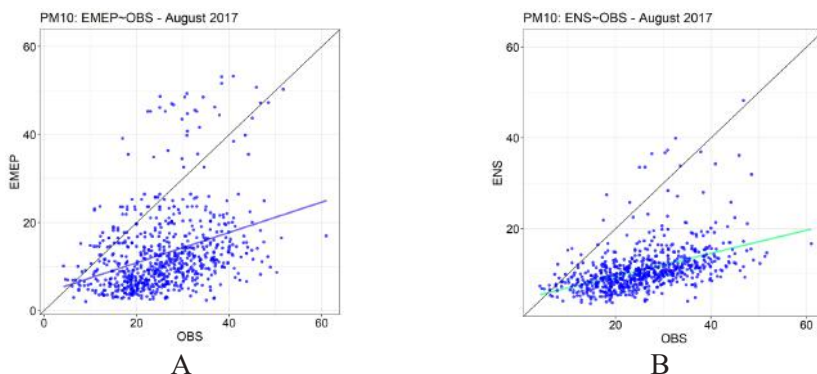


Figure 3. Scatter plots for daily PM_{10} at 24 stations in Bulgaria in August 2017: a) EMEP and b) CAMS-ENS

on average by about 32%, is less than the underestimation for PM_{10} . To note that the number of stations for $PM_{2.5}$ is only 8.

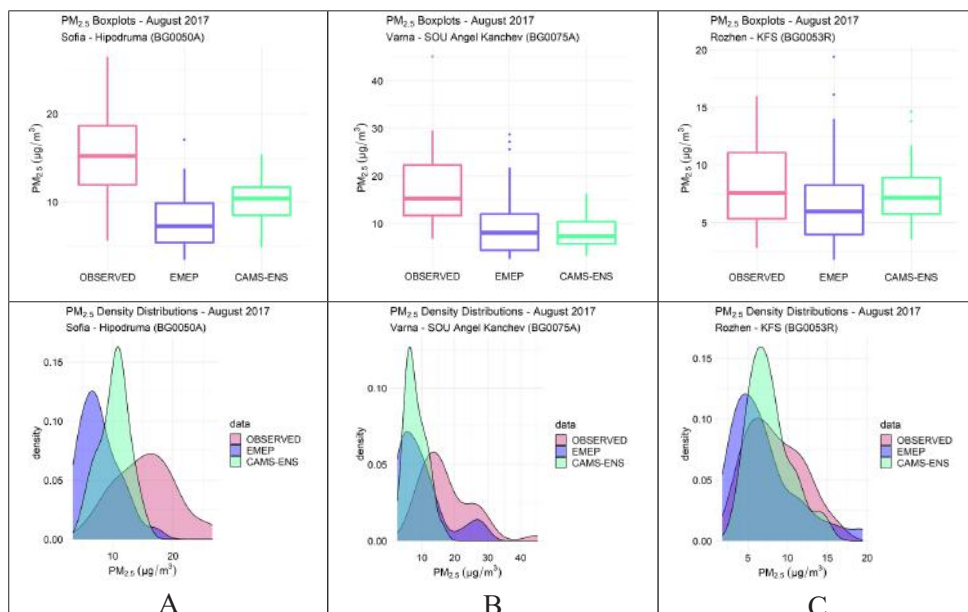


Figure 4. Observed vs modelled $PM_{2.5}$ in August 2017: a) Sofia – Hipodruma, b) Varna, c) Rozhen: Box plots on 1st row and corresponding kernel density estimations on 2nd row

Table2. Statistical indicators of modelled versus observed $PM_{2.5}$ concentrations averaged over 8 stations

| $PM_{2.5}$ (Nstations=8) | Mean_OBS [$\mu g m^{-3}$] | Mean_MOD [$\mu g m^{-3}$] | MBE [$\mu g m^{-3}$] | RMSE [$\mu g m^{-3}$] | Corr | FGE | NMB[%] |
|-----------------------------|--------------------------------|--------------------------------|---------------------------|----------------------------|------|------|--------|
| EMEP | 13.55 | 9.34 | -4.21 | 7.26 | 0.48 | 0.58 | -31.09 |
| CAMS-ENS | 13.55 | 8.82 | -4.73 | 5.93 | 0.66 | 0.45 | -34.90 |

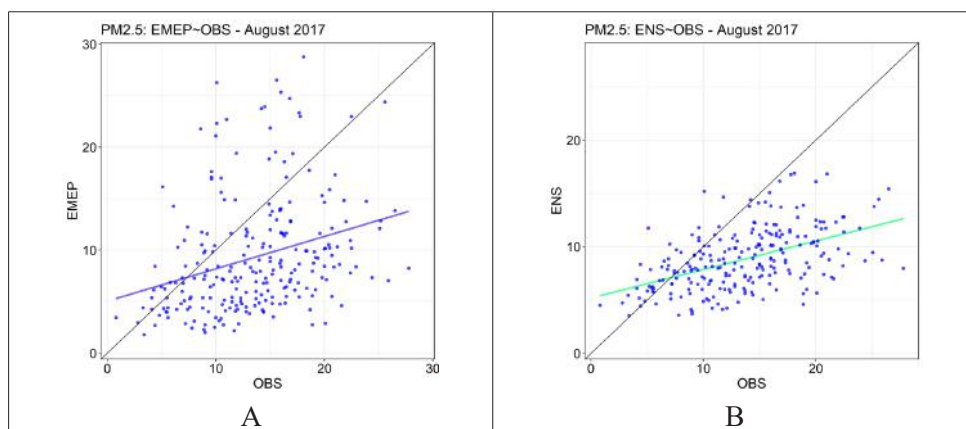


Figure 5. Scatter plots for daily $PM_{2.5}$ at 8 stations in Bulgaria in August 2017: a) EMEP and b) CAMS- ENS

The model to model comparison is based on results for Bulgaria obtained by the three model systems – EMEP, CAMS-ENS and CAMS-ECMWF for August 2017. The spatial distribution of mean monthly concentrations of PM_{10} and $PM_{2.5}$ is shown in Fig. 6, the averaged for the domain monthly values are provided in Table 3. All models simulate higher concentrations in the eastern part of the domain (Black Sea). EMEP results over land indicate some hot spots in correspondence with big cities. Higher concentrations in the Lower Danube plain (north-western part of the domain) are simulated by CAMS-ECMWF. This might be a consequence of emission sources that are not included in the other models, but this system is producing due to satellite data assimilation. The mean monthly map for the Aerosol Optical Depth, as retrieved by MODIS Terra satellite, Fig. 7, also indicates higher aerosol loading north of the country. The character of the spatial distribution by the models is maintained in the maps for $PM_{2.5}$. The domain mean surface concentrations for PM_{10} and $PM_{2.5}$ are with 9 % and 12.5 % higher for CAMS-ECMWF than for EMEP (Table 3). The lowest values are simulated by CAMS-ENS: with 14 % and 15.6 % lower than for CAMS-ECMWF.

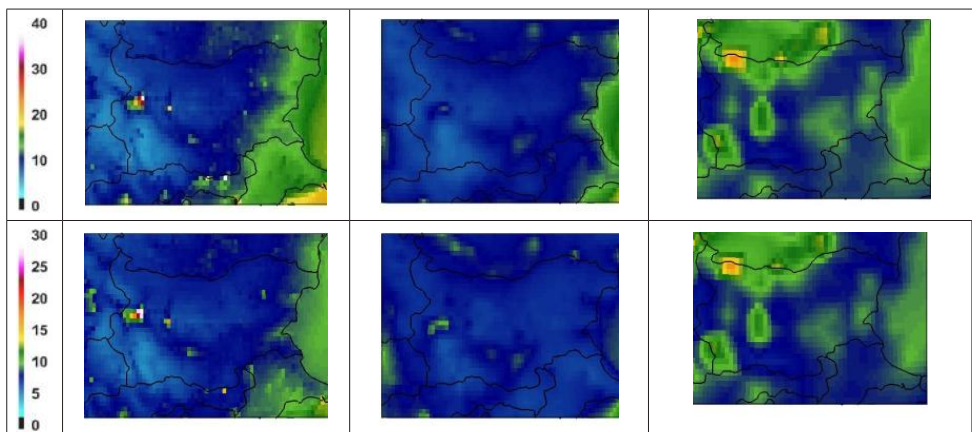


Figure 6. Monthly mean PM_{10} (first row) and $PM_{2.5}$ (second row) concentrations ($\mu\text{g m}^{-3}$) for domain Bulgaria (August 2017): EMEP (left), CAMS-ENS (middle) and CAMS-ECMWF (right)

Table 3. Domain mean surface concentrations [$\mu\text{g m}^{-3}$] for August 2017

| | EMEP | CAMS-ENS | CAMS-ECMWF |
|------------|------|----------|------------|
| PM_{10} | 12 | 11.3 | 13.2 |
| $PM_{2.5}$ | 8.4 | 8.1 | 9.6 |

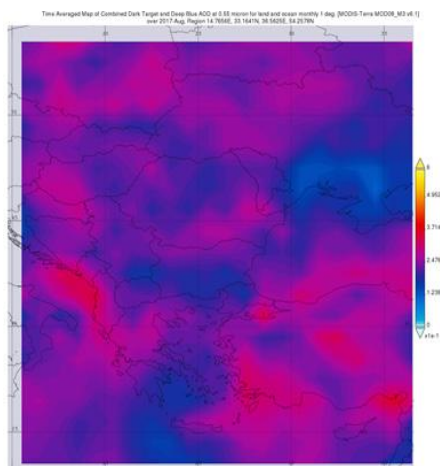


Figure 7. Mean monthly (August, 2017) map of combined dark target and deep blue AOD at 550 nm for land and ocean

CONCLUSIONS

In this study EMEP and CAMS-ENS simulated concentrations for PM₁₀ and PM_{2.5} were compared to data from regular air quality stations in Bulgaria for a test period of one month (August 2017). Both models underestimate the observed concentrations, on monthly basis by about 50 % for PM₁₀ and by about 32 % for PM_{2.5}. The models perform better at the rural remote (mountain) site Rozhen than for the urban background stations indicating that the outputs could be used for indicative values of background PMs concentrations. EMEP model underestimated the observed PM₁₀ and PM_{2.5} values to a lesser extent than CAMS-ENS. The spatial distribution showed higher values in the eastern part of domain Bulgaria and hot spots over main cities. Interestingly, the CAMS-ECMWF model, that has coarser grid resolution, indicates higher surface concentrations north of the country over the Lower Danube plain. This might be due to sources not accounted for in the other models, e.g. fires or mineral dust. As this system assimilates satellite data, it could forecast influence of such events on surface PM concentrations. Further analysis are ongoing in this direction.

Future plans foresee to perform similar analysis for a winter month when surface concentrations of PM are higher due to higher anthropogenic emissions (traffic, domestic heating, and energy production from thermal power plants) and when the conditions for dispersion of atmospheric pollutants are worse due to thermal inversions. Results by BgCWFS will be also included in the analysis.

ACKNOWLEDGMENTS

The work presented here was carried out in the frame of the project SIDIAQ“ Satellite Information Downscaled to Urban Air Quality in Bulgaria”, funded by the Government of Bulgaria through the ESA Contract No.4000124150/18/ NL/SC under the PECS (Plan for European Cooperating States). The view expressed herein can in no way be taken to reflect the official opinion of the European Space Agency.

The European Centre for Medium-Range Weather Forecasts, the Copernicus Atmosphere Monitoring Service and the Meteorological Synthesizing Centre-West of the European Monitoring and Evaluation Programme and Met Norway are acknowledged for providing analyzed and forecasted data on meteorological parameters and atmospheric chemistry. Some analyses and visualizations used in this study were produced with the Giovanni online data system, developed and maintained by the NASA GES DISC.

REFERENCES

Brunner, D., Savage, N., Jorba, O., Eder, B., Giordano, L., Badia, A., Balzarini, A., Baró, R., Bianconi, R., Chemel, C., Curci, G., Forkel, R., Jiménez-Guerrero, P., Hirtl, M., Hodzic, A., Honzak, L., Im, U., Knote,

- C., Makar, P., Manders-Groot, A., van Meijgaard, E., Neal, L., Pérez, J. L., Pirovano, G., San Jose, R., Schröder, W., Sokhi, R. S., Syrakov, D., Torian, A., Tuccella, A., Werhahn, J., Wolke, R., Yahya, K., Zabkar, R., Zhang, Y., Hogrefe, C. and Galmarini, S.. (2015) Comparative analysis of meteorological performance of coupled chemistry-meteorology models in the context of AQMEII phase 2, *Atmospheric Environment*, 115, 470-498.
- EEA (2019) Air Quality in Europe – 2019 Report, EEA Report 10/2019, ISSN 1977-8449, doi:10.2800/822355.
- ECMWF Copernicus Report (2019) CAMS Regional Air Quality User Guide, issued Meteo-France, https://www.regional.atmosphere.copernicus.eu/doc/USER_GUIDE_dataServer.pdf
- Etropolska, I., Prodanova, M., Syrakov, D., Ganev, K., Miloshev, N. and Slavov, K. (2011) Bulgarian Operative System for Chemical Weather Forecast. In: Dimov, I., Dimova, S., Kolkovska, N. (eds) Numerical Methods and Applications. NMA 2010. *Lecture Notes in Computer Science*, vol 6046. Springer, Berlin, Heidelberg, 141-149.
- Georgieva, E., Syrakov, D., Prodanova, M., Etropolska, I. and Slavov, K., (2015) Evaluating the performance of WRF-CMAQ air quality modeling system in Bulgaria by means of the DELTA tool, *International Journal of Environment and Pollution*, Vol. 57, No. 3/4, 272-284.
- Curci, G., Hogrefe, C., Bianconi, R., Im, U., Balzarini, A., Baró, R., Brunner, D., Forkel, R., Giordano, L., Hirtl, M., Honzak, L., Jiménez Guerrero, P., Knote, C., Langer, M., Makar, P., Pirovano, G., Perez, J. L., San José, R., Syrakov, D., Tuccella, P., Werhahn, J., Wolke, R., Žabkar, R. and Zhang, Y. (2015) Uncertainties of simulated aerosol optical properties induced by assumptions on aerosol physical and chemical properties: an AQMEII-2 perspective, *Atmospheric Environment*, 115, Elsevier, 541-552.
- Mailler S., Menut, L., Khvorostyanov, D., Valari, M., Couvidat, F., Siour, G., Turquety, S., Briant, R., Tuccella, P., Bessagnet, B., Colette, A., Letinois, L., and F. Meleux, F., (2017) CHIMERE-2017: from urban to hemispheric chemistry-transport modeling *Geosci. Model Dev.*, 10, 2397-2423, <https://doi.org/10.5194/gmd-10-2397-2017>.
- McMurry, P., Shepherd, M.F and Vickery J.S. (2004) *Particulate Matter Science for Policy Makers: A NARISTO Assessment*, Cambridge University Press.
- Miranda, A., Silveira, C., Ferreira, J., Monteiro, A., Lopes, D., Relvas, H., Borrego, C. and Roebeling, P. (2015) Current air quality plans in Europe designed to support air quality management policies, *Atmospheric Pollution Research* 6, 434-443.

- Naydenova, I., Petrova, T, Velichkova and R., Simova I. (2018) PM10 Exceedance In Bulgaria, CBU International Conference on Innovations in Science and Education, March 21-23, 2018, Prague, Czech Republic.
- Schaap, M., Timmermans, R. M., Roemer, M., Boersen, G., Builtjes, P. J., Sauter, F. J., Velders, G. J., and Beck, J. P. (2008). The LOTOS EUROS model: description, validation and latest developments, *Int. J. Environ. Pollut.*, 32, 270–290.
- Simpson, D., Benedictow, A., Berge, H., Bergström, R., Emberson, L. D., Fagerli, H., Flechard, C. R., Hayman, G. D., Gauss, M., Jonson, J. E., Jenkin, M. E., Nyíri, A., Richter, C., Semeena, V. S., Tsyro, S., Tuovinen, J.-P., Valdebenito, A., and Wind, P. (2012). The EMEP MSC-W chemical transport model – technical description, *Atmos. Chem. Phys.*, 12, 7825–7865, <https://doi.org/10.5194/acp-12-7825-2012>.
- Sofiev, M., Galperin, M., and Genikhovich, E. (2008). A Construction and Evaluation of Eulerian Dynamic Core for the Air Quality and Emergency Modelling System SILAM, in: *Air Pollution Modeling and Its Application XIX*, Springer Netherlands, Dordrecht, 699–701.
- Syrakov, D., Prodanova, M., Slavov, K., Etropolska, I., Ganev, K., Miloshev, N. and Ljubenov, T. (2013): Bulgarian System for Air Pollution Forecast, *Journal of International Scientific Publications ECOLOGY & SAFETY*, Volume 7, Part 1, ISSN: 1313-2563, pp.325-334.

✉ **Hristina Kirova**

<https://orcid.org/0000-0002-1764-2443>

National Institute of Meteorology and Hydrology
Sofia, Bulgaria

E-mail: hristina.kirova@meteo.bg

✉ **Nadya Neykova**

<https://orcid.org/0000-0003-1892-2081>

National Institute of Meteorology and Hydrology
Sofia, Bulgaria

E-mail: nadya.neykova@meteo.bg

✉ **Emilia Georgieva**

<https://orcid.org/0000-0002-8466-4976>

National Institute of Meteorology and Hydrology
Sofia, Bulgaria

E-mail: emilia.georgieva@meteo.bg

CLOUD AND RAIN WATER CHEMICAL COMPOSITION AT PEAK CHERNI VRAH, BULGARIA

**Elena Hristova, Blagorodka Veleva, Krum Velchev,
Emilia Georgieva**

National Institute of Meteorology and Hydrology (NIMH)

Abstract. The purpose of the work is to present and discuss newly obtained data for the chemical composition of cloud water (CW) and rain water (RW) at a high-elevation site in Bulgaria. Sampling of CW and RW was organized in 2017 and 2018 during field experiments at Cherni Vrah, the highest peak in Vitosha Mountain. Passive collectors designed and constructed at NIMH were used. All collected samples (118) were analyzed for acidity (pH), conductivity (EC), main anions - SO_4^{2-} , NO_3^- , Cl⁻, ammonium ions (NH_4^+), macro and micro elements (Na, K, Mg, Ca, Fe, Si, Zn, Cu). The average pH values for both types of samples were in the acidity range (<5.0). The values of EC varied from 5 to $89.2 \mu\text{S}\cdot\text{cm}^{-1}$ for RW and from 0.7 to $202 \mu\text{S}\cdot\text{cm}^{-1}$ for CW. The ion composition was dominated by NH_4^+ , Ca, SO_4^{2-} and NO_3^- , which made up more than 63% of the total ionic content for RW and 75% for CW. The relative contribution of the major compounds to the CW and RW composition is presented and discussed. The effect of long-range transport processes is studied for some selected periods of 2018 using HYSPLIT air mass backward trajectory analysis.

Keywords: Cloud water; rain water; chemical composition; acidity; backward trajectories

INTRODUCTION

The atmosphere is an important environment in which different gaseous and aerosol species are transported. Cloud water (CW) and rain water (RW) play important roles in removing particles and dissolved gaseous pollutants from the atmosphere. They also scavenge sulphur dioxide (SO_2), nitrogen oxides (NO_x), and other atmospheric pollutants, which can affect their acidity and chemical composition and cause ecological damage to ecosystems (Seinfeld and Pandis, 2006, Gioda et al., 2013). The chemical composition of CW and RW depends on pollutants emitted by sources of anthropogenic and natural origin, the dynamical processes in the atmosphere and the chemical reactions that occur during both local and long-range transport. Nitrates (NO_3^-), sulphates (SO_4^{2-}) and other ions such

as ammonium (NH_4^+), chloride (Cl), magnesium (Mg), calcium (Ca), potassium (K), and sodium (Na) are commonly present in the aqueous phase. Some of these species originate from natural sources such as sea spray, soils and forest fires. Other species such as ammonium come from anthropogenic activities, including agricultural fertilizers and biomass burning (Hůnová, et al., 2017, Mihajlidi-Zelić et., 2006).

Several authors worldwide have explored trends in the chemical composition of cloud and rain water since 1990 (Weathers, et al., 1988, Anderson, et al., 2006, Aleksic et al., 2009, Gioda et al., 2013 Schwab et al., 2016). At high-elevation environments, cloud and fog liquid water have generally been recognized as being more acidic than rainwater. In Bulgaria, precipitation chemistry in forest mountain areas was analysed occasionally during field campaigns related to depositions and critical loads to ecosystems (Zeller et al., 1998, Ignatova & Damyanova, 2012, Ignatova & Fikova, 2007). A few studies have focussed on analysis of meteorological conditions and the influence of air mass transport on the chemical composition of precipitations at peaks Cherni Vrah and Moussala (Iordanova & Blaskova, 2011).

In the last years, NIMH is conducting research activities on atmospheric depositions in Bulgaria including both numerical simulations and observational campaigns (Georgieva et al., 2015, Georgieva et al., 2018, Hristova et al, 2016, Hristova, 2017, Hristova & Veleva, 2015). The observational campaigns are organized in areas that could be adversely impacted by the depositions of acidifying and eutrophying compounds, and thus, be exposed to environmental risks (mountain and nature protected areas). The work presented here is part of these recent activities.

The scope of this study is to compare and discuss newly obtained data for the chemical composition of CW and RW at a high-elevation site in Bulgaria – Cherni Vrah (ChV), Vitosha Mountain. Another objective is to analyse the effect of long-range transport processes on the chemical composition that will be briefly outlined for selected case periods.

METHODS

Site description

Vitosha Mountain is the first national park in Bulgaria and in the Balkan Peninsula. It is located on the outskirts of Sofia, with an area of 270.79 km². Cherni vrah is the highest peak where the Meteorological station of NIMH is situated (42.6167 N, 23.2667 E, 2286 m asl), Fig. 1. The CW and RW samples were collected at this meteorological station from June 2017 to November 2018.

The cloud water is sampled by using a passive collector designed and constructed in NIMH (Fig.2a). All construction is made from plexiglas and sampling elements are made from fishing lines with length in total 180 m: 100m - \varnothing 1mm 80 m – \varnothing 0.5mm. The cloud droplets impact on the vertical strings, combine to larger drops, run down the strings, and drip into a 500 ml polyethylene (PE) bottle. The CW



Figure 1. Map of Vitosha Mountain and synoptic station Cherni Vrah

samples were collected on an event basis, resulting in different time duration of typically about several hours.

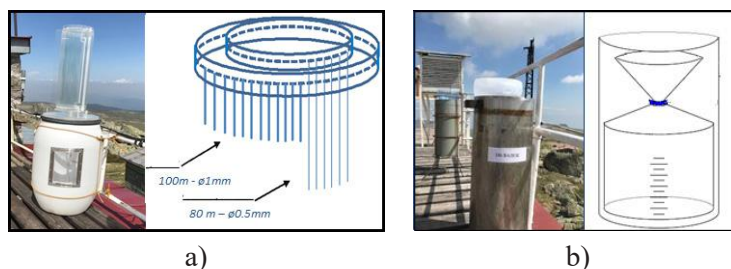


Figure 2. Samplers for (a) cloud water and (b) rain water

Manual (bulk) rain water sampler is used for sampling of rainwater samples (Fig.2b). The material of the collector is polyethylene terephthalate funnel of 20 cm in diameter and bottle with 5l capacity. The bulk sampler is washed every day with deionized water ($<1\mu\text{S}\cdot\text{cm}^{-1}$) to avoid dry deposition. The RW samples were taken on daily basis.

Chemical analysis of cloud and rain water samples

All 40 cloud and 78 rainwater samples were analysed for acidity (pH), electro conductivity (EC), Cl^- , SO_4^{2-} , NO_3^- ; Ca, Mg, K, Na, Fe, Si, Zn, Cu, NH_4^+ . Acidity and electro conductivity were measured at the moment of sampling by a portable pH-meter and conductivity meter. The pH meter was calibrated before each measurement using standard buffer solutions of pH 4.00 and 7.01. The conductivity meter was periodically calibrated against KCl standard solutions. Chemical analysis are performed in certified laboratory by Ion Chromatograph (ICS 1100, DIONEX)

for SO_4^{2-} , NO_3^- , Cl^- ICP OES (Vista MPX CCD Simultaneous, VARIAN) for Ca, Mg, K, Na, Fe, Si, Zn, Cu and Spectrophotometer S-20 for NH_4^+ .

Table 1. Detection limits (DL) for all analysed elements

| | Cl^- | NO_3^- | SO_4^{2-} | <i>Ca</i> | <i>K</i> | <i>Mg</i> | <i>Na</i> | <i>Fe</i> | <i>Si</i> | <i>Zn</i> | NH_4^+ |
|------------------------------|--------|----------|-------------|-----------|----------|-----------|-----------|-----------|-----------|-----------|----------|
| <i>DL, mg.l⁻¹</i> | 0.10 | 0.10 | 0.10 | 0.002 | 0.1 | 0.002 | 0.1 | 0.005 | 0.10 | 0.005 | 0.05 |

The detection limits for all analysed elements are presented in Table 1. The concentration of $nss_SO_4^{2-}$ has been estimated by correction based on assumption that sodium is a sea salt tracer: $[nss_SO_4^{2-}] = [SO_4^{2-}] - (0.25 \times [Na])$, according to WMO GAW, 2004.

Trajectory analysis for long range effects

The origin of the air masses back-ward analysis was conducted using the Hybrid Single Particle Lagrangian Integrated Trajectory (HYSPPLIT), (Stein et al, 2015, Rolph et al., 2017). Three different arrival heights were used: 500, 1000, 1500 m a.g.l (above ground level). The calculations were made for 72h using meteorological input from NCEP GDAS with horizontal resolution of $0.5^\circ \times 0.5^\circ$.

RESULTS AND DISCUSSIONS

Physico-chemical parameters

The CW and RW pH values in this study ranged from 3.5 to 5.7 and the conductivity values from 0.7 to 202 $\mu S\ cm^{-1}$. The distribution of the relative pH and EC frequency for both types of samples are presented in Figure 3. This frequency analysis shows that 100 % of the cloud and 98% of the rain samples have pH value in the acidity range (Figure 3a). The highest percentage of pH values are in the range of 4.0 – 4.5 for both CW and RW (58% and 56%). Only 1.5% of the collected rain water samples are in the neutral range (5.5-6.0), there are not cloud water sample with pH value higher than 5.3. Around 10% of CW and RW samples have pH in the slightly acidic range (5.0 – 5.5), and 28% of RW pH and 18% of CW are in the 4.5 -5.0. In the very acidic range (3.5 – 4.0) are 13% of the CW pH values and 5% of the RW pH values. The frequency analysis of electrical conductivity presented in Figure 3b shows 57% of RW EC values and 33% of CW EC values in the range 0.07 – 20 $\mu S\ cm^{-1}$.

The percentage of EC values in the range 20 – 40 $\mu S\ cm^{-1}$ is very close for both type of samples (23% and 25%). The percentage with EC values in the range > 60 $\mu S\ cm^{-1}$ is very different: 3% for RW and 31% for CW. Cloud water samples have higher conductivities (0.7 – 202 $\mu S\ cm^{-1}$) than rain water (4.7 – 89 $\mu S\ cm^{-1}$) due to dilution factors in the rain, i.e., cloud droplets have lower water content than rain droplets; therefore the ionic concentrations were higher in cloud water (Gioda et

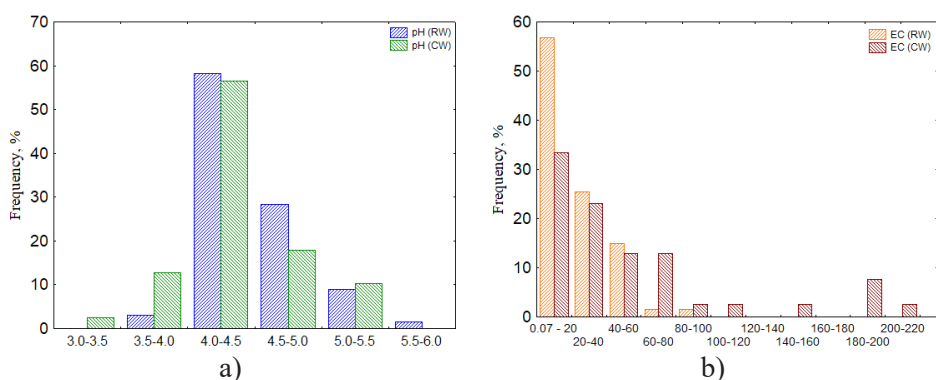


Figure 3. Frequency of pH (a) and EC (b) for cloud and rain water samples

al., 2013). The average EC values for CW and RW are $56 \mu\text{S cm}^{-1}$ and $23 \mu\text{S cm}^{-1}$, respectively.

The CW and RW pH parameter is the result of acid-base reactions in the cloud droplets. Sulphates and nitrates are the main ions that increase the concentration of H^+ ion in rainwater, while NH_4^+ , Ca (usually in the form of CaCO_3), Mg, K are the main neutralizing ions. The total ionic content (TIC) of cloud and rain water samples is ranged from 1.1 to 68 mg l^{-1} and from 4 to 90 mg l^{-1} , respectively. The median of TIC in CW samples is 16.5 mg l^{-1} and for RW samples is 6.2 mg l^{-1} . As

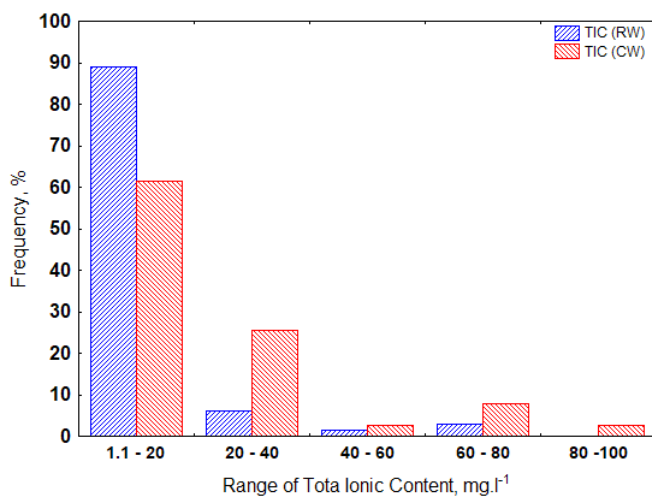


Figure 4. Frequency distribution of Total Ionic Content in cloud and rain water samples

shown by the frequency distribution of TIC in Fig. 4, a fraction of cloud and rain samples have concentrations between 1 and 20 mg l⁻¹ (89% of the RW and 62% of the CW). The percentage of samples in the concentration range 20 – 40 mg l⁻¹ is higher for the CW than for the RW (25% and 6%, respectively). Only 2.6% of the CW samples have TIC in the range 80-100 mg l⁻¹.

The variation in the concentrations of all studied elements is seen on the Box Plot presented in Fig.5. The ion composition of RW and CW was dominated by NH₄⁺, Ca, nss_SO₄²⁻ and NO₃⁻, which made up more than 63% and 75% of the total ionic content. As expected, concentrations of analyzed elements are higher in cloud water than in rain water samples.

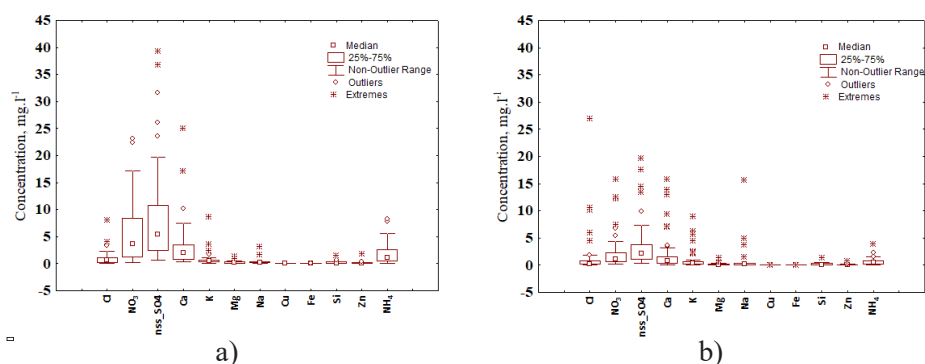


Figure 5. Concentrations of the studied elements in (a) cloud water and (b) rain water samples

The concentrations of the main acidifying ions - SO₄²⁻ for the study period ranged from 0.6 to 39mg.l⁻¹ for CW and from 0.3 to 20.3mg.l⁻¹ for RW. Concentrations of NO₃⁻ vary from 0.15 to 23.1mg.l⁻¹ for CW and from 0.18 to 15.8mg.l⁻¹ for RW. NH₄⁺ ion concentrations for CW and RW samples are ranged from 0.01mg.l⁻¹ to 8.3mg.l⁻¹ and from 0.03mg.l⁻¹ to 3.9mg.l⁻¹. The lowest variations in concentrations were observed for Fe, Cu and Zn. Their concentration is ranged from 0.005 to 1.8mg.l⁻¹. High variation in Cl and Na concentrations are observed in RW samples. The obtained Cl concentration ranged from 0.05mg.l⁻¹ to 27mg.l⁻¹ and for Na from 01 mg.l⁻¹ to 15.6mg.l⁻¹.

Long range transport effects for some selected periods

The origin of air masses was examined by using back-trajectories from the model HYSPLIT (Stein et al, 2015, Rolph et al., 2017) for two periods: 19 – 20 March 2018 and 30 June – 4 July 2018.

The synoptic situation during the period 19 – 20 March 2018 is characterised by Saharan outbreak towards the Balkans, associated with coloured rain and orange

snow in many parts of Eastern Europe. At ChV the arriving air masses were from South (S)-Southwest (SW) (Fig. 6) on 19.03 (rain water sample) and from West (W) on 20.03 (cloud water sample) (Fig. 6). From all analysed samples collected in 2018, the largest concentrations of Cl and Na were obtained in the rain water samples on 19 March. The TIC of the rain sample is 64.1mg.l⁻¹ with 42% contribution of Cl, 24% of Na, 3% ss_SO₄²⁻ (sea salt SO₄²⁻) and only 6% of the sulphates from anthropogenic source (nss_SO₄²⁻) (Fig.6). A very large difference in the SO₄²⁻ concentrations between RW and CW is observed. The TIC of the cloud water sample on 20 March 2018 is 3.9 mg.l⁻¹ containing 28% nss_SO₄²⁻, following by 28.3% Ca, 15.9% Cl and 11.1% K. These results indicated aged air masses with sea salt aerosols (Cl and Na) and mineral dust (Ca and Si) associated with Saharan origin.

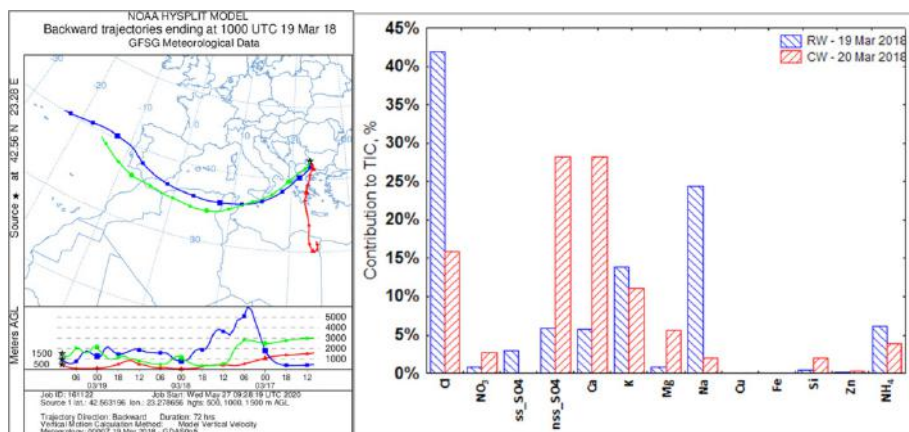


Figure 6. Back-trajectories and contribution of different elements in rain water and cloud waters samples for the period 19 – 20 March 2018

The synoptic situation for the second period, 30 June – 4 July 2018, is characterized by the influence of the slowly moving Mediterranean cyclone “Nefeli” crossing the country from south to northeast.

The atmospheric conditions in the first part of the period were highly unstable with heavy rains and thunderstorms in many places in Bulgaria, while the end of the period was marked by increased surface pressure and occasional convective precipitations (Monthly bulletin, 06 & 07, 2018). The TIC in rain sample collected on 30 June (48.5 mg.l⁻¹) is higher than this for cloud water sample collected on 3 July (36.7 mg.l⁻¹). The trajectory analysis shows that on 30 of June the transport of air masses to the ChV is from North while they are from W, NW on 3 of July (Fig.7). Generally, nss_SO₄²⁻ was found to be the dominant ion in both samples: RW (36%) and CW (43%). The contribution of NO₃⁻ and NH₄⁺ ions in the CW sample

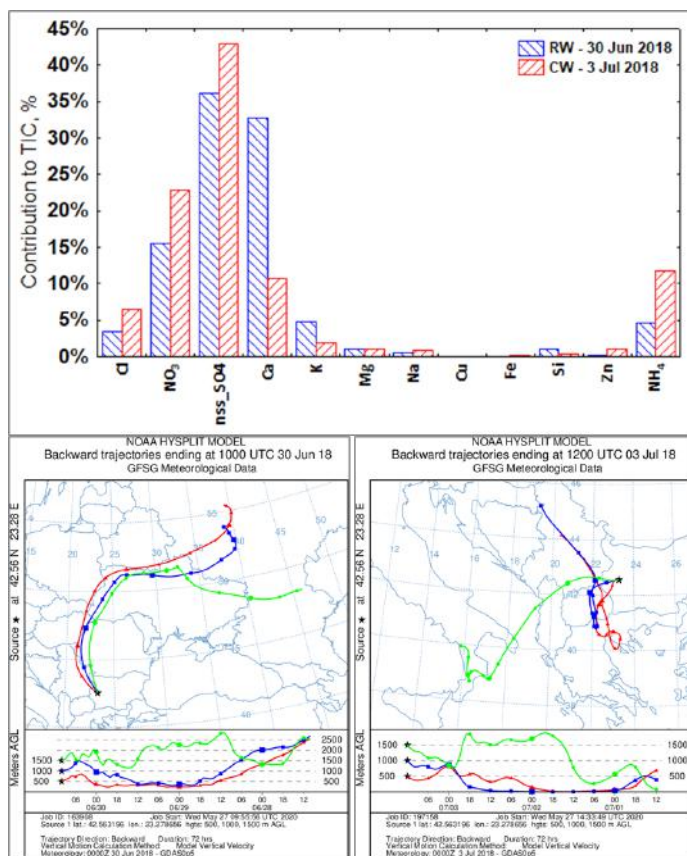


Figure 7. Back-trajectories and contribution of different elements in rain water (30 Jun) and cloud water (3 Jul) samples

(23% and 12%) are higher than in the RW sample (16% and 5%). The contribution of Ca is three times higher in the RW sample than observed in the CW sample. For this selected period the TIC is consisted mainly of nss_SO_4^{2-} , NO_3^- , NH_4^+ and Ca (RW-83% and CW-88%).

CONCLUSIONS

New results for the chemical composition of cloud water (CW) and rain water (RW) at The high-elevation site Cherni Vruh were presented. The results were based on 40 cloud and 78 rainwater samples collected and analysed in the period June 2017 – November 2018. The comparison of the cloud and rain water presents systematic differences concerning the pH, the electric conductivity, and

concentrations of most elements. The frequency analysis showed that 100 % of the cloud and 98% of the rain samples have pH value in the acidity range (<5.0).

Mean concentrations were generally higher in cloud water than in rainwater samples. The ion composition of RW and CW was dominated by NH_4^+ , Ca, nss_SO_4^{2-} and NO_3^- accounting for more than 63% and 75% of the total ionic content. The obtained concentrations of nss_SO_4^{2-} in the cloud water samples are two times higher than those reported for various mountain sites by Marinoni et al., 2004, Schwab et al., 2016 and Gioda et al., 2013. The mean concentrations of NO_3^- and NH_4^+ in the CW samples are lower than ones derived in Marinoni et al., 2004 and Gioda et al., 2013. The study of the origin of the air masses contributed to better understanding of variations in the chemical composition and concentration levels in two specific cases in 2018.

ACKNOWLEDGMENTS

This study was performed with the financial support from the Bulgarian National Science Fund through contract N. DN-04/4-15.12.2016. We acknowledge also to the NOAA Air Resources Laboratory (ARL) for the provision of the HYSPLIT model and READY website (<http://www.ready.noaa.gov>).

REFERENCES

- Aleksic N, K. Roya, G. Sistla, J. Dukett. N. Houck. P. Casson. (2009). Analysis of cloud and precipitation chemistry at Whiteface Mountain. NY. *Atmospheric Environment*, 43, 2709 – 2716.
- Anderson, J.B., Baumgardner, R.E., Grenville, S.E., (2006). Trends in cloud water sulfate and nitrate as measured at two mountain sites in the Eastern United States: regional contributions and temporal changes compared with regional changes in emissions, 1986–1999. *Atmospheric Environment*, 40, 4423 – 4437.
- Fowler. D., Pilegaard. K., Sutton. M.A., et al., (2009). Atmospheric composition change: ecosystems and atmosphere exchange. *Atmospheric Environment*, 43, 5192 – 5263.
- Hristova E., Veleva B, (2015), Experimental study of the chemical composition of precipitation and PM10 in Sofia in 2014, *Bulgarian Journal of Meteorology and Hydrology*, 20, 5, 23 – 32, (in Bulgarian).
- Hristova E., Georgieva E., Velchev K., Kirova H., Oruc I., Nikolov V., Syrakov D., Prodanova M., Batchvarova E., Veleva B., Petrov A., Neikova R., Branzov H., Kolarova M., Etropolski E. (2016). Composition of precipitations in the coastal area of Southeast Bulgaria, 3rd National Congress on Physical Sciences, Section: Physics of Earth, Atmosphere

- and Space, 29 Sep. – 2 Oct. 2016, Sofia, CD, Heron-Press Sofia, 2016, ISBN:978-954-580-364-2.
- Hristova E., Chemical composition of precipitation in urban area. (2017). *Bulgarian Journal of Meteorology and Hydrology*, 22, 1 – 2, 41 – 49, (12).
- Hůnová, P. Kurfürsta, V. Stránika, M. Modlíka. (2017). Nitrogen deposition to forest ecosystems with focus on its different forms. Nitrogen deposition to forest ecosystems with focus on its different forms, *Science of the Total Environment*, 575, 791 – 79.
- Gioda A., Mayol-Bracero O. L., Scatena F. N., Weathers K. C., Mateus V. L., McDowell W. H.. (2013). Chemical constituents in clouds and rainwater in the Puerto Rican rainforest: Potential sources and seasonal drivers, *Atmospheric Environment*, 68, 208 – 220
- Ignatova N. and Fikova R.. (2007). Precipitation chemistry in Sweet Chestnut forests (*Castanea sativa* Mill.) in Belasitza Mountain. Sustainable management of Sweet Chestnut ecosystems-CAST Bul. book with reports from I-st Balkan regional workshop. 2-5 November. Blagoevgrad. Bulgaria. publishing house Petekston. 2007. ISBN: 978-954-457-046-0
- Iordanova L., Blaskova S. (2011). Impact of atmospheric precipitations on the surface water chemistry in the high mountain area of the Bulgarian Danube basin In: Proceedings of the XXV-th conference of the Danube countries on hydrological forecasting and hydrological bases of water management. Budapest. Hungary. Session 7, 6:822 – 830.
- Marinoni, Laj P., Sellegri K., Mailhot G. (2004). Cloud chemistry at the Puy de D'ome: variability and relationships with environmental factors, *Atmospheric Chemistry and Physics*, 4, 715 – 728.
- Mihajlidi-Zelić A., Deršek-Timotić I., Relić D., Popović A., Đorđević D. (2006). Contribution of marine and continental aerosols to the content of major ions in the precipitation of the central Mediterranean, *Science of the Total Environment*, 370, 441 – 451.
- Monthly hydro metrological bulletin, (2018), NIMH, Sofia June, July (in Bulgarian). ISSN 1314-894X
- Schwab, J.J., Casson, P., Brandt, R., Husain, L., Dutkewicz, V., Wolfe, D., Demerjian, K.L., Civerolo, K.L., Rattigan, O.V., Felton, H.D. and Dukett, J.E. (2016). Atmospheric Chemistry Measurements at Whiteface Mountain, NY: Cloud Water Chemistry, Precipitation Chemistry, and Particulate Matter. *Aerosol Air Qual. Res.* 16: 841 – 854. <https://doi.org/10.4209/aaqr.2015.05.0344>
- Stein, A.F., Draxler, R.R, Rolph, G.D., Stunder, B.J.B., Cohen, M.D., and Ngan, F. (2015). NOAA's HYSPLIT atmospheric transport and dispersion modeling system, *Bull. Amer. Meteor. Soc.*, 96, 2059 – 2077.

- Rolph, G., Stein, A., and Stunder, B. (2017). Real-time Environmental Applications and Display sYstem: READY. *Environmental Modelling & Software*, 95, 210 – 228.
- Zeller K., Bojinov Ch., Donev E., Nikolov N.. (1998). Bulgarian Rila Mountain Forest Ecosystems Study Site: Site Description and SO₄²⁻-NO₃-Deposition, In: Proceedings of the International Symposium on Air Pollution and Climate Change Effects on Forest Ecosystems, February 5 – 9. 1996. Riverside. CA Gen. Tech. Rep. PSW-GTR-166. Albany. CA: U.S. Department of Agriculture, Forest Service, Pacific Southwest Research Station, 332 p.
- Weathers, K.C., Likens, G.E., Bormann, F.H., Bicknell, S.H., Bormann, B.T., Daube Jr., B.C., Eaton, J.S., Galloway, J.N., Keene, W.C., Kimball, K.D., McDowell, W.H., Siccama, T.G., Smiley, D., Tarrant, R. (1988). Cloud water chemistry from ten sites in North America, *Environmental Science & Technology*, 22, 1018 – 1025.
- WMO GAW Report No. 160. (2004). *Manual for the GAW precipitation chemistry programme*, Edited by Mary A. Allan Prepared by GAW Precipitation Chemistry Science Advisory Group.

✉ **Elena Hristova**

<https://orcid.org/0000-0002-5681-4375>

National Institute of Meteorology and Hydrology
Sofia, Bulgaria

E-mail: elena.hristova@meteo.bg

✉ **Blagorodka Veleva**

<https://orcid.org/0000-0003-2848-5559>

National Institute of Meteorology and Hydrology
Sofia, Bulgaria

E-mail: blagorodka.veleva@meteo.bg

✉ **Krum Velchev**

National Institute of Meteorology and Hydrology
Sofia, Bulgaria

E-mail: krum.velchev@meteo.bg

✉ **Emilia Georgieva**

<https://orcid.org/0000-0002-8466-4976>

National Institute of Meteorology and Hydrology
Sofia, Bulgaria

E-mail: emilia.georgieva@meteo.bg

CHARACTERISTICS OF ULTRAFINE PM EMITTED DURING GASIFICATION OF BIOMASS

**Iliyana Naydenova¹, Tsvetelina Petrova¹, Ognyan Sandov¹,
Ricardo Ferreira², Rositsa Velichkova³, Mario Costa²**

¹*Technical University of Sofia, College of Energy and Electronics*

²*Universidade de Lisboa, Instituto Superior Técnico,
Mechanical Engineering Department, IDMEC – Lisboa (Portugal)*

³*Technical University of Sofia, Faculty of Power Engineering and Power Machines*

Abstract:

The present work aims at characterising ultrafine particulate matter (PM) that was emitted during biomass gasification in a drop tube furnace (DTF). Three different types of agricultural residue were gasified using the following gasifying agents: O₂/N₂ and O₂/N₂/CO₂. The PM in the flue gases were sampled, using 13 stage impactor. Particulates, having aerodynamic diameter of 1 and 0.65 μm (PM₁ and PM_{0.65}) had the highest mass fraction among all other particulates with aerodynamic diameter up to 10 μm. Thus, the effects of biomass and gasifying agent on particles' mass distribution were studied. Besides, PM₁ and PM_{0.65} were characterised using X-ray fluorescence (XRF) analysis. The PM elemental composition confirmed that volatile ash compounds, such as K and Cl are typical constituents of the ultrafine particulates, when biomass from agricultural residue (colza and sunflower husks) was gasified.

Keywords: particulate matter, biomass, gasification.

INTRODUCTION

Currently in Bulgaria, the air quality investigations are mostly focused on the atmospheric air pollution. Certain attention is drawn on the particulate matter (precisely PM₁₀ and PM_{2.5}), namely the exceedance of their norms (Directive 2008/50/EC), PM₁₀ chemical composition and source apportionment. Chaturkova (Chaturkova, 2015) assessed particulate matter (PM₁₀ and PM_{2.5}) in atmospheric air for the period 2007-2014. Two regions were examined (urbanized and industrial) involving three monitoring stations: city background, transport-oriented, and industrial-oriented. The author reports the average annual PM₁₀ and PM_{2.5} concentrations, the average monthly PM₁₀ concentrations, the maximum PM₁₀ concentrations (μg/m³) and the number of exceedings in the investigated pe-

riod. Vlakenski et al. (Vlakenski, 2015) traced the background air pollution with PM_{10} in three medium-sized urban areas of Central North Bulgaria during 2007-2010. Veleva et al. (Veleva, 2014a and Veleva, 2014b) measured the daily concentration of PM_{10} in a period of four seasons in Bulgaria, as well as the chemical composition of the collected samples through EDXRF analysis. The authors identify more than 23 chemical elements in the structure of the collected PM_{10} . Veleva et al. (Veleva, 2015) organized six experimental campaigns in Sofia within the winter and the summer periods of 2012, 2013 and 2014. The authors report the PM_{10} mass concentration and the elemental composition of more than 20 elements (P, S, Cl, K, Ca, Ti, V, Cr, Mn, Fe, Ni, Cu, Zn, Br, Rb, Sr, Y, Zr, Cd, Sn, Sb, I, Ba, Pb), which show significant variations in maximum and mean concentrations.

Antova et al. (Antova, 2019) collected and identified the main air pollutants in indoor air. The authors studied the concentration of PM_{10} and $PM_{2.5}$, ozone, carbon monoxide, carbon dioxide, formaldehyde, nitrogen dioxide, volatile organic compounds, moisture and mold presence in school classrooms.

The pronounced interest on PM_{10} and $PM_{2.5}$ concentration in the urban atmosphere is challenged by the European and the national regulations, straggling to find efficient solution for various insufficiently controlled processes, such as combustion in terms of residential heating and transport (IIR, 2019, Nikolaev, 2017 and Naydenova, 2018). Gvero et al. (Gvero, 2018) measure the daily average PM_{10} concentrations ($\mu\text{g m}^{-3}$) in one part of Banja Luka city area, with dominant private households, and determine the PM chemical composition. Juda-Rezler et al. (Juda-Rezler, 2020) studied the $PM_{2.5}$ for one calendar year and gave the seasonal concentration of $PM_{2.5}$, 19 trace elements in $PM_{2.5}$, as well as $PM_{2.5}$ sources apportionment – residential combustion, exhaust traffic emissions, non-exhaust traffic emissions. Zalakeviciute et al. (Zalakeviciutea, 2020) identified 28 different elements in the structure of PM_{10} , as well as the existence of ions, such as SO_4^{2-} , NO_3^- and NH_4^+ . Pateraki et al. (Pateraki, 2020) chemically characterized $PM_{2.5}$ and PM_{10} , sampled from Greater Athens Area. The authors identified 20 different PM-bound polycyclic aromatic hydrocarbons (PAH). Chernishev et al. (Chernishev, 2018) investigated the particle size distribution and the chemical composition, e.g. the fraction of particles with structured carbon (crystalline phase state) in the sampled PM_{10} , which originated from the exhausts of two-wheeled vehicles that are typically used in the territory of Vladivostok, Russia.

Recently, the variety of processes for solid biofuels utilization gained significant attention due to the increase of energy demands and shortage of fossil fuels, the main source of energy in the planet (Villetta, 2017). However, the flue gases of such processes are typical source of pollutants, including char and PM of different size and chemical composition. The ultrafine PM contain significant amount of soot particles known to be harmful to the environment and the human beings. They can

penetrate easily into the respiratory system, causing lung malfunction and premature death (Göktepe, 2016 and Naydenova, 2007).

Thus, detailed research is needed about the emission modes and factors of ultrafine PM, as well as on their chemical composition and behavior.

Gasification is one of the possible utilization ways to convert solid biofuels into valuable products. Generally, biomass gasification is a thermo-chemical conversion in a low oxygen environment (using different gasifying agents - usually air, oxygen or steam), producing syngas. It is a mixture mainly made of carbon monoxide (CO), hydrogen (H₂), methane (CH₄) and other hydrocarbons. These substances are flammable and combustible (Villetta, 2017). According to Basu and Duarte (Basu, 2010 and Duarte, 2018) the gasification converts solid or liquid carbonaceous fuels into a synthesis gas or syngas that can be used to produce chemical feedstock, liquid fuels, power or gaseous fuels.

The present work was focused on the ultrafine PM emitted during biomass gasification, which was carried out in a drop tube furnace (DTF). Three different types of biomass were utilized with two types of gasifying agents: O₂/N₂ and O₂/N₂/CO₂. The effects of biomass and gasifying agent on the particles' mass concentration were investigated, along with the chemical characterisation of the PM₁ and PM_{0.65}, using XRF analysis. The work is still in progress and herein only some preliminary results are presented.

METHODS USED

In the present experiment, PM with different sizes was collected during biomass gasification in DTF, which is a laboratory-scale reactor, suitable for pulverised-fuel conversion. Detailed description of the applied experimental set up is provided by Duarte and Duarte et al. (Duarte, 2018 and Duarte, 2019) and Adánez-Rubio et al (Adánez-Rubio, 2020). Duarte et al. (Duarte, 2019) conduct gasification experiments of wheat straw. The authors examine the influence of the operating temperature of the DTF between 900 and 1200 °C on the formation of syngas and soot. The authors obtained that higher operating temperatures result in higher CO and H₂ yields, higher H₂/CO volume ratio, which leads to a higher carbon conversion efficiency but lower yields of CH₄ and CO₂. The formation of soot increases with temperature increase and reaches a maximum at 1000°C, above which it starts to decrease. Adánez-Rubio et.al (Adánez-Rubio, 2020) investigate the pig manure gasification at different temperatures (900-1200 °C) and different gasifying agents (N₂/O₂, N₂/O₂/CO₂, N₂/O₂/H₂O). The results show that the temperature increase leads to a higher production of soot particles, and the use of water decreases the soot production.

The present work was focused on the chemical characterization of ultrafine PM that was sampled from the flue gases during biomass gasification. The experiment was carried out at 1000°C, expecting to have high soot yield, which would highly

affect the yield of ultrafine particulates. The selected types of biomass are woody biomass (softwood and bark) and agriculture residue (colza and sunflower husks). The present study was focused on the Bulgarian alternative biofuels that are easily accessible in large amount annually as a result of food and energy industries. For instance, sunflower husks and softwood are typically used for solid biofuels production. Recent technologies allow co-combustion of biomass with coal in pulverised coal boilers. On the other hand, the softwood is widely used for residential heating purposes (as solid biofuel pellets or it is directly burnt in stoves at some regions in Bulgaria).

Prior to the experiment, the biomass was characterized through proximate, ultimate and ash analyses. The results are presented elsewhere (Naydenova, 2020). The biomass was initially ground and sieved to assure fuel particle size below 1mm.

The biomass flow was kept at 15 g/h throughout all experiments, and the excess air ratio (λ) was constant, at a value of 0.4. Two different gasifying agents were used in the following proportions: (1) a mixture of 1% of O₂ and 99% of N₂ and (2) a mixture of 1% O₂, 94% of N₂ and 5% of CO₂. The nitrogen was used as a carrier gas. The chosen operating conditions were based on the works of Duarte, Duarte et al. and Adánez-Rubio et.al. (Duarte, 2018, Duarte, 2019 and Adánez-Rubio, 2020), as well as on the requirements of Dekati PM sampling system (Dekati, 2013).

During biomass gasification, the PM samples were collected with 13 stage impactor, which assures D50% values (μm) for 13 cutdiameters (cut-off sizes), between 10 μm and 30 nm, (Dekati, 2010). The present work aims at characterizing only the ultrafine particulates, namely the PM with D50% = 0.65 μm (PM_{0.65}) and D50% = 1 μm (PM₁). For simplicity, further in the text, the above described particulates are entitled as PM_{0.65} and PM₁.

The PM elemental composition was obtained using XRF analysis, which was carried out with Fischerscope X-Ray System XDAL. This method for qualitative analysis was chosen as a primary step of PM characterization, because it is non-destructive and allows identifying relatively wide range of chemical elements with atomic numbers from 19 (potassium) to 92 (uranium) in the ppm range.

RESULTS AND DISCUSSION

In the present experiment, the ultrafine particulates (PM_{0.65} and PM₁) constituted the major portion of the PM, collected in the 13-stage cascade. Similar tendency is observed in an independent study, described elsewhere (Naydenova, 2020), on the combustion of five different types of biomass (cherry stones and pellets from softwood, sunflower husk, rape, wheat straw) in fluidized bed conditions. The presently collected ultrafine particulates were subject to further research. The relative mass concentration (wt. %) of both PM₁ and PM_{0.65} among all collected PM in the 13-stage cascade was obtained:

When O_2/N_2 was used as gasifying agent: 71.63% for sunflower husks, 50.63% for softwood and 35.55% for colza;

When $O_2/N_2/CO_2$ was used as gasifying agent: 46.18% for sunflower husks, 43.72% for softwood and 68.46% for colza.

Table 1. Mass of the sampled PM

| Biomass type | Mass (g) | | wt. % | |
|---------------------------------------------------------------------|--------------------|-----------------|--------------------|-----------------|
| | PM _{0.65} | PM ₁ | PM _{0.65} | PM ₁ |
| <i>O₂/N₂ – gasifying agent</i> | | | | |
| Colza | 0.00160 | 0.00038 | 28.73 | 6.82 |
| Softwood | 0.00518 | 0.00367 | 29.63 | 21.00 |
| Sunflower husks | 0.00607 | 0.00562 | 37.19 | 34.44 |
| <i>O₂/N₂/CO₂ – gasifying agent</i> | | | | |
| Colza | 0.00571 | 0.00673 | 31.43 | 37.04 |
| Softwood | 0.00355 | 0.00735 | 14.24 | 29.48 |
| Sunflower husks | 0.00340 | 0.01324 | 9.44 | 36.75 |

Furthermore, the particle mass distribution PM₁ and PM_{0.65} were investigated. Thus, the effect of the biomass type and the gasifying agent on the PM mass and wt. % distribution is presented in Table 1 and Fig. 1. In the case of O_2/N_2 - the following relations were observed for the mass concentration of PM_{0.65} and PM₁ (Fig. 1):

- *Colza*: the mass concentration of PM_{0.65} was about 4 times higher than the one, measured for PM₁;
 - *Softwood*: PM_{0.65} was 29 % higher than PM₁;
 - *Sunflower husks*: PM_{0.65} and PM₁ were with almost equal masses.
- In the case of $O_2/N_2/CO_2$ - the following relations were obtained (Fig. 1):
- *Colza*: PM_{0.65} was about 17% higher than PM₁;
 - *Softwood*: PM_{0.65} was twice times less than PM₁;
 - *Sunflower husks*: PM_{0.65} was about 4 times less than PM₁.

Besides, the gasification of colza resulted in an almost equal mass of PM_{0.65} among all other PM, sampled in the 13-stage cascade, for both gasifying agents. On the other hand, a significant difference in PM₁ mass concentration was observed: 6.82 % in O_2/N_2 and 37.04 % in $O_2/N_2/CO_2$ atmosphere. When softwood was gasified, the fraction of PM_{0.65} among all other PM was 29.63 % in O_2/N_2 and 14.24 % in $O_2/N_2/CO_2$, whereas the PM₁ was 21.00 % in O_2/N_2 and 29.48% in $O_2/N_2/CO_2$ atmosphere. In the case of sunflower husks, the mass concentration of PM_{0.65} was 37.19 % in O_2/N_2 and 9.44 % in $O_2/N_2/CO_2$ atmosphere, whereas in $O_2/N_2/CO_2$ atmosphere the PM₁ showed higher concentration for all investigated biomass types.

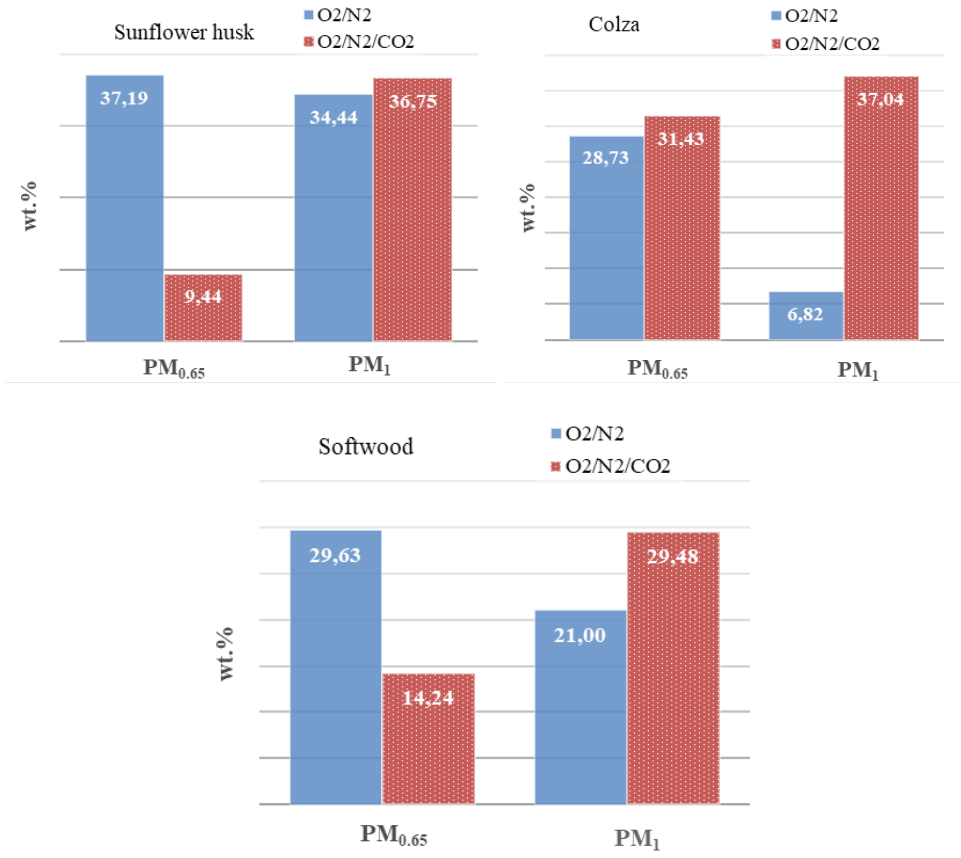


Figure 1. The percentage of PM_{0.65} and PM₁ relative to the total amount of particulate matter

Fig. 2 shows a comparison of the emitted PM_{0.65} and PM₁ depending on the biomass used. When O₂/N₂ was the gasifying atmosphere, the lowest mass of PM_{0.65} and PM₁ was detected in the colza gasification, whereas the highest mass - for the sunflower husks. Slight variations were observed for the PM_{0.65} mass during biomass gasification in O₂/N₂/CO₂ atmosphere: softwood (0.00355 g), sunflower husks (0.0034 g) and colza (0.00673 g). Distinctly higher mass of PM₁ was obtained, when sunflower husks (0.01324 g) were processed.

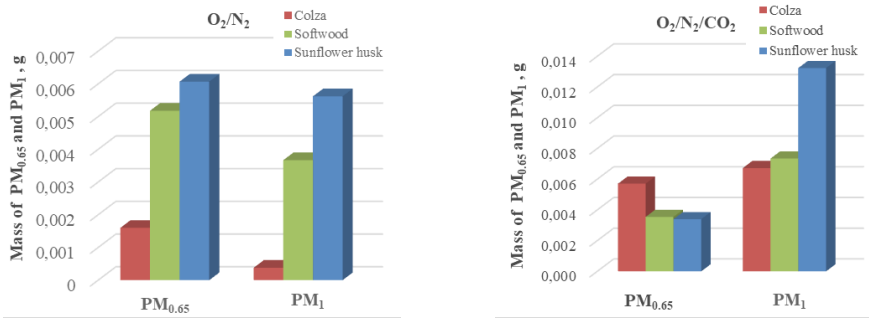


Figure 2. The mass of PM_{0.65} and PM₁

Table 2 presents the elemental composition of the investigated PM_{0.65-1}, resulting from the XRF analysis.

Table 2. Elemental composition of the examined PM

| Biomass type | Gasifying agent | | | |
|-----------------|-------------------------------------------------|-----------------|--------------------------------|-----------------|
| | O ₂ /N ₂ /CO ₂ | | O ₂ /N ₂ | |
| | PM _{0.65} | PM ₁ | PM _{0.65} | PM ₁ |
| Colza | Fe | Fe | Fe | Fe |
| | K | K | K | K |
| | Cl | | | |
| | | | Cu | Cu |
| | | Mn | | Mn |
| Softwood | | Zn | Zn | |
| | Fe | Fe | Fe | Fe |
| | Mn | Mn | Mn | Mn |
| | Zn | Zn | Zn | |
| | Sr | Sr | Sr | Sr |
| | Zr | | Zr | |
| | Cd | | | |
| | | Cu | Cu | |
| | | Sb | | |
| | | | As | |
| Sunflower husks | Fe | Fe | Fe | Fe |
| | Zn | Zn | Zn | Zn |
| | | | | Ca |
| | | | Mn | Mn |
| | | K | | K |

As expected, the ultrafine particulates that were emitted during gasification of agricultural residue (colza and sunflower husks) contained volatile ash compounds,

such as K and Cl. These results correspond with the results from the ultimate and the ash analyses of the same feedstock (Naydenova, 2020) and with the observations of Obernberger et al. (Obernberger, 2006). The authors concluded that the ash, containing elements like K, Na, P and Cl is typically part of the fly ash, whereas elements like Ca, Mg and Si are normally found in the bottom ash. The $PM_{0.65-1}$ from woody biomass (softwood) contained greater variety of heavy metals and Sr was obtained independently of the gasifying agent.

The combined effects of biomass and gasifying agent on the PM chemical composition can be summarized as follows: (a) *colza* - Fe and K were found in all filters, independently of the gasifying agent. However, Cl was detected only in the $PM_{0.65}$ ($O_2/N_2/CO_2$), whereas the elements: Cu, Mn and Zn were obtained in the rest of the filters; (b) *softwood* – Fe, Mn and Sr were the dominant elements in both $PM_{0.65}$ and PM_1 , accompanied by unequally distributed Zn, Zr, Cd, Cu, Sb and As in some of the filters; (c) *sunflower husks* - Fe and Zn were detectable in all samples, while Ca, Mn and K – only in some of the filters. According to Argyropoulos et al. (Argyropoulos, 2012), the biomass burning is a typical source of K, Ca, Mn and Sr.

CONCLUSIONS

The main goal of the present study was to characterise the ultrafine particulates (PM_1 and $PM_{0.65}$), obtained from the flue gases during biomass gasification in DTF. The PM elemental composition was experimentally measured applying XRF technique. Thus, the effect of biomass and gasifying agent on the particulates' mass distribution and elemental composition was investigated.

When biomass was processed in O_2/N_2 , the relative mass concentration of the PM collected on both filters, $PM_{0.65}$ and PM_1 , over the total mass of all other sized PM increased in the following order: 35.55 % (*colza*), 50.63 % (*softwood*), 71.63 % (*sunflower husks*). Nevertheless, when $O_2/N_2/CO_2$ was the gasifying agent: 43.72 % (*softwood*), 46.18 % (*sunflower husks*), 68.46 % (*colza*).

The elemental composition of the ultrafine particulates sampled during gasification of agricultural residue (*colza* and *sunflower husks*) confirmed the existence of volatile ash compounds, such as K and Cl, which were missing in the $PM_{1-0.65}$, sampled during gasification of woody biomass. This result corresponds well with preliminary published observations (Obernberger, 2006) that elements, such as K and Cl, play a significant role in the process of ultrafine particulates formation through the nucleation mechanism.

ACKNOWLEDGMENTS

The PM analysis was funded through the Internal Competition of Technical University of Sofia - 2020 for the scientific project "Perspective leaders", Contract № 201IPP0017-10/26.05.2020. The authors would also like to acknowledge the financial support from the National Science Program "Environmental Protection

and Reduction of Risks of Adverse Events and Natural Disasters”, approved by the Resolution of the Council of Ministers No 577/17.08.2018 and supported by the Ministry of Education and Science of Bulgaria (Agreement No D01-230/06.12.2018 and Agreement No Д01-322/18.12.2019).

REFERENCES

- Adáñez-Rubio, I., Ferreira, R., Rio, T., Alzueta, M.U., Costa, M. (2020). Soot and char formation in the gasification of pig manure in a drop tube reactor, *Fuel*, 281, 118738, doi:10.1016/j.fuel.2020.118738.
- Antova T. G., Panev T. I., Tzoneva M. Tz., Sidjimov M. A., Lukanova R. T. (2019). Indoor air quality assessment (pilot study), *Journal of International Scientific Publications, Ecology & Safety* ISSN 1314-7234, 13, pp.77-85.
- Argyropoulos G., Manoli E., Kouras A., Samara C. (2012). Concentrations and source apportionment of PM₁₀ and associated major and trace elements in the Rhodes Island, Greece, *Science of the Total Environment*, 432, 12–22.
- Basu P. (2010). *Biomass gasification and pyrolysis: Practical design and theory*. 1st ed., Elsevier Inc.
- Bulgaria’s Informative Inventory Report 2019 (IIR, 2019). Submission under the UNECE Convention on Long-Range Transboundary Air Pollution, Centre on Emission Inventories and Projections (CEIP), Umweltbundesamt, Vienna, Austria.
- Chernyshev V.V., Zakharenko A.M., Ugay S.M., Hien T.T., Hai L.H., Kholodov A.S., Burykina T.I., Stratidakis A.K., Mezhuev Ya. O., Tsatsakis A.M., Golokhvast K.S. (2018). Morphologic and chemical composition of particulate matter in motorcycle engine exhaust, *Toxicology Reports*, 5, 224–230.
- Chuturkova R. (2015). Particulate matter air pollution (PM10 and PM2.5) in urban and industrial areas, *Journal Science Education Innovation*, 5, 13-32, Association Scientific and Applied Research International Journal, ISSN 1314-9784.
- Dekati (2013). Dekati DLPI Low Pressure Impactor, <https://www.particleinstruments.com/sites/default/files/pdfs/DLPI%20Brochure%206%2C2013.pdf>
- Directive 2008/50/EC of the European Parliament and of the Council of 21 May 2008 on ambient air quality and cleaner air for Europe, <https://eur-lex.europa.eu/legal-content/EN/TXT/PDF/?uri=CELEX:02008L0050-20150918&from=EN>.
- Duarte F.S. (2018), Biomass Gasification in a Drop Tube Furnace. Thesis to obtain the Master of Science Degree in Mechanical Engineering, Instituto Superior Técnico, Lisboa.
- Duarte F., Ferreira I., Costa M. (2019). Soot formation during the gasification of wheat straw in a drop tube furnace. 5th International Conference WASTES: Solutions, Treatments and Opportunities, Almada, Portugal, 4th – 6th September.

- Göktepe B., Umeki K., Gebart R. (2016). Does distance among biomass particles affect soot formation in an entrained flow gasification process? *Fuel processing Technology*, 141, 99–105.
- Gvero P., Radić R., Kotur M., Kardaš D. (2018). Urban air pollution caused by the emission of PM₁₀ from the small household devices and abatement measures, *Thermal Science*, 152-152, DOI: 10.2298/TSCI180119152G.
- Juda-Rezler K., Reizer M., Maciejewska K., Błaszczak B., Klejnowski K. (2020). Characterization of atmospheric PM_{2.5} sources at a Central European urban background site, *Science of the Total Environment*, 713, 136729.
- Naydenova I. (2007). PhD Thesis, *Soot Formation Modeling during Hydrocarbon Pyrolysis and Oxidation behind Shock Waves*. Ruprecht-Karls-Universität at Heidelberg Interdisziplinäres Zentrum für Wissenschaftliches Rechnen
- Naydenova I., Petrova T., Velichkova R., Simova I. (2018). PM₁₀ exceedance in Bulgaria, *CBU International conference proceedings*, 2018, March 21-23, Prague, Czech Republic, 6, 1129-1138. <http://dx.doi.org/10.12955/cbup.v6.1305>.
- Naydenova I., Sandov O., Wesenauer F., Laminger T., Winter F. (2020) Pollutants formation during single particle combustion of biomass under fluidized bed conditions: An experimental study, *Fuel*, 278, 117958.
- Nikolaev A., Konidari P. (2017). Development and assessment of renewable energy policy scenarios by 2030 for Bulgaria. *Renew Energy*, 111, 792–802. <https://doi.org/10.1016/j.renene.2017.05.007>.
- Obernberger I., Brunner T., Baerenthaler G. (2006). Chemical properties of solid biofuels - significance and impact. *Biomass Bioenergy*, 30, 973–82. <https://doi.org/10.1016/j.biombioe.2006.06.011>.
- Pateraki St., Asimakopoulos D.N., Maggos Th., Assimakopoulos V.D., Bougiatioti A., Bairachtari K., Vasilakos Ch., Mihalopoulos N. (2020). Chemical characterization, sources and potential health risk of PM_{2.5} and PM₁ pollution across the Greater Athens Area, *Chemosphere*, 241, 125026.
- Veleva B., Hristova E., Nikolova E., Kolarova M., Valcheva R. (2014a). Seasonal variation of PM₁₀ elemental composition in urban environment, *Journal of International Scientific Publications: Ecology and Safety* 8, ISSN 1314-7234 (Online), <http://www.scientific-publications.net>.
- Veleva B., Hristova E., Nikolova E., Kolarova M., Valcheva R. (2014b). Elemental composition of air particulate (PM₁₀) in Sofia by EDXRF techniques, *Journal of Chemical Technology and Metallurgy*, 49 (2), 163-169.
- Veleva B., Hristova E., Nikolova E., Kolarova M., Valcheva R. (2015). Experimental study on elemental composition of PM₁₀ in Sofia, 2012-2014, *Science & Technologies*, V (2), Nautical & Environmental studies, DOI: 10.13140/RG.2.1.4570.8562.
- Villetta M., Costa M., Massarotti N. (2017). Modeling approaches to biomass gasification: A review with emphasis on the stoichiometric method, *Renewable sustainable energy reviews*, 74, 71-88.

- Vlaknenski T., Stoychev P., Chuturkova R. (2015). Background air pollution by fine particles in urban areas of central northern Bulgaria, *Environmental technology*, 1 (22), 82-90.
- Zalakeviciutea R., Rybarczyk Y., Granda-Albuja M. G., Suarez M. V. D., Alexandrino K. (2020). Chemical characterization of urban PM₁₀ in the Tropical Andes, *Atmospheric Pollution Research*, 11, 343–356.

✉ **Iliyana Naydenova**

College of Energy and Electronics
Technical University of Sofia
Sofia, Bulgaria
E-mail: inaydenova@tu-sofia.bg

✉ **Tsvetelina Petrova**

<https://orcid.org/0000-0001-8482-4792>
College of Energy and Electronics
Technical University of Sofia
Sofia, Bulgaria
E-mail: tzvetelina.petrova@tu-sofia.bg

✉ **Ognyan Sandov**

<https://orcid.org/0000-0001-7697-669X>
College of Energy and Electronics
Technical University of Sofia
Sofia, Bulgaria
E-mail: o.sandov@tu-sofia.bg

✉ **Ricardo Ferreira**

Mechanical Engineering Department
Instituto Superior Técnico
Universidade de Lisboa
Lisboa, Portugal
E-mail: ricardo1995ferreira@gmail.com

✉ **Rositsa Velichkova**

<http://orcid.org/0000-0003-3757-8685>
Faculty of Power Engineering and Power Machines
Technical University of Sofia
Sofia, Bulgaria
E-mail: rvelichkova@tu-sofia.bg

✉ **Mario Costa**

Mechanical Engineering Department
Instituto Superior Técnico
Universidade de Lisboa
Lisboa, Portugal

BLACK SEA FREEZING AND WINTER SEVERITY: RELATION TO THE TEMPERATURE

Mirna Matov, Elisaveta Peneva, Greta Georgieva
Faculty of Physics, "St. Kliment Ohridski" University of Sofia

Abstract: Black Sea freezing is observed regularly in the northern part and near the Kerch Strait. The reason is the relatively shallow northwestern shelf part and the river inflow of the three major European rivers Danube, Dniepr and Dniestr, carrying large amount of fresh water to this part of the Black Sea. The observed global warming in the latest decades makes these episodes less intense. In 2012 and 2017 the sea ice extended unusually south. The aim of this study is to fill the gap of recent analysis on the Northern Black Sea areas covered regularly with ice. Based on the coastal meteorological stations measurements, we investigate the interannual-to-decadal variability of the thermal regime. The relation with the sea-ice cover based on satellite observations is studied. We define various categories of winter conditions depending on the number of cold days.

Keywords: climate change, Black Sea, winter severity

INTRODUCTION

The Black Sea is a large deep water basin on the border between European and Asian continents lying in the continental mid-latitude climate zone. It is an important climatic factor for all borderline countries (Bulgaria, Romania, Ukraine, Russia, Georgia and Turkey). The open plane in north direction enables the propagation of the Siberian High influence in winter and thus severe winter conditions could occur. From the other side, the Mediterranean Sea influence is significant through the Mediterranean cyclones passing frequently the area, which leads to mild weather conditions.

Black Sea freezing is observed regularly in the northern part and near the Kerch Straits and occasionally spread during cold winters to south reaching Romanian coast (Simonov and Altman, 1991). Since 1972 moderate freezing was observed, but February 2012 was extremely cold and the Black sea ice covered area reached Constanta in Romania (Figure 1). 2017 was also anomalously cold in this area.

There is not a thorough recent study of the areas covered regularly with ice in the Northern Black Sea, and our aim is to fill this gap and to check to what extent the sea ice occurrence is important to be taken into account from numerical models.

The other objective is to study the interannual-to-decadal variability of the thermal regime and winter severity in the region in relation to the freezing.

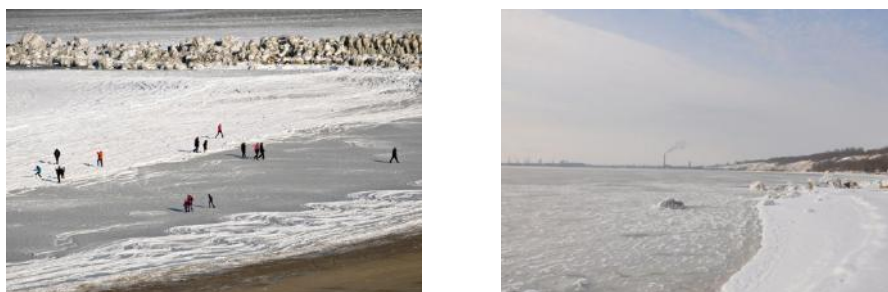


Figure 1. Romanian coast near Constanta in February 2012

DATA USED IN THE STUDY

In order to reveal the interannual variability during the last decades we use three sources of data:



Figure 2. Locations of the meteorological stations used in the study

1) Historical archives and literature material on the Black Sea ice extend and temperature from the Black Sea book (Simonov and Altman, 1991)

2) Data for 2m air temperature coming from 9 coastal meteorological stations along the Black Sea coast - Burgas, Varna, Odessa, Herson, Mariupol, Batumi, Trabzon, Sinop and Istanbul (Figure 2). The sea temperature in Burgas and Varna is also used. The data source is the regular SYNOP telegrams distributed by the Global Surface Summary of the Day – GSOD (data.nodc.noaa.gov). The data are decoded from SYNOP code and cover the period since 1980 till present.

3) Data for the ice extent are taken from the US National Snow and Ice Data Center product Multisensor Analyzed Sea Ice Extent - Northern Hemisphere (MASIE-NH). This provides daily sea ice data from January 1st, 2006 to the present (MASIE, Technical References).

ANALYSIS OF THE WINTER TEMPERATURE VARIATIONS

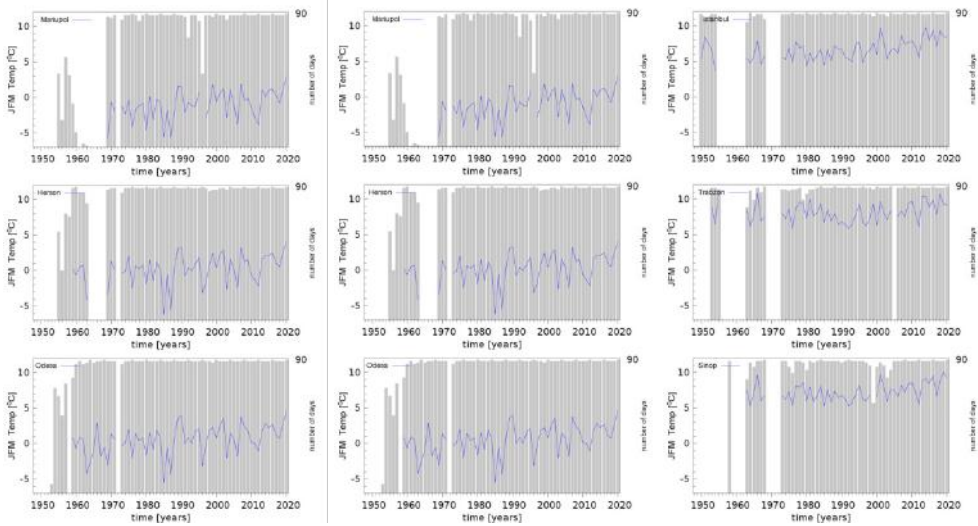


Figure 3. Interannual variability of the winter temperatures (Jan, Feb, Mar) in Burgas, Varna, Bartumi, Odesa, Herson, Mariupol, Trabzon, Sinop and Istanbul. The grey columns in the background refer to the data availability, the periods with no or insufficient data are not taken in the analysis.

We have used data from the NOAA data set Global Surface Summary of the Day – GSOD (data.nodc.noaa.gov). The mean winter temperature is calculated for the 9 meteorological stations along the Black Sea coast – Burgas and Varna in Bulgaria, Odesa, Herson and Mariupol in Ukraine, Batumi in Georgia and Istanbul, Trabzon and Sinop in Turkey, as the mean value for the months January, February and March). The graphs are presented in Figure 3 and show significant interannual variability. As expected the north-coast stations (Odesa, Herson and Mariupol) are much colder than the south ones (Istanbul, Sinop and Trabzon), and the one eastern (Batumi) is similar to the south ones. Burgas and Varna winter temperature on the west coast is in between. Overall, the variations in the 9 stations are very similar and in phase, suggesting that the winter conditions are uniform in the entire area. Interesting fact to notice also is the slight tendency for milder winter.

In order to categorize how cold was the winter, we have followed Simonov and Altman (1991) approach: we define a Winter Severity Index (WSI) as the sum of negative daily temperature values (frozen days) with opposite sign for the months December to March for each of the 9 stations. Figure 4 show that in Odesa, Mariupol and Herson every winter the temperature falls regularly below zero, on the contrary - in Istanbul, Sinop and Trabzon very rare. Burgas and Varna on the west coast are similar to the north but Batumi on the east is like the southern stations. The most indicative for the winter intensity are the north cities and thus in the further analysis we have considered these three locations.

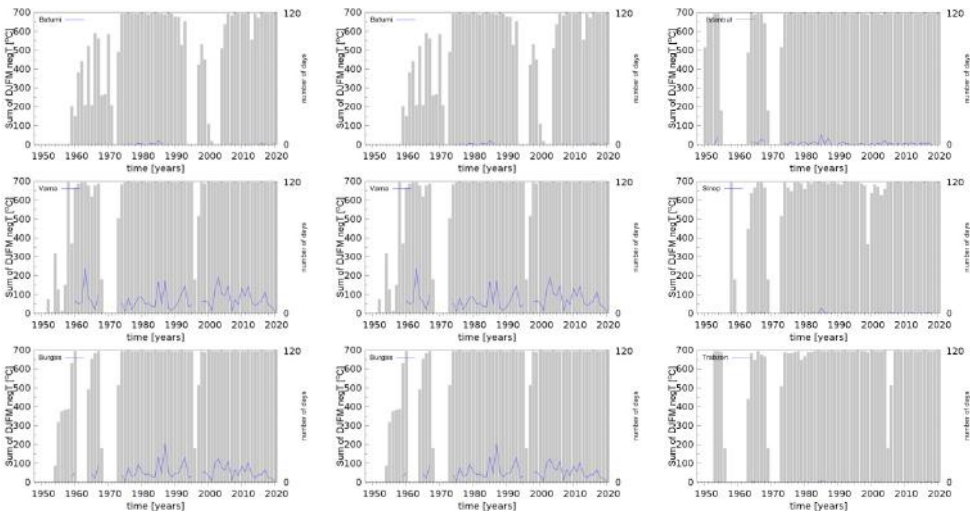


Figure 4. Winter severity index for Burgas, Varna, Bartumi, Odesa, Herson, Mariupol, Trabzon, Sinop and Istanbul. The grey columns in the background refer to the data availability, the periods with no or insufficient data are not taken in the analysis.

WINTER INTENSITY IN THE PERIOD 1925-2020.

The curves in Figure 5 represent the WSI variations for the historical data (Simonov and Altman 1991) and our calculated WSI from the synoptic measurements in Odesa, Herson and Mariupol for the period 1926-2020. It is seen that the curves evolve very similar. Mariupol is the northern-most city and as consequence the winter severity is most pronounced there. Odesa and Herson are similar in latitude but the west position of Odessa is the reason for less values of WSI. Only severe winter cause significant WSI along the southern coast (Figure 4).

Such winter was for example the 1984/1985, which is similar to the coldest from the record . In the past decade the relatively cold winters were the 2002/2003,

2005/2006, 2011/2012 and 2016/2017. An extremely cold winter was 1953/1954. The analysis shows that the “cold” weather in winter decreases from north to south and from west to east: the freezing days are almost absent in the Trabzon station. Another interesting observation is the negative trend of WSI after 2000. Also, the peaks in the last three decades generally decrease in height. This definitively reflects the warming trend in this period.

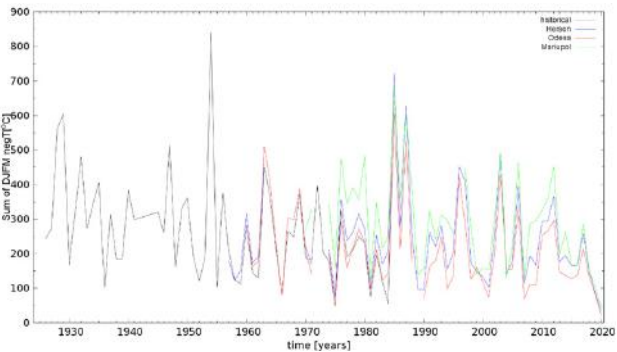


Figure 5. WSI of the historical data for the northern coast of the Black Sea and in Odesa, Herson and Mariupol.

SEA ICE COVER VARIABILITY.

Data for the ice extent are taken from the US National Snow and Ice Data Center product Multi-sensor Analyzed Sea Ice Extent - Northern Hemisphere (MASIE-NH). This provides daily sea ice data from January 1st, 2006 to the present. The satellites used for this research are ALOS, AQUA, DMSP, ENVISAT, GOES, MSG, and RADARSAT-2. Parameters measured by these sensors include sea ice, ice edges, ice extent, and ice growth/melt. Spatial coverage in the study is the entire Northern Hemisphere specified as N 90° to N 0° and E 180° to W -180°. Raster data pixels (grid cells) are 4 km x 4 km thus 16 km² each (MASIE, Technical References).

The available geotiff image in polar stereographic projection (Figure 6) is pre-processed to Mercator projection and using the mask for the Black Sea pixels (Figure 6), only the “sea” pixels with ice are counted. Thus the average and maximal sea ice extent for the four months in the winter season (December to March) are calculated. One can note that the mask contains also the major rivers estuaries.



Figure 6. Figure illustrating the MASIE-NH product; The geotiff image is processed to obtain Mercator projection and only the Black Sea area is cut.

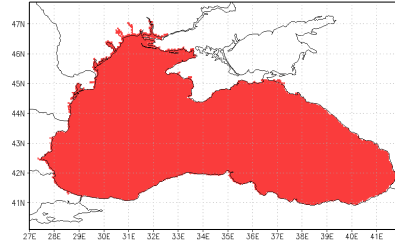


Figure 7. Mask for the Black sea pixels

The results for the daily sea-ice cover in the winters of 2006-2020 period are shown in Figure 8. It is obvious that freezing occurs every year with exception of the winters 2006/2007 and latest one 2019/2020. Maximal ice extent is reached in February 2012 but for relatively short period. The ice coverage in 2006 and 2010 for example is less than that in 2012, but stays for a longer period of time.

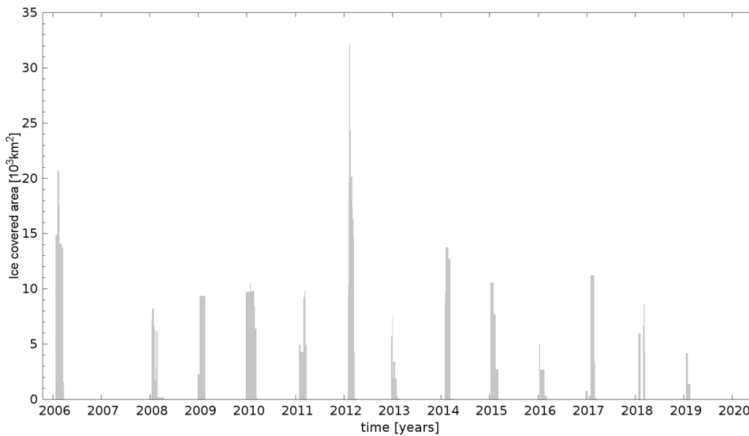


Figure 8. Daily sea ice extent variability in the period 2006-2020 from MASIE-NH.

Figure 9 shows a combined plot of historical data from 1950-1985 for sea ice extend (Simonov and Altman, 1991) and our calculations from MAISIE-NH in the period 2006-2020, processed as described above. Nevertheless global warming trend, it is clear that the freezing occurs rather regularly which leads to the conclusion that it is result from synoptic situations rather than the seasonal averages.

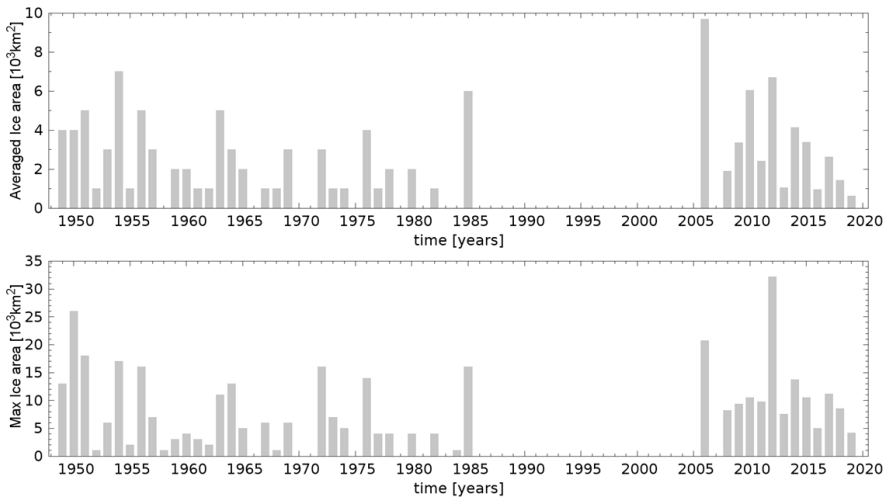


Figure 9. Combined historical data from 1950-1985 from sea ice extent and data from MAISIE-NH in the period 2006-2020

SEA SURFACE TEMPERATURE VARIATION

The available data from synoptic daily measurements of the sea surface temperature (SST) in Burgas and Varna meteorological stations allow us to calculate the winter months mean SST for the period 2000-2020 (Figure 10). The winter months are taken from January to March. The two curves show rather similar in-phase behavior: in Varna the winter SST is generally lower but not always. The comparison of SST with the sea-ice cover together with the winter air temperature and WSI variation reveals that the different sources of data confirm the anomalous cold and warm years: the winters in 2003, 2012 and 2012 were especially cold and on the contrary, the winters in 2001, 2007 and 2020 were very warm.

WINTER CLASSIFICATION

The variation in the ice extent is in agreement with the variations of the WSI and SST. This allows us to make a classification of the winter in the Black Sea region using the sea-ice extent and the threshold values for the winter intensity as defined in the Table 1. In Table 2 the winters in the period from 1926 to 2020 are listed and the type according to the classification in Table 1 is given. Note that since 2003 no “cold” winter conditions are observed, and the relative colder moderate winters are classified as Moderate*.

From the winter classification it could be noted that “cold winter” conditions usually last only one season and the following winter is either mild or moderate. Rarely there are two cold winters in sequence. In this region the very cold synoptic situations are due to the Siberian High expanding to the west and reaching the Cen-

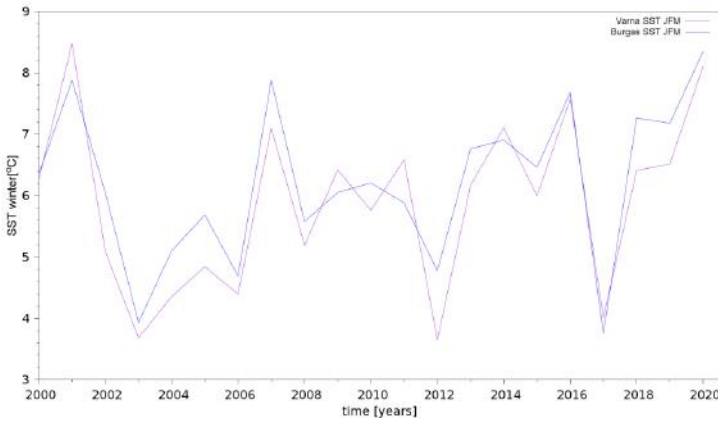


Figure 10. Winter mean SST measured near the coast in the meteorological stations in Varna and Burgas.

tral Europe, thus the next step will consider variations of the Siberian High in order to understand the climate feedback mechanism in the Black Sea region.

Table 1. Winter classification

| WSI value | Winter type |
|------------|-------------|
| [0, 200] | Mild |
| [200, 400] | Moderate |
| [400, -] | Cold |

Table 2. Winter type from 1926 to 2020

| Year | Winter type | Year | Winter type | Year | Winter type |
|------|-------------|------|-------------|------|-------------|
| 1926 | Moderate | 1960 | Moderate | 1991 | Moderate |
| 1927 | Moderate | 1961 | Mild | 1992 | Moderate |
| 1928 | Cold | 1962 | Mild | 1993 | Moderate |
| 1929 | Cold | 1963 | Cold | 1994 | Mild |
| 1930 | Mild | 1964 | Moderate | 1995 | Moderate |
| 1931 | Moderate | 1965 | Moderate | 1996 | Cold |
| 1932 | Cold | 1966 | Mild | 1997 | Cold |
| 1933 | Moderate | 1967 | Moderate | 1998 | Mild |
| 1934 | Moderate | 1968 | Moderate | 1999 | Mild |
| 1935 | Cold | 1969 | Moderate | 2000 | Mild |
| 1936 | Mild | 1970 | Mild | 2001 | Mild |
| 1937 | Moderate | 1971 | Mild | 2002 | Moderate |
| 1938 | Mild | 1972 | Moderate | 2003 | Cold |
| 1939 | Mild | 1973 | Moderate | 2004 | Mild |

| | | | | | |
|------|----------|------|----------|------|-----------|
| 1940 | Moderate | 1974 | Mild | 2005 | |
| 1941 | Moderate | 1975 | Mild | 2006 | Mild |
| 1945 | Moderate | 1976 | Moderate | 2007 | Moderate* |
| 1946 | Moderate | 1977 | Mild | 2008 | Mild |
| 1947 | Cold | 1978 | Moderate | 2009 | Mild |
| 1948 | Mild | 1979 | Moderate | 2010 | Mild |
| 1949 | Moderate | 1980 | Moderate | 2011 | Moderate |
| 1950 | Moderate | 1981 | Mild | 2012 | Moderate |
| 1951 | Mild | 1982 | Mild | 2013 | Moderate* |
| 1952 | Mild | 1983 | Mild | 2014 | Mild |
| 1953 | Mild | 1984 | Mild | 2015 | Mild |
| 1954 | Cold | 1985 | Cold | 2016 | Mild |
| 1955 | Mild | 1986 | Moderate | 2017 | Mild |
| 1956 | Moderate | 1987 | Cold | 2018 | Moderate |
| 1957 | Moderate | 1988 | Moderate | 2019 | Mild |
| 1958 | Mild | 1989 | Mild | 2020 | Mild |
| 1959 | Mild | 1990 | Mild | | |

CONCLUSIONS AND FUTURE PLANS

We have used synoptic observations from 9 coastal Black Sea meteorological stations in order to analyse the interannual-to decadal variations in the mean winter temperature. Our study shows that the variations are very similar and in phase, suggesting that the winter conditions are uniform in the entire area. There is a slight tendency for milder winter in the last 4 decades in all 9 stations.

Along the north coast (Odesa, Mariupol and Herson) every winter the temperature falls below zero, and along the south coast (Istanbul, Sinop, Trabzon and Batumi) only the severe winters cause negative temperatures. For example - 1985/1986 was extremely cold and in the past 20 years there are 4 very cold winters - 2002/2003, 2005/2006, 2011/2012 and 2016/2017.

The sum of daily negative temperatures with opposite sign for the winter season is used to define the winter intensity and is Winter Severity Index (WSI). It presents a negative trend after 2000 reflecting the global warming tendency.

Satellite observations are used to estimate the sea ice cover area and it is found that in the north part freezing is observed rather regularly. The winters in 2007 and 2020 are the unique with no ice observed, and maximal area covered with ice is reached in February 2012 but for relatively short period. The ice cover in 2006 and 2010 for example is less than that in 2012, but stays for a longer period of time. The conclusion is that the freezing results from extremely cold synoptic situations rather than mean seasonal extreme.

The variation of the winter season ice extent is in agreement with the variation of the WSI, estimated from the temperature, as well as the measurements of SST in Burgas and Varna. These data time-series were used to classify the winters' severity in the period 1926-2020 as cold, moderate and mild.

Since 2003 no real “cold” winter conditions are observed, but 2006, 2012 and 2017 are cool. On the other “warm” end are the winters in 2001, 2007 and 2020. The winter 2019/2020 is anomalous warm; the mildest from the analysed period. Future analysis is foreseen to investigate the impact of the Siberian High, as well as the “buffer” role of the Black Sea.

ACKNOWLEDGMENTS

This work has been carried out in the framework of the National Science Program "Environmental Protection and Reduction of Risks of Adverse Events and Natural Disasters", approved by the Resolution of the Council of Ministers № 577/17.08.2018 and supported by the Ministry of Education and Science (MES) of Bulgaria (Agreement № Д01-322/18.12.2019).

REFERENCES

- National Ice Center and National Snow and Ice Data Center. Compiled by F. Fetterer, M. Savoie, S. Helfrich, and P. Clemente-Colón. 2010, updated daily. *Multisensor Analyzed Sea Ice Extent - Northern Hemisphere (MASIE-NH), Version 1*. Boulder, Colorado USA. NSIDC: National Snow and Ice Data Center. doi: <https://doi.org/10.7265/N5GT5K3K>. [May 6th 2019].
- Simonov A. and Altman E (eds) (1991), *Hydrometeorology and Hydrochemistry of the USSR Seas. Vol. IV. Black Sea. Issue 1*. St. Petersburg, Gidrometeoizdat (in Russian)

✉ **Mirna Matov**

<http://orcid.org/0000-0002-9900-0638>

Faculty of Physics
“St. Kliment Ohridski” University of Sofia
Sofia, Bulgaria
E-mail: mirnamatov@gmail.com

✉ **Elisaveta Peneva**

<http://orcid.org/0000-0003-1325-685X>

Faculty of Physics
“St. Kliment Ohridski” University of Sofia
Sofia, Bulgaria
E-mail: elfa@phys.uni-sofia.bg

✉ **Greta Georgieva**

Faculty of Physics
“St. Kliment Ohridski” University of Sofia
Sofia, Bulgaria
E-mail: gretageorgieva7@abv.bg

ASSESSMENT OF THE FUTURE CLIMATE OVER SOUTHEAST EUROPE BASED ON ENSEMBLE OF CLIMATE INDICES – PART ONE: CONCEPT AND METHODS

**Hristo Chervenkov¹, Vladimir Ivanov²,
Georgi Gadzhev², Kostadin Ganev²**

¹*National Institute of Meteorology and Hydrology (NIMH)*

²*National Institute of Geophysics, Geodesy and Geography –
Bulgarian Academy of Sciences (NIGGG-BAS)*

Abstract: Nowadays there is a strong degree of agreement that the climate change is the defining challenge of our time. The analysis based on climate indices is probably the most widely used non-parametric approach for quantification of extreme climate events. This study which consist of two parts, is dedicated on the assessment of the spatial patterns and the temporal evolution of 6 temperature-based and 3-precipitation based indices in projected future climate over south-east Europe up to the end of the century. The annual means of the daily mean and extreme temperatures are also analysed in consistent manner. The indices are computed from the bias-corrected output of 5 CMIP5 global models, forced with all 4 RCP emission scenarios. The multi model ensemble medians of the temperature-based indices shows considerable warming which is consistent with the increase of the mean temperatures and is statistically significant in most cases. The revealed changes of the precipitation-based indices are more complex when compared with temperature changes.

Keywords: climate indices, CMIP5 ensemble, RCPs, future climate, South-east Europe

INTRODUCTION

There is a strong degree of agreement that the climate change is the defining challenge of our time. It will exert influence on the ecosystems, on all branches of the international economy, and on the quality of life. The globally averaged surface temperature of the Earth increased 0.85°C over the 1880 to 2012 period. It is extremely likely that the observed warming of the climate system was caused by the increased anthropogenic emission of greenhouse gases (IPCC, 2013). However, immediate damages to humans and their properties as well as to ecosystems are not

obviously caused by gradual changes in temperature or precipitation but mainly by so-called extreme climate events (Sillmann & Röckner, 2007). The rare occurrence of extremes makes it necessary to investigate long data records to determine significant changes in their frequency and intensity. To this end, global circulation models (GCMs) or, more generally, coupled atmosphere-ocean general circulation models (CAOGCM) are physically consistent way to simulate past, present, and future climate states inclusive extreme events. Regional Climate Models (RCM) applied with higher spatial resolution over a limited area and driven by GCMs can provide more appropriate information on such smaller scales supporting more detailed impact and adaptation assessment and planning (Rummukainen, M., 2010; Belda et al., 2015; Giorgi & Gutowski, 2015). Therefore RCMs have an important role to play by providing projections with much greater detail and more accurate representation of localized extreme events (Gadzhev et al., 2021). The Working Group on Coupled Modelling (WGCM) established the Coupled Model Intercomparison Project (CMIP) as a standard experimental protocol for studying the output of CAOGCMs. CMIP provides a community-based infrastructure in support of climate model diagnosis, validation, intercomparison, documentation and data access (Taylor et al., 2009). The main aim of the fifth phase of CMIP, CMIP5, is to study the climate and climate change in the past, present and future, using a set of simulations with different climate simulators in various spatial and temporal scales (Taylor et al., 2012).

The Mediterranean region lies in a transition zone between the arid climate of North Africa and the temperate and rainy climate of central Europe and it is affected by interactions between mid-latitude and tropical processes. Because of these features, even relatively minor modifications of the general circulation, e.g. shifts in the location of mid-latitude storm tracks or sub-tropical high pressure cells, can lead to substantial changes in the Mediterranean climate (Giorgi & Lionello, 2008). In addition to planetary scale processes and teleconnections, the climate of the Mediterranean is affected by local processes induced by the complex physiography of the region and the presence of a large body of water (the Mediterranean Sea).

Several projects and, consequently, many studies are dedicated in the recent decades on the climate projections over Europe and the Mediterranean basin. The CMIP5 projections generally agree on warming in all seasons in Europe during this century, while precipitation projections are more variable across different parts of Europe and seasons (Belda et al., 2015). Despite of the overall agreement for general reduction of the precipitation amount in the middle and at the end of the 21st century, there are still many differences in the magnitude of the expected changes, annual and seasonal variability and areal distributions (Dai, 2013; Giorgi & Lionello, 2008; Orłowsky & Seneviratne, 2012; Ulbrich et al., 2006). Part of the problems could be attributed to the models deficiencies of the precipitation simulation. The model estimations includes also non-negligible uncertainties which results, in particular, in a less spatially coherent pattern of change, bigger inter-model spread and a lower lev-

el of statistical significance when compared with temperature changes (Alexander et al., 2006). In Sillmann et al. (2013a) is demonstrated that GCMs underestimate observed precipitation magnitudes, although CMIP5 models show an improvement compared to CMIP3. The results of Orłowsky & Seneviratne (2012) show that despite the uncertainty in other regions, droughts have increased in the Mediterranean and are projected to increase further, emphasizing the need for proactive adaptation planning. Central and Eastern Europe is a region where precipitation changes remain also still uncertain (Belda et al., 2015). Although regional climate change amplitudes of temperature and precipitation in Europe follow global trends, they can be also affected by changes in the large-scale circulation and regional feedback processes (Kjellstrom et al., 2011). In the comprehensive study of Stagge et al. (2015) is used of the RCMs outcome from CORDEX (the Coordinated Regional Climate Downscaling Experiment – see Kotlarski et al., 2014 for details), forced with CMIP5 climate projections, to quantify the projected change in meteorological drought for Europe during the 21th century, revealing increasing projected drought throughout the Mediterranean, including the eastern Mediterranean. In agreement with previous studies, in Sillmann & Röckner (2007) is evidenced a considerable intensification of heat and water stress in the region.

The free worldwide exchange of methods, software and especially data is from essential importance for the expert community of the geophysical sciences. Such services are provided either from the primary vendors (institutions, organisations or projects) or from single point access portals as the Copernicus Data Store (CDS). They are reliable source for elaboration of objective climatologies, both in regional (Birsan et al., 2014; Chervenkov et al., 2019; Chervenkov & Slavov, 2019; Spinoni et al., 2018) and global (Sillmann et al., 2013a, 2013b; Orłowsky & Seneviratne, 2012) scale for recent and projected future climate as well as for development of various custom-tailored applications. Our working group uses also this possibility in optimal way. The present article, which is the first part of more common work, describes shortly 5 collected and/or implemented by the authors data bases in our general effort to describe the historical, near past and recent as well as the projected future climate over south-east (SE) Europe most concisely and comprehensively.

The work is organized as follows. The CMIP5 scenarios and the used models are described in Section 1. Section 2 is dedicated on the used methods and the considered data bases. Section 3 and Section 4 are the core of the present study. Due to their importance, the first one, ‘Results for the mean temperatures’, is dedicated solely on these variables. In the second one are described the results for the other indices. The concluding remarks are in the last section.

1. CMIP5 SCENARIOS AND USED MODELS

The CMIP5 experiment uses new emission scenarios called representative concentration pathways (RCP) (Moss et al., 2010) to assess the interactions

between the human activities on the one hand and the environment on the other hand, and their evolution. Unlike the CMIP3 scenarios, the RCPs are mitigation scenarios that assume policy actions will be taken to achieve certain emission targets. For CMIP5, four RCPs have been formulated: RCP2.6, RCP4.5, RCP6.0 and RCP8.5. They are based on a range of projections of future population growth, technological development, and societal responses. The labels for the RCPs provide a rough estimate of the radiative forcing in the year 2100 (relative to pre-industrial conditions). RCP2.6 represents mitigation scenarios that aim to limit the increase of global mean temperature to $<2^{\circ}\text{C}$. Different than other RCPs and earlier CMIP3 scenarios, RCP2.6 has a peak in greenhouse gases (GHG) concentration around 2050 and then declines at a moderate rate. Under RCP4.5, GHG-emissions will peak around the early 2050s and then stabilize, causing a CO_2 equivalent of about 650 parts per million and a temperature increase of approximately $1.8\text{--}2.0^{\circ}\text{C}$ in 2100, compared to the control period of 1986–2005. RCP8.5, on the other hand, predicts a continuous rise of GHG emissions until 2100, causing a CO_2 equivalent larger than 1370 ppm and a global average temperature increase close to 4°C (Spinoni et al., 2018).

The CMIP3 and CMIP5 model output are available from the data archives of the Program for Climate Model Diagnosis and Intercomparison (PCMDI) and the Earth System Grid data distribution portal (ESG). To generate the considered in this study indices for historical and future time periods, bias-corrected climate datasets provided through Inter Sectoral Impact Model Intercomparison Project (ISIMIP 1), Fast Track simulation round have been used. For each simulation round a set of gridded bias-corrected climate variables have been produced to be used as input data for running impact models. These climate datasets contain daily-resolution, bias-corrected climate data from 5 CMIP5 GCMs according Table 1 covering the period 1950-2099 (historical run up to 2005), downscaled to a $0.5^{\circ}\times 0.5^{\circ}$ lat-lon grid. They cover the global land area.

Table 1. Main Features of the Considered Models

| Model Acronym | Institution | Spat. Resolution (Lon×Lat-Lev.) |
|----------------------|--------------------------------------------|----------------------------------------|
| GFDL-ESM2M | Geophysical Fluid Dynamics Laboratory, USA | 144×90L24 |
| HadGEM2-ES | Met Office Hadley Centre, UK | 192×145L40 |
| IPSL-CM5A-LR | Institut Pierre-Simon Laplace, France | 96×96L39 |
| MIROC-ESM-CHEM | AORI, NIES, JAMSTEC, Japan | 128×64L80(T42) |
| NorESM1-M | Norwegian Climate Centre, Norway | 144×96L26 |

Note that the models used in this study differ from the models in Chervenkov & Slavov (2020a, 2020b, 2021). ISIMIP offers significantly fewer models, than the

applied in Sillmann et al. (2013b) and Orłowsky & Seneviratne (2012) but these studies considers only CMIP5 RCP2.6, RCP4.5 and RCP8.5 (i.e. not RCP6.0) and CMIP3 SRES A2 scenario, correspondingly.

2. METHODS

There are various methods to characterize extreme events, but the computation and analysis of climate indices (CIs) based on daily temperature and precipitation data is probably the most widely used non-parametric approach (Sillmann & Röckner, 2007). The modern sets of such indices, among which the most widely used is the collection of the Expert Team on Climate Change Detection and Indices (ETCCDI, Zhang et al., 2011), are statistically robust, cover a wide range of climate conditions, and have a high signal-to-noise ratio (Alexander & Arblaster, 2009). They are used in several projects on climate change with focus on different spatial scales, from planetary to continental, regional, national or local scale, as prevailing indicators of changes of the extreme events (Birsan et al., 2014). Subsequently, the number of publications on this topic is very large (Alexander et al., 2006; Frich et al., 2002; Kiktev et al., 2003; Klein Tank & Können, 2003; Moberg et al., 2006 and many others). Our group has also previous, partially project-driven, experience in CI-based analysis of historical (Chervenkov & Slavov 2020a, 2020b), near past and present (Chervenkov et al., 2019; Chervenkov & Slavov, 2019; Chervenkov & Slavov, 2021; Malcheva et al., 2016) and projected future regional climate (Gadzhev et al., 2021). The free availability of databases of CIs or other climate indicators, with focus on different spatial and temporal scales, facilitates any assessment which includes these parameters. In Table 2 are listed the main features of some gridded databases recently used in our group. It is worth to emphasize that the information from these sources is rarely suitable for direct implementation in the tasks of the regional climatology. Thus, the data from these sources have to be essentially post-processed in order to fit to the specific needs.

The present study is based entirely on the data from ISIMIP Fast Track. Although this project is intended to be a collection of agroclimatic indicators datasets, most of the indices in scope, inclusive all considered in this study, are based on the ETCCDI definitions which makes them universal. Agricultural indicators in ISIMIP Fast Track have been pre-calculated for this complete matrix of 5 GCMs×4 RCPs combinations. In addition, as a proxy for historical observations, the “Watch Forcing Data methodology applied to ERA-Interim (WFDEI)” (Weedon et al., 2014) were used to generate observational historical Agroclimatic indicators. This dataset is available at the same spatial resolution of ISIMIP climate datasets, covers the time range of 1979 to 2013 and its 30 year long part 1981-2010 is used in the study as reference for the current climate.

Table 2. Mean Features of the Used Data Bases

| Acronym | Main Content | Spat. Coverage/ Resolution | Time Span, Scenario(s) | Institution | Basic Reference/ Access |
|-------------------|-----------------------------------------------------------------------------------------------------------------------|---------------------------------------------------------|----------------------------------------------------------|-------------------------------------------------|------------------------------------------------------------------------------------------------------------------------------------------------------|
| SPI DB | 4 data sets of SPI-1, SPI-3, SPI-6, SPI12 based on UDEL/ GEOG/CCR v3.02, GPCP v7.0, NOAA-CIRES 20CR v2c, ECMWF ERA20C | Global, 0.5°×0.5°; 1.5°×1.5° | 1900-2010, 1901-2013, 1851-2011, 1900-2010 | NIMH, Bulgaria | Chervenkov et al. (2016); ftp://xeo.cfd.meteo.bg/SPI/ |
| CECILIA DB | 152 CI based on RCMs | Central&SE Europe, 0.1°×0.1° | 1961-1990 2021-2050 2071-2100 SRES A1B | CECILIA project | Belda et al. (2015); http://cecilia.dmi.dk |
| ClimData | STARDEX&ETCCDI Cis based on E-OBS &CARPATCLIM | E-OBS& CARPATCLIM domains; 0.25°×0.25°, 0.1°×0.1° | 1951-2016 1961-2010 | NIMH, Bulgaria | Chervenkov et al. (2019); https://repo.vi-seem.eu/handle/21.15102/ VISEEM-343 . |
| EIA | ETCCDI Cis based on CMIP5-GCMs | Global, varios res. | 1850-2100; CMIP5 RCP2.6, RCP4.5,RCP8.5 | Canadian Centre for Climate Modelling& Analysis | Sillmann et al. (2013a); http://www.cccma.ec.gc.ca/data/climdex/climdex.shtml |
| ISIMIP Fast Track | 26 Cis based on CMIP5-GCMs | Global, 0.5°×0.5° | 1951-2099; CMIP5 RCP2.6, RCP4.5, RCP6.0, RCP8.5 | ISIMIP 1 | CDS documentation; https://www.isimip.org/protocol/ |

After the download from the CDS the ISIMIP-datasets are significantly post-processed. The most essential stages are:

- The datasets for each model and RCP which are downloadable in 30-years time slices are merged in common data streams for 2011-2099
- The indices with equal temporal resolution are joined in common netCDF4 files
- Multi-model (MM) ensemble quantities as multi-model mean (MMM), MM 25-, 50- and 75-percentile which are often refereed as lower quartile, median and upper quartile and traditionally noted as X25, X50 and X75 are computed.
- Due to storage constrains only a spatial subset over Europe is preserved.

All netCDF manipulations are performed with the powerful tool Climate Data Operators (cdo). Additionally, for the current study only, all of the considered indices are aggregated in time on annual basis. The aggregation method depend on the indicator, e.g. min, max, sum, mean. The magnitude of the trend in time as well as its statistical significance are estimated individually for all grid cells and separately for each scenario by means of the Theil-Sen slope estimator (TSE) and the Mann-

Kendall (MK) test correspondingly. Thus far, the study is constrained over SE Europe only as will be shown in the next section and with details in the next part.

3. RESULTS FOR THE MEAN TEMPERATURES

The annual means of the daily minimum, mean and maximum temperature (noted traditionally TN, TG and TX) are important variables, providing information on the current state as well as on the long-term climate variability and change and thus are studied separately from the other considered indices. We analyse the spatial patterns of the multiyear means of the CMIP5 projections of TN, TG and TX as well as the spatial patterns for the reference period. In order to intercompare them, the ensemble median (MMX50) of the listed in Table 1 models for all 4 scenarios is superimposed to the median for the reference period, as shown on Fig. 1.

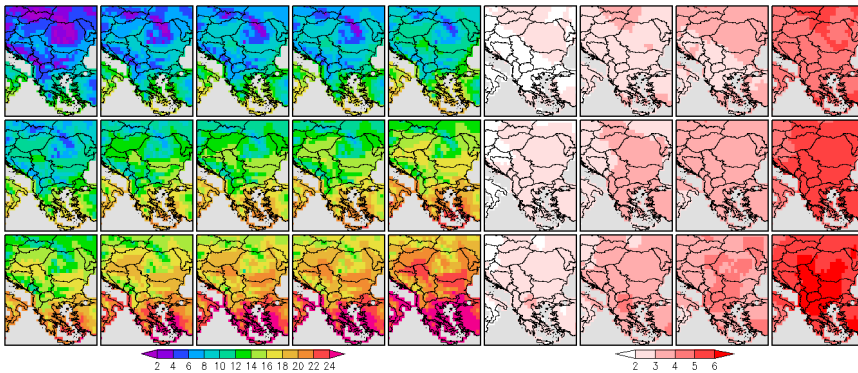


Figure 1. MMX50 of the multiyear means of the TN (first row) TG (second row) and TX (third row) for the reference period (1981-2010) in the first column and multiyear means for 2070-2099 for RCP2.6, RCP4.5, RCP6.0 and RCP8.5 in the second, third, fourth and fifth column correspondingly. The absolute changes of the RCP2.6, RCP4.5, RCP6.0 and RCP8.5 relative to the reference period are shown in the sixth seventh eighth and ninth column correspondingly. The units are °C.

Figure 1 shows for all variables gradual increase of the projected changes from RCP2.6 to RCP8.5, i.e. proportional to the radiative forcing. The changes are similar in magnitude for all parameters for fixed scenario RCP2.6-RCP6.0 and have not clear spatial structure. For RCP8.5 the changes for TG and TX are exceeding 6°C and are somewhat bigger than the changes for TN. All changes are statistically significant at the 5% level.

The area-weighted regional averages over land of TN, TG and TX are shown on Figure 2.

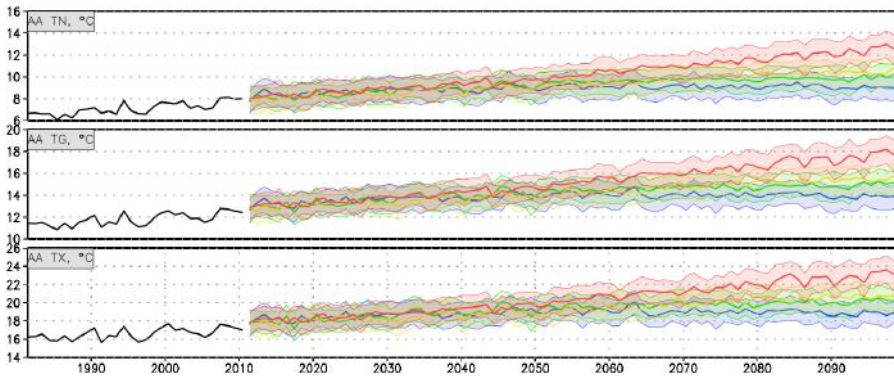


Figure 2. Area-weighted regional averages (index and unit according subplot title) for the reference (solid black line) and simulated by the CMIP5 ensemble for the RCP2.6 (blue), RCP4.5 (green), RCP6.0 (yellow) and RCP8.5 (red). Solid lines indicate the ensemble median (i.e. the 50th quantile) and the shading, respectively the thin lines, indicates the interquartile ensemble spread (25th and 75th quantiles).

Figure 2 shows relatively smooth (in comparison with the other Ci's as will be shown further) but steady increase of the temperatures with apparent difference between scenarios in the second half of the century.

The importance of assessing trends in climate extremes is often emphasized (e.g. Klein Tank & Können, 2003; Meehl et al., 2000; Moberg et al., 2006). The

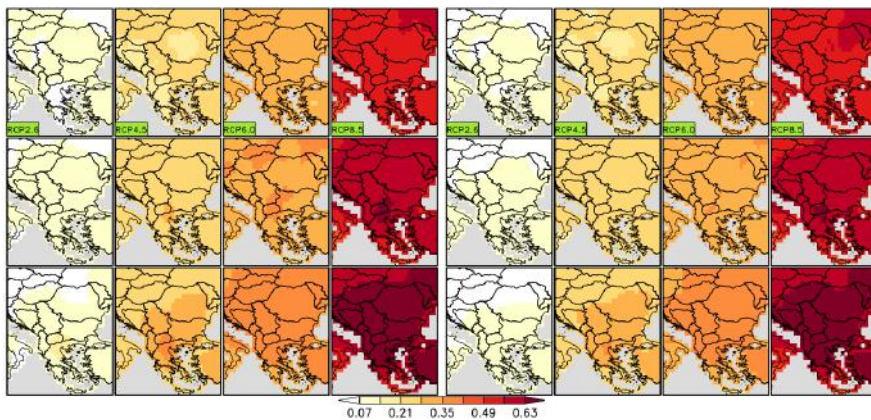


Figure 3. Trend slopes (unit: °C/10 years) of the TN (first row) TG (second row) and TX (third row) of the MMM (left pane) and MMX50 (right pane) for the scenarios according the subtitles in the first row.

main reason is that extreme weather conditions related to temperature, precipitation, storms or other aspects of climate, can cause loss of life, severe damage and large economic and societal losses. Thus, the trend assessment is essential part of the recent climate studies (Alexander et al., 2006; Frich et al., 2002; Sillmann et al., 2013b; and many others). Figure 3 shows the slope of the estimated by means of TSE linear trend of the MMM and MMX50 of the TN, TG and TX for the whole future period 2011-2099.

The most apparent result of analysis of Figure 3 is that the fields of the slopes for MMM and MMX50 are practically identical for each corresponding variable and scenario. As expected, the lowest values are for the scenario with the modest forcing (RCP2.6) and the highest – for the scenario with the strongest forcing (RCP8.5).

CONCLUSION TO PART ONE

The referenced in Table 2 projects and initiatives contributes to the availability of a valuable sets of spatially and temporally representative data to prepare relevant climate change studies in the corresponding domains. These datasets are reliable sources of various climate indicators, which can be presented as continuous, both in space and time, digital maps. The positive consequences to the end user community in exploration of the single point access data portal Copernicus Climate Data Store are manifold, but the free access of data sets standardised file formats via unified transfer protocols seems most significant.

Relevant outcome of the presented part one of the study, is the clearly expressed warming signal in the field of the mean temperatures. It is spatially dominating over the domain and everywhere statistically significant. The amount of warming by scenario generally ranges from high to low as follows: RCP8.5, RCP6.0, RCP4.5 and RCP2.6 which shows principal proportion of the temperature increase to the radiative forcing.

Part two of this study is dedicated on the analysis of the spatial patterns and the time evolution of the other considered indices.

ACKNOWLEDGMENTS

The authors thank the anonymous reviewers for their insightful suggestions. This work has been carried out in the framework of the National Science Program "Environmental Protection and Reduction of Risks of Adverse Events and Natural Disasters", approved by the Resolution of the Council of Ministers № 577/17.08.2018 and supported by the Ministry of Education and Science (MES) of Bulgaria (Agreement № Д01-322/18.12.2019).

This work has been accomplished with the financial support by the Grant No BG05M2OP001-1.001-0003, financed by the Science and Education for Smart Growth Operational Program (2014-2020) and co-financed by the European Union through the European structural and Investment funds.

REFERENCES

- Alexander, L. V., et al. (2006) Global observed changes in daily climate extremes of temperature and precipitation, *J. Geophys. Res.*, 111, D05109, doi:10.1029/2005JD006290
- Alexander, L. V. and Arblaster, J. M. (2009) Assessing trends in observed and modelled climate extremes over Australia in relation to future projections. *Int. J. Climatol.*, 29: 417-435. doi:10.1002/joc.1730
- Belda, M., Skalák, P., Farda, A., et al. (2015) CECILIA Regional Climate Simulations for Future Climate: Analysis of Climate Change Signal, *Advances in Meteorology*, vol. 2015, Article ID 354727, 13 pages, 2015 doi:10.1155/2015/354727
- Birsan, M. V., Dumitrescu, A., Micu, D.M., Cheval, S. (2014) Changes in annual temperature extremes in the carpathians since AD 1961. *Natural Hazards* 74(3), 1899-1910 doi:10.1007/s11069-014-1290-5
- Chervenkov, H., Tsonesky, I., Slavov, K. (2016) Presentation of Four Centennial-long Global Gridded Datasets of the Standardized Precipitation Index, *International Journal of Environmental & Agriculture Research (IJOEAR)* ISSN: 2454-1850 Vol. 2, Issue-3, March-2016 pp. 93-105
- Chervenkov, H., Slavov, K., Ivanov, V., (2019) STARDEX and ETCCDI Climate Indices Based on E-OBS and CARPATCLIM; Part One: General Description, in G. Nikolov et al. (Eds.): NMA 2018, LNCS 11189, pp. 360-367, doi: 10.1007/978-3-030-10692-8_40
- Chervenkov, H., Slavov, K. (2019) STARDEX and ETCCDI Climate Indices Based on E-OBS and CARPATCLIM; Part Two: ClimData in Use, in G. Nikolov et al. (Eds.): NMA 2018, LNCS 11189, 368-374, (2019) DOI: 10.1007/978-3-030-10692-8_41
- Chervenkov, H. Slavov, K. (2020a) Historical Climate Assessment of Temperature-based ETCCDI Climate Indices Derived from CMIP5 Simulations, *Compt. rend. Acad. bulg. Sci.*, 73, No 6, 784-790, DOI: 10.7546/CRABS.2020.06.05
- Chervenkov, H. Slavov, K. (2020b) Historical Climate Assessment of Precipitation-based ETCCDI Climate Indices Derived from CMIP5 Simulations, *Compt. rend. Acad. bulg. Sci.*, 73, No 7, 942-948, DOI: 10.7546/CRABS.2020.07.06
- Chervenkov H., Slavov K. (2021) ETCCDI Climate Indices for Assessment of the Recent Climate over Southeast Europe. In: Dimov I., Fidanova S. (eds) *Advances in High Performance Computing. HPC 2019. Studies in Computational Intelligence*, vol 902. Springer, Cham. doi: 10.1007/978-3-030-55347-0_34
- Dai, A., (2013) Increasing drought under global warming in observations and models, *Nature Clim. Change*, 3: 52-58

- Frich, P., Alexander, L.V., Della-Marta, P.M., Gleason, B.E., Haylock, M.R., Tank, A.M., & Peterson, T.C. (2002). Observed coherent changes in climatic extremes during the second half of the twentieth century., *Climate Research*, Vol. 19, No. 3, pp. 193-212, doi:10.3354/cr019193
- Gadzhev G., Ivanov V., Valcheva R., Ganev K., Chervenkov H. (2021) HPC Simulations of the Present and Projected Future Climate of the Balkan Region. In: Dimov I., Fidanova S. (eds) *Advances in High Performance Computing. HPC 2019. Studies in Computational Intelligence*, vol 902. Springer, Cham. doi: 10.1007/978-3-030-55347-0_20
- Giorgi, F., Gutowski, W. J. Jr. (2015) Regional Dynamical Downscaling and the CORDEX Initiative, *Annu. Rev. Environ. Resour.* 2015. 40:467-490
- Giorgi, F., Lionello, P. (2008) Climate change projections for the Mediterranean region, *Global and Planetary Change*, 63(2-3): 90-104
- IPCC (Intergovernmental Panel on Climate Change), 2013: The physical science basis. In (eds: Stocker, T.F., Qin, D., Plattner, G-K., Tignor, M., Allen, S.K., Boschung, J., Nauels, A., Xia, Y., Bex, V., Midgley, P.M.,) *Contribution of Working Group I to the Fifth Assessment Report of the Intergovernmental Panel on Climate Change*. Cambridge University Press, Cambridge.
- Kiktev, D., Sexton, D. M. H. Alexander, L., Folland, C. K. (2003) Comparison of Modeled and Observed Trends in Indices of Daily Climate Extremes, *Journal of Climate*, Vol. 16, No. 22, pp. 3560-3571 doi:10.1175/1520-0442(2003)016%3C3560:COMAOT%3E2.0.CO;2
- Kjellstrom, E., Nikulin, G., Hansson, U., Strandberg, G., Ullerstig, A. (2011) 21st century changes in the European climate: uncertainties derived from an ensemble of regional climate model simulations, *Tellus, Series A: Dynamic Meteorology and Oceanography*, vol. 63 No.1 pp24-40
- Klein Tank, A.M. and G.P. Können, (2003) Trends in Indices of Daily Temperature and Precipitation Extremes in Europe, 1946-99. *J. Climate*, vol. 16, 3665-3680, doi: 10.1175/1520-0442(2003)016<3665:TIHODT>2.0.CO;2
- Kotlarski, S., Keuler, O. B. Christensen, A. Colette, M. Dèquè, A. Gobiet, K. Goergen, D. Jacob, D. Lüthi, E. van Meijgaard, G. Nikulin, C. Schär, C. Teichmann, R. Vautard, K. Warrach-Sagi, and V. Wulfmeyer (2014) Regional climate modeling on European scales: a joint standard evaluation of the EURO-CORDEX RCM ensemble. *Geosci. Model Dev.*, 7, 1297-1333 doi:10.5194/gmd-7-1297-2014
- Malcheva, K., Chervenkov, H., Marinova, T., (2016) Winter Severity Assessment on the Basis of Measured and Reanalysis data. In: 16th International Multidisciplinary Scientific GeoConference SGEM 2016. SGEM, pp. 719-726

- Meehl, G. A., Zwiers, F., Evans, J., Knutson, T., Mearns, L., & Whetton, P. (2000). Trends in extreme weather and climate events: Issues related to modeling extremes in projections of future climate change. *Bulletin of the American Meteorological Society*, 81(3), 427-436. doi:10.1175/1520-0477(2000)081<0427:TIEWAC>2.3.CO;2
- Moberg, A., et al. (2006) Indices for daily temperature and precipitation extremes in Europe analyzed for the period 1901–2000, *J. Geophys. Res.*, 111, D22106, doi:10.1029/2006JD007103.
- Moss, R. H. et al. (2010) The next generation of scenarios for climate change research and assessment, *Nature*, Vol. 463, No. 7282, 747-756, doi:10.1038/nature08823
- Orlowsky, B. and Seneviratne, S. I. (2012) Elusive drought: uncertainty in observed trends and short- and long-term CMIP5 projections, *Hydrol. Earth Syst. Sci.* 17(5):1765-1781 doi:10.3929/ethz-b-000073994.
- Rummukainen, M. (2010) State-of-the-art with regional climate models. *WIREs: Clim. Change* 1:82-96
- Sillmann, J., Röckner, E., (2007) Indices for extreme events in projections of anthropogenic climate change. *Climatic Change* 86 (1-2), pp. 83-104.
- Sillmann, J., V. V. Kharin, X. Zhang, F. W. Zwiers, and D. Bronaugh (2013a) Climate extremes indices in the CMIP5 multimodel ensemble: Part 1. Model evaluation in the present climate, *J. Geophys. Res. Atmos.*, 118, pp. 1716-1733, doi: 10.1002/jgrd.50203
- Sillmann, J., V. V. Kharin, F. W. Zwiers, X. Zhang, and D. Bronaugh (2013b) Climate extremes indices in the CMIP5 multimodel ensemble: Part 2. Future climate projections, *J. Geophys. Res. Atmos.*, 118, pp. 2473-2493 doi: 10.1002/jgrd.50188.
- Spinoni, J., Vogt, J.V., Barbosa, P., Dosio, A., McCormick, N., Bigano, A. and Füssel, H.-M., (2018) Changes of heating and cooling degree-days in Europe from 1981 to 2100. *Int. J. Climatol*, 38: e191-e208. doi:10.1002/joc.5362
- Stagge, J.H., Rizzi, J., Tallaksen, L. M., and Stahl, K. (2015) Future meteorological drought: projections of regional climate models for Europe, Technical Report No. 25, Future Meteorological Drought Projections of Regional Climate, DROUGHT-RSPI Project, University of Oslo, Oslo, 23 pp.
- Taylor, K. E., Stouffer, R. J., Meehl, G. A. (2009) A summary of the CMIP5 experiment design, PCDMI Rep., 33 pp., 2009 [Available online at http://cmip-pcmdi.llnl.gov/cmip5/docs/Taylor_CMIP5_design.pdf.]
- Taylor, K. E., Stouffer, R. J., Meehl, G. A., (2012) An Overview of CMIP5 and the Experiment Design *Bull. Amer. Meteor. Soc.*, 93, 485-498, 2012 doi:10.1175/BAMS-D-11-00094.1

- Ulbrich, U., et al., (2006) The Mediterranean climate change under global warming. In: Lionello, P., Malanotte-Rizzoli, P., Boscolo, R. (Eds.), R. (Eds.), *Mediterranean Climate Variability*. Elsevier, Amsterdam, pp. 398-415.
- Weedon, G.P., Balsamo, G., Bellouin, N., Gomes, S., Best, M.J. and Viterbo, P., (2014) The WFDEI meteorological forcing data set: WATCH Forcing Data methodology applied to ERA-Interim reanalysis data. *Water Resources Research*, 50(9), pp.7505-7514.
- Zhang, X., Alexander, L., Hegerl, G.C., Jones, P., Tank, A.K., Peterson, T.C., Trewin, B. and Zwiers, F.W. (2011), Indices for monitoring changes in extremes based on daily temperature and precipitation data. *WIREs Clim Change*, 2: 851-870. doi:10.1002/wcc.147

✉ **Hristo Chervenkov**

<http://orcid.org/0000-0002-7658-3041>
National Institute of Meteorology and Hydrology
Sofia, Bulgaria
E-mail: hristo.tchervenkov@meteo.bg

✉ **Vladimir Ivanov**

<https://orcid.org/0000-0001-9768-1049>
National Institute of Geophysics, Geodesy and Geography
Bulgarian Academy of Sciences
Sofia, Bulgaria
E-mail: vivanov@geophys.bas.bg

✉ **Georgi Gadzhev**

<http://orcid.org/0000-0002-6159-3554>
National Institute of Geophysics, Geodesy and Geography
Bulgarian Academy of Sciences
Sofia, Bulgaria
E-mail: ggadzhev@geophys.bas.bg

✉ **Kostadin Ganey**

National Institute of Geophysics, Geodesy and Geography
Bulgarian Academy of Sciences
Sofia, Bulgaria
E-mail: kganey@geophys.bas.bg

ASSESSMENT OF THE FUTURE CLIMATE OVER SOUTHEAST EUROPE BASED ON ENSEMBLE OF CLIMATE INDICES – PART TWO: RESULTS AND DISCUSSION

**Hristo Chervenkov¹, Vladimir Ivanov²,
Georgi Gadzhev², Kostadin Ganev²**

¹*National Institute of Meteorology and Hydrology (NIMH)*

²*National Institute of Geophysics, Geodesy and Geography –
Bulgarian Academy of Sciences (NIGGG-BAS)*

Abstract: Nowadays there is a strong degree of agreement that the climate change is the defining challenge of our time. The analysis based on climate indices is probably the most widely used non-parametric approach for quantification of extreme climate events. This study which consist of two parts, is dedicated on the assessment of the spatial patterns and the temporal evolution of 6 temperature-based and 3-precipitation based indices in projected future climate over south-east Europe up to the end of the century. The annual means of the daily mean and extreme temperatures are also analysed in consistent manner. The indices are computed from the bias-corrected output of 5 CMIP5 global models, forced with all 4 RCP emission scenarios. The multi model ensemble medians of the temperature-based indices shows considerable warming which is consistent with the increase of the mean temperatures and is statistically significant in most cases. The revealed changes of the precipitation-based indices are more complex when compared with temperature changes.

Keywords: climate indices, CMIP5 ensemble, RCPs, future climate, South-east Europe

INTRODUCTION TO PART TWO

This part is dedicated on the analysis of the considered indices except the mean temperatures. The study is continuation of our scientific work, documented in suite of publications (Chervenkov et al., 2019; Chervenkov & Slavov, 2019, 2020a, 2020b, 2020c, 2021) which first part is described in Chervenkov et al., (2021). As in Chervenkov & Slavov, (2021), the present study is inspired from the comprehensive study of Sillman et al., (2013b) and fits in the same conceptual framework. Beside the different models, considered indices and significantly finer

grid spacing, this study differs, however, from Chervenkov & Slavov (2021) in other two substantial aspects: first and foremost, the input data (i.e. daily temperatures and precipitation sums) are bias-corrected, as described by Hempel et al., (2013), prior the computation of the indices. Although some criticism exists, the general view in the expert community is that the bias-corrected climate change signal is more reliable compared with the uncorrected one and thus is more suitable for impact assessments (Chervenkov & Spiridonov 2020, 2021). Second, the study is focused on the multi-model statistics (mean, MMX25, MMX50, MMX75) rather than the simulation output of the individual models. This is modern common approach, adopted in many recent studies (Orlowsky & Seneviratne, 2012; Sillman et al., 2013a, 2013b).

4. RESULTS

4.1. TEMPERATURE INDICES

4.1.1. ABSOLUTE AND THRESHOLD INDICES

We start our analysis with a comparison of the spatial patterns of the multiyear means of the CMIP5 projections of the extreme temperatures, TNn and TXx with their counterparts for the reference period. In order to intercompare them, the ensemble median (MMX50) for all 4 scenarios is superimposed to the median for the reference period, as shown on Fig. 1. for the annual extreme temperatures

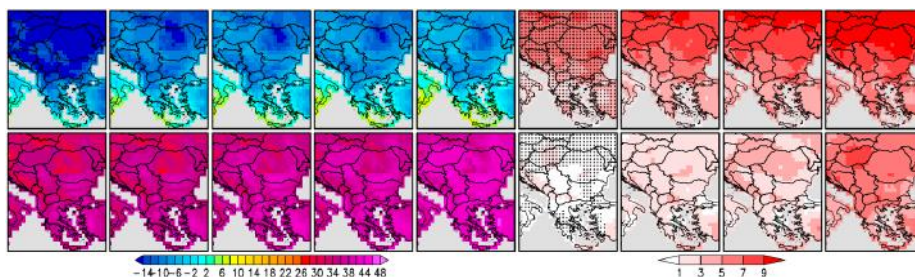


Figure 1. MMX50 of the multiyear means of the TNn (first row) and TXx (second row) for the reference period (1981-2010) in the first column and multiyear means for 2070-2099 for RCP2.6, RCP4.5, RCP6.0 and RCP8.5 in the second, third, fourth and fifth column correspondingly. The absolute changes of the RCP2.6, RCP4.5, RCP6.0 and RCP8.5 relative to the reference period are shown in the sixth seventh eighth and ninth column correspondingly.

Stippling indicates grid points with changes that are not significant at the 5% significance level. The units are °C.

Figure 1 shows gradual increase of the projected changes of the both indices from RCP2.6 to RCP8.5, i.e. proportional to the radiative forcing. The greatest

changes in TNn, exceeding 9°C, are simulated in RCP8.5 over the northern half of the domain. The most apparent difference between the spatial patterns of the changes of the TNn and TXx is the stronger temperature increase for TNn. This difference is well expressed for all four scenarios. Alexander et al., (2006) documents analysis of global data base of historical records, revealing such asymmetric warming. According to their global study (for data since 1951), changes in daily maximum temperatures are less marked, implying that our world in many places has become less cold rather than hotter. Other studies, however, based solely on assimilated European data (see Moberg et al., 2006 and references therein) suggest that this conclusion is not representative for Europe if the entire twentieth century is considered. An overall warming is observed also in Moberg et al., (2006), but they find only a small difference, or no difference at all, between average trends in daily minimum and maximum temperatures when they average trends for 75 stations across Europe. According to the future in the CMIP5 projections, Sillmann et al., (2013b) outlines the differences in the changes of the daily extreme temperatures. In particular, TNn increases more strongly in higher latitudes of the Northern Hemisphere. It is worth to emphasize also that our previous study Chervenkov & Slavov (2021), which is conceptually similar to the present one as underlined above, do not detects clear enough and rigour evidences for 'warming asymmetry' between the indices, based on the minimum temperature from the one hand and these, based on maximum temperature, from the other hand.

The widely used threshold indices tropical nights (TR) and frost days (FD), both based on the daily minimum temperature, have limited applicability over the domain. In the climatological study of the Carpathian region Birsan et al., (2014) is stated that the changes in the occurrence of TR are substantial only in low-elevation areas (below 800 m.), located outside the Carpathian Mountains range, which are particularly exposed to persistent and intense warm spells in summer. Generally, TR are not characteristic to the climate of the mountain regions, which are significant

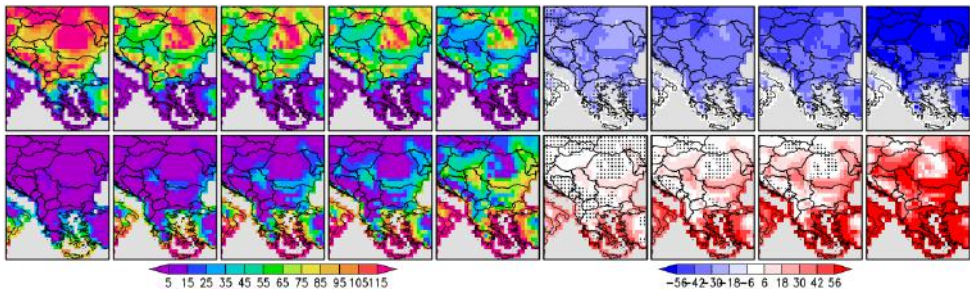


Figure 2. Same as Figure 1 but for the FD (first row) and TR (second row). The units are days.

part of the domain. Similarly, the FD are not very meaningful for maritime climate – this is valid for the southern half of the model region and especially for the areas along the fragmented coastline. Nevertheless, at least for methodological reasons, analysis of these indices have to be performed as shown on Figure 2 in the case for their spatial patterns.

Consistent with the changes of the minimum temperature, the fields of the threshold indices shows progressive (i.e. from RCP2.6 to RCP8.5) decrease of FD and, contrary to FD, increase of the TR. The vertical gradient of the FD is well expressed especially along the main Carpathian ridge. The increase of the TR under RCP2.6, RCP4.5 even RCP6.0 is, over the bigger part of the domain, relatively small and, which is more important, statistically not significant.

The area-weighted regional averages over land of TNn, TXx, FD and TR, which will be called area-averages (AA) for sake of brevity henceforth, are shown on Figure 3.

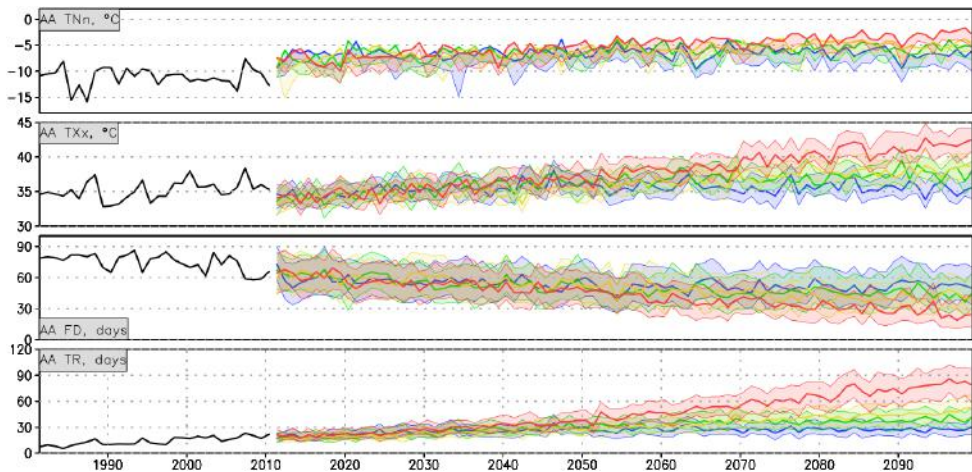


Figure 3. AA of the considered absolute and threshold indices (index and unit according subplot title) for the reference (solid black line) and simulated by the CMIP5 ensemble for the RCP2.6 (blue), RCP4.5 (green), RCP6.0 (yellow) and RCP8.5 (red). Solid lines indicate the ensemble median (i.e. the 50th quantile) and the shading, respectively the thin lines, indicates the interquartile ensemble spread (25th and 75th quantiles).

The overall tendencies, commented above, are markedly expressed for AAs of all indices. In the recent study Chervenkov & Slavov, (2020a), among other problems, are analysed the trends of five temperature-based indices, including TNn and TXx. The trend estimation of the AAs over the domain is based on the gridded

data base of the HadEX2 project and is for the period 1900-2010. The study reveals statistically significant increasing trend for the both parameters with bigger lapse for TNn. These conclusions agrees with the present results, suggesting that the projected changes are natural continuation of the already detected changes in the near past and present climate. The analysis of Figure 3 shows also that the CMIP5 interquartile model spreads in the four RCPs practicality remain overlapping for TXx, FD and TR until the middle and for TNn until the end of the 21st century.

4.1.2. DURATION AND PERCENTILE INDICES

The Cold and Warm Spell Duration Indices (CSDI & WSDI) are most frequently used indicators for cold and heat waves respectively (Alexander et al., 2006; Alexander & Arblaster, 2009; Sillmann &, Röckner, 2007 and many others) inclusive in climatological studies of the considered region (Birsan et al., 2014). Hence these indices are calculated using a percentile based, rather than fixed value, threshold, they could be also considered as percentile indices. The spatial patterns of the CSDI and WSDI for the control period as well as for the projected with the CMIP5 future are shown on Figure 4.

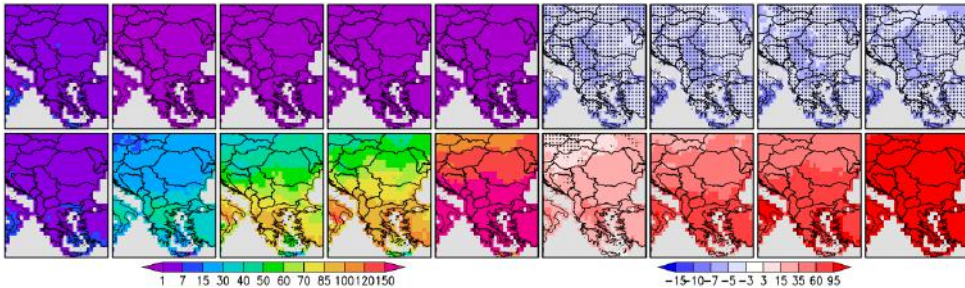


Figure 4. Same as Figure 1 but for the CSDI (first row) and WSDI (second row). The units are days.

Regarding the CSDI, the most obvious result on Figure 4 is that the small on magnitude and uniformly distributed during the reference period index practically disappears in the future even under the scenario with the weakest radiative forcing (RCP2.6). Subsequently, CSDI remains near zero constant under the other three scenarios. The change of the WSDI is very expressive both in magnitude and spatial extent. The differences from RCP to RCP are significant, especially for RCP8.5 compared with others. The absolute increase of WSDI relative to the reference is drastic: more than three months practically over the whole domain. This result, rather embarrassing indeed, is in principal agreement with Sillmann et al., (2013b).

The temporal evolution of the considered duration indices is depicted on Figure 5.

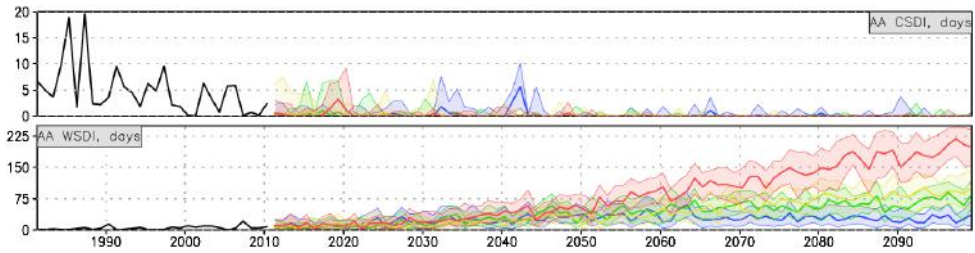


Figure 5. Same as Figure 2 but for the CSDI (first row) and WSDI (second row). The units are days.

Figure 5 confirms the outcomes from the analysis of the spatial patterns of the CSDI and WSDI. Interesting specifics of the dynamics of the AA of the CSDI is considerable changes in both directions for relatively short time during the reference period. This is consequence of single abnormally hot and cold years in this time span documented also in Birsan et al., (2014). The AA of the WSDI during the whole reference period remains with practically negligible values almost constant. In contrast, the dynamics in the projected future demonstrates steady increase, especially for RCP8.5. Consequently, the ensemble median for this scenario is over 150 days around the 2080's.

4.2. PRECIPITATION INDICES

As in many other places of the world, in contrast to the projected changes in the temperature indices, where there is a general agreement on the sign of change independent of the region considered, changes in the precipitation indices over the considered region are less consistent in this regard Sillmann et al., (2013b), Chervenkov et al., (2021).

Our analysis is focused on the indices Annual Precipitation Sum, Heavy Precipitation Days and Consecutive Dry Days, noted RR, RR10mm and CDD correspondingly. These indices are used as key parameters in many studies of present (for example Sillmann and Röckner, 2007) and projected future climate (see Sillmann et al., 2013b and citation therein).

Figure 6 provides a more detailed regional picture of the spatial patterns of the considered precipitation indices for the control period as well as for the future projections. Traditionally, the changes in precipitation sum RR relative to the 1981-2010 reference period are expressed in percentage terms.

First and foremost, Figure 6 demonstrates the complex nature of the expected precipitation changes. Although the total precipitation amount (the first row on Figure 6) shows clear reduction tendency, especially over the southeastern part of the domain, there is no big difference, both in magnitude and spatial distributions, in the relative changes in the scenarios RCP2.6-RCP6.0. Second, which

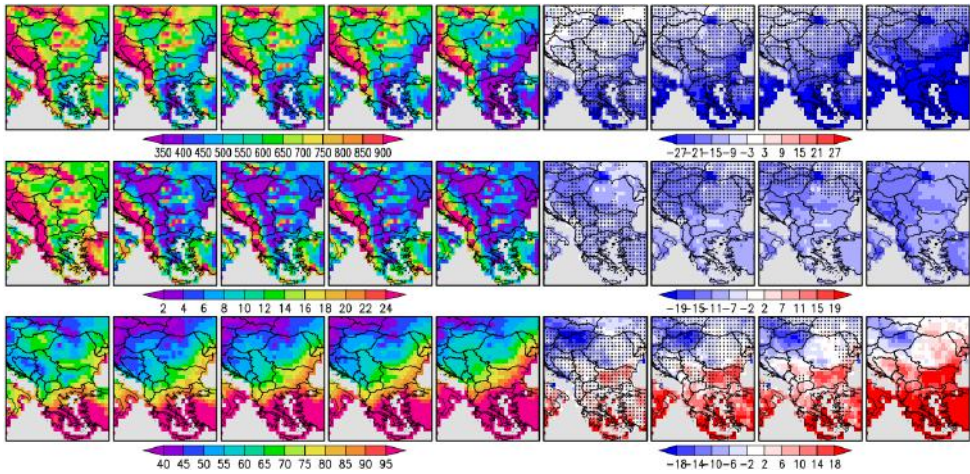


Figure 6. Same as Figure 1 but for the RR (first row), RR10mm (second row) and CDD (third row). Relative instead of absolute changes of the RR are considered. The units of the RR are mm and of the RR10mm and CDD as well as their changes – days. The relative changes of the RR are expressed in %.

is most important, these changes are not statistically significant at the 5% level. This result agrees with Sillmann et al., (2013b). Similar is the overall picture with the days with heavy rain distribution: general reduction, approximately up to a week over the bigger part of the domain, but without substantial difference from scenario to scenario and without statistical significance over wide areas for all RCPs, except RCP8.5. It is notable that this result is somewhat different that the outcomes in Sillmann et al. (2013b): there is shown a small (generally 2-4 days) increase of R10mm over the Balkan Peninsula for all scenarios except RCP8.5 and decrease in the latter of about 2-4 days. It have to be emphasized, however, that in this study is noted that the models disagree even on the sign of change in the total precipitation and R10mm over the Mediterranean. Our recent experiments with the RCM RegCM driven by the GCM HadGEM2-ES (Gadzhev et al., 2021) shows prevailing positive change (i.e. increase) for all seasons except for the summer and on an annual basis. The projected increase is roughly 25–35% for RCP2.6 and 35–45% for RCP8.5. The expected precipitation reduction in the summer reaches values of 35–45% for RCP8.5 over Bulgaria and Romania.

The spatial patterns of the CDD, both in the present and projected future climate is also complex. Most apparent is the well expressed gradient form southeast to northwest. The contrary tendencies in the future, increase of the CDD in southeast and decrease in northwest will leads to strengthening of this contrast. The analysis,

performed in Malcheva et al., (2016) which is based on historical records and on the climate reanalysis ERA20C, outlines the drying tendency over SE Bulgaria and the neighboring territories in Greece and Turkey. In Sillmann et al., (2013b) is noted that in the Mediterranean, the increases in CDD are accompanied by increases in the index R95p (very wet days, not considered in the present study) suggesting that dry spells in these regions become longer, but that precipitation may be more extreme when it occurs. Our previous analysis, based on HadEX2 (Chervenkov & Slavov, 2020a), demonstrates also simultaneous increase of the AAs of the CDD and R95p. It have to be kept in mind, however, that the applicability of HadEX2 in regional climate studies, especially for precipitation-related parameters, is disputable. Possible intensification of the extreme precipitation events in generally dryer climate is also discussed in Giorgi & Lionello, (2008).

It is worth to emphasize, that the projected changes under RCP2.6 and RCP4.5, are not significant over the bigger part of the domain which also indicates the complexity of the phenomena.

The temporal evolution of the considered precipitation indices is shown on Figure 7.

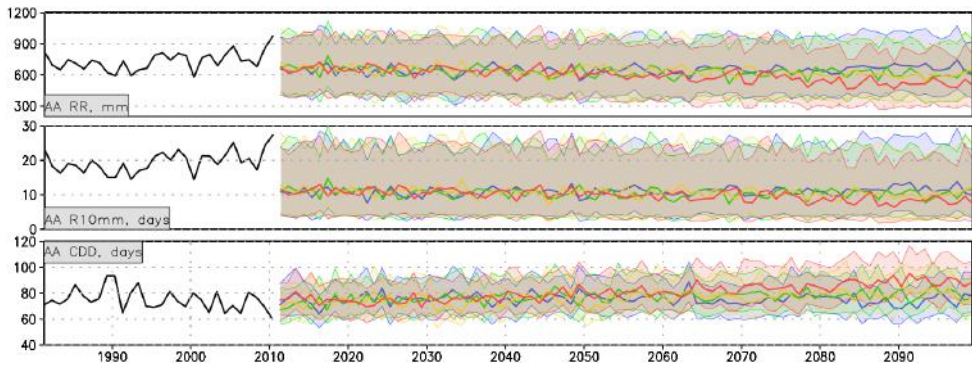


Figure 7. Same as Figure 2 but for the RR (first row) and R10mm (second row) and CDD (third row). The units are according the subplots titles.

As most remarkable on Figure 7 appears the fact that the evolution lines of RR and R10mm and in smaller extent these for CDD, respectively their interquartile ensemble spreads for all scenarios, essentially overlaps for the bigger part of the time span 2011-2099. Such dynamics is expectable, keeping in mind the relatively small changes from RCP to RCP commented above. The absence, at least apparent, of big outliers is also remarkable. The inter-model coherency is demonstrated also in agreement between the models in the simulation of isolated wet years in the 2040s and 2070s in the evolution of the CDD.

SUMMARY AND CONCLUSION

Based on the availability of new sources of information, which represent the state of the art global climate change simulations in the frame of the CMIP5 project and are free accessible from the Copernicus Data Store, we present an updated assessment of future climate change projections over south-east Europe.

In the present study 6 temperature-based and 3 precipitation-based indices, together with the annual means of the daily minimum, mean and maximum temperature are analysed systematically. The indices are calculated in consistent manner in the frames of the Global Agriculture project and the assessment covers the recent climate (1981-2010) as well as CMIP5 multimodel ensemble projections of the 21st century for all four RCP scenarios. The spatial patterns and temporal evolution of changes presented in this work are in principal agreement with previous studies based on GCM output data (Orlowsky & Seneviratne 2012; Sillmann et al., 2013b; Chervenkov & Slavov, 2021), RCM simulations Belda et al., 2015; Gadzhev et al., 2021) or such based on combined analysis of GCMs and RCMs (Giorgi & Lionello 2008; Ulbrich et al., 2006). The results of this study are also coherent with the consolidated outcomes from all Assessment Reports (AR) of the Intergovernmental Panel on Climate Change (IPCC) (see, for example, IPCC, 2007) concerning the expected long-term regional changes. However, the present results are not directly comparable, at least not quantitatively, to theirs, due to different factors. These factors includes, among others, different time spans and model ensemble members and variations in the applied methodology of estimation. Nevertheless, the most general and important conclusion of the study is the distinct warming, expressed in the spatial patterns and time evolution of all of the considered thermal indices. The climate change of the considered temperature-based indices is consistent with the tendencies of the annual means of the daily mean and extreme temperatures. The warming dominates practically over the whole domain and is statistically significant over its essential part in the most cases. The revealed patterns of climate change intensify gradually with the increasing radiative forcing in the considered scenarios, which also agrees generally with the outcome of the prevailing number of the recent studies. The significantly finer grid spacing of 0.5° than this in Sillmann et al. (2013b), Chervenkov & Slavov, (2021), were it is 1.5°, leads to representation (although still not clear enough) of such structures as the vertical gradients of some indices especially along the main Carpathian ridge and the typical spatial pattern of the CDD. Both of them are poorly resolved in the cited above studies. Beside the revealed spatial details which are well known benefit of the increased resolution, this study differs from Chervenkov & Slavov, (2021) in other substantial aspect regarding the results: the clearly demonstrated ‘warming asymmetry’ manifested in the fields of the TNn and TXx. Generally, the revealed warming is, evidently, continuation of already detected tendency in the historical records of the twentieth century over

the region (Chervenkov & Slavov, 2019; Chervenkov & Slavov, 2020; Malcheva et al., 2016; Moberg et al., 2006).

Concerning the precipitation-based indices, the study confirms the complexity of the expected precipitation-related changes and their inherent ambiguity. The latter is clearly evidenced by the lower level of statistical significance for the scenarios RCP2.6-RCP6.0 when compared with temperature changes. It is worth emphasizing that the projected precipitation reduction over the SE part of the domain and increase of the CDD could amplify the negative impact of the expected hotter climate.

The study could be continued in many directions. Key moments as, for example, seasonal variations and detailed regional specifics, could be focal point of further works. The 10-daily temporal resolution of some indices gives unique possibility even for sub-seasonal analysis. Other way is to utilize more actively the output of RCMs, as demonstrated in Belda et al., (2015) and Gadzhev et al., (2021). Such studies are methodologically reliable scientific basis of various impact studies and the development of adaptation strategies.

ACKNOWLEDGMENTS

The authors thank the anonymous reviewers for their insightful suggestions. Hence this study is entirely based on free available data and software, the authors would like to express their deep gratitude to the primary CMIP5 model output vendors as well as all other organizations and institutions (MPI-M, UNI-DATA, Copernicus Data Store), which provides free of charge software and data. Without their innovative data services and tools this work would be not possible.

This work has been carried out in the framework of the National Science Program "Environmental Protection and Reduction of Risks of Adverse Events and Natural Disasters", approved by the Resolution of the Council of Ministers № 577/17.08.2018 and supported by the Ministry of Education and Science (MES) of Bulgaria (Agreement № Д01-322/18.12.2019).

This work has been accomplished with the financial support by the Grant No BG05M2OP001-1.001-0003, financed by the Science and Education for Smart Growth Operational Program (2014-2020) and co-financed by the European Union through the European structural and Investment funds.

REFERENCES

- Alexander, L. V., et al. (2006) Global observed changes in daily climate extremes of temperature and precipitation, *J. Geophys. Res.*, 111, D05109, doi:10.1029/2005JD006290
- Alexander, L. V. and Arblaster, J. M. (2009) Assessing trends in observed and modelled climate extremes over Australia in relation to future projections. *Int. J. Climatol.*, 29: 417-435. doi:10.1002/joc.1730

- Belda, M., Skalák, P., Farda, A., et al. (2015) CECILIA Regional Climate Simulations for Future Climate: Analysis of Climate Change Signal, *Advances in Meteorology*, vol. 2015, Article ID 354727, 13 pages, 2015 doi:10.1155/2015/354727
- Birsan, M. V., Dumitrescu, A., Micu, D.M., Cheval, S. (2014) Changes in annual temperature extremes in the carpathians since AD 1961. *Natural Hazards* 74(3), 1899-1910 doi:10.1007/s11069-014-1290-5
- Chervenkov, H., Slavov, K., Ivanov, V., (2019) STARDEX and ETCCDI Climate Indices Based on E-OBS and CARPATCLIM; Part One: General Description , in G. Nikolov et al. (Eds.): NMA 2018, LNCS 11189, pp. 360-367, doi: 10.1007/978-3-030-10692-8_40
- Chervenkov, H., Slavov, K. (2019) STARDEX and ETCCDI Climate Indices Based on E-OBS and CARPATCLIM; Part Two: ClimData in Use, in G. Nikolov et al. (Eds.): NMA 2018, LNCS 11189, 368-374, (2019) DOI: 10.1007/978-3-030-10692-8_41
- Chervenkov H., Spiridonov V. (2020) Bias Correcting of Selected ETCCDI Climate Indices for Projected Future Climate, In: Lirkov I., Margenov S. (eds) LSSC 2019, LNCS 11958, pp. 292-299, doi:10.1007/978-3-030-41032-2_33
- Chervenkov H., Slavov K. (2020a) Historical Climate Assessment of Temperature-based ETCCDI Climate Indices Derived from CMIP5 Simulations, *C. R. Acad. Bulg. Sci.* 73, No 6, 784-790, DOI: 10.7546/CRABS.2020.06.05
- Chervenkov, H. Slavov, K. (2020b) Historical Climate Assessment of Precipitation-based ETCCDI Climate Indices Derived from CMIP5 Simulations, *Compt. rend. Acad. bulg. Sci.*, 73, No 7, 942-948, DOI:10.7546/CRABS.2020.07.06
- Chervenkov H., Slavov K. (2020c) ETCCDI Thermal Climate Indices in the CMIP5 Future Climate Projections over Southeast Europe, *Proceedings of the 14th Annual Meeting of the Bulgarian Section of SIAM, Studies in Computational Intelligence* (in press)
- Chervenkov H., Slavov K. (2021) ETCCDI Climate Indices for Assessment of the Recent Climate over Southeast Europe. In: Dimov I., Fidanova S. (eds) *Advances in High Performance Computing. HPC 2019. Studies in Computational Intelligence*, vol 902, 398-412, Springer, Cham. doi: 10.1007/978-3-030-55347-0_34
- Chervenkov H., Spiridonov V. (2021) Sensitivity of Selected ETCCDI Climate Indices from the Calculation Method for Projected Future Climate. In: Dimov I., Fidanova S. (eds) *Advances in High Performance Computing. HPC 2019. Studies in Computational Intelligence*, vol 902, 413-427 Springer, Cham. doi:10.1007/978-3-030-55347-0_35

- Chervenkov, H., Ivanov V., Gadzhev G., Ganey K. (2021) Assessment of the future over South-east Europe based on CMIP5 ensemble of climate indices – Part one: General Concept and Methods, Proceedings of the 1st International conference on ENVIRONMENTAL protection and disaster RISKS, 02-04 October 2020, Sofia, Bulgaria (in press)
- Gadzhev G., Ivanov V., Valcheva R., Ganey K., Chervenkov H. (2021) HPC Simulations of the Present and Projected Future Climate of the Balkan Region. In: Dimov I., Fidanova S. (eds) *Advances in High Performance Computing. HPC 2019. Studies in Computational Intelligence*, vol 902, 234-248 Springer, Cham. https://doi.org/10.1007/978-3-030-55347-0_20
- Giorgi, F., Lionello, P. (2008) Climate change projections for the Mediterranean region, *Global and Planetary Change*, 63(2-3): 90-104
- Hempel, S., Frieler, K., Warszawski, L., Schewe, J. and Piontek, F., (2013) A trend-preserving bias correction—the ISI-MIP approach. *Earth System Dynamics*, 4(2), 219-236.
- Intergovernmental Panel on Climate Change (IPCC) (2007) *Climate Change 2007: The Physical Science Basis. Contribution of Working Group I to the Fourth Assessment Report of the Intergovernmental Panel on Climate Change*, edited by S. Solomon et al., Cambridge Univ. Press, Cambridge, U. K.
- Malcheva, K., Chervenkov, H., Marinova, T., (2016) Winter Severity Assessment on the Basis of Measured and Reanalysis data. In: 16th International Multidisciplinary Scientific GeoConference SGEM 2016. SGEM, pp. 719-726
- Moberg, A., et al. (2006), Indices for daily temperature and precipitation extremes in Europe analyzed for the period 1901–2000, *J. Geophys. Res.*, 111, D22106, doi:10.1029/2006JD007103.
- Orlowsky, B. and Seneviratne, S. I. (2012) Elusive drought: uncertainty in observed trends and short- and long-term CMIP5 projections, *Hydrol. Earth Syst. Sci.* 17(5):1765-1781 doi:10.3929/ethz-b-000073994.
- Sillmann, J., Röckner, E., (2007) Indices for extreme events in projections of anthropogenic climate change. *Climatic Change* 86 (1-2), pp. 83-104.
- Sillmann, J., V. V. Kharin, X. Zhang, F. W. Zwiers, and D. Bronaugh (2013a) Climate extremes indices in the CMIP5 multimodel ensemble: Part 1. Model evaluation in the present climate, *J. Geophys. Res. Atmos.*, 118, pp. 1716-1733, doi: 10.1002/jgrd.50203
- Sillmann, J., V. V. Kharin, F. W. Zwiers, X. Zhang, and D. Bronaugh (2013b) Climate extremes indices in the CMIP5 multimodel ensemble: Part 2. Future climate projections, *J. Geophys. Res. Atmos.*, 118, pp. 2473-2493 doi: 10.1002/jgrd.50188.

Ulbrich, U., et al., (2006) The Mediterranean climate change under global warming. In: Lionello, P., Malanotte-Rizzoli, P., Boscolo, R. (Eds.), R. (Eds.), *Mediterranean Climate Variability*. Elsevier, Amsterdam, pp. 398-415.

✉ **Hristo Chervenkov**

<http://orcid.org/0000-0002-7658-3041>

National Institute of Meteorology and Hydrology
Sofia, Bulgaria

E-mail: hristo.tchervenkov@meteo.bg

✉ **Vladimir Ivanov**

<https://orcid.org/0000-0001-9768-1049>

National Institute of Geophysics, Geodesy and Geography
Bulgarian Academy of Sciences
Sofia, Bulgaria

E-mail: vivanov@geophys.bas.bg

✉ **Georgi Gadzhev**

<http://orcid.org/0000-0002-6159-3554>

National Institute of Geophysics, Geodesy and Geography
Bulgarian Academy of Sciences
Sofia, Bulgaria

E-mail: ggadzhev@geophys.bas.bg

✉ **Kostadin Ganev**

National Institute of Geophysics, Geodesy and Geography
Bulgarian Academy of Sciences
Sofia, Bulgaria

E-mail: kganev@geophys.bas.bg

APPLICATION OF BACKWARD TRAJECTORIES AND CLUSTER ANALYSES FOR STUDY OF VARIATIONS IN PM₁₀ CONCENTRATIONS

Rozeta Neykova, Elena Hristova

National Institute of Meteorology and Hydrology (NIMH)

Abstract: This study is on estimation of the influence of the air mass origin on particulate matter (PM₁₀) levels in the city of Plovdiv, Bulgaria during 2019. The HYSPLIT (Hybrid Single-Particle Lagrangian Integrated Trajectory) and the statistical software package “Openair” in R are applied. The cluster analysis statistical method is used to group the back-trajectories into 5 sets according to the angle, direction and speed of the air mass. The Potential Source Contribution Function (PSCF) and Concentration Weighted Trajectory (CWT) statistical methods are also applied in order to identify source areas of pollutants. The PM₁₀ concentrations in two air quality stations in Plovdiv and some meteorological elements are also presented and discussed. The influence of the clusters on PM₁₀ levels is explained.

Keywords: Air quality, PM₁₀, back-trajectories, cluster analysis, PSCF

INTRODUCTION

Air pollution in urban area is one of the main risk factors concerning the human health in medium and high- developed countries according to the World Health Organization (WHO, 2019). Major problem with the air quality in some European countries is the particulate matter (PM) air pollution (EEA Rep. 2018). The major problem in Bulgarian cities is also air pollution with PM. In our country there is still a problem with the regulated number of exceedances of PM₁₀ (EEA, 2018). 78.6 % of the Bulgarian population is exposed to exceedance of the limit values of PM₁₀, while this percent for Europe is about 21% to 41% (MoEW Report, 2019). The harmful effect of PM depends on its size (TSP, PM₁₀, PM_{2.5}, PM₁), the concentration and the chemical composition. It is easy for PM to be inhaled into the respiratory tract, where they can cause inflammatory processes and diseases of the respiratory and cardiovascular systems (Lim et al., 2012; Straif et al, 2013). Despite the plans for improving the air quality and reduction of the emissions in regional and European scales, the decrease of the PM concentration during the last years is still unsatisfactory (EEA, 2018). The PM particles are emitted in the atmosphere by many anthropogenic sources such as

energetic, industry, road transport, burning of fuels, incineration of waste. Significant contribution according to the area can be the resuspension and soil erosion, sea spray and volcanic eruption and etc. (Seinfeld and Pandis, 2006).

The application of Trajectory Statistical Methods as a supplementary tool can be very useful in this type of studies aimed to characterize sources and formation processes of particulate matter (PM). Characterization of wind-flow circulations can help us to identify specific meteorological situations that favour external (transboundary) contributions on ambient levels of atmospheric PM. The best way for interpreting atmospheric pollutant measurements at a receptor site using back-trajectories is by performing the analysis of large sets of them using specific Trajectory Statistical Methods (TSM). The use of TSM deploying large trajectory ensembles can significantly reduce the trajectory uncertainty generated by interpolation and truncation processes, low temporal or spatial resolution of wind data, or an inappropriate selection of the starting heights. Characterizing the synoptic meteorological situations which give rise to low and high concentration levels of PM at a receptor site can help us identify potential source regions of PM which can be transported towards the sampling site.

The main objective is to study the influence of the origin of air mass at a synoptic scale on PM levels at urban air quality monitoring stations in the city of Plovdiv for the period 01.01.2019 – 31.12.2019.

2. METHODOLOGY

2.1. The study area

Plovdiv is city in southern Bulgaria placed in the southern part of the Plain of Plovdiv on the banks of the Maritsa River. The Sredna Gora mountain range rise to the northwest, the Chirpan Heights to the east, and the Rhodope mountains to the south. Plovdiv is the second populated city in Bulgaria, with population 347 851 up to 31.12.2019 according National statistical institute of Republic of Bulgaria (<https://www.nsi.bg/en/content/6710/population-towns-and-sex>). The city has been struggling with poor air quality for years, which mainly results from its location and limited ventilation and also from cumulative impacts of local, regional and transboundary emissions. In Plovdiv there are two official air quality stations, part of the National air quality network, named Plovdiv - Kamenitsa (42.142889° N, 24.765239° E) and Plovdiv - zh.k. Trakia (42.141186° N, 24.787952° E). Both sites are in urban area, but the Kamenitsa is Background type while zh.k. Trakia is Traffic (Figure 1).

2.2. PM₁₀ data

The PM₁₀ hourly concentration levels for 2019 obtained at two air quality monitoring sites on the Executive Environment Agency are used in the statistical analysis.

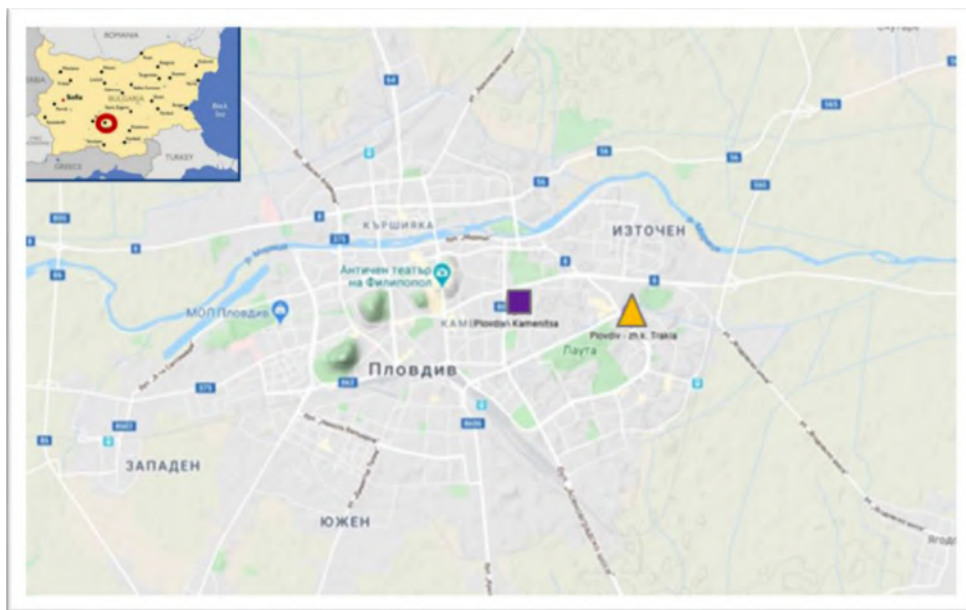


Figure 1. Map of Plovdiv with urban air quality stations – Kamenitsa (square) and zh.k. Trakia (triangle)

2.3. Back-trajectories

A daily meteorological analysis was carried out for the study period to identify the different source regions of the air masses influencing the study area. 3-days back-trajectories at 04:00, 12:00 and 18:00 UTC and at 3 different heights above the starting point located at ground level were computed on a daily basis by using the NOAA (National Oceanic and Atmospheric Administration) HYSPLIT 4.0 model (Air Resources Laboratory 2017) (Stein et al. 2015). The weekly archived data GDAS (Global Data Assimilation System) with resolution 1° were used as input. The best procedure to illustrate the vertical structure of the atmosphere is to run trajectories at several heights above the point of interest. 500, 1500 and 2000 m AGL was chosen in this study.

2.4. Trajectory statistical methods (TSM)

Trajectory statistical methods were applied to the HYSPLIT back-trajectories with the software package “Openair” in R (http://www.opair-project.org/PDF/OpenAir_NewsLetter_Issue14.pdf). Firstly, on the air mass back-trajectories data was performed cluster analysis (CA). CA is a statistical method used to examine data and group it into sets of similar data known as clusters. It is a useful method for

organizing large data sets into smaller, similar groups. Trajectory coordinates are used as the clustering variables. CA can be used to classify the air mass origins that arrive at a site (Dorling et al., 1992; Brankov et al., 1998; Salvador et al., 2008), but CA does not provide any information on the geographical location of potential source regions. This information can be obtained by using Potential Source Contribution Function.

Potential Source Contribution Function (PSCF) calculates the probability that a source is located at latitude i and longitude j (Fleming et al., 2012; Pekney et al., 2006). The basis of PSCF is that if a source is located at (i, j) , an air parcel back trajectory passing through that location indicates that material from the source can be collected and transported along the trajectory to the receptor site. PSCF solves

$$PSCF = m_{ij} / n_{ij} \quad (1)$$

where n_{ij} is the number of times that the trajectories passed through the cell (i, j) and m_{ij} is the number of times that a source concentration was high when the trajectories passed through the cell (i, j) .

The criterion for determining m_{ij} is controlled by percentile, which is by default 90. Note also that cells with few data have a weighting factor applied to reduce their effect (The openair Project newsletter Issue 14, February 2013).

Finally, the potential source regions of particles were evaluated by the Concentration Weighted Trajectory (CWT) statistical method, available in the above mentioned “Openair” package computing a concentration field to identify source areas of pollutants (Seibert et al. 1994). For each cell of the grid domain a weighted mean concentration of the pollutant species under study is calculated. The weight for each concentration value of the pollutant’s time series is the time spent in that grid cell by the associated trajectory. Areas with high CWT values in the concentration field indicated that, on average, air parcels residing over them resulted in high concentrations of the atmospheric pollutant at the receptor site. Thus, these concentration fields show those potential source areas whose emissions can be transported to the measurement site by prevailing synoptic winds (López, V., et al., 2019)

3. RESULTS AND DISCUSSION

3.1. Particulate matter levels

Time series of PM_{10} hourly concentration levels obtained at two air quality monitoring stations (Trakia and Kamenitsa) during the study period is presented in Figure 2. There is a good relation between the cases of increasing values at the two air quality stations. The exceedance of the 24-h limit value ($50 \mu\text{g}\cdot\text{m}^{-3}$) is observed in both air quality stations during 2019. 93 days are with exceedance in the Trakia station and 66 days for the Kamenitsa station. There are some days with exceedance only in Trakia station (27 days). Most of those days are during the cold period of the year.

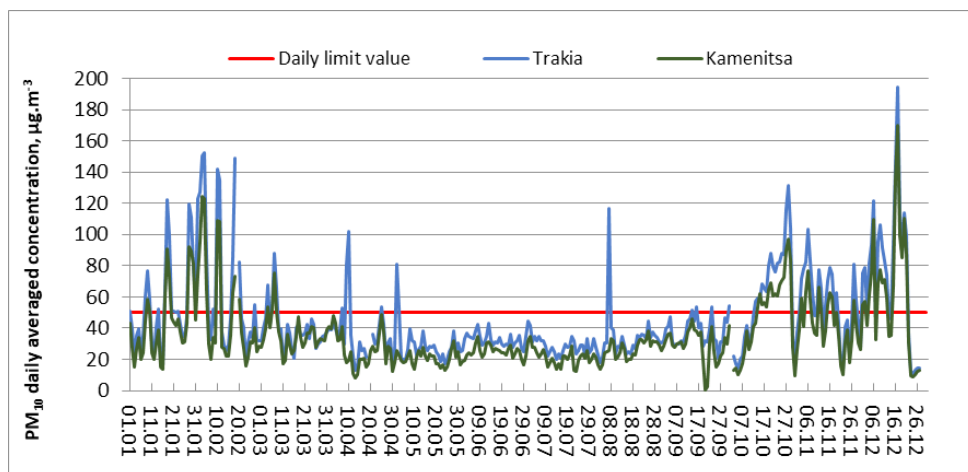


Figure 2. Annual course of the daily mean PM_{10} values in Trakia and Kamenitsa air quality stations

There are some days with PM_{10} concentration above $50 \mu\text{g}\cdot\text{m}^{-3}$ during the warm period of 2019.

Very high differences in the PM_{10} concentration between Trakia and Kamenitsa are observed on 11 April, 03 May and 08 August. Probably these cases of exceedance are due to local sources of air pollution.

The PM_{10} concentrations for the periods with exceedance are between 54.3 and $194.5 \mu\text{g}\cdot\text{m}^{-3}$ at the Trakia station and from 50.2 to $169.6 \mu\text{g}\cdot\text{m}^{-3}$ at the Kamenitsa station. 24 days with fog are registered and 60 with rain. 90% of cases with rain are with 0 mm amount. The daily averaged wind speed is ranged from 0.1 to $4 \text{ m}\cdot\text{s}^{-1}$.

3.2. TSM results

A total of 3285 backward trajectories were obtained ending at 04:00, 12:00 and 18:00 UTC hours in Trakia station ($42.141186^\circ \text{ N}$, $24.787952^\circ \text{ E}$) for each day of the period 1.01.-31.12.2019, at 3 different heights (500, 1500, 2000 m agl). They have been clustered using “Openair” to establish the different air-flow patterns. Five typical meteorological synoptic situations (clusters) were obtained. The comparison of obtained clusters, PSCF and weighted mean PM_{10} concentration for three different highs are presented in Figure 3.

Back-trajectories with the origin at 500 m agl were grouped into 5 different origins of air mass (Figure 3). Cluster 1 (C1) indicated a 30% air mass movement from the north western (central Europe). A flow movement from the north was represented by Cluster 2 (C2). Cluster 3 (C3) is characterized by air mass coming from the south west (18.3%). Cluster 4 (C4) contained short back-trajectories of

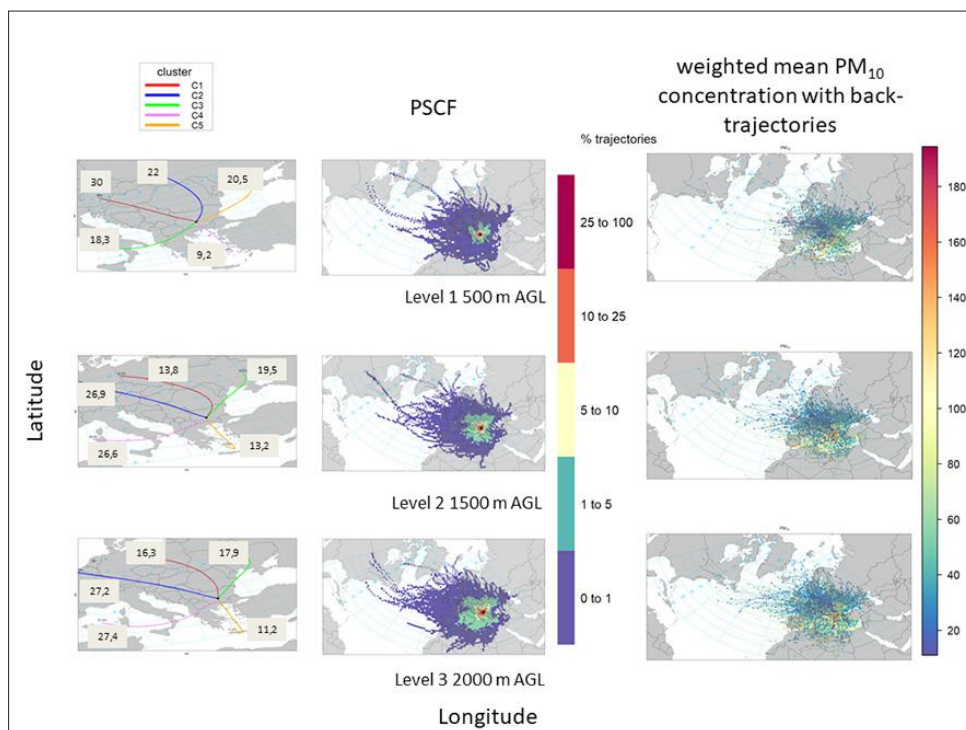


Figure 3. Cluster analysis (CA) on the left side, PSCF in the middle and weighted mean PM_{10} concentration with back-trajectories for 2019

air mass recirculating south (9.2%) and Cluster 5 (C5) is characterized by air mass coming from the east (20.5%).

The 5 clusters obtained from the set of back-trajectories at 1500 m agl and 2000 m agl presented similar origins but different from the 500 m agl. Clusters containing back-trajectories coming from the south western and north western (C2 and C4 respectively), are presented similar percentages of trajectories (~27%). C2 and C4 grouped around 60% of all trajectories for each data set. On the other hand, short scale back-trajectories contained in C5 have represented less than 15% of all the trajectories with origin in 1500 and 2000 m agl. C3 represented 17-19% of all back-trajectories.

The PSCF and weighted mean PM_{10} concentration for three different highs presented in Figure 3 give us information for source regions of the PM_{10} component understudy or as preferred air mass pathways.

The lowest mean concentration values for all data sets were obtained for periods with north, north-western air mass advection (C1 and C2) (Table 1).

Table 1. Mean PM₁₀ concentration (µg.m⁻³) by trajectory cluster at 3 different levels

| | Level 500 | Level 1500 | Level 2000 |
|-----------|-----------|------------|------------|
| Cluster 1 | 36 | 38.3 | 35.6 |
| Cluster 2 | 37.7 | 36.3 | 38 |
| Cluster 3 | 64.4 | 40 | 40.4 |
| Cluster 4 | 58.1 | 58.5 | 57.7 |
| Cluster 5 | 44.4 | 52.5 | 55.1 |

Two regions are identified as the main source regions of contributing to increasing PM₁₀ levels in Plovdiv (C4 and C5). However, it should be considered that with the CWT methodology and the back-trajectories obtained with the HYSPLIT model it is not possible to correctly perform an identification of the main local sources of PM₁₀.

4. CONCLUSIONS

In this study different trajectory statistical methods were applied to a set of 1 year of back trajectories in order to describe the air mass influence on the atmospheric particulate matter (PM₁₀) levels in Plovdiv. Potential Source Contribution Function (PSCF) and Concentration Weighted Trajectory (CWT) methods are applied for the first time on PM data from urban air quality observations. Air mass back-trajectories were grouped into 5 clusters, representing a typical meteorological scenario. The results obtained suggest that the levels of atmospheric particulate matter in Plovdiv could be influenced by cross-border natural and anthropogenic sources (south, south-wets). To prove this more studies with input data with higher resolution is needed. The obtained results are a step towards scientifically based studies on identifying different source areas of different air pollutants. The development of new methods enabling identification and assessment of the reasons behind this condition and their further application for air quality management is necessary. Further studies on combining observations on PM chemical composition and Trajectory Statistical Methods are necessary.

ACKNOWLEDGMENTS

This study was performed with the financial support from the National Programme “Young scientists and post-doctoral”. We acknowledge also to the NOAA Air Resources Laboratory (ARL) for the provision of the HYSPLIT model and READY website (<http://www.ready.noaa.gov>) and also to the R-project website (<https://www.r-project.org/>) for Package ‘openair’.

REFERENCES

- Brankov, E., Rao, S.T., Porter, P.S., (1998), A trajectory-clustering-correlation methodology for examining the long-range transport of air pollutants, *Atmospheric Environment* 32, 1525-1534.
- Dorling, S.R., Davies, T.D., Pierce, C.E., (1992), Cluster analysis: a technique for estimating the synoptic meteorological controls on air and precipitation chemistry – method and applications, *Atmospheric Environment* 26A, 2575-2581.
- EEA, (2018), Air Quality in Europe-2016 report, Report No 12, European Environmental Agency, Copenhagen, ISSN 1977-8449
- Fleming, Z.L., Monks, P.S. and Manning. A.J.,(2012), Review: Untangling the influence of air-mass history in interpreting observed atmospheric composition, *Atmospheric Research*,104-105:1–39, doi:10.1016/j.atmosres.2011.09.009.
- López, V., Salvador, P., Artíñano, B. et al. (2019) Influence of the origin of the air mass on the background levels of atmospheric particulate matter and secondary inorganic compounds in the Madrid air basin. *Environ Sci Pollut Res* 26, 30426–30443 <https://doi.org/10.1007/s11356-019-06205-8>.
- National State of the Environment (SoE) Report, (2019), MoEW, Sofia (in bulg.)/МОСВ Доклад, 2019. Национален доклад за състоянието и опазването на околната среда, 2019.
- Pekney, N. J. , Davidson C. I., Zhou, L. and Hopke, P. K., (2006), Application of PSCF and CPF to PMF-Modeled Sources of PM_{2.5} in Pittsburgh. *Aerosol Science and Technology*, 40(10):952–961, doi: 10.1080/02786820500543324.
- Salvador, P., Artíñano, B., Querol, X., Alastuey, A., (2008), A combined analysis of backward trajectories and aerosol chemistry to characterise long-range transport episodes of particulate matter: the Madrid air basin, a case study, *Science of the Total Environment* 390, 495e506.
- Seibert P, Kromp-Kolb H, Baltensperger U, et al (1994) Trajectory analysis of aerosol measurements at high alpine sites. *Transp Transform Pollut Troposph* 15:689–693
- Seinfeld J.H. and Pandis N.S., (2006), *Atmospheric Chemistry and Physics. From Air Pollution to Climate Change*, 2-nd Ed. John Wiley & Sons, Inc. USA. 1225p.
- Stein AF, Draxler RR, Rolph GD, et al (2015) NOAA’s HYSPLIT atmospheric transport and dispersion modeling system. *Bull Am Meteorol Soc* 96:2059–2077
- Stephen S. Lim et al., (2012), A comparative risk assessment of burden of disease and injury attributable to 67 risk factor clusters in 21 regions,

1990-2010: a systematic analysis for the Global Burden of Disease Study 2010. *The Lancet*, 380 (9859) 2224-2260.

Straif, K., Cohen, A., Samet, J. (Eds.), (2013), *Air Pollution and Cancer*, International Agency for Research on Cancer (IARC), Lyon, France, p. 487.

✉ **Rozeta Neykova**

National Institute of Meteorology and Hydrology
Sofia, Bulgaria
E-mail: rozeta.neikova@meteo.bg

✉ **Elena Hristova**

<https://orcid.org/0000-0002-5681-4375>
National Institute of Meteorology and Hydrology
Sofia, Bulgaria
E-mail: elena.hristova@meteo.bg

RELATIONSHIP BETWEEN PARTICULATE MATTER AND HEALTH INDICATORS FOR ACUTE MORBIDITY IN SOFIA

Petar Zhivkov¹, Aleksandar Simidchiev²

¹ *Institute of Information and Communication Technologies –
Bulgarian Academy of Sciences (IICT-BAS)*

² *Medical Institute of Ministry of Interior*

Abstract: The objective of this paper is to assess the relationship between fine Particulate Matter (PM) concentrations and health indicators for acute morbidity. The methods used are linear correlation and non-parametric correlation analysis of a time series study conducted in Sofia from 1 January 2017 to 31 May 2019. Data from 4 local health sources that cover hospital admissions and all Emergency Medical Aid registrations from Sofia's population of 1.3 million. **Results were obtained:** The mean daily PM₁₀ concentration was 35 µg/m³ with a range from 5 to 336 µg/m³. The mean daily PM_{2.5} concentration was 11.7 µg/m³ with a range from 2 to 136 µg/m³. In 15.3% of the times, the daily PM_{2.5} or PM₁₀ concentrations did not meet the WHO Air Quality Guidelines target during the study period. At these excesses, acute infections of the upper respiratory tract and pneumonia increase by 47% and 60%, respectively. COPD increases with 36%, there are also changes and acute bronchitis. **Conclusions:** The findings provide a justification that exceeds the concentrations of PM₁₀ and PM_{2.5} were significantly associated with indicators of acute morbidity in Sofia.

Keywords: particulate matter, acute morbidity, health indicators, PM₁₀, PM_{2.5}.

INTRODUCTION

The human health effects of exposure to outdoor air pollutants is considered a global health concern (Thurston et al., 2017). The links between urban air pollution and human health are consistently and clearly established by many researchers (J. Samet & Krewski, 2007) (Li et al., 2013), especially for short-term effects such as cardiovascular events (Vermylen, Nemmar, Nemery, & Hoylaerts, 2005), neurovascular (Tallon, Manjourides, Pun, Salhi, & Suh, 2017; Wing et al., 2017) and asthma (Ward & Ayres, 2004).

Significant literature of epidemiologic studies suggests a correlation between acute morbidity and exposure to air pollution from particulate matter (Pope,

Dockery, & Schwartz, 1995). Most of this data comes from time series analyses (Bell, Samet, & Dominici, 2004) comparing the variations in hospitalization with the average particulate matter variations (Dominici, Sheppard, & Clyde, 2003). Also, multicity studies exist such as the European Air Pollution and Health: a European Approach (APHEA) project (Katsouyanni et al., 1996) and the American National Morbidity, Mortality, and Air Pollution Study (NMMAPS) (J. M. Samet et al., 2000) that both provide a consistent evidence for association health and air pollutants for multiple cities by covering a large geographic area.

The consequences of air pollution can be seen as an enhancement to a person's risk of illness or injury or as an additional general well-being risk acquired by a population (Gochfeld & Burger, 2011). The aim of air quality management is to control or avoid adverse impacts on air pollution to public health. Therefore, it is important to define such effects that are deemed "adverse," and to distinguish them from those effects that are not deemed adverse, thus concentrating protection efforts on the contaminants that cause the most extreme health impacts.

Air Quality Control - Difference in norms and legislation

There is difference between legislation and recommendations illustrated in Table 1. The WHO guidelines for air pollution can be looked more like recommendations, they do not have a mandatory character. While the EU Air Quality Directive can be looked as a legislation that every EU member has to follow.

Table 1. Difference between EU Air Quality Directive and WHO Guidelines

| | | EU Air Quality Directive | WHO Guidelines |
|-------------------|----------|-------------------------------------------------------|-------------------------------------------------------|
| Pollutant | Period | Concentration (limit value $\mu\text{g}/\text{m}^3$) | Concentration (limit value $\mu\text{g}/\text{m}^3$) |
| PM _{2.5} | 24 Hours | - | 25 |
| | Annual | 25 | 10 |
| PM ₁₀ | 24 Hours | 50 | 50 |
| | Annual | 40 | 20 |

For the purpose of this research we will use the WHO guidelines as they are advisable worldwide and having purely health aspects in the consideration, while the EU Directive includes some also politico-economic aspects in recital.

Case study

Sofia is the only European capital situated in a valley and is characterized by high quantity of anthropogenic emissions and by frequent occurrence of stagnant meteorological conditions. The city has a population of 1.2 million people (NSI, 2019) and is situated in the Sofia valley. The area is recognized as a problematic location where especially during winter there are numerous exceedances despite

the European legislation that aims at air pollution control. The combination of cold winters and its situation predisposes to temperature inversions that last several days to a week.

Many urban areas located in a valley without adequate air exchange encounter significant air pollution problems that are linked with the local atmospheric peculiarities (Rendón, Salazar, Palacio, Wirth, & Brötz, 2014). A strong inversion and light precipitation and/or wind were the major causes for trapping pollutants in the air mainly during winter time. The air quality in Sofia deteriorates significantly during winter compared to summer. Hence it will be a good model to test our hypothesis of a significant link between air pollution and health consequences.

The literature abounds with models that can be used to assess the pollution/health hypothesis. A correlation between temperature and mortality around Sofia is made by using models with linear and non-linear terms (Pattenden, Nikiforov, & Armstrong, 2003). Other research that examines the genotoxicity of ambient air in 3 European cities, including Sofia shows that winter air pollution is six- to 10-fold higher in comparison with summer air (Gábelová et al., 2004).

This will be the first such study with real data from official and civil sources of information on particulate air pollution, comprehensive data from the activities of the center for emergency medical care, data from two of the largest hospitals related to the access to emergency care in Sofia. The results can be compared and contrasted with other international studies with local data.

The aims of this paper are to:

- (1) Compare data from air pollution in Sofia with health data originating from hospitals and ambulance services.
- (2) Highlight the key problem areas.
- (3) Identify future prospects and summarize the key areas where further research is needed to improve model performance.

DATA AND MODELLING

Health data

Due to the voluntary nature of data provision, there are different time characteristics and formats from different sources:

- Summarized data on the activity of the Center for Emergency Medical Aid Sofia by diagnoses of the center - from 01.01.2017 to 14.03.2019
- Information on the activity of diagnoses from DCC Tokuda - 02.01.2018 to 31.12.2018
- Information on the activity of diagnoses from Pirogov outpatient clinic - 01/01/2018 to 31/05/2019
- Information on the activity of hospitalized diagnoses from Pirogov - 01/01/2018 to 31/12/2018

The research uses the International Classification of Diseases (ICD) and more specifically ICD-10 for segmentation of the diseases and the identified morbidity. ICD-10 is the 10th revision of the ICD, a medical classification list by the World Health Organization (WHO) that is used by the time this study is conducted. It contains codes for diseases, signs and symptoms, abnormal findings, complaints, social circumstances, and external causes of injury or diseases (Organization, 1978, 2018).

Air pollution data

Air quality data in a form of hourly average concentrations of $PM_{2.5}$ and PM_{10} is obtained for 2019 as independent series for each element from official sensors provided from (a) the Executive Environment Agency (EEA) and (b) low-cost stations from the air.bg network (a contributors driven global sensor network that creates Open Environmental Data). PM_{10} is particulate matter 10 micrometers or less in diameter, $PM_{2.5}$ is particulate matter 2.5 micrometers or less in diameter. The data is collected from 5 official monitoring sites (Druzhba, Nadezhda, Hipodruma, Pavlovo, and Mladost), and over 500 citizen science monitors.

Beta attenuation method is used for PM_{10} and $PM_{2.5}$ according to the European Directive 2008/50/EC (Directive, 2008). Air quality monitoring networks are situated in.

The use of air quality data from low-cost stations aims to increase the potential benefits from traditional monitoring networks with additional geographic and temporal measurement resolution (Castell et al., 2017). Furthermore, low cost stations can contribute to data where limited air quality stations exist (Zimmerman et al., 2017). In Sofia, at the moment of the research there are with additional geographic and temporal measurement resolution.

Methods

For this research we use a time series analysis with correlation methods for analyzing the air quality and health data. The statistical methods in the research fall in the two categorizations: parametric and nonparametric. Parametric comparisons are based on the premise that the variable is continuous and normally distributed. Nonparametric approaches are used where data is continuous with non-normal distribution or any other form of data other than continuous variables.

The parametric Pearson correlation test (1) is used for comparing the two sources of air quality data. It provides a measure of the linear association between the two continuous variables (usually just referred to as correlation coefficient). To conduct the test, correlation coefficients are calculated for each (x,y) pair, and the values of x and y are subsequently replaced with their ranks. Application of the test results in a correlation coefficient that ranges from -1 to 1.

$$r = \frac{\sum_{i=1}^n (x_i - \bar{x})(y_i - \bar{y})}{\sqrt{\sum_{i=1}^n (x_i - \bar{x})^2 \sum_{i=1}^n (y_i - \bar{y})^2}} \tag{1}$$

Parametric methods are better ways to measure the difference between the groups relative to their equivalent nonparametric methods, but due to certain strict criteria, including data normality and sample size, we cannot use parametric tests in any situation and instead use their alternate nonparametric methods:

- For correlation analysis between pairs of variables is also used the non-parametric method Spearman's rho (2).

$$\rho = 1 - \frac{6 \sum d_i^2}{n(n^2 - 1)} \tag{2}$$

- Intergroup comparison for two unpaired groups is used the non-parametric Mann – Whitney U test between means.

Aggregation of air quality data

For PM₁₀ all measurements above 1000 µg/m³, which is the limit of the sensor are removed. A separate assessment based only on the days with below 70% humidity is made. These conditions do not necessarily mean that the data is incorrect, but under such conditions the manufacturer does not guarantee the predicted accuracy of 10% (Jayaratne, Liu, Thai, Dunbabin, & Morawska, 2018).

RESULTS

The results for daily concentrations of PM₁₀ and PM_{2.5} are summarized in Table 2. The mean daily PM₁₀ concentration was 35 µg/m³ with a range from 5 to 336 µg/m³. The mean daily PM_{2.5} concentration was 11.7 µg/m³ with a range from 2 to 136 µg/m³. 13.2% of the daily PM₁₀ or PM_{2.5} concentrations did not meet WHO Air Quality Guidelines target (50 µg/m³ for PM₁₀ and 25 µg/m³ for PM_{2.5}) during the study period. Some of the sources of health effects were with missing data for weekends (Saturday, Sunday, public holidays), so an analysis of gaps to exclude the possibility of bias was undertaken.

Table 2. Daily concentration of PM₁₀ and PM_{2.5} divided into working days and weekends + holidays

| Source | Day of the week | N | Mean | Median | SD | Min | Max | Percentiles | | Z | P |
|-------------------|-----------------|-----|-------|--------|-------|-----|-----|-------------|----|------|-----|
| PM ₁₀ | working day | 522 | 34,17 | 27,5 | 30,67 | 5 | 336 | 20 | 36 | 0,76 | 0,4 |
| | weekend | 230 | 37,1 | 26 | 38,45 | 6 | 290 | 18 | 38 | | |
| PM _{2.5} | working day | 522 | 11,15 | 9 | 12,61 | 2 | 104 | 4 | 14 | 0,09 | 0,9 |
| | weekend | 230 | 12,93 | 8 | 17,13 | 2 | 113 | 3 | 16 | | |

The conclusions are that there are no significant differences between weekends and working days in PM levels, and the lack of medical data for the weekends would not significantly affect the relevance of the results.

The correlation between the two sources of information for air quality (official satiations from EEA and citizen stations from AirBG) is significant PM_{10} ($n = 340$) $PM_{2.5}$ ($n = 296$) as seen in Table 3. and corresponds to other sources comparing these sources (National Institute of Meteorology and Hydrology and AirSofia.info).

Table 3. Pearson correlation coefficient (r) between the two sources

| | AirBG PM_{10} | AirBG $PM_{2.5}$ |
|----------------|-----------------|------------------|
| EEA PM_{10} | 0.967 | 0.937 |
| EEA $PM_{2.5}$ | 0.898 | 0.884 |

Correlation (Spearman's rho) of the measured values of PM_{10} -AS and $PM_{2.5}$ -AS and the number of EMA contacts by groups of diseases are shown in Table 4 and Table 5. Please keep in mind that the demand for EMA is usually initiated by a patient, and diagnoses are usually preliminary. As exposure requires time to develop effects outside the respiratory system, lag-shift analyzes of 1, 2 and 3 days were also introduced. The red numbers are significantly correlated ($p < 0.05$). The clearest correlation is observed to the total number of emergency contacts.

Table 4. Correlation (Spearman's rho) of the measured values of PM_{10} -AS and the number of EMA contacts by groups of diseases

| Name of the disease / identified morbidity | Without LAG period | LAG period 1 day | LAG period 2 days | LAG period 3 days |
|--------------------------------------------|--------------------|------------------|-------------------|-------------------|
| | R | R | R | R |
| Individuals received EMA | 0.211** | 0.195** | 0.226** | 0.234** |
| Heart attacks | 0,073* | 0,058 | 0,013 | 0,085* |
| Strokes | 0,069 | 0,108** | 0,086* | 0,002 |
| Rhythmic diseases | 0,058 | 0,052 | 0,063 | 0,111** |
| Acute heart failure | 0,064 | 0,144** | 0,121** | 0,066 |

Table 5. Correlation (Spearman's rho) of the measured values of $PM_{2.5}$ and the number of outpatient examinations in hospitals by groups of diseases

| Name of the disease / identified morbidity | Without LAG period | LAG period 1 day | LAG period 2 days | LAG period 3 days |
|--------------------------------------------|--------------------|------------------|-------------------|-------------------|
| | R | R | R | R |
| Individuals received EMA | 0.524** | 0.516** | 0.535** | 0.561** |
| Heart attacks | 0,148** | 0,153** | 0,120** | 0,161** |

| | | | | |
|---------------------|---------|---------|---------|---------|
| Strokes | 0,029 | 0,042 | 0,029 | -0,001 |
| Rhythmic diseases | 0,166** | 0,171** | 0,185** | 0,217** |
| Acute heart failure | 0,161** | 0,202** | 0,199** | 0,165** |

The correlation is significant for cardiovascular and cerebrovascular conditions, fully coinciding with the rapid increase in risk, albeit to a lesser extent, with a low level fractions of PM_{2,5} contamination from published data. (Shin et al., 2019; Wang et al., 2019; Zhang et al., 2018).

The results shown in Table 6 and Table 7 revealed an increase in EMA contacts with 11% on days with exceedances of PM₁₀ and 13.5% on days with exceedances of PM_{2,5}, for a period of at least 3 days. Mean increase (relative to background levels) in neuroses on day 2 after PM₁₀ exceedance by 1%, on heart attacks on day 3 after excess by 8%, on strokes immediately after excess by 9%, lasting up to day 3 after excess. The same applies to hypertensive conditions, which increase by 5% immediately around the exceedance and until the third day following the event.

Table 6. Comparison of non-parametric data from EMA contacts with WHO norms for average daily concentration of PM₁₀

| Name of the disease / identified morbidity | Without LAG period | | LAG period 1 day | | LAG period 2 days | | LAG period 3 days | |
|--------------------------------------------|--------------------|--------------|------------------|--------------|-------------------|--------------|-------------------|--------------|
| | Z | p | Z | P | Z | p | Z | p |
| Individuals received EMA | -6.49 | <0.001 | -5.95 | <0.001 | -7.11 | <0.001 | -7.81 | <0.001 |
| Neurosis | -0,079 | 0,937 | -1,102 | 0,271 | -2,305 | <u>0,021</u> | -0,412 | 0,680 |
| Heart attacks | -1,289 | 0,198 | -0,882 | 0,378 | -1,283 | 0,199 | -2,555 | <u>0,011</u> |
| Strokes | -2,151 | <u>0,032</u> | -2,153 | <u>0,031</u> | -2,419 | <u>0,016</u> | -1,500 | 0,134 |
| Hip. diseases | -2,101 | <u>0,036</u> | -2,270 | <u>0,023</u> | -2,182 | <u>0,029</u> | -2,507 | <u>0,012</u> |
| Ischemic heart disease | -2,238 | <u>0,025</u> | -2,225 | <u>0,026</u> | -1,591 | 0,112 | -1,779 | 0,075 |
| Rit. diseases | -0,762 | 0,446 | -1,202 | 0,229 | -2,121 | <u>0,034</u> | -3,160 | <u>0,002</u> |
| Acute heart failure | -0,823 | 0,410 | -2,413 | <u>0,016</u> | -2,314 | <u>0,021</u> | -1,670 | 0,095 |

Table 7. Comparison of non-parametric data from EMA contacts with WHO norms for average daily concentration of PM_{2,5}

| Name of the disease / identified morbidity | Without LAG period | | LAG period 1 day | | LAG period 2 days | | LAG period 3 days | |
|--------------------------------------------|--------------------|--------|------------------|--------------|-------------------|--------------|-------------------|--------|
| | Z | P | Z | p | Z | p | Z | p |
| Individuals received EMA | -6.34 | <0.001 | -6.12 | <0.001 | -7.08 | <0.001 | -7.34 | <0.001 |
| Neurosis | -1,065 | 0,287 | -0,738 | 0,461 | -2,421 | <u>0,015</u> | -1,058 | 0,290 |
| Strokes | -1,484 | 0,138 | -2,140 | <u>0,032</u> | -1,609 | 0,108 | -1,424 | 0,154 |

| | | | | | | | | |
|---------------------|--------|--------------|--------|--------------|--------|--------------|--------|--------------|
| Hip. diseases | -2,154 | <u>0,031</u> | -2,365 | <u>0,018</u> | -1,550 | 0,121 | -2,476 | <u>0,013</u> |
| Rit. diseases | -1,536 | 0,125 | -0,894 | 0,371 | -1,490 | 0,136 | -3,282 | <u>0,001</u> |
| Acute heart failure | -0,248 | 0,804 | -3,369 | <u>0,001</u> | -2,414 | <u>0,016</u> | -2,028 | <u>0,043</u> |

In the data of hospitalized patients with more serious condition, we observe the following correlations (Table 8 and Table 9). An increase (relative to background levels) of respiratory and thoracic diseases from the 1st to the 3rd day after excess of PM10 by 120%, as well as heart failure in the same time period by 18%. Excess PM2.5 was associated with a 59% increase in pulmonary embolism rate on days 2 and 3, with a 19% increase in heart failure on days 1 to 3.

Table 8. Comparison of non-parametric data from hospitalized patients in serious conditions with WHO norms for average daily concentration of PM₁₀

| Name of the disease / identified morbidity | ICD-10 | Without LAG period | | LAG period 1 day | | LAG period 2 days | | LAG period 3 days | |
|--------------------------------------------|---------|--------------------|-------|------------------|--------|-------------------|-------|-------------------|-------|
| | | Z | p | Z | p | Z | p | Z | p |
| Respiratory system and chest | C30-C39 | -1,504 | 0,133 | -2,211 | 0,027 | -2,870 | 0,004 | -2,862 | 0,004 |
| Heart failure | I50 | -1,729 | 0,084 | -3,656 | <0,001 | -3,475 | 0,001 | -2,821 | 0,005 |

Table 9. Comparison of non-parametric data from hospitalized patients in serious conditions with WHO norms for average daily concentration of PM_{2.5}

| Name of the disease / identified morbidity | ICD-10 | Without LAG period | | LAG period 1 day | | LAG period 2 days | | LAG period 3 days | |
|--------------------------------------------|---------|--------------------|-------|------------------|-------|-------------------|-------|-------------------|-------|
| | | Z | p | Z | p | Z | p | Z | p |
| Respiratory system and chest | C30-C39 | -0,361 | 0,718 | -1,270 | 0,204 | -1,265 | 0,206 | -2,119 | 0,034 |
| Pulmonary embolism | I26 | -1,601 | 0,109 | -2,302 | 0,021 | -2,894 | 0,004 | -1,852 | 0,064 |
| Heart failure | I50 | -1,586 | 0,113 | -2,831 | 0,005 | -3,195 | 0,001 | -2,799 | 0,005 |

With regard to outpatient examinations in hospitals for mild conditions that do not require hospitalization, we logically find an increased presence of respiratory diagnoses (Table 10 and Table 11).

Table 10. Correlation (Spearman's rho) of the measured values of PM₁₀-AS and the number of outpatient examinations in hospitals by groups of diseases

| Name of the disease / identified morbidity | ICD-10 | Without LAG period | LAG period 1 day | LAG period 2 days | LAG period 3 days |
|-------------------------------------------------|---------|--------------------|------------------|-------------------|-------------------|
| | | R | R | R | R |
| Respiratory system and chest | C30-C39 | 0,025 | 0,046 | 0,097* | 0,058 |
| Cerebral infarction | I63 | 0,109* | 0,138** | 0,100* | 0,112* |
| Acute upper respiratory tract infections | J00-J06 | 0,159** | 0,090* | 0,102* | 0,142** |
| Bacterial pneumonia | J13-J18 | 0,125** | 0,145** | 0,098* | 0,131** |
| Chronic diseases of the lower respiratory tract | J40-J47 | 0,044 | 0,122** | 0,072 | 0,079 |
| Acute bronchiolitis | J21 | 0,053 | 0,097* | 0,112* | 0,127** |
| Asthma with a predominant allergic component | J45.0 | 0,053 | 0,040 | 0,056 | 0,123** |

Table 11. Comparison of non-parametric data from outpatient examinations in hospitals with WHO norms for average daily concentration of PM₁₀

| Name of the disease / identified morbidity | ICD-10 | Without LAG period | | LAG period 1 day | | LAG period 2 days | | LAG period 3 days | |
|---------------------------------------------------------|-------------------|--------------------|-------|------------------|-------|-------------------|-------|-------------------|-------|
| | | Z | p | Z | p | Z | p | Z | p |
| Respiratory system and chest | C30-C39 | -1,515 | 0,130 | -2,950 | 0,003 | -2,941 | 0,003 | -2,423 | 0,015 |
| Diseases of the ear and mastoid process | H65.0, H66.0, H81 | -0,754 | 0,451 | -0,976 | 0,329 | -1,580 | 0,114 | -2,322 | 0,020 |
| Acute myocardial infarction | I20-I25 | -0,244 | 0,807 | -1,393 | 0,164 | -1,876 | 0,061 | -2,104 | 0,035 |
| Heart failure | I50 | -0,771 | 0,440 | -2,840 | 0,005 | -2,559 | 0,010 | -2,972 | 0,003 |
| Acute upper respiratory tract infections | J00-J06 | -3,218 | 0,001 | -3,507 | 0,000 | -3,910 | 0,000 | -4,605 | 0,000 |
| Bacterial pneumonia | J13-J18 | -3,171 | 0,002 | -3,395 | 0,001 | -2,556 | 0,011 | -3,683 | 0,000 |
| Acute bronchitis, Acute bronchiolitis | J20-J21 | -3,096 | 0,002 | -2,848 | 0,004 | -1,606 | 0,108 | -1,588 | 0,112 |
| Chronic diseases of the lower respiratory tract | J40-J47 | -3,988 | 0,000 | -4,049 | 0,000 | -2,842 | 0,004 | -3,481 | 0,001 |
| Skin and subcutaneous tissue infections | L00-L08 | -2,552 | 0,011 | -1,379 | 0,168 | -0,267 | 0,789 | -0,489 | 0,625 |
| Acute bronchitis caused by <i>Mycoplasma pneumoniae</i> | J20.0 | -2,330 | 0,020 | -2,327 | 0,020 | -0,430 | 0,667 | -0,431 | 0,667 |
| Acute bronchitis, unspecified | J20.9 | -2,496 | 0,013 | -1,449 | 0,147 | -0,039 | 0,969 | -1,292 | 0,197 |
| Asthma with a predominant allergic component | J45.0 | -2,426 | 0,015 | -2,808 | 0,005 | -3,577 | 0,000 | -3,643 | 0,000 |
| Other types of angina | I20.8 | -1,971 | 0,049 | -0,763 | 0,445 | -0,773 | 0,440 | -0,674 | 0,500 |

Acute infections of the upper respiratory tract and pneumonia 0-3 days increase by 47% and 60%, respectively, Chronic Obstructive Pulmonary Disease (COPD) after a day is 36% more, there are changes and acute bronchitis. Regarding asthma, the allergic asthma records raise more in days with increased pollution in comparison to non-allergic asthma. In the other studied diseases shown in Table 10 and Table 11, a smaller correlation is seen.

CONCLUSIVE COMMENTS

In conclusion, similar to data from published studies in cities in Europe, America and Asia, increased levels of air pollution are associated with higher levels of diagnosing health consequences. The process of exposure and impact is complex, and it is very difficult to obtain accurate measurements except in an exposure chamber, but with the methods of epidemiological studies and population statistics it becomes clear that pollution leads to predictable increases in disease and hence adverse economic consequences for society.

Low-cost stations have a significant error threshold (10%) and a problem when humidity levels exceed 70%. Even if a better sensor of this type is used, the fog still distorts the results as it is detected as dust (shows increased values). But still they are highly valuable for explaining how air pollution affects health as they show a lot more about what we actually breathe specifically near our own home and vicinity compared to official sensors. This pollution data can include the background pollution, as well as heating of neighboring buildings or homes, burning garbage, barbecue nearby, cars under the window and even wind picking up dust from the dirty facade. Official stations should meet the requirements for distance, classification, etc. They are intentionally not placed directly next to sources of pollution because their purpose is to account for background pollution.

Future research:

With few exceptions, short-term health effects are measured by using averaged citywide air pollution concentrations for exposure indicators. This can lead to exposure misclassification and thus to bias (Laurent et al., 2008). Measurements of the relations between health effects and air pollution can be improved with more geographically precise exposure measurements and a method to calculate personal exposure during the day, and compare it to the health condition of each individual.

There are methods to reduce the error threshold (10%) in low-cost stations, but there is a risk to have a lower consistency in the measurements and make the individual station more expensive and thus make it not feasible for having such high quantity.

Lastly, economic effects of air pollution on a local level worth further investigation. Existing software such as EPA's BenMap can be adapted to local aspects such as concentration-response relationships, population files, and health and economic data to quantify these impacts.

ACKNOWLEDGEMENTS:

The authors would like to thank the anonymous reviewers for their valuable comments to improve the paper, but also, to the hospitals Pirogov, Tokuda, the Emergency Medical Aid Sofia, Faculty of Public Health at MU Sofia, Sofia Municipality, Air for Health, Air Solutions, and air.bg for kindly providing the data for this research.

REFERENCES

- Bell, M. L., Samet, J. M., & Dominici, F. (2004). Time series studies of particulate matter. *Annu. Rev. Public Health, 25*, 247-280.
- Castell, N., Dauge, F. R., Schneider, P., Vogt, M., Lerner, U., Fishbain, B., . . . Bartonova, A. (2017). Can commercial low-cost sensor platforms contribute to air quality monitoring and exposure estimates? *Environment international, 99*, 293-302.
- Dominici, F., Sheppard, L., & Clyde, M. (2003). Health effects of air pollution: a statistical review. *International Statistical Review, 71*(2), 243-276.
- Gábelová, A., Valovičová, Z., Horváthová, E., Slameňová, D., Binková, B., Šrám, R. J., & Farmer, P. B. (2004). Genotoxicity of environmental air pollution in three European cities: Prague, Košice and Sofia. *Mutation Research/Genetic Toxicology and Environmental Mutagenesis, 563*(1), 49-59.
- Gochfeld, M., & Burger, J. (2011). Disproportionate exposures in environmental justice and other populations: the importance of outliers. *American Journal of Public Health, 101*(S1), S53-S63.
- Jayaratne, R., Liu, X., Thai, P., Dunbabin, M., & Morawska, L. (2018). The influence of humidity on the performance of a low-cost air particle mass sensor and the effect of atmospheric fog. *Atmospheric Measurement Techniques, 11*(8), 4883-4890.
- Katsouyanni, K., Schwartz, J., Spix, C., Touloumi, G., Zmirou, D., Zanobetti, A., . . . Pönkä, A. (1996). Short term effects of air pollution on health: a European approach using epidemiologic time series data: the APHEA protocol. *Journal of Epidemiology & Community Health, 50*(Suppl 1), S12-S18.
- Laurent, O., Pedrono, G., Segala, C., Filleul, L., Havard, S., Deguen, S., ... Bard, D. (2008). Air pollution, asthma attacks, and socioeconomic deprivation: a small-area case-crossover study. *American journal of epidemiology, 168*(1), 58-65.
- Li, P., Xin, J., Wang, Y., Wang, S., Li, G., Pan, X., . . . Wang, L. (2013). The acute effects of fine particles on respiratory mortality and morbidity in Beijing, 2004–2009. *Environmental Science and Pollution Research, 20*(9), 6433-6444.
- Organization, W. H. (1978). *International classification of diseases:[9th] ninth revision, basic tabulation list with alphabetic index*: World Health Organization.

- Pattenden, S., Nikiforov, B., & Armstrong, B. (2003). Mortality and temperature in Sofia and London. *Journal of Epidemiology & Community Health, 57*(8), 628-633.
- Pope, C. A., Dockery, D. W., & Schwartz, J. (1995). Review of epidemiological evidence of health effects of particulate air pollution. *Inhalation toxicology, 7*(1), 1-18.
- Rendón, A. M., Salazar, J. F., Palacio, C. A., Wirth, V., & Brötz, B. (2014). Effects of urbanization on the temperature inversion breakup in a mountain valley with implications for air quality. *Journal of Applied Meteorology and Climatology, 53*(4), 840-858.
- Samet, J., & Krewski, D. (2007). Health effects associated with exposure to ambient air pollution. *Journal of toxicology and environmental health, Part A, 70*(3-4), 227-242.
- Samet, J. M., Zeger, S. L., Dominici, F., Curriero, F., Coursac, I., Dockery, D. W., Zanobetti, A. (2000). The national morbidity, mortality, and air pollution study. *Part II: morbidity and mortality from air pollution in the United States Res Rep Health Eff Inst, 94*(pt 2), 5-79.
- Shin, S., Burnett, R. T., Kwong, J. C., Hystad, P., van Donkelaar, A., Brook, J. R., Chen, H. (2019). Ambient Air Pollution and the Risk of Atrial Fibrillation and Stroke: A Population-Based Cohort Study. *Environ Health Perspect, 127*(8), 87009. doi:10.1289/EHP4883
- Tallon, L. A., Manjourides, J., Pun, V. C., Salhi, C., & Suh, H. (2017). Cognitive impacts of ambient air pollution in the National Social Health and Aging Project (NSHAP) cohort. *Environ Int, 104*, 102-109. doi:10.1016/j.envint.2017.03.019
- Thurston, G. D., Kipen, H., Annesi-Maesano, I., Balmes, J., Brook, R. D., Cromar, K., Frampton, M. W. (2017). A joint ERS/ATS policy statement: what constitutes an adverse health effect of air pollution? An analytical framework. *European Respiratory Journal, 49*(1).
- Vermeylen, J., Nemmar, A., Nemery, B., & Hoylaerts, M. F. (2005). Ambient air pollution and acute myocardial infarction. *Journal of Thrombosis and Haemostasis, 3*(9), 1955-1961.
- Wang, W., Liu, C., Ying, Z., Lei, X., Wang, C., Huo, J., Kan, H. (2019). Particulate air pollution and ischemic stroke hospitalization: How the associations vary by constituents in Shanghai, China. *Sci Total Environ, 695*, 133780. doi:10.1016/j.scitotenv.2019.133780
- Ward, D., & Ayres, J. G. (2004). Particulate air pollution and panel studies in children: a systematic review. *Occupational and environmental medicine, 61*(4), e13-e13.
- Wing, J. J., Adar, S. D., Sanchez, B. N., Morgenstern, L. B., Smith, M. A., & Lisabeth, L. D. (2017). Short-term exposures to ambient air pollution and

- risk of recurrent ischemic stroke. *Environ Res*, 152, 304-307. doi:10.1016/j.envres.2016.11.001
- Zhang, R., Liu, G., Jiang, Y., Li, G., Pan, Y., Wang, Y., . . . Wang, Y. (2018). Acute Effects of Particulate Air Pollution on Ischemic Stroke and Hemorrhagic Stroke Mortality. *Front Neurol*, 9, 827. doi:10.3389/fneur.2018.00827
- Zimmerman, N., Presto, A. A., Kumar, S. P., Gu, J., Hauryliuk, A., Robinson, E. S., . . . Subramanian, R. (2017). Closing the gap on lower cost air quality monitoring: Machine learning calibration models to improve low-cost sensor performance. *Atmos. Meas. Tech. Discuss*, 1-36.
- Bell, M. L., Samet, J. M., & Dominici, F. (2004). Time-series studies of particulate matter. *Annu. Rev. Public Health*, 25, 247-280.
- Castell, N., Dauge, F. R., Schneider, P., Vogt, M., Lerner, U., Fishbain, B., . . . Bartonova, A. (2017). Can commercial low-cost sensor platforms contribute to air quality monitoring and exposure estimates? *Environment international*, 99, 293-302.
- Dominici, F., Sheppard, L., & Clyde, M. (2003). Health effects of air pollution: a statistical review. *International Statistical Review*, 71(2), 243-276.
- Gábelová, A., Valovičová, Z., Horváthová, E., Slameňová, D., Binková, B., Šrám, R. J., & Farmer, P. B. (2004). Genotoxicity of environmental air pollution in three European cities: Prague, Košice and Sofia. *Mutation Research/ Genetic Toxicology and Environmental Mutagenesis*, 563(1), 49-59.
- Gochfeld, M., & Burger, J. (2011). Disproportionate exposures in environmental justice and other populations: the importance of outliers. *American Journal of Public Health*, 101(S1), S53-S63.
- Jayarathne, R., Liu, X., Thai, P., Dunbabin, M., & Morawska, L. (2018). The influence of humidity on the performance of a low-cost air particle mass sensor and the effect of atmospheric fog. *Atmospheric Measurement Techniques*, 11(8), 4883-4890.
- Katsouyanni, K., Schwartz, J., Spix, C., Touloumi, G., Zmirou, D., Zanobetti, A., . . . Pönnkä, A. (1996). Short term effects of air pollution on health: a European approach using epidemiologic time series data: the APHEA protocol. *Journal of Epidemiology & Community Health*, 50(Suppl 1), S12-S18.
- Laurent, O., Pedrono, G., Segala, C., Filleul, L., Havard, S., Deguen, S., . . . Bard, D. (2008). Air pollution, asthma attacks, and socioeconomic deprivation: a small-area case-crossover study. *American journal of epidemiology*, 168(1), 58-65.
- Li, P., Xin, J., Wang, Y., Wang, S., Li, G., Pan, X., . . . Wang, L. (2013). The acute effects of fine particles on respiratory mortality and morbidity in Beijing, 2004–2009. *Environmental Science and Pollution Research*, 20(9), 6433-6444.
- NSI. (2019). Population by cities. Retrieved from <https://www.nsi.bg/bg/content/2981/%D0%BD%D0%B0%D1%81%D0%B5%D0%BB%D0>

%B5%D0%BD%D0%B8%D0%B5-%D0%BF%D0%BE-%D0%B3%D1%80%D0%B0%D0%B4%D0%BE%D0%B2%D0%B5-%D0%B8-%D0%BF%D0%BE%D0%BB.

- Organization, W. H. (1978). *International classification of diseases: [9th] ninth revision, basic tabulation list with alphabetic index*: World Health Organization.
- Organization, W. H. (2018). *International Classification of Diseases (ICD) Information Sheet*. 2018. In.
- Pattenden, S., Nikiforov, B., & Armstrong, B. (2003). Mortality and temperature in Sofia and London. *Journal of Epidemiology & Community Health*, 57(8), 628-633.
- Pope, C. A., Dockery, D. W., & Schwartz, J. (1995). Review of epidemiological evidence of health effects of particulate air pollution. *Inhalation toxicology*, 7(1), 1-18.
- Rendón, A. M., Salazar, J. F., Palacio, C. A., Wirth, V., & Brötz, B. (2014). Effects of urbanization on the temperature inversion breakup in a mountain valley with implications for air quality. *Journal of Applied Meteorology and Climatology*, 53(4), 840-858.
- Samet, J., & Krewski, D. (2007). Health effects associated with exposure to ambient air pollution. *Journal of toxicology and environmental health, Part A*, 70(3-4), 227-242.
- Samet, J. M., Zeger, S. L., Dominici, F., Curriero, F., Coursac, I., Dockery, D. W., . . . Zanobetti, A. (2000). The national morbidity, mortality, and air pollution study. *Part II: morbidity and mortality from air pollution in the United States Res Rep Health Eff Inst*, 94(pt 2), 5-79.
- Shin, S., Burnett, R. T., Kwong, J. C., Hystad, P., van Donkelaar, A., Brook, J. R., Chen, H. (2019). Ambient Air Pollution and the Risk of Atrial Fibrillation and Stroke: A Population-Based Cohort Study. *Environ Health Perspect*, 127(8), 87009. Retrieved from <https://www.ncbi.nlm.nih.gov/pubmed/31449466>
- <https://www.ncbi.nlm.nih.gov/pmc/articles/PMC6792368/pdf/ehp-127-087009.pdf>. doi:10.1289/EHP4883
- Tallon, L. A., Manjourides, J., Pun, V. C., Salhi, C., & Suh, H. (2017). Cognitive impacts of ambient air pollution in the National Social Health and Aging Project (NSHAP) cohort. *Environ Int*, 104, 102-109. Retrieved from <https://www.ncbi.nlm.nih.gov/pubmed/28392067>. doi:10.1016/j.envint.2017.03.019
- Thurston, G. D., Kipen, H., Annesi-Maesano, I., Balmes, J., Brook, R. D., Cromar, K., Frampton, M. W. (2017). A joint ERS/ATS policy statement: what constitutes an adverse health effect of air pollution? An analytical framework. *European Respiratory Journal*, 49(1).

- Vermeylen, J., Nemmar, A., Nemery, B., & Hoylaerts, M. F. (2005). Ambient air pollution and acute myocardial infarction. *Journal of Thrombosis and Haemostasis*, 3(9), 1955-1961.
- Wang, W., Liu, C., Ying, Z., Lei, X., Wang, C., Huo, J., . . . Kan, H. (2019). Particulate air pollution and ischemic stroke hospitalization: How the associations vary by constituents in Shanghai, China. *Sci Total Environ*, 695, 133780. Retrieved from <https://www.ncbi.nlm.nih.gov/pubmed/31416039>. doi:10.1016/j.scitotenv.2019.133780
- Ward, D., & Ayres, J. G. (2004). Particulate air pollution and panel studies in children: a systematic review. *Occupational and environmental medicine*, 61(4), e13-e13.
- Wing, J. J., Adar, S. D., Sanchez, B. N., Morgenstern, L. B., Smith, M. A., & Lisabeth, L. D. (2017). Short-term exposures to ambient air pollution and risk of recurrent ischemic stroke. *Environ Res*, 152, 304-307. Retrieved from <https://www.ncbi.nlm.nih.gov/pubmed/27829205>. doi:10.1016/j.envres.2016.11.001
- Zhang, R., Liu, G., Jiang, Y., Li, G., Pan, Y., Wang, Y., . . . Wang, Y. (2018). Acute Effects of Particulate Air Pollution on Ischemic Stroke and Hemorrhagic Stroke Mortality. *Front Neurol*, 9, 827. Retrieved from <https://www.ncbi.nlm.nih.gov/pubmed/30333790>. doi:10.3389/fneur.2018.00827
- Zimmerman, N., Presto, A. A., Kumar, S. P., Gu, J., Hauryliuk, A., Robinson, E. S., . . . Subramanian, R. (2017). Closing the gap on lower cost air quality monitoring: Machine learning calibration models to improve low-cost sensor performance. *Atmos. Meas. Tech. Discuss*, 2017, 1-36.

✉ **Petar Zhivkov**

<https://orcid.org/0000-0001-5687-5277>

Institute of Information and Communication Technologies

Bulgarian Academy of Sciences

Sofia, Bulgaria

E-mail: pzhivkov@iit.bas.bg

✉ **Aleksandar Simidchiev**

<https://orcid.org/0000-0003-4643-9388>

Medical Institute of Ministry of Interior

Sofia, Bulgaria

E-mail: alex@simidchiev.net

NOCTURNAL BOUNDARY-LAYER CHARACTERISTIC IN A COSTAL SITE USING LONG-TERM SODAR DATA

Damyan Barantiev, Ekaterina Batchvarova
*Climate, Atmosphere and Water Research Institute –
Bulgarian Academy of Sciences*

Abstract: The coastal Atmospheric Boundary Layer (ABL) structure is subject of research in many countries as large number of cities and industrial activities are located onshore seas, oceans or lakes. Mean characteristics of ABL at a Bulgarian Black Sea coastal site are obtained based on unique long-term (August 2008 - October 2016) acoustic remote sensing measurements. Marine and land nocturnal air flow vertical profiles are studied. Exploring data of wind and turbulence profiles with high spatial (10 m) and temporal (10 min) resolution from SCINTEC MFAS sodar revealed typical parameters as the height of the Internal Boundary Layer (IBL), nocturnal ABL height over sea and land, etc. The seasonal variability of coastal ABL characteristics is explored. The reported results can be used for verification of theoretical, mesoscale and air quality models. The study contributes to the understanding of wind regime and turbulent structure of ABL in a region with modest observation networks and data near the surface and no measurements and data in vertical direction.

Keywords: SCINTEC MFAS sodar, remote sensing data, Black Sea region, wind profiles, turbulent profiles, vertical structure, climatological studies, coastal area.

INTRODUCTION

The recent significant technological development of ground-based instruments for remote sensing made them most reliable and indispensable to study of the main meteorological parameters and turbulence in the ABL (Cimini, Marzano, & Visconti, 2011; Coulter & Kallistratova, 2004; Dirk, 2009; Emeis, 2011; A. Illingworth et al., 2013; Peña et al., 2016). Substantial interest in coastal ABL is noted, due to the complexity of the transformation processes at the abrupt change in the physical characteristics of the surface. The challenges in describing coastal processes are related to IBL formation and its height growing with the distance from the shore (Batchvarova, 2006; Hsu, 1986). Due to the formation of sublayers and the presence of local circulation in coastal zones, the atmosphere is complexly

stratified resulting in different diffusion characteristics, and hence intricate processes of air pollution dispersion compared to regions with homogeneous surface (Simpson, 1994).

A number of scientific experiments with doppler lidars, sodars, high meteorological masts, surface and aerological measurements aim to provide data to evaluate the mesometeorological models performance in coastal areas and to ensure further development of parameterizations.

Wilczak, Dabberdt, and Kropfli (1991) present the results of a complex experiment to study varying scales of airflows in California, with a center in Santa Barbara. The experiment was conducted on September 20, 1985. Doppler wind lidars, sodars, multiple stations with surface observations, and radio sounding were used. IBL study in a complex coastal area was based on airborne lidar measurements, mesometeorological modeling with CSU-RAMS and use of analytical models for the Pasific 93 experiment, Vancouver, Canada. Good agreement of modeled and measured IBL height was noted (Batchvarova, Cai, Gryning, & Steyn, 1999).

Batchvarova and Gryning (1998) investigate the IBL development in Athens during MEDCAPHOT-TRACE 1994 experiment which helped air quality management for the 2004 Olympic Games. Using tethered balloons, IBL height of 400 m was found at 4 km, and of 700 m at 13 km inland.

De Leo et al. (2008) analyze sodar data and mesometeorological modeling of the breeze circulation in the area of Lamezia Terme, at the Tyrrhenian Sea in Calabria in the summer of 2007.

Prabha, Venkatesan, Mursch-Radlgruber, Rengarajan, and Jayanthi (2002) describe observations with sodar and the formation of a Thermal Internal Boundary Layer (TIBL) during sea breeze in India for 10 days in February 1998 at transition from winter to summer.

Petenko et al. (2016) present turbulent characteristics and ABL height at Concordia Station (Dome C) in Antarctica. A sodar with an exceptional resolution of 2 m and a range of about 200 m was used.

Sodar measurements are used in a number of coastal studies around the world, but mainly for short periods. The analysis of long-term data proposed in this paper brings new information on the coastal ABL not only for Bulgaria. Except for theoretical research, the created database can be used for regime studies and evaluation of model performance in coastal areas.

MEASURING SITE AND EXPERIMENT EQUIPMENT

Meteorological Observatory (MO) Ahtopol is located at the Bulgarian Black Sea coast (Figure 1 - middle) at about 2 km southeast of the town of Ahtopol. Well expressed breeze circulation is typical in the region during warm seasons. Local circulation of lower frequency and smaller temporal and spatial scales is registered also during the cold season (Barantiev, 2017). MO Ahtopol is situated on a primarily

flat grassland at about 400 m inland and 30 m height above sea level. The coast line is stretching out from NNW to SSE with a steep about 10m high cost (Figure 1 – left and middle). For studying the wind profiles and turbulence in coastal ABL, an acoustic mono-static Doppler remote sensing system - SCINTEC Flat Array Sodar MFAS was used with a frequency range of 1650-2750 Hz, 9 emission / reception angles ($0^\circ, \pm 9.3^\circ, \pm 15.6^\circ, \pm 22.1^\circ, \pm 29^\circ$), a vertical range from 150 m to 1000 m and a vertical resolution of 10 m. The accuracy of wind speed measurement is $0.1 - 0.3 \text{ ms}^{-1}$ and for the wind direction is 2 - 3 Deg. The sodar system is mounted on the roof of the administrative building of MO Ahtopol (Figure 1 - right) at an approximate height of 4.5 m. The data records were made every 10 minutes and the average period is 20 minutes. The first measurement level is 30 m and the maximum vertical range for the study reaches 700 m.



Figure 1. Location of MO Ahtopol in southeastern Bulgaria (middle) with views of the terrene (left) and sodar system on the roof of the administrative building of MO Ahtopol (right)

DATA AND ANALYSIS OVERVIEW

Data availability

The exploration of coastal ABL characteristics in this work covers a 3014-day period from 1 August 2008 to 31 October 2016. The continuity of sodar operation was disturbed by frequent cuts of power supply until 2011 and prohibited sounding during night in 2008 and 2009 summers.

The data availability is presented in Table 1. The low data availability (yellow markings) is in summer of 2008 and 2009, because of no sodar operation during nights. Data with availability above 70% is given in green, between 40 and 70% in yellow, and below 40% in red. The actual sodar range is also presented graphically in Table 1 with one bar filled at a height of 510 m, 2 bars over 610 m, 3 bars over

710 m and 4 bars over 810 m. In this study all profiles are up to 700 m due to low availability of data above that height.

Applied analyzes

For the presented analysis, the direction from 0 to 120 Deg was assigned for marine air masses and direction from 170 to 290 Deg for the air masses from land. The entire 3014-day study period contains total of 2708 days with measurements, representing nearly 90% availability. A summary of the analyzes of the marine air masses and those from the land are presented in Table 2.

Firstly, all nocturnal land (brown color) and marine (blue color) air masses are studied, and then separately for cold and warm parts of the year to reveal specific coastal ABL characteristics. The cold part of the years is defined from November to March and the warm part from May to September (Table 2- first column). Due to the presence of breeze circulation in the studied area, the number of profiles involved in the averaged characteristics of land air masses (10.5 %) are significantly higher than marine air masses profiles (2.5 %). The conditions fulfilled in the various analyzes (fourth column at Table 2) are as follows:

- ✓ 1* - continuous profiles to fixed heights with simultaneous availability of 12 sodar output parameters (wind direction /WD/, wind speed and its dispersion /WS, sigWS/, vertical wind speed and its dispersion /W, sigW /, horizontal wind speed components and their dispersions /U, sigU, V, sigV/, eddy dissipation rate /EDR/, turbulent intensity /TI/ and turbulent kinetic energy /TKE/);
- ✓ 2 - continuous profiles with a minimum height of 110 m and simultaneous availability of 12 sodar output parameters;
- ✓ 3 - profiles consisting of a minimum of 3 points in height satisfying the wind direction condition and permitting an interruption only for lack of data.

The complexity of different fulfilled conditions in the extracted profiles (1*, 2 or 3) determines the number of profiles involved in the various analyzes (Table 2 - third column) and the maximum height to which the average profiles reach (Table 2 - second column). The lowest availability of profiles is observed under the strongest condition 1* - continuous profiles of the 12 different parameters simultaneously to fixed heights (150 m, 250 m, 270 m, 300 m, 320 m, 350 m, 450 m and 550 m). The complexity of fulfilling this condition lies in the fact that there can be heights with missing data or such rejected by the signal quality algorithms of the instrument. Using conditions 2 and 3 results in averaged profiles based on different data availability at different heights, while the condition 1* implies the same numbers of values across all heights. In this paper we analyze data fulfilling conditions 2 and 3, in order to use all data up to 700 m. During nights the range of the sodar allows to search the ABL height in the data as it can be stable ABL over land or stable/convective ABL over sea, while during days the convective ABL height over land is well above the range of the instrument.

Table 1. Monthly data availability and maximum effective height reached by the sodar (01.08.2008 - 10.31.2016)

| | I | II | III | IV | V | VI | VII | VIII | IX | X | XI |
|---------------|--------|-------|-------|--------|-------|-------|-------|-------|-------|-------|-------|
| 2008 | - | - | - | - | - | - | - | 45,2% | 40,3% | 57,7% | 59,5% |
| max range [m] | 520 | 520 | 680 | 680 | 680 | 680 | 680 | 520 | 520 | 520 | 520 |
| 2009 | 99,9% | 99,6% | 99,2% | 96,7% | 98,3% | 99,3% | 94,6% | 57,5% | 59,9% | 58,4% | 96,7% |
| max range [m] | 520 | 520 | 680 | 680 | 680 | 680 | 680 | 680 | 680 | 680 | 680 |
| 2010 | 97,5% | 98,3% | 89,0% | 68,5% | 96,8% | 86,4% | 99,9% | 98,3% | 99,9% | 92,6% | 99,6% |
| max range [m] | 680 | 680 | 680 | 680 | 680 | 680 | 560 | 510 | 510 | 510 | 510 |
| 2011 | 96,8% | 94,8% | 99,8% | 96,7% | 96,8% | 96,2% | 92,2% | 99,9% | 38,8% | 78,8% | 99,2% |
| max range [m] | 510 | 460 | 510 | 510 | 510 | 510 | 510 | 510 | 560 | 620 | 620 |
| 2012 | 75,3% | 95,8% | 99,7% | 96,7% | 99,3% | 93,3% | 99,1% | 31,9% | 96,6% | 30,6% | 23,3% |
| max range [m] | 620 | 620 | 620 | 620 | 620 | 620 | 700 | 620 | 720 | 670 | 640 |
| 2013 | 96,6% | 96,4% | 50,6% | 100,0% | 98,3% | 54,7% | 95,3% | 96,3% | 96,7% | 58,0% | 74,7% |
| max range [m] | 720 | 720 | 720 | 620 | 680 | 670 | 680 | 680 | 720 | 720 | 720 |
| 2014 | 100,0% | 99,9% | 99,7% | 100,0% | 97,1% | 99,8% | 90,0% | 59,4% | 51,7% | 98,5% | 97,5% |
| max range [m] | 720 | 720 | 720 | 720 | 720 | 720 | 720 | 720 | 750 | 750 | 750 |
| 2015 | 99,9% | 96,3% | 94,9% | 97,8% | 69,5% | 73,3% | 57,4% | 97,9% | 99,5% | 99,9% | 65,9% |
| max range [m] | 750 | 750 | 750 | 750 | 750 | 750 | 590 | 750 | 750 | 750 | 750 |
| 2016 | 80,1% | 70,0% | 76,1% | 49,9% | 35,6% | 93,2% | 99,9% | 93,0% | 75,0% | 45,4% | - |
| max range [m] | 750 | 750 | 750 | 750 | 750 | 1000 | 1000 | 1000 | 1000 | 750 | - |

AVERAGED VERTICAL PROFILES OF NOCTURNAL COASTAL BOUNDARY LAYER

Estimating the ABL height through the turbulent profiles characteristics (*sigW*, *TKE*, *BP*, etc.) has been suggested in recent years in studies based on

Table 2. Long-term analyzes of night coastal air masses by wind direction and different conditions.

| Period of analysis from 08/2008 to 10/2016 (total - 3014 days). Days with observations - 2708 days | | | |
|----------------------------------------------------------------------------------------------------|-----------------------------------------------------------------|--------------------------------------------------------------------------------|----------------------------------------|
| Analysis of land air masses /170 ÷ 290 Deg/ | Height [m] | Available profiles | Conditions |
| Nocturnal air masses /21 ÷ 05h/ (45 549 profiles) 10.5 % | 700/ 630/ 550* / 450* / 350* / 320* / 300* / 270* / 250* / 150* | 45 549/ 8 671/ 39* / 244* / 1 388* / 2 027* / 2 571* / 3 523* / 4 278* / 8022* | 3/ 2/ 1* / 1* / 1* / 1* / 1* / 1* / 1* |
| from the total period | | | |
| Nocturnal /November÷ March/ (18 616 profiles) 4.3 % | 700/ 630/ 550* / 450* / 350* / 320* / 300* / 270* / 250* / 150* | 18 616/ 4 458/ 21* / 178* / 799* / 1 224* / 1 596* / 2 143* / 2540* / 4262* | 3/ 2/ 1* / 1* / 1* / 1* / 1* / 1* / 1* |
| from the total period | | | |
| Nocturnal /May ÷ September/ (18 769 profiles) 4.3 % | 730/ 610/ 550* / 450* / 350* / 320* / 300* / 270* / 250* / 150* | 18 769/ 2 603/ 18* / 37* / 379* / 504* / 602* / 811* / 1 021* / 2 311* | 3/ 2/ 1* / 1* / 1* / 1* / 1* / 1* / 1* |
| from the total period | | | |
| Analysis of marine air masses /0 ÷ 120 Deg/ | Height [m] | Available profiles | Conditions |
| Nocturnal air masses /21 ÷ 05h/ (10 919 profiles) 2.5 % | 700/ 590/ 550* / 450* / 350* / 320* / 300* / 270* / 250* / 150* | 10 919/ 3 731/ 3* / 9* / 25* / 55* / 89* / 196* / 400* / 3 120* | 3/ 2/ 1* / 1* / 1* / 1* / 1* / 1* / 1* |
| from the total period | | | |
| Nocturnal /November÷ March/ (3 937 profiles) 0.9 % | 700/ 340/ 320* / 300* / 270* / 250* / 150* | 3 939/ 1 141/ 22* / 36* / 91* / 159* / 854* | 3/ 2/ 1* / 1* / 1* / 1* / 1* / 1* / 1* |
| from the total period | | | |
| Nocturnal /May ÷ September/ (4 666 profiles) 1.1 % | 700/ 590/ 550* / 450* / 350* / 320* / 300* / 270* / 250* / 150* | 4 666/ 1 863/ 3* / 9* / 21* / 26* / 35* / 54* / 151* / 1 654* | 3/ 2/ 1* / 1* / 1* / 1* / 1* / 1* / 1* |
| from the total period | | | |

data from remote sensing measurements (A. J. Illingworth et al., 2015; A. Illingworth et al., 2013). In the absence of temperature and humidity profiles, these analyzes allow to retrieve more information from wind data. While with the lidars the calculations of $\text{sig}W$ are based on a backscatter signals from aerosols, the measurement of turbulent characteristics with the sodars are direct. In this paper, all profiles of the turbulent parameters are presented and explored first as information from long-term measurements with high spatial and temporal resolution that are unique for Bulgaria and secondly, as the basis for retrieving of ABL characteristics, including its height.

Nocturnal land air masses

■ All nocturnal land air masses and condition 3

Characteristics of all nocturnal land air masses are shown in Figure 2 (averaged 45549 individual profiles representing 10.5% of the total period - Table 2) through 12 averaged profiles (color lines) and their dispersions (green area). A color indication expresses the availability of the data at each height. The lowest profiles availability was observed in 4 parameters ($\text{sig}WS$, $\text{sig}U$, $\text{sig}V$ and TI) due to the fact that they are calculated as a second statistical moment. Linear increase of wind speed is observed up to 540 m (1318 individual profiles available at that height). Slightly expressed peaks in the shape of the $\text{sig}W$, EDR and TKE profiles are observed at 430 m with respectively 3625, 1756 and 3011 individual profiles involved in the averaging. This suggests nocturnal stable ABL height of about 430 m. The surface layer (SL) height is detected between 50 and 100 m with characteristic changes in $\text{sig}W$, EDR and TKE profiles.

■ Nocturnal land air masses and condition 2 during the warm part of the year

Averaged nocturnal land air masses (May to September) are presented in Figure 3. The analysis with condition 2 is chosen to ensure availability of data on all levels up to 110 m and all 12 sodar parameters simultaneously. This set allows to identify peculiarity of signal at specific heights with higher confidence. These individual profiles constitute about 30% of all registered nocturnal land air masses (Table 2). Well expressed changes near 400 meters are observed in all graphics. The observed peaks in the $\text{sig}W$, EDR and TKE mean profiles are with maximum at 410 m (98 individual profiles). Almost a linear decrease in the averaged TI profile is observed after the main peak at 140 m (2412 individual profiles) and it is interrupted by a second smaller peak at 430 m (59 individual profiles). This result is the reason for the peak in the mean $\text{sig}W$, EDR and TKE profiles in Figure 2 at 430 m. Close to the ground, at a height between 50 and 80 m, changes in the $\text{sig}W$, EDR , TI and TKE profiles suggest the SL height.

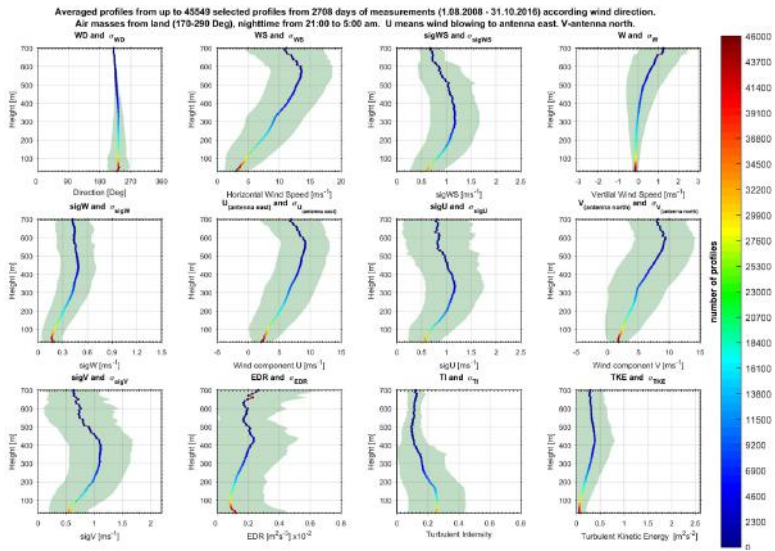


Figure 2. Averaged nocturnal land air masses characteristics with performed condition 3. Mean profiles and their dispersions from left to right and from top to bottom: *WD*, *WS*, *sigWS*, *W*, *sigW*, *U*, *sigU*, *V*, *sigV*, *EDR*, *TI*, *TKE*

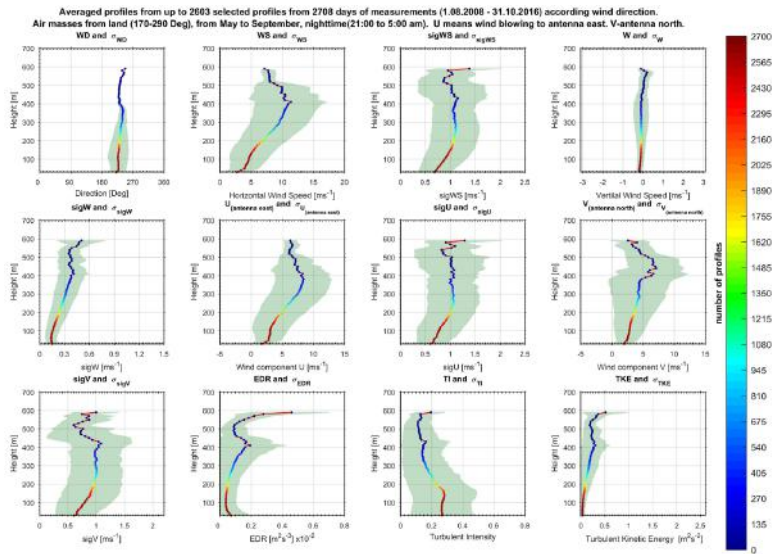


Figure 3. Averaged nocturnal land air masses characteristics during warm part of the year with performed condition 2. Details as in Fig. 2

Nocturnal marine air masses

■ Nocturnal marine air masses during the cold part of the year and condition 3

Up to 3937 individual profiles of the period November to March are used for the averaged profiles (fulfilling condition 3) and their dispersion in Figure 4. Peak at 300 m exists in $sigW$ and TKE profiles (406 and 289 individual profiles). Such a pronounced peak is also observed in EDR profile, but at 340 m (103 individual profiles). The ABL height of the slightly unstable or neutral marine air mass during the cold months is 300 - 340 m. Positive peak at 40 - 50 m in TI profile, supported by the almost constant values of $sigW$ up to 50 m and EDR up to 40 m, as well as the observed weak peaks of WD , WS and W at 40 m can be associated with height of IBL with a dominant factor the roughness surface change.

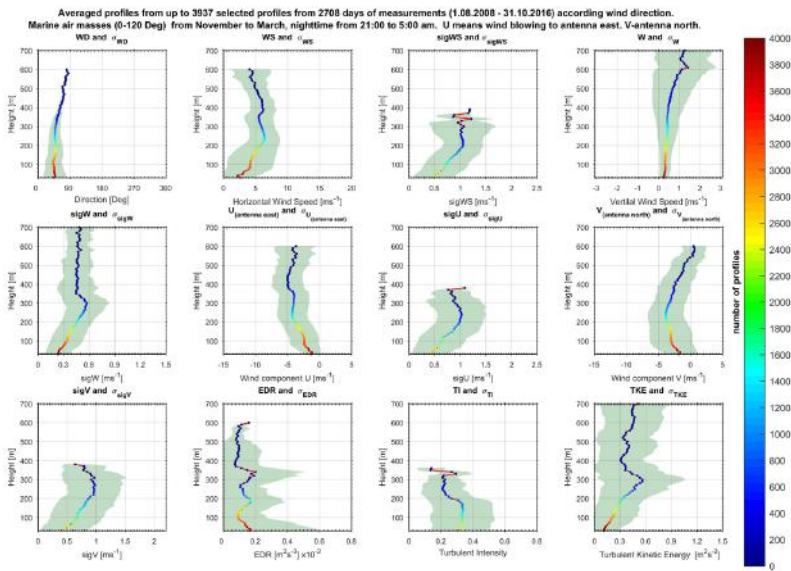


Figure 4. Averaged nocturnal marine air masses characteristics during cold part of the year with performed condition 3. Details as in Fig. 2

CONCLUSIONS

The presented results for all nocturnal land air masses with applied condition 3 show a super position of all seasonal profiles with imposed minimum restriction in their selection. Reducing the number of profiles only during the warm part of the year with applied condition 2 confirmed the results and increased the confidence in them. Choosing of the warm period suggests neutral and slightly stable air masses above land, which allows to search ABL height within the range of the sodar. The third analysis is performed at minimum restrictions (condition 3) and for the cold

period when the sea is relatively warmer than the air and neutral or slightly unstable stratification of the ABL is expected. During warm periods, due to the land breeze, the number of marine nocturnal flows is very small.

The analysis is based on 82% of the data on nocturnal land air masses. The nocturnal air masses from the land were characterized by prevailing conditions between neutral and slightly stable stratification. Indications of a nocturnal stable ABL height at 410-430 m and corresponding SL height of 50-80 m were identified.

Prevailing conditions of neutral stratified and slightly unstable stratification were revealed in the results for nocturnal marine air masses. Indication of nocturnal IBL height of about 40 – 50 m and a nocturnal marine ABL of about 300 m were identified.

Such analyzes allow not only climatological studies for a number of ABL parameters, but also assessing the fraction of time when theoretical profiles can be used in coastal areas.

ACKNOWLEDGMENTS

This work was supported by the Bulgarian Ministry of Education and Science under the National Research Programme “Young scientists and postdoctoral students” approved by DCM # 577 / 17.08.2018

REFERENCES

- Barantiev, D., Batchvarova, E. and Novitsky, M. (2017). Breeze circulation classification in the coastal zone of the town of Ahtopol based on data from ground based acoustic sounding and ultrasonic anemometer. *Bulgarian Journal of Meteorology and Hydrology (BJMH)*, 22(5), 24.
- Batchvarova, E. (2006). *Theoretical and experimental studies of the atmospheric boundary layer over different surface types*. (Dissertation for obtaining the scientific degree Doctor of Physical Sciences (Doctor Habil.). Scientific specialty: Meteorology 01.04.11), National Institute of Meteorology and Hydrology (NIMH) and the Bulgarian Academy of Sciences (BAS), Sofia.
- Batchvarova, E., Cai, X., Gryning, S.-E., & Steyn, D. (1999). Modelling internal boundary-layer development in a region with a complex coastline. *Boundary-Layer Meteorology*, 90(1), 1-20. doi:10.1023/A:1001751219627
- Batchvarova, E., & Gryning, S.-E. (1998). Wind climatology, atmospheric turbulence and internal boundary-layer development in Athens during the MEDCAPHOT-TRACE experiment. *Atmospheric Environment*, 32(12), 2055–2069. doi:https://doi.org/10.1016/S1352-2310(97)00422-6

- Cimini, Domenico, Marzano, Frank S., & Visconti, Guido. (2011). *Integrated Ground-Based Observing Systems* (Domenico Cimini, Frank S. Marzano, & Guido Visconti Eds.): Springer-Verlag Berlin Heidelberg.
- Coulter, R. L. , & Kallistratova, M. A. . (2004). Two decades of progress in SODAR techniques: a review of 11 ISARS proceedings. *Meteorology and Atmospheric Physics*, 85, 3-19. doi:<https://doi.org/10.1007/s00703-003-0030-2>
- De Leo, L., Federico, S., Sempreviva, A.M., Pasqualoni, L., Avolio, E. , & Bellecci, C. (2008). *Study of the development of the sea breeze and its micro-scale structure at a coastal site using a Multi -Tone Sodar system*. Paper presented at the 14th International Symposium for the Advancement of Boundary Layer Remote Sensing, 23-25 June 2008, Copenhagen, Denmark.
- Dirk, A.M. Engelbart et al. (Eds). (2009). *COST 720 - Final Report: Integrated ground-based remote-sensing stations for atmospheric profiling* : . Luxembourg Office for Official Publication of the European Communities.
- Emeis, Stefan. (2011). *Surface-based remote sensing of the atmospheric boundary layer* (1st ed.): Springer Netherlands.
- Hsu, S. A. (1986). A note on estimating the height of the convective internal boundary layer near shore. *Boundary-Layer Meteorology*, 35(4), pp 311-316. doi:<https://doi.org/10.1007/BF00118561>
- Illingworth, A. J., Cimini, D., Gaffard, C., Haeffelin, M., Lehmann, V., Löhnert, U., . . . Ruffieux, D. (2015). Exploiting Existing Ground-Based Remote Sensing Networks to Improve High-Resolution Weather Forecasts. *Bulletin of the American Meteorological Society*, 96(12), 2107-2125. doi:<http://dx.doi.org/10.1175/BAMS-D-13-00283.1>
- Illingworth, A., Ruffieux, D., Cimini, D., Lohnert, U., Haeffelin, M., & Lehmann, V. (2013). *COST Action ES0702 Final Report: European Ground-Based Observations of Essential Variables for Climate and Operational Meteorology*. Retrieved from COST Office, PUB1062: http://cfa.aquila.infn.it/wiki.eg-climet.org/Final_Report_EG_CLIMET.pdf
- Peña, Alfredo, Floors, R. R., Sathe, A., Gryning, S-E., Wagner, R., Courtney, M., . . . Hasager, C.B. (2016). Ten Years of Boundary-Layer and Wind-Power Meteorology at Høvsøre, Denmark. *Boundary-Layer Meteorology*, 158(1), 1-26. doi:<https://doi.org/10.1007/s10546-015-0079-8>
- Petenko, Igor , Argentini, Stefania , Casasanta, Giampietro , Kallistratova, Margarita , Sozzi, Roberto , & Viola, Angelo (2016). Wavelike Structures in the Turbulent Layer During the Morning Development of Convection at Dome C, Antarctica. *Boundary-Layer Meteorology*, 1–19. doi: <https://doi.org/10.1007/s10546-016-0173-6>

- Prabha, T. V. , Venkatesan, R., Mursch-Radlgruber, E., Rengarajan, G. , & Jayanthi, N. . (2002). Thermal Internal Boundary Layer characteristics at a tropical coastal site as observed by a mini-SODAR under varying synoptic conditions. *Journal of Earth System Science*, 111(1), 63-77. doi:<https://doi.org/10.1007/BF02702223>
- Simpson, J. E. . (1994). *Sea breeze and local winds*. Cambridge, UK: Cambridge University Press.
- Wilczak, J. M., Dabberdt, W. F., & Kropfli, R. A. (1991). Observations and Numerical Model Simulations of the Atmospheric Boundary Layer in the Santa Barbara Coastal Region. *Journal of Applied Meteorology*, 30(5), 652–673. doi:[https://doi.org/10.1175/1520-0450\(1991\)030<0652:OANMSO>2.0.CO;2](https://doi.org/10.1175/1520-0450(1991)030<0652:OANMSO>2.0.CO;2)

✉ **Damyan Barantiev**

<https://orcid.org/0000-0001-9908-9014>

Climate, Atmosphere and Water Research Institute

Bulgarian Academy of Sciences

Sofia, Bulgaria

E-mail: dbarantiev@cawri.bas.bg

✉ **Ekaterina Batchvarova**

<https://orcid.org/0000-0002-1293-9440>

Climate, Atmosphere and Water Research Institute

Bulgarian Academy of Sciences

Sofia, Bulgaria

E-mail: ekbatch@cawri.bas.bg

ENVIRONMENTAL IMPACT OF QUARRY ACTIVITIES: THE CASE STUDY OF A GNEISS DEPOSIT IN THE REGION OF BLAGOEVGRAD

**Radostina A. Angelova¹, Rositsa Velichkova¹,
Sylvia Alexandrova²**

*¹ Centre for Research and Design in Human Comfort,
Energy and Environment (CERDECEN),
Technical University of Sofia*

*² Department of Hydroaerodynamics and Hydraulic Machines,
Technical University of Sofia*

Abstract. The extraction of rock materials from the landscape is accompanied by severe influence on the nature. The research presents the assessment of the impact of the quarry activities in a gneiss deposit in the region of Blagoevgrad on the environment. The effect of the blasting operations and other quarry works are discussed in terms of the geomorphic impact, air and water pollution, noise, and influence on biota. Some measures for improvement of the quarry works and further quarry reclamation are suggested.

Keywords: quarry activities; blasting operations; environmental impact

INTRODUCTION

The nowadays knowledge on quarry activities, based on modern technologies and research, has significantly reduced the effect of quarries on the environment. However, the extraction of rock materials from the landscape cannot be performed without causing environmental consequences.

The engineering processes, related to the extraction and treatment of the rock materials, leads to a change in the use of the land, scenery, and geomorphology. Responsible operational practices can be used to control and keep at tolerable levels the engineering impacts (Luttig, 1994; Langer & Arbogast, 2002; Jin, Chen & Soboyejo, 2015; Edokpayi, Odiyo & Shikwambana, 2016). However, the environmental effects could have a cascade form: the engineering activities provoke a reaction of the natural system, which, in turns, leads to another environmental reaction, and on and on. Cascading effects could influence the environment beyond the limits of the quarry activities (Langer, 2001).

Geomorphic impact

The principal geomorphic impact of quarrying is associated with rocks and stones removal. It results in a dramatic effect on the landscape, destroys the natural habitat of relicts, affects natural sinkholes and caves (Dávid, 2010). The size of the geomorphic impact depends on the location of the quarry and its size. The disadvantage is that all quarries increase in size over time. Stanton (1996) researched the advantages of deep quarrying, as it was found that the geomorphic impact of numerous small quarries is worse than the effect of a large size quarry.

Blasting strongly preconditions the geomorphic impact of quarrying. Due to poor control or design of the blasts, stones could be projected far beyond the blast site that is considered to be a serious hazard (Langer, 2001). Besides the rock crush from the quarry face, the blast energy provokes vibrations in both the ground and air. The earth vibrations could lead to ground shaking and additional geomorphic impact: fracture of the walls of the quarry, collapse of caves, change in the sub water trajectory. Blasting could initiate even flooding events (Tan et al., 2020).

Air pollution

Air pollution in the form of dust particles of different size occurs due to blasting and both digging and crushing the rocks. Dust is one of the most visible and potentially irritating impacts of the quarry on workers, nearby settlements, and the ecosystem (Sayara, 2016). The amount of air pollution depends on the type of rocks, humidity, scale of the excavation works, air currents and prevailing winds, as well as the presence of other nearby sources of dust. As the quarry terrain recedes, the effects of dust air pollution, dust deposition and hazardous impacts rapidly diminish (Gunn & Gagen, 1987).

Noise

The main source of quarry noise is blasting, drilling, the processing machines, and stones-moving machines. Truck traffic can also be an important source of the noise. The impact of noise strongly depends on the sound source, terrain, climatic conditions. The noise is more noticeable in cold and humid days than in hot summer days (Angotzi et al., 2005) In an urban or industrial environment, background noise can mask the noise of quarry operation, while the same noise level in a rural or quiet residential suburb may be more noticeable to humans. The noise could adversely affect biota (Christian, 2003).

Water impact

Usually, the first impact of the quarry on the landscape is the removal of superficial vegetation and soil. In temperate areas, this reduces evaporation and increases effective rainfall. Excavation works can direct surface water to the groundwater system. If runoff and sediment control measures are not taken, groundwater deterioration is possible (Gunn & Hobbs, 1999).

The quarry can cause the collapse of the sinkhole, which can lead to the capture of surface water. At the same time, blasting operations can close existing groundwater passages or open a new passageway, leading to a change in the direction of groundwater and risk of contamination. Blasting itself does not necessarily affect groundwater quality: Moore and Hughes (1979) found that there was no relationship between blasting and water quality in springs. Large amounts of slime and other quarry products (fuel, waste, oil) can pollute both rivers and groundwater far beyond the quarry field.

Biota

Any species that inhabit the rocks, destroyed by the quarry, are at risk. Some species are limited to special habitats (e.g. single cave systems) and are little known. White et al. (1995) reported the discovery of 47 species of aquatic and terrestrial invertebrates in the Movile Cave and its surrounding springs, 30 of which have been completely unknown and are considered endemic.

The quarry destroys the rocky habitats or the passages to them. Only animals that are mobile and can find new homes survive. The other species die. The quarry can disturb active groundwater courses or lead to their blockage with adverse consequences for the species. The risk to groundwater and the diversion of surface water may lead to the drying up of surface and groundwater hydrological systems with the relevant biota.

It has been found that noise and air concussions can disrupt habitats at a distance of 1500 m from the quarry (Vermeulen & Whitten, 1999). Noise interferes with communication signals between animals, masks the sounds of predators and prey, and can even cause temporary or permanent hearing loss (Fletcher & Busnel, 1978).

In dry weather, dust, if uncontrolled, can spread through the air, penetrate the soil, and create harmful conditions for flora and fauna (Fletcher & Busnel, 1978). If it suffocates the leaf surface, the vegetation can be damaged due to inhibited gas exchange and reduced photosynthesis (Howard & Cameron, 1998).

The present study was performed in a real quarry for extraction of gneiss: the “Buchaka” quarry, near the city of Blagoevgrad. The aim of the study was to assess the impact of the quarry on the environment and to suggest activities for improvement of the present situation.

GENERAL DESCRIPTION OF THE DEPOSIT

Location and weather conditions

“Buchaka” quarry for making crushed stone for road pavements is located about 2 km northeast of the village of Buchino, Blagoevgrad municipality. According to data for inhabitants at a permanent and current address, 61 persons live in the village, which is situated at approx. 10 km from the city of Blagoevgrad – Fig. 1 (Google Maps, 2020). The quarry occupies part of the eastern side of the hill of the same name.

The quarry has final area dimensions of 300 x 200 m. The terrain is extremely mountainous, rocky and sparsely forested - only in the northern slope, there are

single low-stemmed trees and shrubs. The slope of the terrain is about 30 - 40 ° in the southeast direction. The displacement between the lowest and highest parts of the deposit is 50 m on average. Its altitude varies between 350 - 410 m. The lowest exploitation level of the deposit is above the level of the local erosion base (Struma River that flows in the vicinity, east of the deposit). The dominated cracked and broken rocks facilitate the drain of the fallen atmospheric precipitation in depth.



Figure 1. Location of the village of Buchino (Google Maps, 2020)

Quality of the gneisses

The geological structure of the deposit involves biotite and two-mica gneisses and gneiss-schists of Precambrian age, overlapped in places with Quaternary clays mixed with rock fragments. The two-mica striped gneisses with quartz veinlets (10-15 m thickness) predominate. According to the assessment of the Ministry of Environment and Water (Report NB-12, 2007), the quantity of the inert materials in the “Buchaka” deposit is as mentioned in Table 1.

Table 1. Amount of inert materials

| Field number | Opencast (m ³) | Deposit (m ³) |
|--------------|----------------------------|---------------------------|
| 1 | 7292 | 148565 |
| 2 | 36921 | 1279945 |
| Total | 44213 | 1428510 |

The gneisses (Fig. 2) can be used for making road groundworks (not treated with binders) for very light, light, and medium category of traffic. They could also

be involved in asphalt mixtures, as the material corresponds to the requirements of the BDS EN 13043 (2017) standard. The extracted from the deposit crushed gneiss sand is not suitable for the production of concrete and mortars, as it does not correspond to the requirements of the BDS EN 12620 (2017) standard.

Engineering characteristics

The characteristics of the excavation works in the quarry are as follows:

- Height of the working step:
 - up to 17 m for level 390 m;
 - 20 m for level 370 m;
 - up to 14 m for level 356 m.
- Angle of inclination of the working step: 75°;
- Angle of inclination of the final non-working board: 65°;
- General angle of inclination on a non-working board: 51°;
- Minimum width of the work site: 40 m;
- Width of the safety berms: 5 m;
- Slope for gravity drainage of the levels: 1% to the south-east.

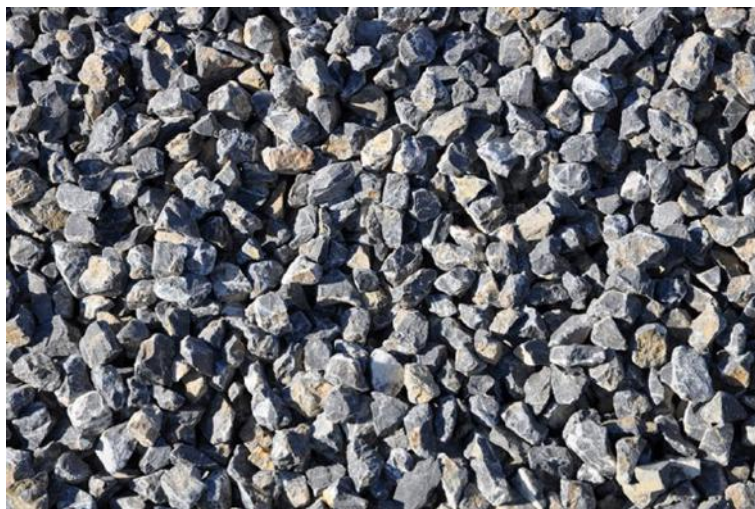


Figure 2. The processed material from the quarry

ASSESSMENT OF THE IMPACT OF THE QUARRY ON THE ENVIRONMENT AND SUGGESTIONS FOR IMPROVEMENT

Blasting operations

The blasting works in the “Buchaka” quarry are carried out by inclined drilling from the upper horizon. They are divided into:

- primary works – with the help of which the mineral is diverted from the massif;
- secondary – for additional fragmentation of the oversized pieces obtained during the primary blasting.

The primary blasting works are carried out with via blasting wells. Secondary drilling and blasting works are performed by open charges or blasting holes (depending on the size of the oversized piece) or are crushed with a hydraulic excavator-hammer. The annual opencast in the “Buchaka” quarry is 9180 m³, which corresponds to 75 m³ per working day.

Before the explosion, a signal is given with a siren. After the explosion, but not earlier than 30 minutes, the detonation field is inspected for failures. People and equipment are allowed working in the field no earlier than 14 hours after the blasting.

The nearest neighbouring objects are outside the range of the safe distance of 400.0 m. Due to the proximity of the gravel pit, the work there during the blasting works stops and both people and machinery are evacuated outside the safe area. The posts guarding the blasting works are located outside the protected zone with a radius in all directions of the blasting field of not less than 400.0 m.

To prevent gassing after blasting, the safety procedures in the quarry state that people should enter the quarry after a mandatory measurement with a gas analyzer. In addition, it is recommended to carry out mass blasting once a quarter – on the last day of the working week.

A systematic survey of the behaviour of the slopes is organized to establish movements in the working sides of the quarry and to take effective measures to prevent landslides or falling of individual rocks. To protect the neighbouring agricultural and forest lands from disturbance and pollution, no movement of machines and disposal of materials and waste is allowed on them. The produced crushed fractions and the technological waste from the processing of rock materials are placed at designated places.

On the 26th of September 2017 (Tuesday) the blasting works in the quarry however led to effect of a shock wave, which was felt in the city of Blagoevgrad in the form of an earthquake (<http://pirinsko.com>). The check in the European-Mediterranean Seismological Centre (EMSC) showed that there were no registered earthquakes in the region that could be felt in city of Blagoevgrad. The further questioning showed that the population of the Buchino village complained en masse about the explosions in the quarry. People also commented their worry about the possible change in the sub water trajectory, as all households in the village are supplied with water from underground sources. The real water impact of the quarry is commented below.

Air pollution

Blasting operations and the additional on-site fragmentation of the oversized pieces (Fig. 3) provoke the appearance of in-air particles of different size. The

access of dust particles into the human lungs depends on their physical size and chemical composition (MacNee & Donaldson, 2003). Large particles may not be able to penetrate the upper respiratory system. Most particles with an aerodynamic diameter of over 10 μm are thought to be unlikely to enter the airways of the lungs (Tranter, 2004).

As the air-pollution is strongly related to the humidity, irrigation of both work sites and transport routes in the quarry are performed during each shift. The ban on access 14 hours after the blasting operations leads to the deposition of dust particles before the presence of workers in the quarry. Mining equipment and vehicles that do not meet the requirements for the concentration of pollutants in the exhaust gases are not allowed to operate. All the equipment passes annual technical inspections.



Figure 3. On-site machine operations

Noise

The quarry and its management are responsible for assuring that the emitted noise is within the levels, set by regulations. The quarry site is located away from populated areas. However, the relief could hardly be used as a sound-deadening structure. To decrease the noise of transportation, conveyors could be used for in-pit movement of materials.

Noisy operations could be limited to certain times of the day. Similar to blasting, the noisy operations could be scheduled. A problem is the very close location of the in-pit site to the village (Fig. 4), which could be seen from Fig. Personal protective

equipment is foreseen for all workers in the quarry, including the drivers of the heavy machinery and trucks.



Figure 4. In-pit site: the neighbour houses are visible

Water impact

The quarry exploits the high parts of the sloping hill, which is intensely cracked, cavernous in places. At the establishment of the quarry, the risk assessment for the water resources were assessed as low. During the exploration works, no outflows of water or water levels in the deposit were recorded. Fallen precipitation quickly drains to a depth below the lowest operating level on the horizon + 390 m. The hydrogeological conditions could be defined as simple.

Biota

A preliminary assessment of the effect of the quarry on the biota had not been performed. In any case, the quarry works have changed the habitat of some animals, due to the human presence, blasting and noise. The effect on plants is smaller, as the low-strength soil layer is 5-10 cm thick and disappears on several places. However, all species, inhabiting the rocks, are at risk.

The start of reclamation is considered to be the beginning of the end of a career's environmental impact (Langer, 2001). Just as the natural resource of the quarry is used to improve the quality of human life, so the reclamation of the landscape improves the quality of human life. A design plan is needed for the good formation of the land from the field. There are examples of the use of quarries for recreational, tourist and even residential purposes [26]. But for the biota, it is much more important to recultivate the massif. There are examples of organized reclamation of rock

quarries to almost natural conditions. There is also evidence of natural ecosystem restoration in abandoned quarries after a period of 20 to 100 years.

CONCLUSIONS

The performed analysis highlighted the impact of “Buchaka” quarry works on the environment. The assessment showed that the quarry has a considerable impact on the natural landscape, natural resources, and biota. However, the right management and planning could minimize the negative effects and put them into control. The analysis showed that most of the prescriptions of the legislation are followed in “Buchaka” quarry. However, blasting operations and noise from drilling, machinery works, and trucks are the main sources of risks for the population in the vicinity. The impact on biota is still not highlighted enough. Plans for the further re-cultivation of the area should be elaborated.

ACKNOWLEDGMENTS

This work has been carried out in the framework of the National Science Program “Environmental Protection and Reduction of Risks of Adverse Events and Natural Disasters”, approved by the Resolution of the Council of Ministers № 577/17.08.2018 and supported by the Ministry of Education and Science (MES) of Bulgaria (Agreement № ДО-230/06-12-2018).

REFERENCES

- Angotzi, G., Bramanti, L., Tavarini, D., Gragnani, M., Cassiodoro, L., Moriconi, L., ... & Bovenzi, M. (2005). World at work: Marble quarrying in Tuscany. *Occupational and environmental medicine*, 62(6), 417 – 421.
- Arbogast, B. F., Knepper, D. H., & Langer, W. H. (2000). *The human factor in mining reclamation* (Vol. 1191). US Department of the Interior, US Geological Survey.
- BDS EN 12620:2002+A1:2008 (2017). Aggregates for concrete – National Annex (NA)
- BDS EN 13043:2005+AC:2005 (2017). Aggregates for bituminous mixtures and surface treatments for roads, airfields and other trafficked areas – National Annex.
- Christian, J. (2003). White’s Cove quarry blasting: potential impacts on American lobster. *LGL Limited, St. John’s, NL*.
- Dávid, L. (2010). Quarrying and other minerals. In *Anthropogenic Geomorphology*, 113 – 130, Springer, Dordrecht.
- Edokpayi, J. N., Odiyo, J. O., & Shikwambana, P. P. (2016). Seasonal variation of the impact of mining activities on Ga-Selati River in Limpopo Province, South Africa. *International Journal of Biological and Ecological Engineering*, 10(2), 156 – 161.

- Fletcher, J. L., & Busnel, R. G. (Eds.). (1978). *Effects of noise on wildlife*. Academic Press.
- Google Maps, 2020. *Buchino*. Imagery @2020 CNES / Airbus, Maxar Technologies, Map data @2020 [Accessed 19 August 2020].
- Gunn, J., & Gagen, P. (1987). Limestone quarrying and sinkhole development in the English Peak District. In *Multidisciplinary conference on sinkholes and the environmental impacts of karst*, 2, 121 – 125.
- Gunn, J., & Hobbs, S. L. (1999). Limestone quarrying: hydrogeological impacts, consequences, implications. *Karst hydrology and human activities—Impacts, Consequences and Implications Handbook*, 192 – 201.
- Howard, B., & Cameron, I. (1998). Dust control: Best Practice Environmental Management in Mining. *Environment Australia*.
<http://pirinsko.com/moshten-grym-ot-kariera-na-agromah-raztrese-bлаго-евград-36299.html>
- Jin, R., Chen, Q., & Soboyejo, A. (2015). Survey of the current status of sustainable concrete production in the US. *Resources, Conservation and Recycling*, 105, 148 – 159.
- Langer, W. H. (2001). *Potential environmental impacts of quarrying stone in karst: a literature review*. US Department of the Interior, US Geological Survey.
- Langer, W. H., & Arbogast, B. F. (2002). Environmental impacts of mining natural aggregate. In *Deposit and geoenvironmental models for resource exploitation and environmental security*, 151 – 169, Springer, Dordrecht.
- Luttig, G. W. (1994). Rational management of the geo-environment. In *Aggregates-Raw Materials' Giant Report on the 2n^o International Aggregate Symposium* (pp. 1 – 34).
- MacNee, W., & Donaldson, K. (2003). Mechanism of lung injury caused by PM10 and ultrafine particles with special reference to COPD. *European Respiratory Journal*, 21(40 suppl), 47 – 51.
- Moore, J. D., & Hughes, T. H. (1979). Effect of quarry blasting on groundwater quality in a limestone terrane in Calhoun County. *Alabama: Water Resources Research Institute Bulletin*, 38.
- Report NB-12 (2007). Report from 07.03.2007, Ministry of Environment and Water, Republic of Bulgaria.
- Sayara, T. (2016). Environmental impact assessment of quarries and stone cutting industries in Palestine: case study of Jamma'in. *Journal of Environment Protection and Sustainable Development*, 2(4), 32 – 38.
- Stanton, W. (1966). The impact of quarrying on the Mendip Hills. *Somerset: Proceedings of the University of Bristol Speleological Society*, 11, 54 – 62.

- Tan, Y., Zhang, S., Guo, W., Liu, X., & Shen, B. (2020). Mine Stability and Water Inrush in Coal Mine. In *Modelling Rock Fracturing Processes*, 361 – 403. Springer, Cham.
- Tranter, M. (2004). *Occupational hygiene and risk management*. Allen & Unwin.
- Vermeulen, J., & Whitten, T. (1999). *Biodiversity and cultural property in the management of limestone resources: lessons from East Asia*. The World Bank.
- White, W. B., Culver, D. C., Herman, J. S., Kane, T. C., & Mylroie, J. E. (1995). Karst lands. *American scientist*, 83(5), 450 – 459.

✉ **Radostina A. Angelova**

<https://orcid.org/0000-0002-6943-7695>

Centre for Research and Design in Human Comfort, Energy and Environment
Technical University of Sofia
Sofia, Bulgaria
E-mail: joy_angels@abv.bg

✉ **Rositsa Velichkova**

<http://orcid.org/0000-0003-3757-8685>

Centre for Research and Design in Human Comfort, Energy and Environment
Technical University of Sofia
Sofia, Bulgaria
E-mail: rositsavelichkova@abv.bg

✉ **Sylvia Alexandrova**

Department of Hydroaerodynamics and Hydraulic Machines
Technical University of Sofia
Sofia, Bulgaria
E-mail: sidial@abv.bg

***PENIOPHORA PROXIMA* (PENIOPHORACEAE, BASIDIOMYCOTA): NEWLY RECORDED FOR THE BULGARIAN MYCOTA**

Aneta Lambevska-Hristova, Svetlana Bancheva

*Department of Plant and Fungal Diversity and Resources,
Institute of Biodiversity and Ecosystem Research – Bulgarian Academy of Sciences*

Abstract: *Peniophora proxima* Bres. is corticioid fungus belonging to family *Peniophoraceae* (Basidiomycota). It is easily distinguished by the numerous encrusted cystidia, gloeocystidia and ellipsoid spores. The species is considered a common white rot saprobe restricted only to the *Buxus* representatives. One of the most popular species of the Old world is *Buxus sempervirens* L. (European boxwood), native to western and southern Europe, northwest Africa, and southwest Asia. Although the species does not belong to the native flora of Bulgaria, for many years, the European boxwoods have been one of the most popular and widely used landscaping plants, in the form of ornamental shrubs or dense, evergreen hedges in shady places. *P. proxima* has been reported from different parts of Europe, but it has not been previously reported for Bulgaria. This article reports this new find from three localities in Bulgaria, while providing information about the morphological and ecological features of the species and commenting on the pattern of its distribution.

Keywords: first record, Bulgarian mycota, *Buxus sempervirens*, lignicolous fungi.

INTRODUCTION

Buxus L. (with common names box or boxwood) is a genus of about 100 species in the family *Buxaceae*, native to western and southern Europe, southwest, southern and eastern Asia, Africa, Madagascar, northernmost South America, Central America, Mexico and the Caribbean (<http://www.theplantlist.org>¹). One of the most popular species of the Old world is *Buxus sempervirens* L. (European box), native to western and southern Europe, northwest Africa, and southwest Asia. It represents a small tree or shrub with small evergreen leaves and can reach 800 years of age. Although the species does not belong to the native flora of Bulgaria, for many years, boxwoods have been one of the most popular and widely used landscaping plants, in the form of ornamental shrubs or dense, evergreen hedges in shady places

(Jordanov, 1979). It is found in parks, gardens and yards throughout the country. In the past, boxwood has been used also to treat persistent and recurrent fever due to malaria, gout, rheumatism, urinary tract infections, hemorrhoids (Tashev & Tsavkov, 2008) and in some in folkloric traditions and customs (Boycheva & Marinova, 2017).

B. sempervirens can be a host to other organisms that use it as a substrate on which they grow (likes the fungus *Peniophora proxima* Bres.) or feed on parts of it and cause damage by destroying its tissues and organs, the lepidoptera *Cydalima perspectalis* (Walker, 1859).

Mordecai Cubitt Cooke (1879) described *Peniophora* as the first genus of corticioid fungi based on microscopic features (incrusted cystidia). According to Andreassen & Hallenberg (2009) it is a member of the section *Gloeopeniophora* Höhn. & Litsch. (with *P. incarnata*-group) which possess ellipsoid to narrow ellipsoid spores.

P. proxima belongs to the corticioid fungi with restricted range that follows the spread of *B. sempervirens*. The species is known only from *Buxus*, which makes it easy for determination (Bernicchia & Gorjón, 2010). In addition, it can be easily recognized by the numerous encrusted cystidia, gloeocystidia and ellipsoid spores (Lambevska, Rusevska & Karadelev, 2013). *P. proxima* has been reported from different parts of Europe, but it has not been previously reported for Bulgaria.

The box tree moth [*Cydalima perspectalis* (Walker, 1859) (Lep.: Crambidae)] is an invasive species of pest, native to Japan, China and Korea, but from 2006 was introduced accidentally in Europe where it spreads extremely rapidly on ornamental *Buxus* communities (Leraut, 2012). The larvae feed on the leaves and shoots and causes very serious damage. It was registered as new for Europe by Billen (2007) in Germany, where the species was probably introduced in 2005, while his first finding in Bulgaria was in 2014 by Beshkov, Abadjiev & Dimitrov (2015) in three remote locations.

Material and methods

For identification of lignicolous fungi standard methods have been applied, implying microscoping and application of reagents (Melzer's reagent and 5% KOH). Measurements and photographs were examined at magnification up to 1000×, with a LW scientific microscope and MiniVID camera.

The specimens were identified by the following sources: Eriksson & Ryvardeen (1973); Breitenbach & Kränzlin (1986); Andreassen & Hallenberg (2009); Bernicchia & Gorjón (2010), Yurchenko (2010). The nomenclature follows Index Fungorum² and Mycobank³. The studied specimens were deposited in the Mycological Collection of the Institute of Biodiversity and Ecosystem Research, Bulgarian Academy of Sciences (SOMF).

Results and discussion

During field research in the natural habitats of the genus *Juniperus* L. and in some parks in Bulgaria, in connection with a project, in connection with a project under the National Research Programme “Young scientists and postdoctoral students” of the Bulgarian Ministry of Education and Science, a species of corticoid fungi, *Peniophora proxima* Bres., was accidentally found on the *Buxus sempervirens*, which later turned out to be new to the Bulgarian mycota.

***Peniophora proxima* Bres., Bull. Soc. Mycol. Fr. 28(4): 402 (1912).**

Morphological description. Basidiome resupinate, effused, hymenophore smooth to tuberculate, reddish-pink, margin loosening from the substrate, hyphal system monomitic, hyphae with clamps, hyaline, thin-walled, somewhat agglutinated, gloeocystidia cylindrical to fusiform, thin-walled, lamprocystidia numerous, fusiform, 15-40 x 5-7 μm , basidia up to 50 x 10 μm , with 4-sterigmata, and with a basal clamp, basidiospores ellipsoid, thin-walled, smooth, 8-14 x 6-7 μm , hyaline (Fig. 1, A-B).

Ecological remarks and host. It is known to be exclusively found on *B. sempervirens*.

General distribution. *P. proxima* has been reported from different parts of Europe, Russia, France, Poland, Hungary, Belgium, United Kingdom, Slovakia, Portugal, Turkey, Sweden, Denmark, Norway, Finland, Ukraine, Macedonia, Turkey and the Caucasus (Bernicchia & Gorjón, 2010; Lambevska, Rusevska & Karadelev, 2013).

Distribution in Bulgaria. Sofia region and Central Balkan Range.

Material examined. Sofia Valley, Sofia city, “King Boris’Garden” park, urban vegetation, old tree on *B. sempervirens*, N 42.68861° E 23.33953°, 545 m,

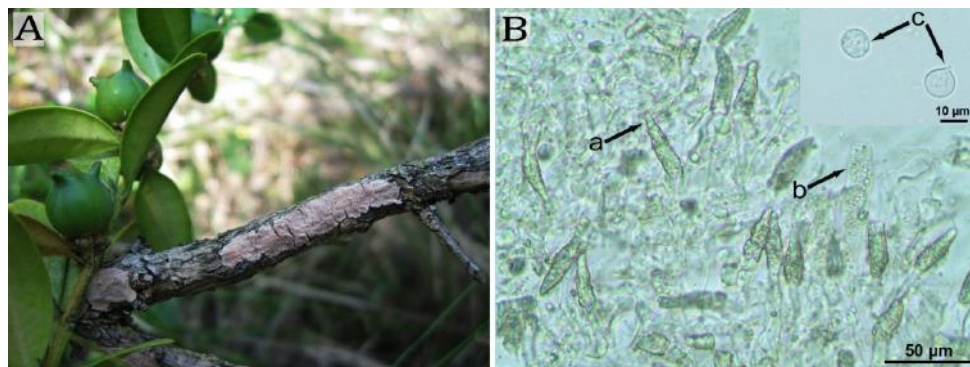


Fig. 1. A) Macroscopic view of basidiome of *P. proxima*; B) Microscopical features of *P. proxima*: section of basidiome, a) presence of numerous incrusting cystidia (lamprocystidia), b) gloeocystidia with granular content, c) basidiospores.

28.VI.2020, leg. A. Lambevsk-Hristova & G. Hristov, det. A. Lambevsk-Hristova (SOMF 30 274); Park-Museum “Vrana”, urban vegetation, old tree on *B. sempervirens*, N 42.639763° E 23.433025°, 572 m, 04.IV.2018, leg. A. Lambevsk-Hristova & G. Hristov, det. A. Lambevsk-Hristova (SOMF 30 275); Stara Planina Mt., Bozhentsi village, urban vegetation, old tree on *B. sempervirens*, N 42.872408° E 25.424716°, 531 m, 01.III.2020, leg. A. Lambevsk-Hristova & G. Hristov, det. A. Lambevsk-Hristova (SOMF 30 276).

P. proxima is microscopically easily diagnosed by its typical ellipsoid spores, gloeocystidia and the numerous encrusted cystidia. It is considered a common white rot saprobe that is apparently restricted to *Buxus* sp. (Lambevsk, Rusevsk & Karadelev, 2013). Bondartseva & Seman (1978) mentioned it as destructor of processed wood materials.

Up to now, *P. proxima* is known only from three localities in Bulgaria: two in Sofia region, “Vrana” and “King Boris’Garden” parks and one in Central Balkan Range in the Bozhentsi village.

ACKNOWLEDGEMENTS

Financial support by the Bulgarian Ministry of Education and Science under the National Research Programme “Young scientists and postdoctoral students” approved by DCM # 577 /17.08.2018 is gratefully acknowledged.

NOTE:

1. <http://www.theplantlist.org/>
2. <http://www.indexfungorum.org/Names/Names.asp>
3. <http://www.mycobank.org/>

REFERENCES

- Andreasen, M. & Hallenberg, N. (2009). A taxonomic survey of the *Peniophoraceae*. *Synopsis Fungorum*, 26, 56-119.
- Bernicchia, A. & Gorjón, S.P. (eds.) (2010). *Corticaceae* s.l. *Fungi Europaei*. Edizioni Candusso, Italia.
- Beshkov, S., Abadjiev, S. & Dimitrov, D. (2015). *Cydalima perspectalis* (Walker, 1859) (Lepidoptera: Crambidae: Spilomelinae) – new invasive pest moth in Bulgaria. *The Entomologist's Record and Journal of Variation*, 127, 18-22.
- Billen, W. (2007). *Diaphania perspectalis* (Lepidoptera: Pyralidae) – a new moth in Europe. *Mitteilungen der Entomologischen Gesellschaft Basel*, 57(2/4), 135-137.

- Bondartseva, M. A. & Seman, E. O. (1978). Fungi ex excavationibus artificialibus subterraneis RSS Armeniae. *Nov. Syst. Pl. non Vasc.*, 15, 76-81.
- Boycheva, P. & Marinova, V. (2017). An Ethnobotanical study of the medicinal plants in the Beloslav area, Northern Black Sea Coast region (Bulgaria). *International Journal of Advanced Research*, 5(12), 205-218.
- Breitenbach, J. & Kränzlin, F. (1986). Fungi of Switzerland. Vol. 2: A Contribution to the Knowledge of the Fungal Flora of Switzerland. Non-Gilled Fungi. *Heterobasidiomycetes* (jelly fungi), *Aphyllorphorales* (non-gilled fungi), *Gasteromycetes* (puffballs), *Verlag Mykologia*, Lucerne.
- Eriksson, J. & Ryvarde, L. (1973). The Corticiaceae of North Europe. Vol. 2: *Aleurodiscus-Confertobasidium*. Oslo: Fungiflora.
- Jordanov, D. (ed.). (1979). Flora Reipublicae Popularis Bulgaricae. Vol. 7. Aedibus Acad. Sci. Bulgaricae, Serdicae (in Bulgarian).
- Lambevska, A., Rusevska, K. & Karadelev, M. (2013). New data on the taxonomy, distribution and ecology of the genus *Peniophora* Cooke (Basidiomycota, Fungi) in the Republic of Macedonia. *Macedonian Journal of Ecology and Environment*, 15(2), 69-79.
- Lerout, P. (2012). Moths of Europe. Vol. 3: *Zygaenids, Pyralids 1 and Brachodids*. N.A.P. Editions, *Verrières-le Buisson*, 600.
- Tashev, A. & Tsavkov, E. (2008). Medicinal plants of the Bulgarian dendroflora. *Phytologia balcanica*, 14(2), 269-278.
- Yurchenko, E. (2010). *The genus Peniophora (Basidiomycota) of Eastern Europe: morphology, taxonomy, ecology, distribution*. National Academy of Sciences of Belarus, VF Kuprevich Institute of Experimental Botany.

✉ **Aneta Lambevska-Hristova**

<https://orcid.org/0000-0003-0061-1015>

Department of Plant and Fungal Diversity and Resources

Institute of Biodiversity and Ecosystem Research

Bulgarian Academy of Sciences

Sofia, Bulgaria

E-mail: aneta.lambevska@gmail.com

✉ **Svetlana Bancheva**

<https://orcid.org/0000-0001-7365-9971>

Department of Plant and Fungal Diversity and Resources

Institute of Biodiversity and Ecosystem Research

Bulgarian Academy of Sciences

Sofia, Bulgaria

E-mail: bancheva@bio.bas.bg

APPLICABILITY OF MTDNA CONTROL REGION FOR ASSESSMENT OF TURBOT POPULATIONS ALONG THE BULGARIAN BLACK SEA COAST

Petya Ivanova¹, Nina Dzhembekova¹, Ivan Atanassov², Krasimir Rusanov², Violin Raykov¹, Ivelina Zlateva¹, Maria Yankova¹

¹ *Institute of Oceanology – Bulgarian Academy of Sciences*

² *AgroBioInstitute – Agricultural Academy (ABI)*

Abstract: Turbot is a valuable commercial fish species classified as endangered. Knowledge of the level and distribution of genetic diversity in turbot is important for designing conservation strategies for their sustainable survival and to preserve their evolutionary potential. Mitochondrial control region sequences were investigated to evaluate variability in population genetic structure of one population along the northern Black Sea coast. 19 CR haplotypes were found in the Shabla population, which were shared with turbot haplotypes, previously described for the Black Sea and the Mediterranean. A pattern with a high level of haplotype diversity ($h=0.954\pm 0.022$) and a very low level of nucleotide diversity ($\pi=0.00563\pm 0.00063$) indicated a high number of closely related haplotypes and suggested that this population may have undergone a recent expansion. Tajima's D test and Fu's F_s test both suggest recent population growth. The haplotypes found in the Shabla population were typical for the north Black Sea populations and could be used for distinguishing the population along the Bulgarian Black Sea coast.

Keywords: control region (mt DNA), turbot, population structure, Bulgarian Black Sea coast

INTRODUCTION

The turbot (*Scophthalmus maximus* L.) is a fish species widely distributed throughout the European waters, from Northeast Atlantic to the Arctic Circle. It occurs in the Baltic and the Mediterranean, as well as in the Black Sea. It is one of the most valuable commercial species in the Black Sea and represents an endangered fishery resource. Turbot is represented by several local populations that could be considered independent units of the stock (Daskalov & Ratz, 2011), and state-of-the-art knowledge of local Black Sea turbot populations is needed for accurate assessment of general turbot stock.

Understanding the evolutionary dynamics of population structure and genetic diversity of marine fish species is of great importance for fishery management and resource conservation (Xu et al., 2018). In recent years, different molecular markers (nuclear and mitochondrial DNA) provided new information concerning the genetic variability of the Black Sea turbot populations (Nikolov et al., 2015, Turan et al., 2019a, Bessonova & Nebesikhina, 2019, Turan et al., 2019b) permitting the delineation of management units and allowing assessment of conservation priorities.

Mitochondrial DNA has been widely used in the studies of genetic structure, evolution, and population biology. Due to its simple structure, the lack of recombination, multi-copy status in a cell, maternal inheritance, and high evolutionary rate, the mtDNA has been extensively used for population genetic study and phylogenetic analysis (Shi et al., 2011). Therefore, mtDNA variations can be extremely useful for identifying and managing stocks of fish species (Billington et al., 1992, Martins et al. 2003).

The control region (CR) has been shown to evolve faster than the coding genes present in fish mitogenomes (Mate' et al., 2004), and has been utilized to trace population differentiation, phylogeographic distribution and phylogenetic reconstruction (Faber & Stepien, 1998; Martinez et al., 2006; Sivasundar et al., 2001, according to Jondeung & Karinthanyakit, 2015).

The analysis of the control region haplotype sequence data of turbot along the west Black Sea coast did not provide clear indications on the phylogeographic differentiation (Atanassov et al., 2011) and support the Suzuki et al. (2004) opinion proposed that the Mediterranean turbot populations belong to two main genetically distinct lineages, 'western Mediterranean' and 'eastern secluded Mediterranean basins'.

The genetical structure of the turbot population along the Bulgarian Black Sea coast is unclear and more population and markers have to be investigated to specify it.

The **aim** of this study is to assess the population structure of one turbot population along the northern Bulgarian Black Sea coast based on the application of one mitochondrial DNA marker (CR).

MATERIAL AND METHODS

Sample collection and DNA extraction

DNA analysis was performed on 30 turbot samples caught by a local fishing vessel in March 2019 in Shabla region (43° 30' 49.802"N 28° 44' 25.962"E), the north part of Bulgarian Black Sea coast. All tissue samples were taken from dorsal fin and stored in 96% ethanol at 40°C until the analyses. Genomic DNA was extracted using DNeasy Blood & Tissue Kit (QIAGEN).

PCR and Sequence analysis of mitochondrial DNA (CR)

The polymerase chain reaction (PCR) using mitochondrial primers (CR) was carried out in a reaction volume of 50 µl containing 2 µl of each

primer, 25 µl of mastermix (MyTaq™ HS Mix) and 2 µl of target DNA. The mitochondrial control region was PCR amplified using universal primers (L15924: 5'- AGCTCAGCGCCAGAGCGCCGGTCTTGTAAG and H16498-5'-CCTGAAGTAGGAACCAGATG, according to Atanassov et al., 2011). The conditions of PCR amplification included the following parameters: 35 cycles (94°C for 5min, 95°C for 45 sec, 50°C for 1min, 72°C for 1 min), and 72°C for 5 min. PCR product quality control was performed by electrophoresis on 2% agarose gel. The sequencing was performed by MacroGen Europe B.V. The newly described CR sequences were deposited in the GenBank under the accession numbers MN556856 – MN556885.

The new sequences and sequences extracted from the GenBank database covering all available complete CR sequences of different populations of *S. maximus* were compiled and analyzed.

Statistical analyses

MEGA7 (Kumar et al., 2018) was used to analyze mtDNA sequence data. After sequence alignment, the number of haplotypes, haplotype connectivity, and TCS Networks using Popart (Clement et al., 2002) was also constructed. The statistical robustness in the nodes of the resulting tree was determined by 1000 bootstrap replicates. Analysis performed by Tajima's D test (Tajima, 1989) tested the conformity of DNA sequence evolution to neutrality.

RESULTS AND DISCUSSION

The mitochondrial genome has been used as an effective tool for phylogenetic and population genetic analyses in vertebrates (Saitoh et al., 2016). Mitochondrial DNA polymorphism is widely used to determine population structure, species differences, and evolutionary relationships. In this study, *S. maximus* individuals from one population in the northern Black Sea were sampled to examine genetic diversity and population structure by investigating sequences of the mitochondrial control region.

The DNA sequencing of the CR PCR products produced 431 - 432 bp sequence for each turbot samples. Among the 30 individual turbot sequences, 19 CR haplotypes were found (Table 1). Nine of the haplotypes observed in Shabla were new and 10 haplotypes were identical to some haplotypes previously reported (Atanassov et al., 2011, Suzuki et al., 2004). Among the haplotypes observed in Shabla Hap7, Hap9, Hap13, and Hap16 were previously found in the north Bulgarian Black Sea coast and Hap19 was detected in the Romanian coast (Atanassov et al., 2011). The haplotypes Hap2 and Hap5 (Shabla, Black Sea) correspond to Sma15-16, both reported in the Black Sea and the second one found also in the Atlantic Ocean. The haplotypes Hap3, Hap6, and Hap14 (Sma05-08) were shared between the Shabla population (Black Sea) and

the Azov Sea population, with Hap6 found also in the Mediterranean. Two haplotypes Hap2 and Hap17 were shared with the Sea of Marmara and the former one found also in the Aegean (Suzuki et al., 2004). The data received did not support the Suzuki et al. (2004) opinion about the lack of common haplotypes between “western” and “eastern” lineages and the existence of two distinct turbot mitochondrial lineages. At the same time, there are common haplotypes between north Black Sea populations according to our data and data provided by Atanassov et al. (2011). The haplotypes of the south Black Sea populations (Atanassov et al., 2011) were not found in the Shabla population, which proposed that these markers are enough appropriate for distinguishing north and south Bulgarian population but could not be used for differentiation at a global scale as western and eastern lineages.

Table 1. Distribution of CR haplotypes of *S. maximus* populations in Shabla (SHA) (current study) and reference data from north Bulgarian coast (BS/N) (Atanassov et al., 2011), the Black Sea (BS), the Azov Sea (AS), the Aegean Sea (AGS), the Marmara Sea (MS), the Mediterranean Sea (MDS) and the Atlantic Ocean (AO) (Suzuki et al., 2004).

| Haplo type | SHA | BS/N | BS | AS | AGS | MS | MDS | AO |
|------------|-----|--------|----|----|-----|----|-----|----|
| Hap 1 | 1 | | | | | | | |
| Hap 2 | 2 | | 4 | | 2 | 1 | | |
| Hap 3 | 2 | | | 1 | | | | |
| Hap 4 | 1 | | | | | | | |
| Hap 5 | 5 | | 4 | | | | | 1 |
| Hap 6 | 4 | | | 1 | | | 1 | |
| Hap 7 | 1 | 1 | | | | | | |
| Hap 8 | 1 | | | | | | | |
| Hap9 | 1 | 1 | | | | | | |
| Hap10 | 1 | | | | | | | |
| Hap11 | 1 | | | | | | | |
| Hap12 | 1 | | | | | | | |
| Hap12 | 1 | | | | | | | |
| Hap13 | 1 | 2 | | | | | | |
| Hap14 | 2 | | | 2 | | | | |
| Hap15 | 1 | | | | | | | |
| Hap16 | 1 | 1 | | | | | | |
| Hap17 | 2 | | | | | 1 | | |
| Hap18 | 1 | | | | | | | |
| Hap19 | 1 | 1 (Ro) | | | | | | |

The CR datasets with haplotype distribution were star-like (Fig. 1), with a central predominant haplotype. The star-like topologies are often viewed as evidence of recent population expansion (Slatkin and Hudson, 1991).

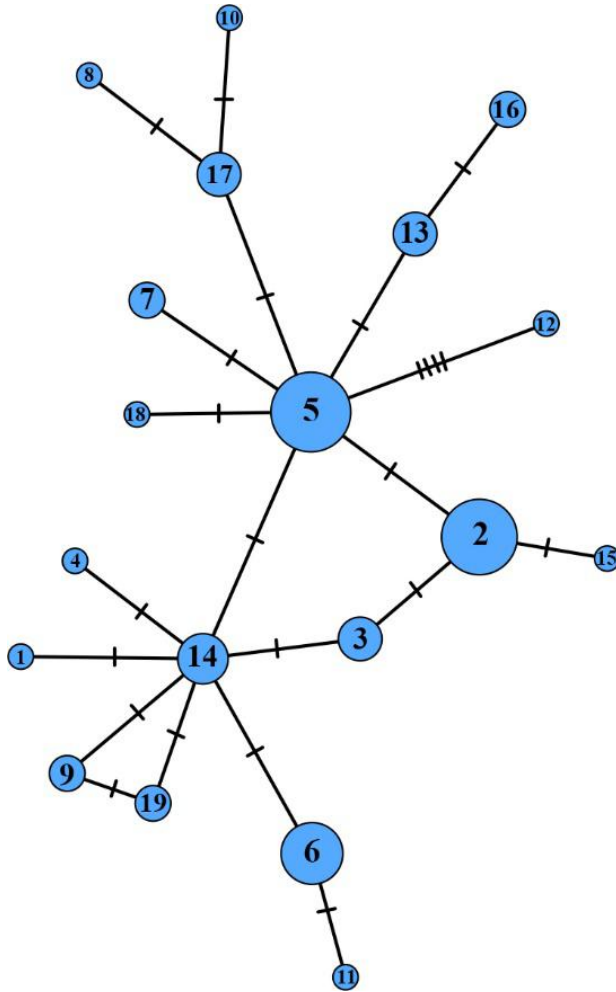


Figure 1. Haplotype network obtained from the TCS analysis. The size of the circle represents the frequency of each haplotype. Small lines represent substitutions between haplotypes.

The Shabla population of turbot showed high levels of haplotype diversity (0,954) but very low nucleotide diversity (0,00563) in the mtDNA control region

(Table 2). A high level of haplotype diversity in the same region was also reported for turbot along the Bulgarian Black Sea coast (Atanassov et al., 2011). The reason for that is that the majority of the identified haplotypes originate from a small set of dominant haplotypes (Hap 5, 2 and 14) following single nucleotide substitution.

Table 2. The genetic information of the turbot *S. maximus* populations in Shabla (SHA) (current study) and reference data from north and south Bulgarian coast (BS/N and BS/S) (Atanassov et al., 2011), the Black Sea (BS), the Azov Sea (AS), the Aegean Sea (AGS), (Suzuki et al., 2004).

| Population | Hap | pHap | Hd | π | k | D | Fs |
|------------|-----|------|---------------|-----------------|---------|-----------|---------|
| SHA | 19 | 9 | 0,954±0,022 | 0,00563±0,00063 | 2,42529 | -1,71288 | -15,924 |
| BS/N | 26 | 14 | 0,946±0,00035 | 0,00722±0,0036 | 3,11224 | -1,19452 | -19,796 |
| BS/S | 9 | 4 | 0,978±0,054 | 0,00700±0,00085 | 9,0222 | -1,299864 | -5,201 |
| BS | 9 | 2 | 0,901±0,039 | 0,00689±0,00074 | 2,97076 | -0,49028 | -1,951 |
| AS | 12 | 7 | 0,844±0,054 | 0,00513±0,00078 | 2,20899 | -1,45864 | -5,201 |

Hap: the number of haplotypes; pHap: the number of private haplotypes; Hd: haplotype diversity; π : nucleotide diversity; k: the mean number of pairwise nucleotide differences; D: Tajima's D value; Fs: Fu's Fs value.

High haplotype diversity suggests a large, stable, effective population size over time in the continental shelf fishes (Stepien, 1999), and in concurrence, with low nucleotide diversity, it has been linked to population growth after a period of low effective population size (Grant & Bowen, 1998). Low nucleotide-diversity values indicated that haplotypes were closely related; most haplotypes differed by only 1 or 2 nucleotides. Common haplotypes among populations and haplotypes from several populations indicate high genetic connectivity among the populations. High levels of haplotypic diversity and low nucleotide diversity is indicative of a population bottleneck followed by rapid population growth and accumulation of mutation (Avise, 2000). Concerning the demographic history of the population, the negative value of Tajima's D indicates a bias towards rare alleles, the latter being a signature of recent population expansion. Fu's FS test is based on the distribution of alleles or haplotypes, and negative values can indicate recent population growth (Jong et al., 2011). Tajima's D and Fu's Fs were all non-significant and negative, as expected for a recent population expansion or selection (Alcaraz & Gholami, 2018).

CONCLUSION

The mt DNA haplotypes (CR region) found in the Shabla population could be used for distinguishing of north and south Bulgarian Black Sea turbot populations. The obtained data can be useful in selecting fish stocks that preserve a better genetic diversity of *S. maximus* in conservation and/or hatchery programs.

The assessment of the genetic structure detected provides new perspectives on population structuring of turbot along the Bulgarian Black Sea coast, which can enhance the scientific foundations for the sound management of this fishery species. Effective management and conservation programs require knowledge of species' genetic diversity, population structure, and mediating factors. The data for Shabla population genetic diversity could be an essential background for the scientific management of the turbot populations along the Bulgarian Black Sea coast. To specify the genetic structure of the Black Sea turbot populations further studies are needed for increasing the number of populations analyzed and investigating more informative genetic markers.

ACKNOWLEDGMENTS

This work has been carried out in the framework of the National Science Program "Environmental Protection and Reduction of Risks of Adverse Events and Natural Disasters", approved by the Resolution of the Council of Ministers № 577/17.08.2018 and supported by the Ministry of Education and Science (MES) of Bulgaria (Agreement № D01-230/06.12.2018).

REFERENCES:

- Alcaraz, C. & Gholami, Z. (2020). Diversity and structure of fragmented populations of a threatened endemic cyprinodontid (*Aphanius sophiae*) inferred from genetics and otolith morphology: Implications for conservation and management. *J Zool Syst Evol Res.*; 58, 341–355. <https://doi.org/10.1111/jzs.12333>
- Atanassov, I., Ivanova, P., Panayotova, M., Tsekov, A., and Rusanov, K. (2011). Mitochondrial control region DNA variation in turbot populations from the Bulgarian and Romanian Black Sea coasts. *Biotechnol. Biotechnol. Equip.* 25(4), 2627-2633. doi:10.5504/BBEQ.2011.0068.
- Avice J. (1998). The history and preview of phylogeography: A personal reflection. *Mol Ecol* 7, 371–379.
- Avice J. (2000). *Phylogeography: The history and formation of species.* Cambridge, MA: Harvard University Press.
- Bessonova, N.A. & Nebesikhina, N.A. (2019) Investigation of the genetic structure of the Black Sea turbot *Scophthalmus maeoticus* (Scophthalmidae) population in the Azov and Black Seas, *Aquatic Bioresources & Environment*, vol.2, 4, 60-67.
- Billington N, Barrette RJ & Hebert PDN (1992) Management implications of mitochondrial DNA variation in walleye stocks. *North Am J Fish Manag* ,12,276-284.

- Clement M, Snell Q, Walke P, Posada D, Crandall, K (2002). TCS: estimating gene genealogies. *Proc 16th Int Parallel Distrib Process Symp* 2:184.
- Daskalov, G., & H. J. Rätz. (2011). Scientific, Technical and economic Committee for Fisheries (STECF), Opinion by written procedure: Assessment of Black Sea Stocks (STECF-OWP-11-06). EUR 25020 EN – 2011. Publications Office of the European Union, Luxembourg. [online] URL: http://stecf.jrc.ec.europa.eu/documents/43805/218009/2011-11_OWP+11-06++Black+Sea+Stock+Assessments_JRC67414.pdf
- Grant W.S. & Bowen B.W. (1998) Shallow population histories in deep evolutionary lineages of marine fishes: insights from sardines and anchovies and lessons for conservation. *Genetics*, 89, 415–426.
- Jondeung, A. & Karinthanyakit, W. (2015). Mitochondrial DNA control region of three mackerels, genus *Rastrelliger*: structure, molecular diversity and phylogenetic relationship, *Mitochondrial DNA*, Early Online: 1–6, 2015 Informa UK Ltd. DOI: 10.3109/19401736.2015.1028047ISS N: 1940-1736 (print), 1940-1744 (electronic)
- Jong MA, Wahlberg N, van Eijk M, Brakefield PM, Zwaan BJ (2011) Mitochondrial DNA Signature for Range-Wide Populations of *Bicyclus anynana* Suggests a Rapid Expansion from Recent Refugia. *PLoS ONE* 6(6): e21385. doi:10.1371/journal.pone.0021385
- Kumar S, Stecher G, Li M, Knyaz C. & Tamura K. (2018). MEGA X: Molecular Evolutionary Genetics Analysis across computing platforms, *Molecular Biology and Evolution* 35:1547-1549.
- Martins, C. Wasko, A.P., Oliveira, C. & Foresti, F. (2003). Mitochondrial DNA variation in wild populations of *Leporinus elongatus* from the Paraná River basin. *Genetics and Molecular Biology*, 26, 1, 33-38.
- Li, C., Bessert, M. L., Macrander, J., & Orti, G. (2009). Low variation but strong population structure in mitochondrial control region of the plains topminnow, *Fundulus sciadicus*. *Journal of Fish Biology*, 74, 1037–1048.
- Mate ML, Di-Rocco F, Zambelli A, Vidal-Rioja L. (2004). Mitochondrial DNA structure and organization of the control region of South American camelids. *Mol Ecol Notes*, 4, 765–767.
- Nikolov, V., Ivanova, P., Dzhebekova, N., Panayotova, M., Raykov, V., and Dobrovlov I. (2015). Application of allozyme markers for screening of turbot populations along the Western Black Sea coast. *ZooNotes*, 79, 1-15.
- Satoh, T.P., Miya, M., Mabuchi, K. & Nishida, M. (2016). Structure and variation of the mitochondrial genome of fishes. *BMC Genomics*, 17, 719, <https://doi.org/10.1186/s12864-016-3054-y>

- Shi W, Kong XY, Wang ZM, Jiang JX (2011) Utility of tRNA genes from the complete mitochondrial genome of *Psetta maxima* for implying a possible sister-group relationship to the Pleuronectiformes. *Zool Stud*, 50(5):665–681.
- Slatkin M, Hudson RR. 1991. Pairwise comparisons of mitochondrial DNA sequences in stable and exponentially growing populations. *Genetics*. 129:555–562.
- Stepien C. (1999). Phylogeographical structure of the Dover sole *Microstomus pacificus*: The larval retention hypothesis and genetic divergence along the deep continental slope of the northeastern Pacific Ocean. *Mol Ecol* 8, 923–939.
- Suzuki, N., Nishida, M., Yoseda, K., Ustundag, C., Sahin, T., & Amaoka, K., (2004). Phylogeographic relationships within the Mediterranean turbot inferred by mitochondrial DNA haplotype variation. *Journal of Fish Biology*, 65(2), 580–585.
- Tajima F. (1989). Statistical method for testing the neutral mutation hypothesis by DNA polymorphism. *Genetics*. 123:585–595.
- Turan, C., Ivanova, P., Gürlek, M., Yağlıoğlu, D., Ergüden, D., Karan, S., Doğdu, S. A., Ali Uyan, A., Öztürk, B., Nikolov V., Raykov, V., Dobrovlov, I., Khanaychenko, A. (2019 a). Phylogenetic Relationships of Turbot Species (Scophthalmidae) Inferred from the Mitochondrial COIII Gene and Morphological Characters. *NEsciences*, 2019, 4(1): 28–41doi: 10.28978/nesciences.522593.
- Turan, C., Ivanova, P., Raykov, V., Gürlek, M., Ergüden, D., Yaglioglu, D., Karan, S., Doğdu, S., Uyan, A., Oztürk, B., Nikolov, V., Dobrovlov, I., Khanaychenko, A., Giragosov, V. (2019 b). Genetics Structure Analysis of Turbot (*Scophthalmus maximus*, Linnaeus, 1758) in the Black and Mediterranean Seas for Application of Innovative Management Strategies. *Frontiers in Marine Science*. 6. 10.3389/fmars.2019.00740.
- Wang, S-Y., Shi, W., Miao X-G., & Kong X-Y., (2014) Complete mitochondrial genome sequences of three rhombosoleid fishes and comparative analyses with other flatfishes Pleuronectiformes), *Zoological Studies*, 53:80 <http://www.zoologicalstudies.com/content/53/1/80>
- Xiao, Yo., Ren, G., Song, Na., Li, J., and Gao, T. (2014). Genetic diversity and population structure of largehead hairtail, *Trichiurus japonicus*, based on mtDNA control region. *Mitochondrial DNA*, 25(6): 473–481, ISSN: 1940-1736 (print), 1940-1744 (electronic).
- Xu, S., Wang, Zh. Zhang, Y., Gao, T., Zou, J.& Zhang, X. (2018). Evidence for intra-mitochondrial variation in population genetic structure of *Platycephalus sp.1* In the Northwestern Pacific, Mitochondrial DNA Part A, DOI: 10.1080/24701394.2018.1484119

✉ **Petya Ivanova**

<https://orcid.org/0000-0002-7487-9033>

Institute of Oceanology
Bulgarian Academy of Sciences
Varna, Bulgaria
E-mail: pavl_petya@yahoo.com

✉ **Nina Dzhebekova**

<http://orcid.org/0000-0001-9620-6422>

Institute of Oceanology
Bulgarian Academy of Sciences
Varna, Bulgaria
E-mail: sonata_bg@yahoo.com

✉ **Ivan Atanassov**

<https://orcid.org/0000-0002-7771-3629>

AgroBioInstitute
Agricultural Academy
Sofia, Bulgaria
E-mail: ivan_atanassov@abv.bg

✉ **Krasimir Rusanov**

<https://orcid.org/0000-0001-8131-3364>

AgroBioInstitute
Agricultural Academy
Sofia, Bulgaria
E-mail: krusanov@abv.bg

✉ **Violin Raykov**

<http://orcid.org/0000-0003-4322-6352>

Institute of Oceanology
Bulgarian Academy of Sciences
Varna, Bulgaria
E-mail: vio_raykov@abv.bg

✉ **Ivelina Zlateva**

<https://orcid.org/0000-0003-4133-5627>

Institute of Oceanology
Bulgarian Academy of Sciences
Varna, Bulgaria
E-mail: ibikarska@yahoo.com

✉ **Maria Yankova**

<https://orcid.org/0000-0002-3333-7131>

Institute of Oceanology
Bulgarian Academy of Sciences
Varna, Bulgaria
E-mail: maria_y@abv.bg

<https://doi.org/10.48365/envr-2020.1.21>

OPEN SOURCE GIS DECISION SUPPORT TOOLS FOR WILDFIRE AND FLOOD NATURAL HAZARDS WITH EMBEDDED INTERACTIVE TRAINING RESOURCES

Stefan Stefanov¹⁾, Nina Dobrinkova¹⁾, Emilia Tosheva²⁾

*¹⁾Institute of Information and Communication Technologies –
Bulgarian Academy of Sciences (IICT-BAS)*

²⁾South-West University “Neofit Rilski”, Technical Faculty

Abstract. Training of volunteers that participate in natural hazard suppression measures is very important and time consuming. The volunteers do not have unlimited amount of time to dedicate on educational activities. Thus, interactive training platforms are the next step of the training processes. In our paper we will describe an open source Geographic Information System (GIS) tool specifically designed to support decision making for field operations in cases of natural disasters. The training activities for the tool implementation were based on Google G-Suite cloud application. The GIS application was developed to deliver field situation alerts in operational room and G suite was used before the field work as preparatory training for the teams working with it. The combination of the online tools described in the paper is presented as potential first step of real time volunteer training system that in future can be further elaborated and improved.

Keywords: G Suite; volunteer's training; open source GIS applications

INTRODUCTION

GIS tools in general are very costly licensed applications that can support georeferenced datasets analyses. This is the reason why such applications are very hard to get in everyday use for volunteer or operational groups activities in most Bulgarian municipalities. In the last two years our work was focused on GIS application development, that is based on free data and open source GIS solutions supporting decision making in cases of wildland fires and flood events. The main goal was improving accessibility, time response and communication between field operation teams. The application had to be able to visualize Points of Interest (POIs) which operational teams on the field need to know during suppression measures. Such POIs could be logistic centers for water supplies and firefighting tools for example. All of this information is very good source if the people having the tools

know how to operate with georeferenced databases. This was not the case with most of the volunteer group members in the municipalities we were working with. Thus, we decided to use Google cloud-based platform called G Suite (G-Suite) for developing of training application along with the main one. The second tool could deliver in an easy way an interactive training interesting for the volunteers and applicable in real time. G Suite is cloud-based and gives the opportunity to be used on different devices such as smart phones, tablet devices, laptops and etc. Even after the main training the resource can be used as follow up reference (Tosheva, 2019).

STUDY AREAS

The study areas used as base for development of our application have been selected based on two different international projects operating in two countries – Bulgaria and Armenia. The Bulgarian test area is situated on the territory of Zlatograd forestry department and was focused on forest fires. The flood related area was selected for Armenia in the catchment of river Voghji – Kapan region.

Bulgarian test area

The Zlatograd forestry department covers the territories of the municipalities of Zlatograd, Madan and Nedelino. All three of the municipalities are located in southern Bulgaria, at the end of the Eastern Rhodopes, to the last Rhodope hill, after which the Aegean Plain begins. The relief of the municipalities is low and medium mountainous and extends in the south-western part of the Eastern Rhodopes. The area belongs to the continental – Mediterranean climate area, the South-Bulgarian climatic sub-region and the low mountain climatic region of Eastern Rhodopes. The temperature is continental and prevails in the low mountainous regions, with a marked influence of the Aegean Sea, while in the mountainous areas there is a decrease in temperature, an increase in the amount of precipitation and the wind speed. The wildfire regime is occurring in the periods of the late spring (mid-March by mid-May) and during the second half of the summer season. Most of the wildfires have potential to cross the Bulgarian-Greek border zone and monitoring of the fire prone areas is the main concern of the local municipal authorities.

Armenian test area

The test areas covering the flood events in Armenia used in our application web-based tool are covering the territories of The Geghi reservoir and Geghanoush Tailing Storage Facility (TSF).

The Geghi reservoir is located in Syunik, the southernmost province of Armenia (Figure 1). The reservoir is situated on the Geghi River, the left-bank tributary of the river Voghji. The maximum water level discharge occurs during the spring. Due to the high-altitude nature of the area, snow melt increases gradually as does

the level of the river and the reservoir. Snow melt typically lasts from March to August (Armenian State Hydrometeorological and Monitoring Service officially used sources).

The surface of the Geghi reservoir is 50 ha and the elevation above sea level is nearly 1400 m. The height of the dam is 70 m and the length along the crest is 270 m. The total volume of reservoir is 15 million cubic meters, but the effective volume is about 12 million cubic meters. Nearly 4,300 people would be affected by in a case of a dam break of the reservoir.

The Geghanoush TSF is located in the gorge of the Geghanoush River, in the southern part of Kapan (Figure 2). The difference of relative heights between the tailing dam, on one hand, and city buildings and transport infrastructure, on the other hand, is 75 meters. In case the reservoir dam is broken due to an earthquake, the sliding mass could cover industrial and residential buildings, and as a result of barrage, the polluted water could flood central quarters of the city. The existing Geghanoush Tailings Repository was designed in early 1960's and had been operated between 1962 and 1983, when the Kajaran Tailings Repository at Artsvanik was commissioned. The Geghanoush tailings repository was re-commissioned in 2006 after the completion of the diversion works and continues to be used today along with an upstream extension currently under construction. The volume of the tailing is 5.4 million m³ and the dam height is 21.5 m.



Figure 1. The location of Geghi reservoir. The inset shows its location within Armenia. Background image: Sentinel-2, RGB composite (source: American University of Armenia)



Figure 2. The location of Geghanoush Tailing Dam. The inset shows its location within Armenia. Background image: Sentinel-2, RGB composite (source: American University of Armenia)

DESKTOP APPLICATION STRUCTURE

The wildland fire and flood events applications include features and tools which can be used by volunteers or operational teams on the field for improved response in cases of wildland fires or floods.

Wildland fires application

The developed Wildland Fire Application was implemented in the work of volunteer groups of Zlatograd municipality. It presents fire zones and POI's in the municipalities of Zlatograd, Madan and Nedelino as predefined layers and base map layers via the OpenStreetMaps (OSM) platform (Figure 3). The used techniques are based on (Singh & Gambhir, 2012), (Das, Prakash, Sandilya & Subhani, 2014), (García, Perotto-Baldivieso & Hallett, 2010). This application is able to show both active and previous fires on the tested area together with the logistic centers for water supply and other firefighting tools. The Wildland Fire Application passed the testing phase and now targeted users are working with it in order to produce better feedback for its future development and improvements.

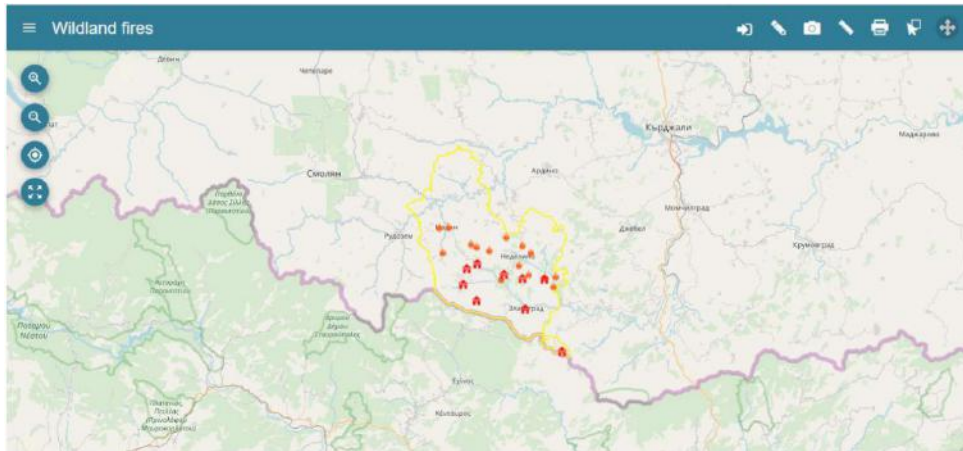


Figure 3. Wildland fires application main screen

The Wildland Fire Application has different features that can be used by firefighting or volunteer groups on the field. It is suitable for operational room operators too. The module maintains the Geolocation feature which is helpful when the first arrived team alerts the rest of the groups where the problem is. Via the Draw feature they are able to mark the locations of fires so that they become visualized and possible to be seen in the operational room. As a result, firefighters can request help or firefighting tools faster. The Draw feature is able not only to mark signs but also to depict the fire area with polygons. The Measure and Distance features are used to measure the distances between the fires and the nearest POI's and also can determine the areas of the fire zone. The module has the ability of switching the predefined layers and the base map layers. The base map layers include Street maps, Satellite maps, Shaded relief maps and NatGeo maps. These can be used mainly for analysis in the operational rooms. The Pop-Up feature visualizes information about the number and tools available in the POI's together with their locations. The Export feature is able to save the maps with the new data in map-printable format files. These outcomes can be applied for further analysis. The application provides detailed information about the current or future weather conditions via the Openweather platform. In addition, it is connected to the EFFIS emergency management services, which offer extra satellite data if the fire is big enough to be captured.

Flood events application

The Flood Event Application is able to analyze conditions that can cause flood events for the area of Armenian region Kapan located in the south east part of the country (Figure 4). The tool was used by the local civil protection teams. The software

of interest by polygon or by line in order to be visualized and to be seen in the operational rooms. As a result, civil protection teams could request more resources or specialized equipment. The Pop-Up feature visualizes information about the most vulnerable buildings such as schools, kindergartens and others. The Export feature can supplement the maps with new data, such as picture format files. These options can be used in analysis for future actions of the teams. The application is connected to the OpenWeather platform, which provides detailed information about the current or future weather conditions. It is connected to the EFAS emergency management service that provides extra satellite data about the situation through the European Emergency Services.

TRAINING

The presented open source tools that have been developed for the wildland fires and the flood events include different features, which are basic GIS skills, but if not trained, hard to be utilized. Simple and understandable training is needed in order to facilitate the work with them. To support the learning process, we used some of the Google G Suite options (G-Suite is open source platform to develop an interactive courses). G Suite is a set of cloud computing, productivity and collaboration tools, software and products. It comprises of Gmail, Hangouts, Calendar for communication, Currents, Drive for storage, Docs, Sheets, Slides, Forms, and Sites for productivity and collaboration. To develop our teaching platform, we selected to use Docs, Slides, Drive and Sites in order to set up the training platform (Tosheva, 2019). Video materials, presentations and documents were included in the web resources of both applications. The training for the Wildland Fire Tool was developed in Bulgarian language (Figure 5).

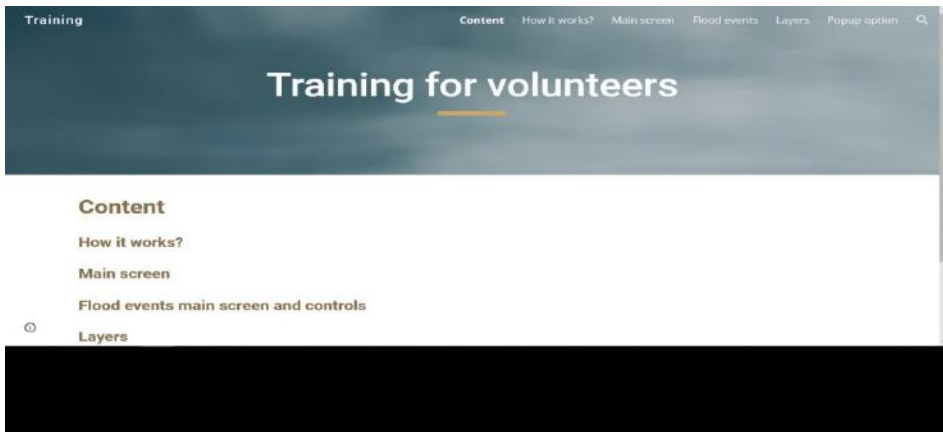


Figure 5. Wildland fires application training web resource main screen

It included lessons for different tools that are available in the application. General orientation how the application works, navigation instruction through the main menu, getting familiar with layers and how to add a new information were the main topics in the educational materials. The training set of lessons for the flood event application were developed in English language (Figure 6).



Figure 6. Flood events application training web resource main screen

The flood educational platform included lessons for different capabilities related to the flood phenomena. The lectures were based on main skills on how the application works, how navigation can be done among all features, work analyses with layers and usage of pop-up options.

CONCLUSION

The presented article gave an overview on the way of building open source web based GIS tools in support of volunteer or civil protection operational teams from the field. The main ideas how the architecture of the application can be established is described in details in (Singh & Gambhir, 2012), (Das, Prakash, Sandilya & Subhani, 2014), (García, Perotto-Baldivieso & Hallett, 2010). The future use of the platforms can be mainly from volunteer groups, firefighting or civil protection teams in their decision making on the field or in the operational rooms (Traneva, Atanasova & Tranev, 2019), (Traneva & Tranev, 2019), (Traneva, Tranev & Atanasova, 2019). This kind of ICT solutions are essential due to the growing requirements in efficient actions in the context of wildland fires and flood monitoring activities. Our tools provide opportunity for delivering critical data and knowledge in a timely manner to all participants in hazard response operations. The main goal of the Wildland Fire Application was to deliver information about fire locations and the available equipment and resources in the nearest Points of Interest (POIs) – logistic centers for water supplies and firefighting tools. In this way the Information and Communication Technologies (ICT) were able to

meliorate the orientation of the volunteer's groups on field and the reaction of the first respondents in operational rooms. The Flood Event Application main goal was to visualize the most vulnerable areas and buildings in cases of floods. It presented different scenarios that can be analyzed in operational room in order to support and improve the reaction and management of the current or future situations of flood events. The tools have been tested during both projects' lifetime. They proved to be suitable for access from everywhere where Internet connection is in place by different devices like desktop computers, smart phones, tablets and laptops.

ACKNOWLEDGMENT

This paper has been supported partially by the Bulgarian National Scientific Fund project number DFNI DN12/5 "Efficient Stochastic Methods and Algorithms for Large-Scale Problems" and the National Scientific Program "Environmental Protection and Risk Reduction Under Adverse Events and Natural Disasters" – NNP-OS contract number Д01-322/18.12.2019.

REFERENCES

- E. Tosheva (2019), *Technological model for training students in the cloud environment*, Conference on Information Technology and Development of Education – ITRO 2019 Zrenjanin, Republic of Serbia, ISBN 978-86-7672-322-5 (Tosheva, 2019).
- H. Singh, D. Gambhir, "An Open Source Approach to Build a Web GIS Application", *International Journal of Computer Science and Technology (IJCSST)*, Volume 3, ISSN: 2229-4333, p110 – p112, 2012 (Singh & Gambhir, 2012).
- A. K. Das, P. Prakash, C. Sandilya, S. Subhani, "Development of Web-Based Application for Generating and Publishing Groundwater Quality Maps Using RS/GIS Technology and P. Mapper in Sattenapalle, Mandal, Guntur District, Andhra Pradesh", In *ICT and Critical Infrastructure: Proceedings of the 48th Annual Convention of Computer Society of India*, Vol. 2, 2014, pp. 679 – 686. (Das, Prakash, Sandilya & Subhani, 2014).
- V. G. García, H. L. Perotto-Baldivieso, S. Hallett, "A prototype design for a Web-GIS disaster support system: The Bolivia Amazon case study", 2010. (García, Perotto-Baldivieso & Hallett, 2010).
- [Online] Available: <https://gsuite.google.com> (G-Suite)
- Traneva V., Atanassova V., Tranev S. *Index matrices as a decision-making tool for job appointment*, Springer Nature Switzerland AG, G. Nikolov et al. (Eds.): NMA 2018, LNCS 11189, 1 – 9, 2019. https://doi.org/10.1007/978-3-030-10692-8_19 (Traneva, Atanassova & Tranev, 2019).

Traneva V., S. Tranev. *An interval-valued intuitionistic fuzzy approach to the assignment problem. Advances in Intelligent Systems and Computing, Intelligent and Fuzzy Techniques in Big Data Analytics and Decision Making.* In: C. Kahraman et al. (Eds.). Proceedings of the INFUS Conference, July 23 – 25, 2019, Istanbul, Turkey, AISC, Vol. 1003, 1-9, 2020, ISBN 978-3-030-23755-4

DOI: 10.1007/978-3-030-23756-1_72 (Traneva & Tranev, 2019).

Traneva V., Tranev S., Atanassova V. *Index Matrices as a Cost Optimization Tool of Resource Provisioning in Uncertain Cloud Computing Environment.* In: S. Fidanova (ed.), Recent advances in computational optimization, Studies in computational intelligence, vol 838. Springer, Cham, 2020, 1 – 20. https://doi.org/10.1007/978-3-030-10692-8_19 (Traneva, Tranev & Atanasova, 2019).

✉ **Stefan Stefanov**

<https://orcid.org/0000-0001-6012-533X>

Institute of Information and Communication Technologies

Bulgarian Academy of Sciences

Sofia, Bulgaria

E-mail: stefans.stefanov303@gmail.com

✉ **Nina Dobrinkova**

<https://orcid.org/0000-0002-6506-748X>

Institute of Information and Communication Technologies

Bulgarian Academy of Sciences

Sofia, Bulgaria

E-mail: ninabox2002@gmail.com

✉ **Emilia Tosheva**

<https://orcid.org/0000-0002-3409-125X>

Technical Faculty

South-West University “Neofit Rilski”

Blagoevgrad, Bulgaria

E-mail: emilia_tosheva@swu.bg

<https://doi.org/10.48365/envr-2020.1.22>

METHODOLOGY FOR CALCULATING THE PARAMETERS OF RADIO PATHS WITH IONOSPHERIC REFLECTION

Rumiana Bojilova, Plamen Mukhtarov

*National Institute of Geophysics, Geodesy and Geography –
Bulgarian Academy of Sciences (NIGGG-BAS)*

Abstract: A methodology for calculating the parameters of radio paths operating with ionospheric reflection that depends on the state of the ionosphere and at a given distance of radio communication is presented. Based on the critical frequencies of the ionospheric regions E (foE) and F (foF2) and the maximum usable frequency at a distance of 3000 km (MUF3000), the electron density profile is reconstructed and the geometry of the radio wave reflection from the ionosphere is determined. As a result of the modeling, the frequency range of the radio waves at which radio communication is possible is determined; the latter is limited by the lowest usable frequency (LUF) and the highest usable frequency (MUF) illustrated by an example.

Keywords: radio waves, radio paths, ionosphere, critical frequencies.

INTRODUCTION

Long-distance radio communication dates back to the early twentieth century (1901 or 1902) with Marconi's experiments on radio communication across the Atlantic Ocean. At the same time, Heaviside and Kennelly suggested the existence of an ionized layer in the atmosphere that allowed radio waves to reflect off it. In the first half of the twentieth century, the work of Appleton and Ginzburg built the theory of propagation and reflection of radio waves from plasma (Appleton, 1925; Ginzburg, 1964). This theory is based on Maxwell's system of equations. The value of complex dielectric constant is introduced specifically for the electromagnetic field in plasma (Gadzhev et al., 2011; 2012). This makes it possible to use the laws of geometric optics, to derive values of the refractive index and to determine the trajectory of radio waves in the ionosphere (Rawer, 2013).

METHOD

The task for the calculation of radio paths contains the determination of the frequency range at which a radio communication at a given distance between the two

radio communication points can take place. The frequency range is limited by the minimum and maximum usable frequencies (LUF and MUF respectively), which depend on the distance of the radio communication and the state of the ionosphere at the respective time.

To solve this problem, the altitude profile of the electron concentration up to the ionospheric maximum in the reflection area of radio waves (it is the middle of the radio path) has to be known. The calculation methodology is based on the theory of radio wave propagation without taking into account the influence of Earth's magnetic field. We note that this simplification does not reduce the accuracy of the calculation. Upon entering the ionosphere, radio waves suffer the so-called magneticion splitting, i.e. they break up into two separate waves that propagate at different speeds. Traditionally, the data from the ionograms take into account ionospheric characteristics (e.g. critical frequencies) of the reflections of the ordinary wave. The propagation of an ordinary wave is not affected by the presence of the Earth's magnetic field.

The following theorems of the vertical propagation of an ordinary wave in an ionized layer prove to be sufficient for the calculation of LUF and MUF.

The formula (1) represents the dependence of the virtual height of reflection on the height profile of the electron concentration $N(z)$ in $1/\text{cm}^2$, where z is the height above the Earth in km, and the frequency of the radio signal f in MHz.

$$h'_{\text{vert}}(f) = \int_0^{z_0} \frac{dz}{\sqrt{1 - 80.8 \frac{N(z)}{f^2}}} \tag{1}$$

$$80.8 \frac{N(z_0)}{f^2} = 1$$

The reflection height z_0 is determined by the condition for equality of the operating and plasma frequency. The integral is improper (indefinite) because at the height of reflection the denominator of the sub-integral function is canceled. The ratio allows the ionogram for the vertical radio-wave propagation to be calculated, if the electron concentration profile is known.

Figure 1 shows the geometry of the oblique propagation of radio waves in the ionosphere. The secant and equivalence theorems apply to it is:

$$h'(f_{ob}) = AC = h'_{\text{vert}}(f_{\text{vert}}) \sec \varphi_0$$

$$f_{ob} = f_{\text{vert}} \sec \varphi_0 \tag{2}$$

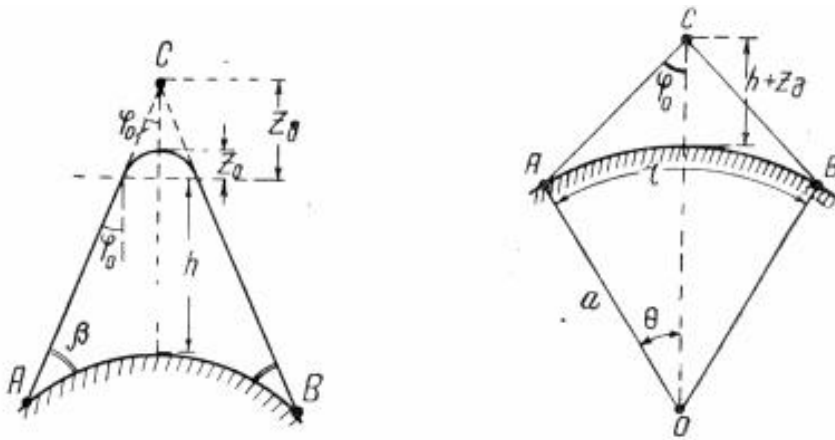


Figure 1. Basic geometrical ratios at oblique reflection of radio signals from the ionosphere

The secant theorem shown in the formula (2) reflects the following regularity. An oblique ray with a frequency f_{ob} incident on the ionosphere at an angle j_0 is reflected by the ionosphere at the same height as a vertical ray with a frequency f_{vert} .

The shown in Figure1 geometry contains a triangle with vertices at the two endpoints of the radio path (points A and B) and the upper part of the virtual reflection height h'_{vert} (point C) located in the middle of the path of the oblique frequency f_{ob} . The frequency of the oblique ray is equal to the frequency of the vertical ray multiplied by the secant of the angle j_0 , which is determined by the following formula (3), following the geometry shown in Figure1 (right plot).

$$tg \varphi_0 = \frac{a \sin(\theta)}{h'_{vert} + a(1 + \cos(\theta))} \quad (3)$$

Where a is the radius of the Earth (about 6370 km), the angle q is half of the central angle between the two endpoints of the radio path. If the length of the radio path on the Earth's surface is denoted by r , as in the Figure 1 (right plot), then its angle q in radians can be calculated by formula (4):

$$\theta [rad] = \frac{r}{2a} \quad (4)$$

The procedure for calculating the radio path begins with the synthesis of a model electron density profile based on the predicted critical frequencies $foF2$, $MUF3000$ and foE . The used model, called by the names of its creators, is the profile of Di Giovanni - Radicella (Di Giovanni & Radicella, 1990).

For daily conditions the profile is constructed according to the following formula (5):

$$\begin{aligned}
 & h \leq h_{mE}; \\
 & N(h) = N_{mE} \operatorname{sech}^2 \left(\frac{h_{mE} - h}{2B_{Eb}} \right) \\
 & h > h_{mE}; \\
 & N(h) = \left(N_{mE} - N_{mF} \operatorname{sech}^2 \left(\frac{h_{mF2} - h_{mE}}{2B_F} \right) \right) \operatorname{sech}^2 \left(\frac{h - h_{mE}}{B_{Et}} \right) + \\
 & \quad \left(N_{mF2} - N_{mE} \operatorname{sech}^2 \left(\frac{h_{mF2} - h_{mE}}{2B_{Et}} \right) \right) \operatorname{sech}^2 \left(\frac{h - h_{mF2}}{B_F} \right)
 \end{aligned} \tag{5}$$

For night conditions the respective representation is formula (6):

$$\begin{aligned}
 & f_{oE} = 0; \\
 & N(h) = N_{mF2} \operatorname{sech}^2 \left(\frac{h_{mF2} - h}{B_f} \right)
 \end{aligned} \tag{6}$$

This model is based on the representation of the electron density profile with hyperbolic secant functions (Stankov et al., 2003). The values of the three critical frequencies are sufficient to calculate the model electron density profile for heights up to the height of the F-region maximum; the latter is calculated by the given below formulas (7). The maximum electron concentration of the E and F- layers are determined directly by the critical frequencies.

The height of the E-layer maximum is assumed to be fixed 120 km. The model uses the empirically determined by Dudeney & Kressman (1986) dependence of the height of the F2-layer maximum $hmF2$ on the parameter, the ratio $foF2/foE$ and the correction value D_m according to the given below formulas (8). The parameter B_f , related to the half-thickness of the ionospheric F- layer, is expressed by an empirical dependence of the derivative of the electron profile dN/dh , which in turn is expressed by the values of $foF2$ and $M3000F2$. The half-thicknesses of the E- layer (B_{Eb} -below and B_{Et} -above the maximum of the E-region) take fixed values.

$$N_{mE} [cm^{-2}] = 1.24 \cdot 10^4 foE^2 [MHz]$$

$$N_{mF2} [cm^{-2}] = 1.24 \cdot 10^4 foF2^2 [MHz]$$

$$h_{mE} = 120 km, B_{Eb} = 7.5 km, B_{Et} = 7 km$$

$$h_{mF2} = 1470 \frac{M_f}{M3000 F2 + D_m} - 176$$

$$M3000 F2 = \frac{MUF3000}{foF2} \tag{7}$$

$$B_f = 0.04774 \cdot 10^{11} \frac{foF2^2}{dN/dh}$$

$$M_f = M3000 F2 \sqrt{\frac{0.0196 M3000 F2^2 + 1}{1.2967 M3000 F2^2 - 1}}$$

$$dN/dh = 1 \cdot 10^9 \exp(-3.467 + 0.857 \lg(foF2^2) + 2.02 \lg(M3000 F2))$$

$$foE = 0; D_m = 0;$$

$$\frac{foF2}{foE} < 1.807; D_m = -0.725 \frac{foF2}{foE} + 1.725$$

$$D_m = \frac{0.253}{\frac{foF2}{foE} - 1.215} - 0.012 \tag{8}$$

After calculating the electron profile with a vertical resolution of about 1 km, the model ionogram is calculated by numerical integration. Figure 2 shows an exemplary electron density model profile (left plot) and its respective model ionogram (right plot).

The values of the ionospheric characteristics are accepted on the basis of the data from the virtual sounding of the ionosphere with radio waves in the ionospheric station “Plana” at the National Institute of Geophysics, Geodesy and Geography - Bulgarian Academy of Sciences.

After calculating the model ionogram, which represents the function $h'_{vert}(f_{vert})$, i.e. the dependence of the virtual height on the frequency of the vertically propagating radio waves, then the calculation of the model oblique ionograms at a given distance of the radio communication (or the coordinates of the two endpoints of the radio path) according to the formulas above can be obtained.

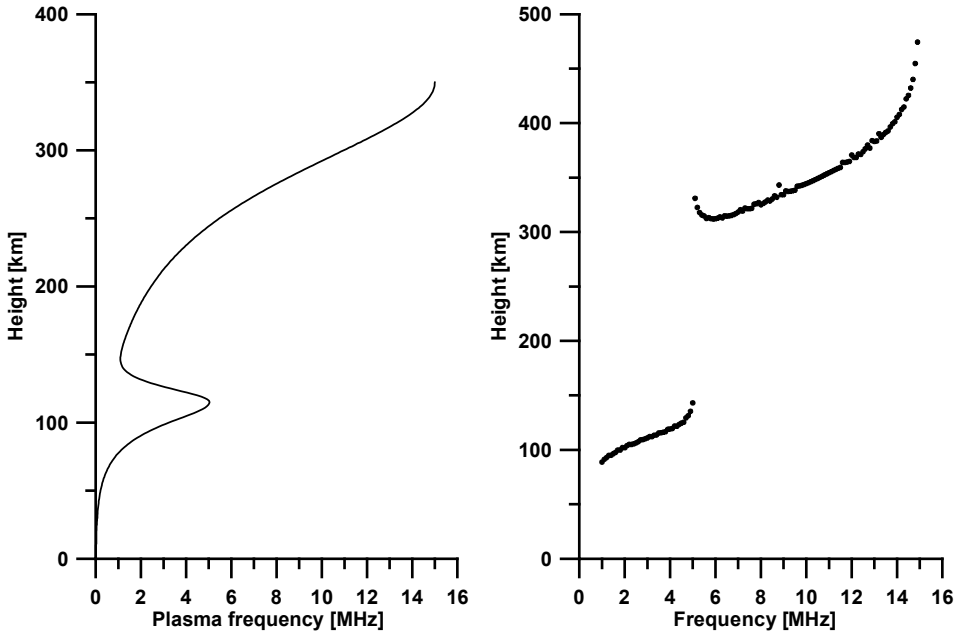


Figure 2. An example model of the electron density profile in daily conditions (left panel) and the relevant model ionogram (right panel).

The results for distances respectively 0-100 km, 250 km и 500 km are shown in Figure 3.

It can be assumed that for radio distances of up to 100 km, with sufficient accuracy for practice, the reflection of the radio waves is close to the vertical propagation. At longer distances, it is possible certain frequencies to reflect from the E and F regions. Traditionally, stable radio communications take place at reflections in F- region. Reflections from E region are accompanied by large absorption of radio wave energy due to reflection from a region with a high neutral air concentration.

The presented in Figure 3 oblique ionograms for given distances define the limits of the frequency range for radio waves reflecting from the F region at the respective distances.

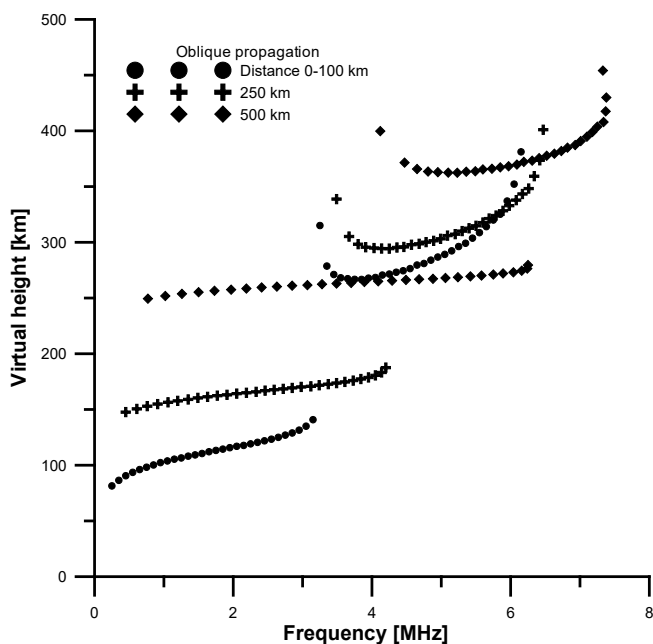


Figure 3 Oblique ionograms based on the model profile of Figure 2 at radio communication distances 0-100 km (points), 250 km (crosses) и 500 km (diamonds)

CONCLUSION

The methodology proposed in the present paper is intended for servicing users who carry out long-distance radio communications, as radio amateurs and government organizations. The methodology is suitable for organizing automatic data processing. In order to make a forecast for the propagation of radio waves at a given hour of the day, only three ionospheric characteristics are needed: foE, foF2 and MUF3000, which values can be obtained from both direct measurements and forecasting models (Pancheva & Mukhtarov, 1996, 1998).

ACKNOWLEDGMENTS

The present work is supported by the Bulgarian Ministry of Education and Science under the National Research Programme “Young scientists and postdoctoral students” approved by DCM № 577/ 17.08.2018. The presentation of the results is financed by Contract No D01-282/17.12.2019 - Project “National Geoinformation Center (NGIC)” funded by the National Roadmap for Scientific Infrastructure 2017-2023 of Bulgaria.

REFERENCES

- Appleton, E. V., (1925), Geophysical influences on the transmission of wireless waves, *Proc. Phys. Soc.*, 37, 16D.
- Gadzhev G., Syrakov, D., Ganev, K., Brandiyska, A., Miloshev, N., Georgiev, G., Prodanova, M., (2011), Atmospheric composition of the Balkan region and Bulgaria. Study of the contribution of biogenic emissions, *AIP Conference Proceedings*, 1404, pp. 200-209. DOI: 10.1063/1.3659921
- Gadzhev G., Ganev, K., Syrakov, D., Miloshev, N., Prodanova, M. (2012) Contribution of biogenic emissions to the atmospheric composition of the Balkan Region and Bulgaria. *International Journal of Environment and Pollution*, 50 (1-4), pp. 130-139. DOI: 10.1504/IJEP.2012.051187
- Ginzburg, V. L., (1964), Propagation of Electromagnetic Waves in Plasmas, *Pergamon Press*, Oxford.
- Di Giovanni, G., & Radicella, S. M. (1990). An analytical model of the electron density profile in the ionosphere. *Advances in Space Research*, 10(11), 27-30.
- Dudeney, J. R., & Kressman, R. I. (1986). Empirical models of the electron concentration of the ionosphere and their value for radio communications purposes. *Radio Science*, 21(3), 319-330.
- Pancheva, D. V., & Mukhtarov, P. Y. (1996). A single-station spectral model of the monthly median F-region critical frequency. *Annals of Geophysics*, 39(4).
- Pancheva, D., & Mukhtarov, P. (1998). A single-station spectral model of the monthly median foF2 and M (3000) F2. *Studia Geophysica et Geodaetica*, 42(2), 183-196.
- Rawer, K. (2013). Wave propagation in the ionosphere (Vol. 5). *Springer Science & Business Media*.
- Stankov, S. M., Jakowski, N., Heise, S., Muhtarov, P., Kutiev, I., & Warnant, R. (2003). A new method for reconstruction of the vertical electron density distribution in the upper ionosphere and plasmasphere. *Journal of Geophysical Research: Space Physics*, 108(A5).

✉ **Rumiana Bojilova**

National Institute of Geophysics, Geodesy and Geography
Bulgarian Academy of Sciences
Sofia, Bulgaria
E-mail: rbojilova@geophys.bas.bg

✉ **Plamen Mukhtarov**

National Institute of Geophysics, Geodesy and Geography
Bulgarian Academy of Sciences
Sofia, Bulgaria
E-mail: engpjm@abv.bg

<https://doi.org/10.48365/envr-2020.1.23>

GIS IN CRISES MANAGEMENT USE OF SMART PHONE GIS APPLICATION IN THE EVENT OF NATURAL DISASTER

Aleksandar Petrovski, Nenad Taneski, Jugoslav Ackoski

University "Goce Delchev" Shtip

Military Academy "General Mihailo Apostolski" – Skopje, North Macedonia

Abstract. Today it has become both the government and citizens concern to care human beings against ever-increasing crisis around the globe. There are so many natural disasters like: forest fire incidents, earthquakes, floods, eruptions, tsunami and etc. despite all this kinds of natural and man-made disasters from a social perspective, it their potentiality to seriously and irreversible damage regions. In addition the extent and severity of such incidents may significantly affect the population. For that reason and the fact that Geographic information system is recognized as a useful system for alleviation the risk during the crisis management we develop the idea to promote a new model to have a practical and applicable method of GIS adoption within the crisis management in order to save as many lives as it can be done. This study aims to come out with a model that will not allow drop links. Each smart phone will have application in the event of natural disaster and it switched due to the change of the vital function of man in trouble. This will help departments respond as soon as they can and save lives as many as they can and to reduce the percentage of people who could not call for help. This work highlights the design challenges and required technical innovations towards the goal of making GIS much more useful.

Keywords: GIS, disaster, crisis management, rescue, emergency response.

INTRODUCTION

The risks posed by climate change are real and its impacts are already taking place. The UN estimates that all but one of its emergency appeals for humanitarian aid in 2007 were climate related. Climate change is best viewed as a threat multiplier which exacerbates existing trends, tensions and instability. The core challenge is that climate change threatens to overburden states and regions which are already fragile and conflict prone. The effects of climate change are being felt now: temperatures are rising, icecaps and glaciers are melting and extreme weather

events are becoming more frequent and more intense¹⁾. The following section outlines some of the forms of conflicts driven by climate change which may occur in different regions of the world. Some impacts from increasing temperatures are already happening: Ice is melting worldwide, especially at the Earth's pole. Sea levels are rising faster over the last century. Precipitation (rain and snowfall) has increased across the globe, on average. Other effects could happen later this century, if warming continues. Sea levels are expected to rise between 7 and 23 inches (18 and 59 centimeters) by the end of the century, and continued melting at the poles could add between 4 and 8 inches (10 to 20 centimeters). Hurricanes and other storms are likely to become stronger. Floods and droughts will become more common. Some diseases will spread such as malaria carried by mosquito. Forest fires will become everyday situation, because of the rising temperatures caused by climate changes and will be real danger in every place on the earth, which will increase people movement in northern countries. This is a huge problem for all of us, and if we don't use all our technological resources and knowledge to small the effects of climate changes and to put all investments in prevention and reduction on it.

GIS IN CRISES MANAGEMENT

Climate change is a geographic problem, and we believe solving it takes a geographic solution. GIS has a long history of driving environmental understanding and decision making. Policymakers, planners, scientists, and many others worldwide rely on GIS for data management and scientific analysis. GIS users represent a vast reservoir of knowledge, expertise, and best practices in applying this cornerstone technology to climate science, carbon management, renewable energy, sustainability, and disaster management. When natural disasters alter the world around us, high-quality data must be collected and examined to accurately assess the damage and plan restoration efforts. Rapid response and attention to detail are both of the utmost importance. Through the use of mobile GIS, these often-opposing objectives can be achieved simultaneously. Operating PDAs equipped with Arc Pad and GPS, trained field personnel can take advantage of custom forms and other time-saving data entry features that render obsolete the use of pen, pad, and paper map. Upon return to the office, field data is integrated into the project geo-database with no additional data entry needed, allowing more time to analyze the data and develop maps and reports.

SMART PHONE GIS APPLICATION IN THE EVENT OF NATURAL DISASTER

For that porpoise it should be made a complex system of software for managing crisis situations and disasters. The system it will be able to help in all aspects of crisis management.

The system must comply with the objectives, functions and powers of the territorial bodies of executive authorities and departments of the countries, in the field of prevention, combating and elimination of criminal crises, terrorism, natural and manmade, anti-terrorist and anti-criminal protection, safety and security. Creating a system should be comprehensive interdepartmental aimed at improving information technology and information and communication infrastructure of public administration in general. To create a comprehensive system is to ensure the safety of protection by reducing the probability of threats of natural, man-made, criminal, terrorist and other situations due to:

- Effective monitoring of the current situation and providing information for the authorities;

- Providing information about the current state of security facilities, protection services and operational headquarters;

- Providing analysis and management of the threats, natural, man-made, criminal, terrorist and other character crisis;

With an integrated system must be provided:

- Development of technical regulations (conditions) to equip the objects of protection (and their components) technical means of security and control, as well as the functioning of the monitoring tools and equipment (systems).

- The ability to monitor the status of security protection objects (their elements), as well as the movement of persons and transport facilities for protection;

- Automation of the process of collecting and transmitting information to the monitoring objects of protection (their elements);

- The possibility of collecting and transmitting information from existing and emerging security products to protect and control objects;

- The possibility of collecting and transmitting information to the services of territorial bodies;

- The possibility of sharing information between services (including situational centers) with the task of ensuring human safety both on a bilateral and multilateral basis;

Must be implemented automated control mechanisms, information analysis monitoring, forecasting situations. Integrated system it will be based on geographically distributed principle and will be consisting of a single point of management, transport network, as well as places of gathering, processing and analysis of information.

The whole system it will consists of four phases.

- Phase one: Software that helps in locating, guiding and directing the people;

- Phase two: Flying drones that search and detect disasters and people;

- Phase three: Specialized machines for helping people;

- Phase four: human resources or specialized people working on field.

1st phase: Is to create a GIS software that will detect the crisis situation or disaster and to classify it. (What sort of disaster (crisis situation) and the proportions of it).

Then it will be created an appropriate application for all types of smart phones, for all types of operating systems (Android, IOS, Microsoft). The application it will have access to the location of the smart phone, calls, messages, emails and the phone contacts. This will allow locating phones in crisis areas and access to vital content on the phone (name of the user, numbers of the closest or most used phone calls), for those phones that are turned on (operational)²⁾.

The application will consist of three main functions / tools:

- Prevention or procedures and actions what to do before the disaster,
- Instructions what to be done during the crisis and
- Instructions after the crisis, how to take an appropriate measures and procedures.

1. The first function of the application will inform the users about the possible natural disaster, what to do and how to do it. Directions on how to protect provide or avoid possible situation (flood, forest fire, tsunamis, NHB pollution ...). It will inform the consumers where to head, with the appropriate address, phone numbers and how to reach the place with a particular map.

2. The second function it will be based on the morale and stability during the disaster. How the users to remain calm and not to panic, but to think realistically and rationally. Of course, the application will have all the previous functions, where, how and what to do. The most useful part in this phase is that every person can send real time SMS to crises centre with useful geo-data information that will help to people on the ground about them and their condition.

3. The third tool will consist of basic survival manuals with pictures. And measures where people to go and how to reach the most basic needs.

For all non-smart phones and cell phones that don't have GPS, this will also be possible. It can still be tracked. This is because a cell phone is basically an advanced two way radio in which communication are made via cell towers. These cell towers are within a network of cell towers which its main function is send and receive the radio signals emitting from your phone. And cell phone is basically transmitting radio signal to the nearest cell tower. The closer your phone to a cell tower, the stronger the signal that is emitted. So, by measuring the signal strength and also through triangulation method with other cell tower; that is by measuring how strong or weak signal emitted by your phone, your phone location can be pinpointed almost accurately. However, there are some disadvantages to this technique as big buildings or trees can affect the signal and therefore affect the signal strength. All users of these phones will receive un SMS and MMS with instructions.

2nd phase: The second phase will be consisting of a series of little flying drones which it will be equipped with a various sensors and cameras (video live stream, thermal scanning, structural laser scanning, Wi-Fi hotspots servers, signal scanner and receiver). Sensors for identifying the crisis and sensors for tracking and founding people. All flying drones will be communicating with one HQ that will control the drones.



Figure 1. Parrot beob drone

3rd phase will be for those who cannot reach the emergency centers and basic needs. On them will be sent help from ground and air with adequate machines (robots and drones) in the form of food, water, first aid and medicine. The machines will choose where to go alone and where to deliver the packages.

4th phase will consist of specialized teams for different kind of disasters and teams dedicated for managing crisis situations. Every team will be equipped with equipment and tools for dealing with every situation on field and in every HQ. This phase will have an option of including the Army of the country that has a crisis situation or every available people.

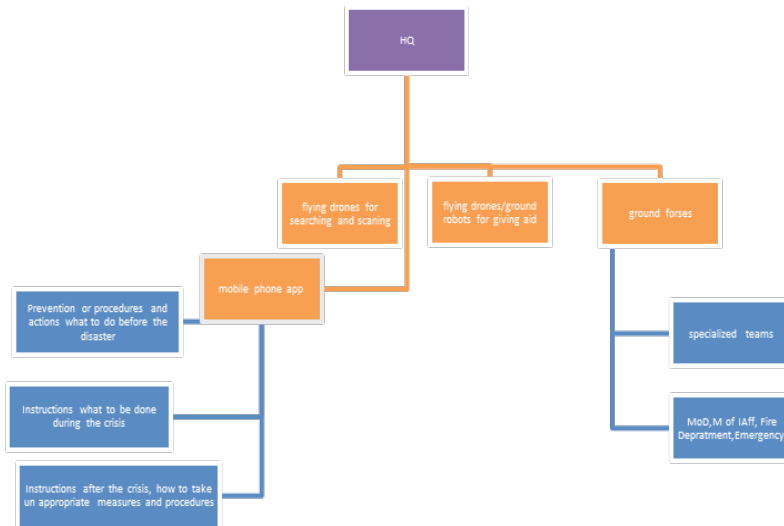


Figure 2. Structure of Geo HQ organization

NAMED DISTANCE MODEL

The second model *named distance model* is more complex and its without UAV, the position of the soldier is send via the VHF military radio from the built-in GPS. The distance and the angle to the target is determinate by the two team members using Laser Rangefinder and send to the TOC using voice communication³). There will be addition to the algorithm that will calculate the coordinates of the target using the coordinated of the rescue member, and the known distance to the target. This is done using simple geometry to determine third point when two points and all sides (distance) are known (Charles & Grinstead) and is calculating the coordinated of the victim and send them as an input to the algorithm with the received GPS data from the radios. The following steps are same as the UAV model.

System architecture of this model is represented in the following figure. Two team members use standard radio and laser rangefinder, and then the data is send via land mobile radio, to the team leader, and forwarded via Harris RF7800M and VHF Radio network to the TOC where the algorithm calculates the coordinate of the victim and makes the decision in accordance to the created algorithm.

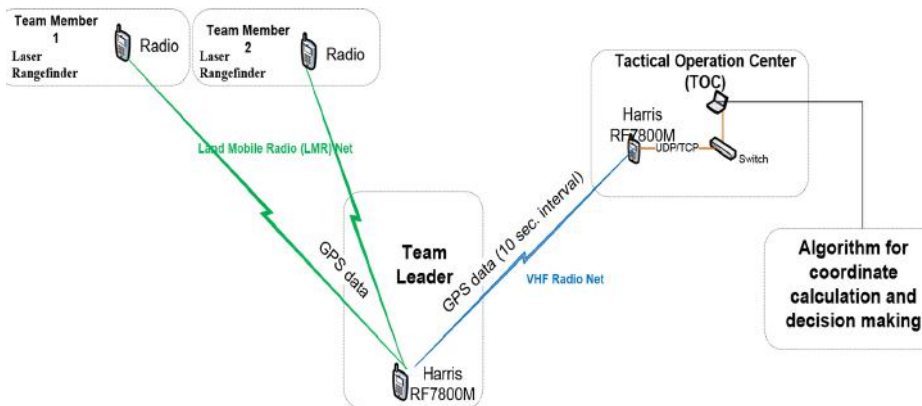


Figure 3. System architecture for the distance model

ALGORITHM

Steps of the algorithm:

First: for all our team members we are checking the visibility to the goal by our GIS connected by UAV or voice communication.

Second for team member that have visibility we measure the distance to the victim.

Third we get the information for weather conditions from nearby weather stations or our meteorological data.

Fourth from the appropriate tables we get the appropriate probabilities to save the victim.

Fifth (and finally) the team member with the biggest probability to save the victim gets an order to save the man in trouble.

EXPLAINING ONE REAL SITUATION ON THE GROUND

We are giving real description of our algorithm. We have five team members and for them we know the number of saves to the goal from 100 attempts. Also we have number of saves in different weather condition: sun weather, haze weather, poor rain, and straight rain. Another important characteristic that we must to now is distance from the team member to the man in trouble.

Table 1. Sun weather

| SUN WEATHER | | | |
|--------------------|--------------|------------|------------|
| Soldier 1 | 100 attempts | 600 meters | 0,93 goal |
| Soldier 2 | 100 attempts | 800 meters | 0,749 goal |
| Soldier 3 | 100 attempts | 800 meters | 0,89 goal |
| Soldier 4 | 100 attempts | 800 meters | 0,91 goal |
| Soldier 5 | 100 attempts | 500 meters | 0,98 goal |

Table 2. Haze weather

| HAZE WEATHER | | | |
|---------------------|--------------|------------|------------|
| Soldier 1 | 100 attempts | 600 meters | 0,793 goal |
| Soldier 2 | 100 attempts | 800 meters | 0,65 goal |
| Soldier 3 | 100 attempts | 800 meters | 0,79 goal |
| Soldier 4 | 100 attempts | 800 meters | 0,79 goal |
| Soldier 5 | 100 attempts | 500 meters | 0,86 goal |

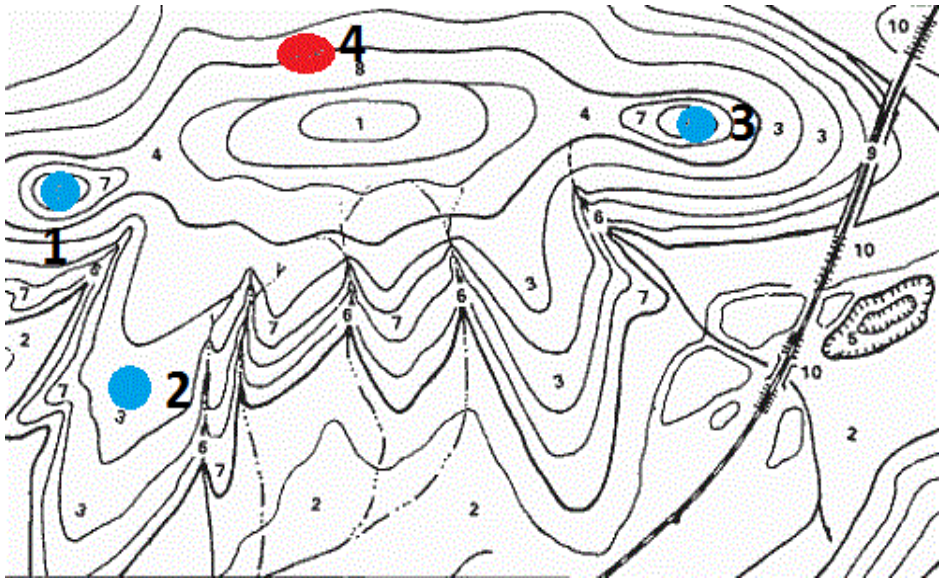
Table 3. Poor rain weather

| POOR RAIN WEATHER | | | |
|--------------------------|--------------|------------|-----------|
| Soldier 1 | 100 attempts | 600 meters | 0,80 goal |
| Soldier 2 | 100 attempts | 800 meters | 0,82 goal |
| Soldier 3 | 100 attempts | 800 meters | 0,89 goal |
| Soldier 4 | 100 attempts | 800 meters | 0,85 goal |
| Soldier 5 | 100 attempts | 500 meters | 0,73 goal |

Table 4. Straight rain weather

| STRAIGHT RAIN WEATHER | | | |
|------------------------------|--------------|------------|-----------|
| Soldier 1 | 100 attempts | 600 meters | 0,39 goal |
| Soldier 2 | 100 attempts | 800 meters | 0,41 goal |
| Soldier 3 | 100 attempts | 800 meters | 0,31 goal |
| Soldier 4 | 100 attempts | 800 meters | 0,55 goal |
| Soldier 5 | 100 attempts | 500 meters | 0,54 goal |

On the this picture we have example of one possible situation on the field. Our three (blue circle) and one man in trouble (red circle) team members are at the positions.



Picture 1. Real position on the field

ALGORITHM WORKFLOW

First: From the ground situation team member with number 1 and 3 have visibility to the goal.

Second: The distance from team member with number 1 to the victim is 600 m and the distance from team member 3 to the victim is 800m.

Third: The team member from the field reports us that the weather is sunny, and we are checking weather condition on android application.

Fourth: From the tables, we can see that probability for team member with number 1 is 0,93 and 0,89 for team member with number 3. This calculating will be automatically done by the application in our TOC center.

Fifth: Algorithm gives us final result that team member with number 1 is most suited to finish the task.

Six: The commanding centar gives the executive order.

CONCLUSION

This integrated system should allow:

- Ensure compatibility of existing and emerging information and technical systems to improve the efficiency of management in the field of safety of life of the population;
- Increase the effectiveness of control objects with mass stay of people and critical facilities;
- Improve the efficiency of solving the territorial problems;
- Increase the effectiveness of measures to eliminate the consequences of natural and man-made disasters;
- To reduce the loss of life in emergencies, fires, earthquakes.

Every day, we are confronted with disasters of varying degrees. Those that have adequately developed, maintained, and exercised their contingency plans will survive. Yet many people continue to take the uninhibited operations of their lives for granted. They remain complacent, assuming that the power will always be available, the telephone system will not fail, there will be no fire or earthquake--everything will always be normal. Very few people plan for their own, if we want to survive, organizational “strategic” and “tactical” battle planning is essential. However, it is only as good as the foundation upon which it was built. The foundation is, of course, the concept.

This document is the means by which a particular mission, program, or policy directive is translated into a fundamental organizational and operational methodology. Once the system is developed, and is sanctioned by both management and the operating elements, construction of the contingency plan may commence. A fundamental premise of successful contingency planning is that plans are developed by those who must actually carry them out in the event of an actual disaster. Disaster planning is truly a vital part of the overall business plan. With every year rising disasters the people are more and more threatened. We are hoping that with this software will help them all. The software is expected to decrease the casualties all around the world, in the crisis areas. And also organize the management in these situations. The low cost of the software is a big advantage in the development of the system (Petrovski, Bogatinov & Boshkovski, 2017).

NOTES

1. <http://environment.nationalgeographic.com/environment/global-warming/>;
2. <http://myphonelocater.com/category/triangulation/>;
3. Disaster Recovery Plan Strategies and Processes February 2002 pp 11-12.

REFERENCES

Charles M. Grinstead, J. Laurie Snell. Introduction to Probability. 520.

Tortonesi M, Stefanelli C, Benvegna E, Ford K, Suri N, Linderman M. Multiple-UAV coordination and communications in tactical edge networks. *IEEE Communications Magazine*. 2012 Oct 1;50(10):48-55.
Petrovski A., Bogatinov D., Boshkovski D., GIS IN ARMY: Usage of GIS in shooting with weapon in purpose to minimize resources and maximize the results, DOI: <http://dx.doi.org/10.18509/GBP.2017.15>, UDC: 528:004]:623.6.09, proceedings Geobalcanica 2017, Skopje

✉ **Dr. Aleksandar Petrovski, Assoc. Prof.**

ORCID iD: 0000-0002-5265-5813
University "Goce Delchev" Shtip
Military Academy "General Mihailo Apostolski"
Vasko Karangjeleski bb
Skopje, North Macedonia
E-mail: aleksandar.petrovski@ugd.edu.mk

✉ **Nenad Taneski**

<https://orcid.org/0000-0002-6471-0189>
University "Goce Delchev" Shtip
Military Academy "General Mihailo Apostolski"
Vasko Karangjeleski bb
Skopje, North Macedonia
E-mail: nenad.taneski@ugd.edu.mk

✉ **Jugoslav Ackoski**

<https://orcid.org/0000-0003-2782-3739>
University "Goce Delchev" Shtip
Military Academy "General Mihailo Apostolski"
Vasko Karangjeleski bb
Skopje, North Macedonia
E-mail: jugoslav.ackoski@ugd.edu.mk

<https://doi.org/10.48365/envr-2020.1.24>

FRAMEWORK FOR WILDFIRE DANGER PREDICTION SYSTEM

Nina Dobrinkova¹, Maria Asenova²

¹Institute of Information and Communication Technologies – Bulgarian Academy of Sciences

²University of Forestry, Faculty of Forestry, Department of Forest Management

Abstract: Wildland fires are natural hazard that occur every year in different parts of the world. European Mediterranean countries often are suffering from this disaster and in some cases human casualties plus infrastructure damages are in place. Bulgaria as part of the north east Mediterranean basin is affected by wildland fires in the last three decades more often than before. In our article we will present a framework for wildfire danger prediction system by usage of wireless sensor networks collecting real data and elaborating it into alerts. The test area is located on the territory of South-West state-owned forestry district. The described approach is based on the national fire danger rating algorithm, but in our case downscaled to daily prognosis. The system is under construction at the time of the paper writing thus the framework of the system main functionalities is the main scope of the article.

Keywords: wildfire, fire danger, sensor network.

INTRODUCTION

Wildland fires are becoming a global threat in the last decades worldwide. They are damaging forests and every economy sphere connected to the forestry products. As a result, after wildland fire vast amounts of valuable timber is lost. Other direct negative impacts are disruption and degradation of forest plantations, deforestation of big areas, deterioration of the protective functions of forests, reduction of the forest ecosystem water protection role, increasement of soil erosion, especially in mountain areas with steep slopes. Agricultural conditions become less productive in zones after fires. Animals, people, industrial buildings and housing, critical infrastructure, other important facilities are endangered if they are affected directly or indirectly by firestorms.

Since the middle of the last century, the problem of wildland fires gets a critical dimension due more often and more dangerous scale of the fire behaviour. This problem mostly affected large forest areas in the USA, Canada, Australia, Russia and Southern Europe countries. Substantial human, financial, material and scientific

resources are allocated for finding a solution of the above problems associated with the adverse effects of forest fires and finding a solution for them at national, regional and international level. With this regard significant funds are allocated also in EU programs for wildland fire protection of the Union's forests. Main objectives of the resource provision programs are measures for fire protection with reduction of the number and size of the burnt areas.

Wildland Fire Occurrence in Bulgarian Forests

In 2016 (Lyubenov, 2016) has done an analysis of fire activity in Bulgarian forests based on the official published data from the European Fire Database (EFD). The analysis and the follow-up assessments are based on data for the period 1990 – 2013 (24 years). The total wildland fires in numbers for the period is 12 905 fires or 538 average fires per year. Total burnt areas for the same period are 234 858 ha that represents 6.02% of the forest land of Bulgaria, or 0.25% thereof is burnt average per year. 0.14 fires occur average per year on area of 1000 ha (10 km²), and the area burnt thereby is 2.51 ha per 1000 ha forest land. Average area of a medium fire is 18.2 ha.

The dynamics of the number of forest fires occurred for the 1990 – 2013 period shows that the number of fires per year is explicitly dynamic figure characterising with significant unevenness in different years for the different Bulgarian regions. Other specification of this fire activity indicator is that it is characterised with relative permanence and clearly demonstrate cyclical peaks over the years, as for the period 1990 – 2007 these peaks occur exactly over seven years — 1993, 2000

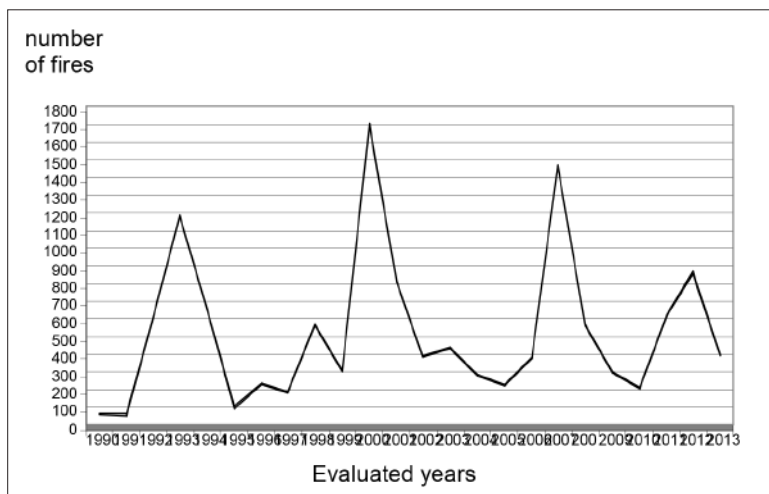


Figure 1. Dynamics of the number of forest fires occurred in Bulgaria for the 1990 – 2013 period (based on (Lyubenov, 2016)).

and 2007. The last peak for the period occurs after 5 years — in 2012. The values of peaks (maximum levels) for 1993, 2000, 2007 and 2012 exceed the average value for the period for the number of fires occurred respectively 2,21; 3,18; 2,75 and 1,63 times more (Figure 1).

Figure 2 shows the dynamics of magnitude of burnt areas for the same period (1990 – 2013). The chart clearly shows the large unevenness and direct relation of this magnitude with the data about the number of fires occurred (Fig. 1). For the peak years of the fire occurrence — 1993, 2000, 2007 and 2012 the size of burnt area exceeds the average for the period respectively 1,86; 5,87; 4,39 and 1,3 times more.

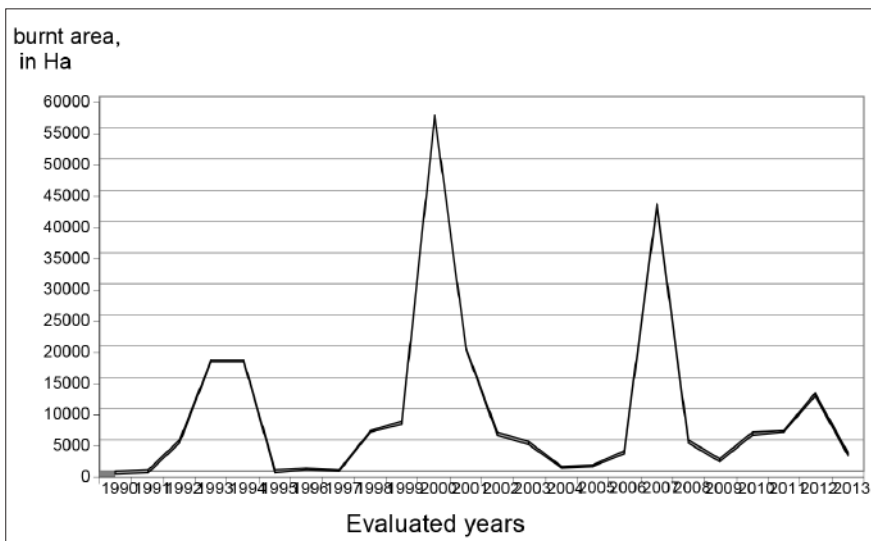


Figure 2. Dynamics of the burnt areas in Bulgaria for the period 1990 – 2013 (based on (Lyubenov, 2016)).

The analysis of fire activity and forest fire risk in the Bulgarian forest areas evaluated by (Lyubenov, 2016) was proved to be constant, with dynamic character and peaks on every 5 to 7 years.

METHODOLOGY DETERMINING FOREST FIRE RISK IN BULGARIA

The first attempt for determining the “fire risk” in Bulgaria was made in 2000 (Lyubenov-Panov, 2000). When determining the so called “fire risk” as main indicator it was used the average annual burnt area for the period 1991 – 2000 by Regional Forest Departments (RFD). The existing forest fire databases were elaborated and summarised for the first fire risk estimation results for Bulgaria. A scale for determining the “risk level” by RFD and the relevant ranking was

developed at the same time. Table 1 shows the results for “fire risk level” by RFD based on (Lyubenov-Panov, 2000) for 9 years of the analysed period.

Table 1. Fire risk level by RFD (1991 – 2000)
(based on (Lyubenov-Panov, 2000))

| Fire risk level | Regional forest departments |
|-----------------|-----------------------------------------------------------|
| low | Ruse, Varna, Blagoevgrad, Shumen, Veliko Tarnovo, Smolyan |
| medium | Sofia, Plovdiv, Burgas, Pazardzhik |
| high | Berkovitsa, Lovech, Kyustendil |
| very high | Kardzhali, Stara Zagora, Sliven |

Ranking according to that indicator was concluded that gives significant disparities between different RFD. For example: RFD-Kardzhali reported values of burnt average annual area exceeded the values in RFD-Smolyan and RFD-Blagoevgrad respectively with 38.5 and 12.3.

On the other hand, the number of fires occurred average per year in RFD-Kardzhali exceeds these in RFD-Smolyan and RFD-Blagoevgrad respectively with 1.5 and 2.2 times. If calculating the average area of a contingent fire for the example RFDs used only the average fire area than the Kardzhali case was exceeding the values for Smolyan and Blagoevgrad respectively with 27.5 and 5.9 times. This approach was not the best solution for future fire risk estimations. Thus, the conclusion for the first fire risk attempt for Bulgaria was that the forest fire risk established only by average annual burnt area indicator is not sufficient for Bulgarian regions.

In 2008, immediately after the second major peak of fire activity in Bulgarian forests, a new methodology for determining the forest fire danger risk was proposed by (Lyubenov-Konstantinov, 2008). The essence of the method consisted from a common (inclusive) criterion for determining the “fire danger (forest fire risk level)” in a forest area. The key indicators for characterizing fire activity in a forest area that were used for the determination of this criteria were: average number of fires occurred in a given territory and the average area annually burnt for the same zone. The outcome of combining these two indicators was the integrated fire danger assessment criteria called after for short: “forest fire risk in the area”. The cases could be refined where the number of fires was high and burnt area relatively small or the other way round — a small number of fires and large burnt area. Such approach indirectly took into consideration the average burnt area per fire. The summarised results for the second attempt for fire risk estimation was based on forest fire data sets per RFD for a period of 18 years (1991 – 2008) by (Lyubenov-Konstantinov, 2008). In Table 2 is given a summary of the main outcomes of the second forest fire risk assessment for Bulgaria:

Table 2. Fire danger level by RFD (1991 – 2008)
(based on (Lyubenov-Konstantinov, 2008))

| Fire danger level | Degree level | Regional forest departments |
|-------------------|--------------|---------------------------------------------|
| I | low | Shumen, Blagoevgrad, Veliko Tarnovo, Ruse |
| II | medium | Smolyan, Burgas, Varna, Pazardzhik |
| III | high | Sofia, Plovdiv, Kyustendil, Sliven |
| IV | very high | Lovech, Stara Zagora, Berkovitsa, Kardzhali |

Table 3 represents the summarized fire danger data in forest areas of the country of Bulgaria according to the second proposed methodology by (Lyubenov-Konstantinov, 2008) and its following relevant estimates for the 18 years period.

Table 3. Summarized data on forest fire danger
(based on (Lyubenov-Konstantinov, 2008))

| Fire danger extent and level | Number of fires occurred, % | Burnt area, % | Average burnt area per year, % of the total for Bulgaria |
|------------------------------|-----------------------------|---------------|----------------------------------------------------------|
| I – low | 13.88 | 5.23 | 0.065 |
| II – medium | 22.40 | 13.18 | 0.138 |
| III – high | 29.60 | 26.57 | 0.288 |
| IV – very high | 34.12 | 55.02 | 0.605 |
| For the country | 100.0 | 100.0 | 0.270 |

After these two attempts for establishment of common methodology for fire danger level in Bulgaria general conclusion was made that the dynamic values in the estimations are very dependent on the period that is determined for evaluation.

In 2016 has been done a third version of the Methodology determining forest fire risk in Bulgaria by (Lyubenov, 2016). The basic inputs that he used for his estimations were:

1. Historical period of assessment of only 10 years (2006-2015),
2. Number of fires reported regardless of the size of the area burnt,
3. Division of the country of Bulgaria by administrative units – districts under NUTS3 code (28 for the territory of Bulgaria)
4. The areas (wooded or non-wooded) were considered burnt if signs of fire were visible on combustible matter in the living or dead forest,
5. The total classes for fire danger extend level was limited to only 3 classes (low, medium and high).

The risk of forest fires is determined by an integrating indicator ($R_{f.risk}$), which is a product of the numerical values for the density of forest fires (R_{dens}) and the

actual flammability ($R_{f.comb.}$) of the territories per districts in Bulgaria (demonstrated in eq. (1)):

$$R_{f.risk} = R_{dens.} \times R_{f.comb.} \tag{1}$$

The classification according to the degree of forest fire risk is performed according to the scale shown in Table. 4, according to the indicator ($R_{f.risk}$).

Table 4. Determining the degree of forest fire risk (based on (Lyubenov, 2016))

| Values of the integrated indicator $R_{f.risk}$ | Degree of forest fire risk |
|-------------------------------------------------|----------------------------|
| $R_{f.risk} \leq 0,1$ | Low (green) |
| $R_{f.risk} > 0,1 \text{ u } \leq 0,3$ | Medium (yellow) |
| $R_{f.risk} > 0,3$ | High (red) |

Based on these criteria the third methodology developed by (Lyubenov, 2016), estimated that the average values for the country which are: average forest cover - 34.52%, average density of fires - 0.13, average flammability of forest areas - 2.11 and integrated indicator for the forest fire risk for the state is - 0.273.

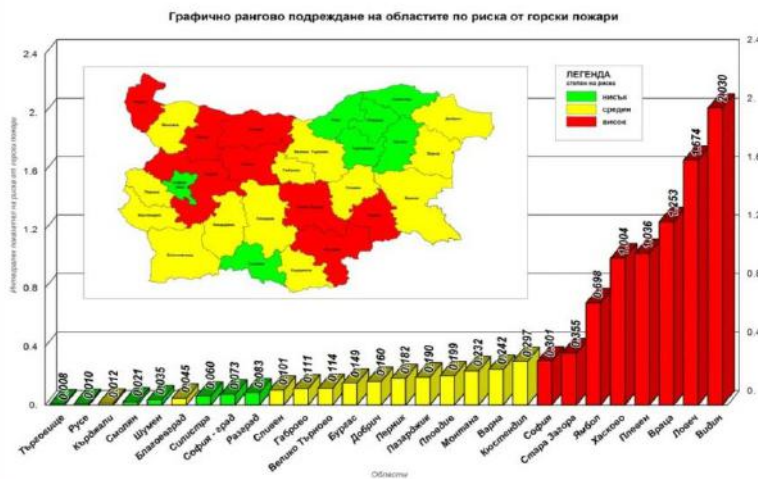


Figure 3. Ranking of the districts in Bulgaria according to an integrated indicator of forest fire risk based on the third methodology for the estimation period (2006-2015) (based on (Lyubenov, 2016)).

OTHER FOREST FIRE RISK APPROACHES

The current Canadian Forest Fire Danger Rating System (CFFDRS) has been developed for more than 10 years combining four separate modules:

1. Fire danger assessment according to the weather conditions (FWI);
2. Forest fire behaviour prediction (FBP);
3. Assessment of flammable materials moisture content (AFMS), and
4. Forest fires occurrence predicting system.

The Canadian system attempts to unite the three individual components of the overall forest fire danger in one indicator (constant fire danger, dynamic fire danger and fire risk). This system works only in Canada and is recommended for use in the Russian boreal forests (Sofonov, 2005). The FWI module determining only dynamic fire danger is used by the Joint Research Centre (JRC) of EC to predict the dynamic fire danger (according to weather conditions) for all countries using the European Forest Fire Information System (EFFIS).

In USA the national Fire Danger Rating System (NFDRS) is established for the needs of the USA Forest Department. According to this system forest areas of USA from Alaska to Florida are divided in four groups by types of flammable materials: grasslands, bushes, wooded and lands occupied by clearing residues. Additionally, the system requires division of combustible materials in 20 separate types. Separate combustible model is developed for each type serving as basis for defining the fire danger level. This system is in limited use in New Zealand and South African Republics (Sofonov, 2005).

In France based on (Lyubenov, 2016) for the most fire dangerous French region — Mediterranean, has been adopted methodology for determining the risk measure named “average annual risk” (AR, %) based on statistical data for certain period of years. This methodology also attempts to combine both indicators for fire activity assessment in the given region — percentage of burnt area for the period and likelihood of fire occurrence in the same area expressed in years. Such approach and evaluation for determining the “forest fire risk level” is not applicable for Bulgaria. Such values in percentage of burnt forest area annually for a region can not be reached in other countries and regions. Furthermore, this methodology does not take into account important measurable indicator as the number of fires occurred averagely per year or for the reported period.

In Russia has been consistently worked on the issue of classification of forest areas by “fire danger level”. A scale for determining the so-called “real combustibility of forests” (Lomov, 2007) was developed and validated for Russia. The Russian approach complies the general requirements for classification of forest areas by “forest fire risk”. However, its direct application in Bulgaria is not possible, given the scales of regions and field work done for the Russian Federation forestry zones. A newer methodology and scale including integrated indicator associated with both

the number of fires and burnt average annual area for a given forest area (Sofronov, 2005) is proposed in Russia to the current date, which will increase the accuracy of the assessment of “real combustibility of forests”. Although more precise this scale with the integrated indicator “aggregate perimeter” is likely to be used for plain terrains where in equal other conditions the shape of burnt area is relatively correct, approaching circular one. For oblique, steep and rugged terrain the shape is extremely complex and this classification is difficult to be applied.

In Germany the fire activity assessment is determined in “fire danger classes” by evaluating different forestry units (Misbach, 1989). This approach is applied in the former German Democratic Republic (east German provinces) where forest fire activity recently is increasing.

This methodology divides forestry in four fire danger classes:

1. *Fire danger class A1*: forests where three or more fires have occurred per year, with sizes of burnt area larger than 100 ha and with more than 50 ha burnt area per 100 000 ha forest land.
2. *Fire danger class A*: forests with over 50 ha completely burnt area per 100 000 ha per year.
3. *Fire danger class B*: forests with completely burnt area of 5 to 50 ha per 100 000 ha per year.
4. *Fire danger class C*: forests with less than 5 ha completely burnt area per 100 000 ha per year.

The first attempt for classification of forest fire risk areas in EU is for the Southern European countries (Portugal, Spain, Italy, France and Greece). That study has been launched with a pilot project for creation of an forest fire information system using the database for the period 1989 – 1993 described in details in (Regulation (EES) № 2158/92). For areas with high fire risk are considered those where 4,000 or more fires occur averagely per year. The number of fires may also be smaller, but if the average size per fire exceeds 30 hectares the risk remains high again. As high-risk under these conditions are classified only areas in Portugal, Spain and Greece plus 7 regions in France and 11 in Italy defined in (Regulation (EEC) No 2158/92). In 1997, the European Commission established a working group for development and proposal of methods for forest fire risk assessment and evaluation of burnt areas in the European Union discussed in details in (Forest Fires in Europe: Report № 11/2010). This group is part of the Institute for Environment and Sustainability of the European Commission and is part of the Joint Research Centre (JRC) in Ispra. The work of this group ends with the development of the European Forest Fire Information System (EFFIS) launched in 2000. This system was approved by the European Council and European Parliament with Regulation (EC) No 2152/2003 (Forest Focus) as a tool for monitoring of forests and environment.

On 23.02.2005 was held the third meeting of the Working Group on forest fires, which initiated a discussion called: “Key proposals to EU 25 for the classification of forests by fire risk”. The concept of “fire risk” and components included therein was introduced for the first time at that meeting and since then every EU member state is obligated to provide information for its forest fire risk zones. However there is still lack within the European Union of a unified methodology for determining the classes (degree) of fire risk or forest fire risk. Because of that reason is required each EU Member State to develop its own methodology to classify their forest areas by forest fire risk and monitor them with state specific systems and technologies.

FRAMEWORK FOR WILDFIRE DANGER PREDICTION SYSTEM

The chronological overview of the fire risk assessment methodologies in Bulgaria and the most famous approaches used worldwide gave to the team of IICT-BAS a good start to work for a pilot study case as part of the National Scientific Program for Environmental protection. Our test area is located in the south-west state forestry district. The zone is classified with medium range of forest fire risk based on the methodology of (Lyubenov, 2016). That part of Bulgaria has large number of touristic zones in the mountains of Pirin and Rila. This is the reason why most of the wildfires in south-west district are caused by human mistakes working with fire in open spaces.

After careful evaluation we have estimated that a combination between Wireless Sensor Network and the Canadian Fire Danger Rating System approaches will be the best for our test area. The sensor technology offers many benefits and a lot of features in detecting fire in the forest which cannot be achieved through traditional physical observations. Our approach includes module-based system that consist in each node of specially designed sensor stations collecting information for: rain, soil temperature, soil moisture for shallow depth, wind speed and wind direction, air temperature, humidity and atmospheric pressure, data logger, solar panel, battery and SIM card for transmission of the collected data.

The features of Wireless Sensor Technology that have sensors deployed in the field provide high coverage for the analyzed area, low costs, scalability, network access, greater resiliency, hypervisor protection against network attacks and less maintenance in energy compared to the other technologies (Lee et. all, 1999). Our sensor stations will have solar panels with battery that will feed the sensors with the needed power consumption.

The proposed solution is based on three core components Wireless Sensor Network, Processing software and Web Application with embedded alerting functionalities. The components are coupled with each other so that the early detection of the forest fires can be achieved and alerts to predefined groups of responsible actors can be sent out.

The System deployment consists of three phases – preparatory, instalment with tests and implementation into every day work.

The preparatory phase took us a year and covered the following activities – selection of wildland test territory, field observations and sensor network map elaboration. The map on (figure 4) is the final outcome of this first phase of evaluations and selections. The test zone is located in the south-west forestry district nearby Kresna Gorge. It has been first evaluated about its geography – flat or hilly and what kind of vegetation is covering that area. As second step has been done sensor network estimation for high coverage with fewer nodes. The final phase of the preliminary evaluations ended with creation of the node map and achieving special permission by the south-west forestry district director for instalment of the sensor network stations.

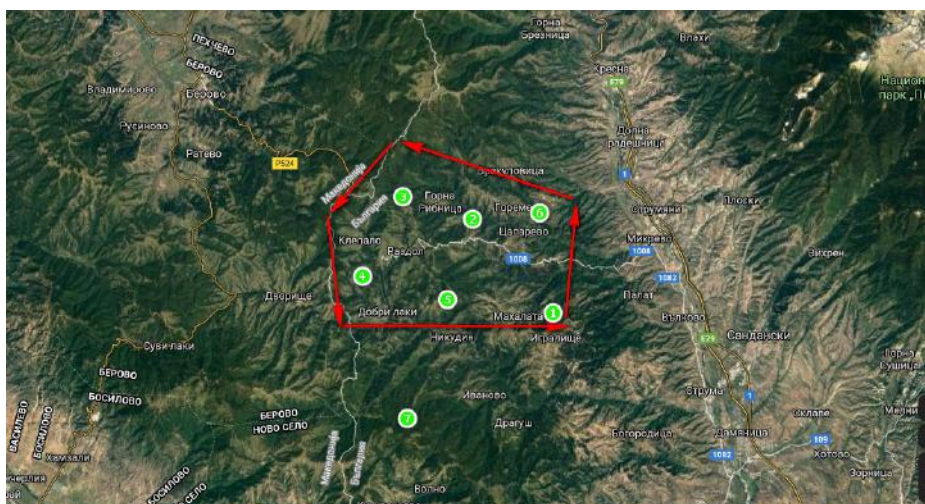


Figure 4. The test case sensor network in the zone of south-west forestry district of Bulgaria located nearby Kresna Gorge.

The second phase where is planned to be the instalments with tests is still in its beginning. It will cover the system architecture development in practice (figure 5). The system main three components are Fire Weather Observation, Fuel Moisture and Fire Behaviour. This modules are based on the Canadian Fire Danger Rating System and are discussed in details in (Bagheri 2007) and (Groot, 1998). Our main goal is to build up the physical network and develop the software collecting the sensor data, elaborating it into alerts and presenting it into daily maps that in cases of potential fire occurrence will transmit automatically alerts to predefined stakeholders.

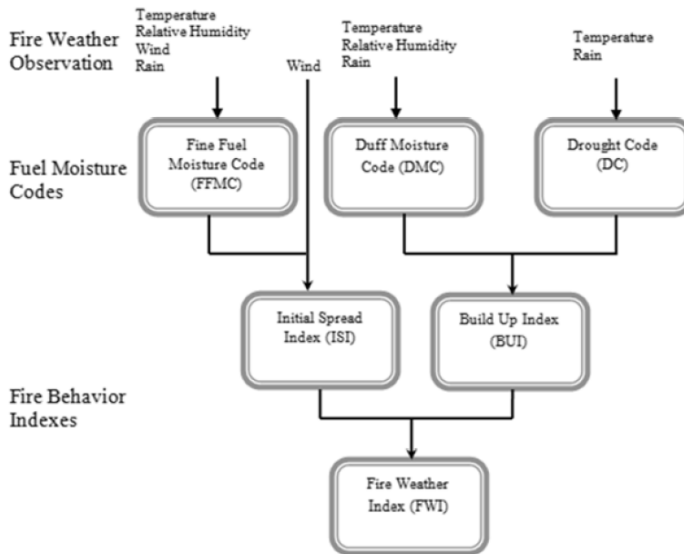


Figure 5. The test case sensor network in the zone of south-west forestry district of Bulgaria located nearby Kresna Gorge.

The test case sensor network is supposed to be physically available to transmit its data by March 2021, with the idea to work on a small area of south-west forestry giving demo case working in practice for vulnerable zone. In case this test case is giving sufficient results, this architecture will be further expanded and elaborated.

CONCLUSIONS

The proposed framework for a sensor network with the capacity of fire danger rating and early identification of starting forest fire is something that has not been done so far in Bulgaria. In the last seven years Firewatch towers have been placed in vulnerable areas, however this technology is very expensive and after the end of the project that funded its building the hardware maintenance is gone. This led to the situation that facilities with average price 300 000 euro each start to fail doing its job and eventually stop working. Our approach is aiming to provide low cost, but effective tool for everyday use and alerting system that can be reliable to capture fire danger and the initial source of fire start.

ACKNOWLEDGMENTS

This work has been supported by the NNP-OS contract number Д01-322/18.12.2019 and the Bulgarian National Scientific Fund project number DFNI DN12/5 “Efficient Stochastic Methods and Algorithms for Large-Scale Problems”.

REFERENCES

- Lyubenov, K. 2016. "Methodology for determining the risk of forest fires on the territory of the country of Bulgaria" for the needs of measure 8 "Investments in forest areas - development and improvement of forest viability" of the funding period (2014 - 2020). (in Bulgarian)
- Lyubenov, K., P. Panov. *Forest fires in Bulgaria (1991 – 2000)*. Forester Ideas journal, No. 2/2000.
- Lyubenov, K., Vl. Konstantinov. *Analysis and evaluation of fires and forest fire danger*. Forester Ideas journal, No. 1-2/2008
- Sofonov, M.A., I.G. Holldammer et al. *Fire danger in natural conditions*. Krasnoyarsk, 2005 (book).
- Lomov, V.D., S.N. Volkov *Easy Pyrology* Moscow, 2007 (book).
- Karl Misbach. *Forest fires*. Sofia, 1989 (book)
- Forest Fire in the South of the European Union (Regulation (EES) № 2158/92). Brussels, 1996
- Council (Regulation (EEC) No 2158/92) on protection of the Community's forests against fire OJ No. L 217, 31.07.1992.
- Lee, S.-J., Gerla, M., & Toh, C.-K. (1999). A simulation study of table-driven and on-demand routing protocols for mobile ad hoc networks. *Network, IEEE*, 13 (4), 48-54.
- Bagheri, M. (2007). Efficient K-Coverage Algorithms for Wireless Sensor Networks and Their Applications to Early Detection of Forest Fires. *Computing Science, SIMON FRASER UNIVERSITY*. MSc: 75.
- Groot., W. J. (1998). Interpreting the Canadian Forest Fire Weather Index (FWI) System. In Proc. of the Fourth Central Region Fire Weather Committee Scientific and Technical Seminar, Edmonton, Canada.

✉ **Nina Dobrinkova**

<https://orcid.org/0000-0002-6506-748X>

Institute of Information and Communication Technologies

Bulgarian Academy of Sciences

Sofia, Bulgaria

E-mil: ninabox2002@gmail.com

✉ **Maria Asenova**

<https://orcid.org/0000-0002-9660-0275>

Department of Forest Management

Faculty of Forestry

University of Forestry

Sofia, Bulgaria

E-mail: m_asenova@abv.bg

<https://doi.org/10.48365/envr-2020.1.25>

EVALUATION OF SENTINEL-3A OLCI OCEAN COLOR PRODUCTS IN THE WESTERN BLACK SEA

**Violeta Slabakova, Snejana Moncheva,
Natalyia Slabakova, Nina Dzhembekova**

Institute of Oceanology – Bulgarian Academy of Sciences (IO-BAS)

Abstract: Ocean color remote sensing has entered a new era with the successful launch of the Ocean and Land Colour Instrument (OLCI) on board Copernicus Sentinel-3 satellites. The representativeness and accuracy of the OLCI geophysical products are poorly quantified in the Black Sea which is featured by high bio-optical complexity. This paper addresses the evaluation of the OLCI/3A sensor's performance for retrieving ocean color products of the western Black Sea waters, by carrying out qualitative and quantitative match-up analysis between *in situ* and OLCI data. Results indicate a systematic underestimate of the water-leaving radiances (more pronounced at 412 and 665 nm) in contrary to the OLCI standard Chlorophyll (CHL) products which significantly overestimate the *in situ* records. These findings confirm the need of consistent reference *in situ* bio-optical data with improved spatial and temporal coverage for further satellite ocean color missions calibration and validation activities in the Black Sea.

Keywords: OLCI, ocean color, Black Sea, validation

INTRODUCTION

The Ocean and Land Color Instrument (OLCI) on board the Sentinel-3 satellites as a joint European Space Agency (ESA) and EC initiative for Earth observations – Copernicus has been designed to provide continuous global and regional observations of the land and ocean surface at high accuracy allowing operational monitoring of environmental parameters and climate studies. Of particular interest are the ocean colour measurements related to coastal zone monitoring in order to support environmental assessment of water quality and risk phenomena (such as harmful algal blooms) and to improve management of coastal habitats (EUMETSAT, 2018a). The OLCI sensor is a follow up of Medium Resolution Imaging Spectrometer (MERIS) on board the ESA/ENVISAT platform (Donlon et al., 2012). It incorporates several significant technological improvements comparing to MERIS including a) increased number of spectral bands from 15 to 21, b) reduction of sun glint effects, c) better global coverage, d) improved spatial

resolution of 300 m and signal-to-noise ratio. Calibration and validation of ocean color products in open-sea and coastal waters are critical element of each satellite ocean color mission (Hooker et al., 2000). The most fundamental among the parameters determined from space are the water-leaving radiance L_{WN} and the remote sensing reflectance R_{rs} . The uncertainties in quantification of these primary ocean color products may affect the subsequent estimation of optical (e.g. absorption and back-scattering coefficients) and biogeochemical products (e.g. chlorophyll (CHL) and Total Suspended Matter (TSM) concentrations), which further may challenge the assessment results.

The Black Sea is an extraordinarily complex water body for ocean colour remote sensing, as it belong to Case 2 waters (Kopelevich et al., 2004), which are characterized by relatively high absorption by Colored Dissolved Organic Matter (CDOM) while the concentration of non-pigmented particulate matter does not covary in a predictable manner with chlorophyll *a* (Babin et al., 2003; Churilova et al., 2017). The optical complexity of the Black Sea is the reason why the standard bio-optical algorithms developed for Case 1 waters, are the source of large uncertainties (of the order of hundreds of percent) of chlorophyll *a* concentration in the coastal areas (Sancak et al., 2005, Oguz, & Ediger, 2006, Slabakova et al., 2011). Nonetheless, results demonstrate reasonable performance of ocean color remote sensing, at least at local scales and/or in the open Black Sea. Different remote sensing algorithms for determination of optically active constituencies have been developed or adopted for the Black Sea (Zibordi et al, 2015; Suslin& Churilova, 2016; Kopelevich et al, 2013). Some of the studies rely on MERIS data and the results can be implemented on Sentinel-3 OLCI data as well. The aim of this research is to evaluate the performance of Sentinel-3A OLCI primary ocean color products and standard Level 2 algorithms for CHL retrieval based on comprehensive bio-optical *in situ* reference data set collected in western Black Sea.

DATA AND METHODS

In situ data

In order to increase the number of match-ups in the assessment of Sentinel-3A OLCI ocean colour products, we used *in situ* data from three different sources (Fig.1).

AOP of seawater were determined from multispectral free-fall system (Satlantic Micro profiler) which simultaneously measures the upwelling radiance $L_u(z, \lambda)$, the downward irradiance $E_d(z, \lambda)$ and the upward irradiance $E_u(z, \lambda)$ as a function of depth z and wavelength λ , in addition to the above-water downward irradiance $E_d(0^+, \lambda)$. Data products from the free-fall optical profiler include spectral values of: irradiance reflectance, remote sensing reflectance, normalized water-leaving radiance, diffuse attenuation coefficient and the so called Q-factor. The processing and quality assurance of data products are made using the Optical Processor

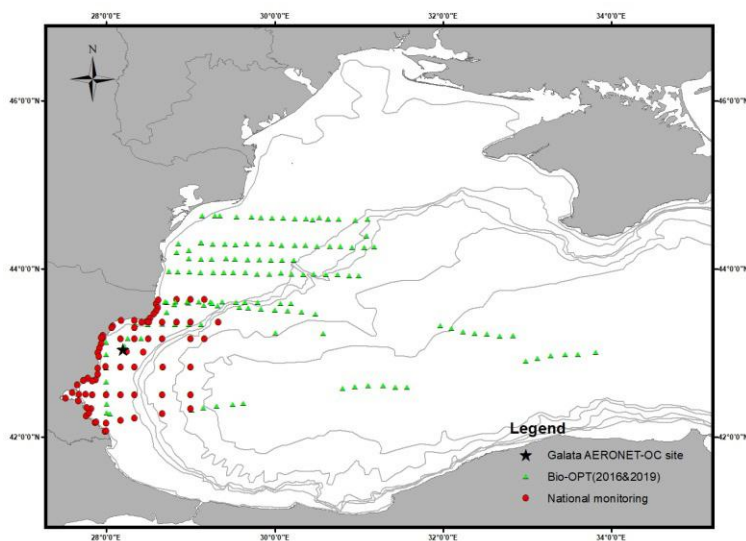


Figure 1. Location of measurement stations: 1) star, L_{WN} obtained from the Galata AERONET-OC; 2) Triangles, Apparent optical properties (AOP) measurements and subsurface water samples for CHL analysis collected during Bio-Opt 2016 and 2019 campaigns and 3) Circles, subsurface water samples for CHL analysis collected during seven national monitoring campaigns onboard R/V Akademik” in the period 2016-2018.

developed at the JRC (D'Alimonte et al., 2002). The processing steps, defined in agreement with consolidated protocols are documented in Zibordi et al., 2011.

CHL was determined by filtering the water samples through Whatman GF/F glass microfibre filters (pore size $0.7\mu\text{m}$, diameter 47 mm), extracting the pigments with acetone (90%) and spectrophotometrically measuring absorption at wavelengths of 480, 630, 645, 663, 664, 665 nm and 750 nm (Edler, 1999). The values of CHL were calculated with the trichromatic equations (Jeffrey & G. Humphrey, 1975).

L_{WN} from the Galata AERONET-OC site for the period April 2016 - August 2019 were obtained from AERONET Ocean Color web site. The match-up analyses were based on fully quality controlled AERONET-OC Level 2.0 radiometric products determined at different center wavelengths λ in the 412–1020 nm spectral region (Zibordi et al., 2009).

Satellite data

Match-ups for the *in situ* data were constructed using Sentinel-3 OLCI Level-2 (L2) data with 300 m spatial resolution, mode “Non Time Critical” (NTC), Processing Baseline 2.23 (EUMETSAT, 2018a, 2018b) for the period 26 April 2016

– 29 November 2017 over the western Black Sea obtained from Copernicus Online Data Access Reprocessed archive (CODAREP). The operational OLCI L2, Full Resolution (FR) mode “NTC” data from 30 November 2017 to August 2019 for the same geographic domain were downloaded from the EUMETSAT Data Centre.

The OLCI spectral reflectance data ρ_w were converted to normalized water-leaving radiance L_{wN} according to:

$$L_{wN} = \rho_w E_0 / \pi \quad (1)$$

where E_0 is mean extraterrestrial solar irradiance (Thuiller et al., 2003).

Sentinel-3 Toolbox Kit Module (S3TBX) in Sentinel Application Platform (SNAP) version 7.0.3 on Windows 10 was used to process the OLCI images.

Match-Up Construction

The match-up constructions were obtained from arithmetic average of valid OLCI full-resolution data calculated over the box of 3×3 – image elements centered on the measurements location. These OLCI averages were discarded when data: 1) were affected by the main OLCI standard flags (EUMETSAT, 2018a) with exception of ANNOT flags (Zibordi et al., 2018); 2) sensor and sun zenith angles were greater than 60° and $< 70^\circ$, respectively; 3) the time window between *in situ* measurements and satellite overpass were higher than ± 3 h; and 4) the coefficients of variation of all 9 pixels within the box were higher than 0.2. Finally, the percentage of valid pixels in each box was checked, and when this percentage was not less than 50%, the mean values of the valid pixels in the box was calculated and compared to the *in situ* data.

Statistical Method

OLCI L2 ocean color products were evaluated by standard statistics - coefficient of determination R^2 , root-mean-square error (RMSE), Mean Percentage Difference (MPD), Mean Absolute Percentage Difference (MAPD). The log_RMSE was used for the assessment of OLCI pigment concentrations because of lognormal natural distribution of CHL (Campbell, 1995).

RESULT AND DISSCUSSION

Assessments of the OLCI/SENTINEL 3A normalized water – living radiance data

The analysis of Galata and satellite L_{wN} spectra was restricted to the bands for which *in situ* data exist (i.e. those identified by the center wavelengths at 412, 443, 490, 560, and 665 nm). The comparison between the two data sets benefited of 115 matchups. The quantitative analysis of match-up spectra and their averages and standard deviations indicated agreement between the satellite and AERONET-OC

water-leaving radiances, with exception of OLCI L_{WN} data in the blue spectral band (412 nm), where negative values frequently occurred (Fig. 2).

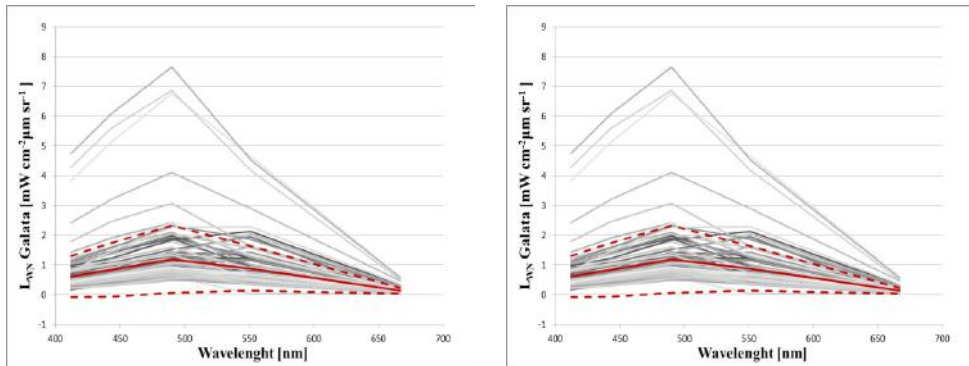


Figure 2. (Left) in situ L_{WN} and (Right) OLCI L_{WN} spectra for the Galata match-ups. The red continuous lines indicate the spectral averages and the red dashed lines indicate \pm one standard deviation.

The spectra of Galata and OLCI radiance data showed extremely high L_{WN} (λ) values for both data sets in June 2017 (Fig. 2). The phytoplankton samples collected on 23.05.2017 in the area around Galata platform confirmed the presence of coccolithophore *Emiliana huxleyi* with abundance of 2 265 120 cells/l during the initial phase of the bloom. The full development of the bloom during late spring of 2017 in the Black Sea is clearly visible in the OLCI RGB images (Fig. 3).

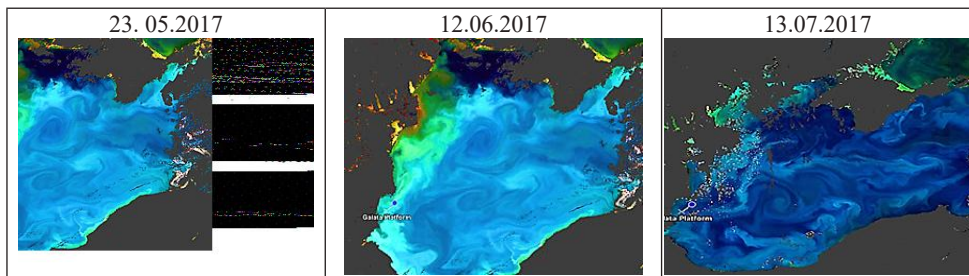


Figure 3. Sentinel-3 OLCI RGB images for 23.05.2017, 12.06.2017 and 13.07.2017.

In general there was a good correlation between OLCI L_{WN} and Galata records for all the wavelengths (Fig 4. Tab.1). The coefficient of determination R^2 varies from 0.84 at 665 nm to 0.98 at 490 and 560 nm, indicating that most of the OLCI data

products appear to agree with the *in situ* data. Still, a significant number of OLCI negative L_{WN} values were observed at 412 and 665 nm. This indicates that OLCI L_{WN} data are likely underestimated. The highest RMSE of $0.37 \text{ mW cm}^{-2}\mu\text{m}^{-1}\text{sr}^{-1}$ is determined for L_{WN} at 412 nm that considerably decreases to 0.07 for L_{WN} at 665 nm, in agreement with the lower L_{WN} values. The lower MPD of -10.63% and -11.20% were estimated at 490 and 560 nm, respectively.

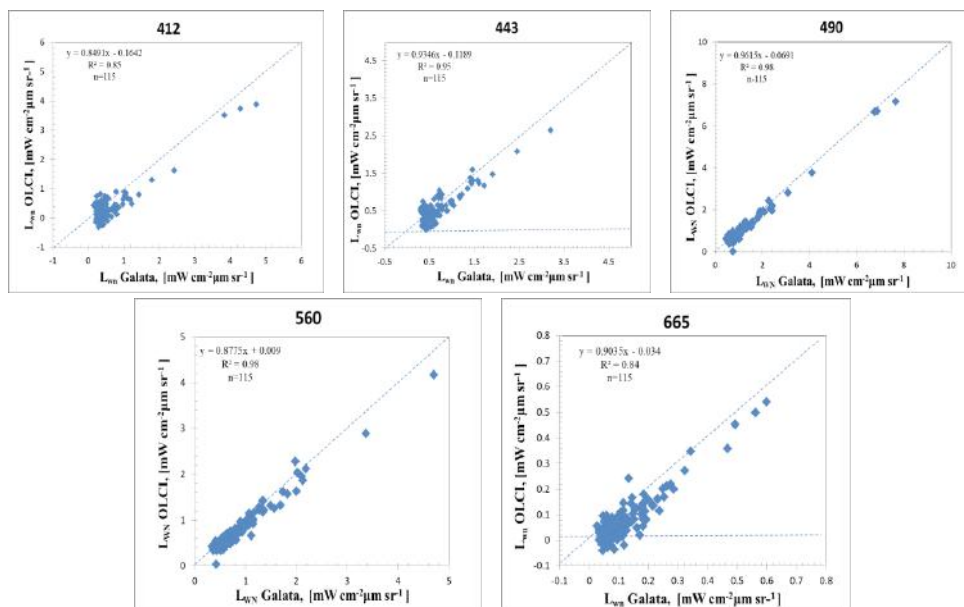


Figure 4. Scatter plots of OLCI and Galata AERONET OC L_{WN} match-up data at 412, 443, 490, 560, and 665 nm.

Table 1. OLCI $L_{WN}(\lambda)$ vs Galata $L_{WN}(\lambda)$ statistics (N=115).

| λ , nm | MPD, % | MAPD, % | RMSE, $\text{mW cm}^{-2}\mu\text{m}^{-1}\text{sr}^{-1}$ | R^2 |
|----------------|--------|---------|---------------------------------------------------------|-------|
| 412 | -47.11 | 72.7 | 0.37 | 0.86 |
| 443 | -24.06 | 39.22 | 0.27 | 0.95 |
| 490 | -10.63 | 17.21 | 0.19 | 0.98 |
| 560 | -11.20 | 14.80 | 0.29 | 0.98 |
| 665 | -42.89 | 52.10 | 0.07 | 0.84 |

The comparison of in-water radiometric $L_{WN}(\lambda)$ and satellite L_{WN} spectra was performed for the bands for which *in situ* data exist (i.e. those identified by the

center wavelengths at 412, 443, 490, 510, 560, and 665 nm). The total number of matchup pairs was 13. The OLCI estimates displayed systematic negative errors (Tab.2), thus, an underestimation of $L_{WN}(\lambda)$ showed up at 412, 443, 490, 560 and 665 nm compared to sea-truth data. The positive MPD was found only for 510 nm. The highest underestimate of about -32% was measured at 665 nm while the lowest (bellow 5%) occurred at 443, 490 and 560 nm. Relatively low correlation of OLCI L_{WN} and *in situ* records was observed in the blue spectral band - 412 nm (Tab. 2).

Table 2. OLCI $L_{WN}(\lambda)$ vs in-water radiometric $L_{WN}(\lambda)$ statistics (N=13)

| λ , nm | MPD, % | MAPD, % | RMSE, $mW\ cm^{-2}\ \mu m^{-1}\ sr^{-1}$ | R ² |
|-------------------|-----------|------------|---------------------------------------------|----------------|
| 412 | -14.19 | 21.51 | 0.24 | 0.36 |
| 443 | -3.35 | 13.78 | 0.22 | 0.60 |
| 490 | -2.91 | 11.53 | 0.16 | 0.72 |
| 510 | 8.2 | 13.27 | 0.24 | 0.60 |
| 560 | -2.34 | 12.18 | 0.17 | 0.77 |
| 665 | -31.85 | 34.10 | 0.07 | 0.52 |

Generally, the highest uncertainty of OLCI normalized water-leaving radiances with respect to the *in situ* data were observed in the blue (412nm) and red (665 nm) spectral bands which could be linked to CDOM dominated Black Sea waters with significantly varying concentrations of non-pigmented particles, displaying maxima at either 490 nm or 555 nm and minima at 412 nm and 665 nm (Churilova et al., 2017) as well as issues in the atmospheric correction and its calibrations coefficients in shorter wavelengths bands (Toming et al.,2017). The OLCI $L_{WN}(\lambda)$ bands with the best performances were 490, 510 and 560 nm, which agree with the results presented in Zibordi et al., (2018).

Assessments of the OLCI/SENTINEL 3A CHL products

The OLCI L2 standard CHL products were evaluated in respect to the 26 *in situ* measurements. The CHL concentrations were derived from the two standard bio-optical algorithms: *i*) "OC4Me" Maximum Band Ratio (MBR) semi-analytical algorithm, developed by Morel et al., (2007) following the approach of O'Reilly et al., (1998) and *ii*) Neural network (NN) inverse radiative transfer bio-optical model, originally developed for MERIS by Doerffer & Schiller, (2007), and updated to the Case 2 Regional / Coast Color (C2RCC) processor. The CHL values used in the analysis ranged between 0.15 and 2.3 $mg\ m^{-3}$, with average concentration $>0.8\ mg\ m^{-3}$.

The CHL_OC4ME product shown an overestimate of *in situ* chlorophyll by about 160% (MAPD), while CHL_NN was about two times lower (81.29%) – Table 3. A moderately good correlation ($R^2=0.65$) was observed between satellite and

in situ data for CHL_OC4ME, whereas the CHL_NN products exhibit a determination coefficient of 0.09. The estimated log_RMSE values for both satellite products are 0.42 and 0.43 mg m⁻³ for CHL_OC4ME and CHL_NN, respectively. Despite the significantly high MPD error estimated for OLCI_OC4ME algorithm it was almost 2 times lower comparing to the standard MODIS (OC3M) and SeaWiFS (OC4) algorithms, while the results of CHL_NN agreed to those obtained for regional algorithm (Suslin et al, 2018).

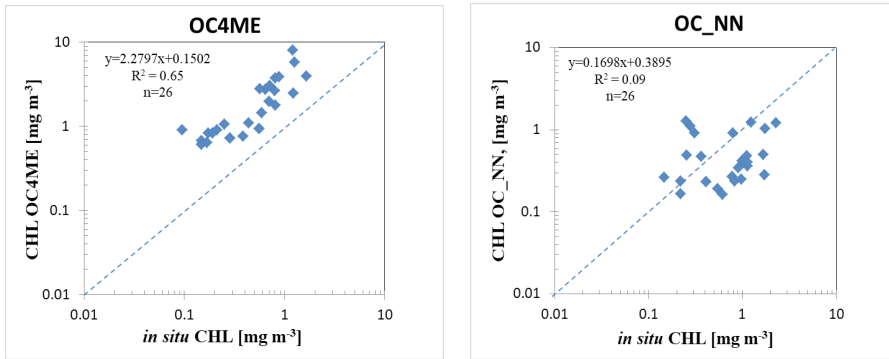


Figure 5. Scatter of OLCI derived pigments concentration [i.e., (Left) OC4ME and (Right) CHL_NN] versus *in situ* CHL data.

Table 3. OLCI L2 CHL products vs *in situ* data (N=26)

| Product | MPD, % | MAPD, % | RMSE, mg m ⁻³ | R ² |
|-----------|-----------|------------|-----------------------------|----------------|
| CHL_OC4ME | 160.47 | 160.47 | 0.42 | 0.65 |
| CHL_NN | 2.77 | 81.29 | 0.43 | 0.09 |

CONCLUSIONS

The comparison carried out over almost a three year period of Sentinel 3A/OLCI Level 2 FR data based on *in situ* measurements obtained from three different data sources in western Black Sea, indicated:

- ✓ systematic underestimation of satellite normalized water-leaving radiances $L_{WN}(\lambda)$ with effects more pronounced in the blue and red spectral regions;
- ✓ significant overestimation of CHL_OC4ME (160% MPD) and CHL_NN (about 80% MPD) derived pigments concentration.

The results of the study showed that there are strong needs of consistent reference *in situ* bio-optical data set with improved spatial and temporal (including bloom events in the coastal area) coverage for calibration and validation of present and future satellite ocean color missions in the Black Sea.

ACKNOWLEDGMENTS

The authors would like to thank Dr. Zibordi from Joint Research Center for providing the quality controlled Level 2 data from Galata AERONET-OC site and for his support with the AOP data processing and quality determination. Thanks also go to the EUMETSAT for the distribution of OLCI data products. This research was supported by contract №4000123951/18/NL/SC “Bio-optics for ocean color remote sensing of the Black Sea under the ESA Programme for European Cooperating States for Bulgaria and contract DOI-161/28.08.2018 “NGIC – National Geoinformation Center for monitoring, assessment and prediction natural and anthropogenic risks and disasters” under the Program “National Roadmap for Scientific Infrastructure 2017-2023” financed by Ministry of Education and Science of the Republic of Bulgaria.

REFERENCES

- Babin, M., Stramski, D., Ferrari, G. M., Claustre, H., Bricaud, A., Obolensky, G., and Hoepffner, N. (2003). Variations in the light absorption coefficients of phytoplankton, nonalgal particles, and dissolved organic matter in coastal waters around Europe. *J. Geophys. Res.*, 108(C7), 3211.
- Churilova, T., Moiseeva N., Efimova, T., Suslin, V., Krivenko, O., & E. Zemlianskaia (2017). Annual variability in light absorption by particles and colored dissolved organic matter in coastal waters of Crimea (the Black Sea). *Proc. SPIE 10466, 23rd International Symposium on Atmospheric and Ocean Optics: Atmospheric Physics*, 104664B; <https://doi.org/10.1117/12.2288339>
- Campbell, J. (1995). The Lognormal Distribution as a Model for Bio-Optical Variability in the Sea. *Journal of Geophysical Research: Oceans* 100 (C7), 13237–54.
- D'Alimonte, D., Zibordi, G. & Berthon, J.-F. (2002). The JRC processing system. In *Results of the second SeaWiFS data analysis roundrobin*, NASA Tech. Memo. 206892, 15, 15.
- Donlon, C. Berruti, B., Buongiorno, A., Ferreira, M., Féménias, P., Frerick, J., Goryl, P., Klein, U., Laur, H., Mavrocordatos, C., et al. (2012). The global monitoring for environment and security (GMES) Sentinel-3 mission. *Remote Sensing of Environment*, 120, 37–57.
- Doerffer, R. & Schiller, H. (2007) The MERIS Case 2 Water Algorithm. *International Journal of Remote Sensing*. 28, 517-535.
- Edler, L. (1979). Recommendations on methods for marine biological studies in the Baltic Sea. Phytoplankton and Chlorophyll. *Baltic Marine Biologists*, Publication No. 5, 1- 38.
- EUMETSAT. (2018a). Sentinel-3 OLCI Marine User Handbook. Doc. No. EUM/OPS-SEN3/MAN/17/907205.v.1H. 2018.
- EUMETSAT. (2018b). Sentinel-3A Product Notice – OLCI Level-2 Ocean Colour Operational Products and Full-Mission Reprocessed Time Series.

- Jeffrey, S., & Humphrey, G. (1975). New spectrophotometric equations for determining chlorophylls a and c2 in higher plants, algae and natural phytoplankton. *Biochem. Physiol.* 167, 194–204.
- Kopelevich O., Burenkov V., Ershova S., Sheberstov S., & Evdoshenko M. (2004) Application of SeaWiFS data studying variability of bio optical characteristics in the Barents, Black and Caspian Seas. *Deep-Sea Research. Part II: Tropical studies in Oceanography.* V.51, N 10-11, 1063-1091.
- Kopelevich, O., Sheberstov, S., Burenkov, V., Vazyulya, S., & I. V. Sahling. (2013). Bio-Optical Characteristics of the Russian Seas from Satellite Ocean Color Data of 1998–2012. In *Current Problems in Optics of Natural Waters: Proceeding of VII International Conference (ONW'2013)*, 168–171.
- Morel, A., Gentili, B., Claustre, H., Babin, M., Bricaud, A., Ras, J., et al. (2007). Optical properties of the “clearest” natural waters. *Limnology and Oceanography*, 52, 217-229.
- Oguz, T. & Ediger, D. (2006). Comparison of in situ and satellite-derived chlorophyll pigment concentrations, and impact of phytoplankton bloom on the suboxic layer structure in the western Black Sea during May–June 2001. *Deep Sea Res. II*, 53, 1923-1933.
- Sancak, T., Besiktepe, A., Lee, M., & Frouin, R. (2005) Evaluation of SeaWiFS chlorophyll-a in the Black and Mediterranean Sea. *International Journal of Remote Sensing*, 26, 2045-2060.
- Slabakova, V., Slabakova, N., Hristova, O., & Dzhurova, B. (2011). Assessment of MERIS ocean color products using in situ data collected in the Northwestern Black Sea. *Proceedings of 5th International Conference on Recent Advances in Space Technologies - RAST2011*, 132-136.
- Suslin, V., & Churilova, T. (2016). The Black Sea regional algorithm of separation of light absorption by phytoplankton and colored detrital matter using ocean color scanner’s bands from 480-560 nm. *Int. J. Remote Sens.* 37, 4380–4400.
- Suslin, V., Churilova, T., Lee M., Moncheva S. & Finenko, Z. (2018). Comparison of the Black Sea chlorophyll-a algorithms for SeaWiFS and MODIS instruments. *Fundamentalnaya i Prikladnaya Gidrofizika.* 11, 3, 64–7.
- Thuillier, G., Hersé, M., Labs D., Foujols, T., Peetermans, W., Gillotay, P., Simon, C., and Mandel, H. (2003). The solar spectral irradiance from 200 to 2400 nm as measured by the SOLSPEC spectrometer from the Atlas and Eureca missions. *Solar Physics* 214, 1–22.
- Toming, K., Kutser, T., Uiboupin, R., Arikas, A., Vahter, K. & Paavel, B. (2017). Mapping Water Quality Parameters with Sentinel-3 Ocean and Land Colour Instrument Imagery in the Baltic Sea, *Remote Sens.*, vol. 9, 1070.

- Zibordi, G., Mélin, F., Berthon, J. F., Holben, B., Slutsker, I., Giles, D., et al. (2009). AERONET-OC: A network for the validation of ocean color primary products. *Journal of Atmospheric and Oceanic Technology*, 26, 1634–1651.
- Zibordi, G., Berthon, J.-F., Mélin, F. & D. D’Alimonte. (2011). Cross-site consistent in situ measurements for satellite ocean color applications: the BiOMaP radiometric dataset. *Remote Sensing of Environment*, 115, 2104–2115.
- Zibordi, G., Mélin, F., Berthon, J.-F., and Talone, M. (2015). In situ autonomous optical radiometry measurements for Satellite Ocean color validation in the Western Black Sea, *Ocean Sci.* 11, 275–286.
- Zibordi, G., Mélin, F., Berthon, J.-F. (2018). A regional assessment of OLCI data products. *IEEE Geoscience and Remote Sensing Letters*, 15, 1490–1494.

✉ **Violeta Slabakova**

<https://orcid.org/0000-0002-3089-0126>

Institute of Oceanology
Bulgarian Academy of Sciences
Varna, Bulgaria
E-mail: v.slabakova@io-bas.bg

✉ **Snejana Moncheva**

<http://www.orcid.org/0000-0002-2679-5062>

Institute of Oceanology
Bulgarian Academy of Sciences
Varna, Bulgaria
E-mail: snejanam@abv.bg

✉ **Natalyia Slabakova**

<https://orcid.org/0000-0002-3294-5346>

Institute of Oceanology
Bulgarian Academy of Sciences
Varna, Bulgaria
E-mail: n.slabakova@abv.bg

✉ **Nina Dzhembekova**

<https://orcid.org/0000-0001-9620-6422>

Institute of Oceanology
Bulgarian Academy of Sciences
Varna, Bulgaria
E-mail: sonata_bg@yahoo.com

<https://doi.org/10.48365/envr-2020.1.26>

A MODELLING SYSTEM FOR NUMERICAL WEATHER PREDICTION IN THE BULGARIAN ANTARCTIC BASE AREA

Boriana Chtirkova, Elisaveta Peneva, Gergana Georgieva

*“St. Kliment Ohridski” University of Sofia, Faculty of Physics,
Department of Meteorology and Geophysics*

Abstract: The weather forecast of good quality is essential for the humans living and operating in the Bulgarian Antarctic Base (BAB), located on the Livingston Island coast at 62.64° S and 60.36° W. The numerical weather prediction models in southern high latitude regions still need improvement as the user community is limited, little test cases are documented and validation data are scarce. The modelling system is based on the WRF model, configured in three nested domains down to 1 km horizontal resolution, centered over BAB. The main objective of the study is to configure and validate the WRF model and to recommend certain set-up parameters like model area coverage, topography, land use, vertical levels, physics parametrization schemes, preparation of initial and boundary conditions and run configuration on HPC machines. Three test periods of “bad” weather events are considered during the summer seasons in 2016, 2017 and 2020. The ability of the 3 days forecast to capture the basic meteorological events in this period is discussed. Sensitivity experiments to the land use type are conducted and while the MODIS land data is found to be the most accurate for the region, a slight increase in the soil thermal capacity results in better model performance.

Keywords: numerical weather prediction, Antarctica, horizontal resolution, land use type

INTRODUCTION

The Bulgarian Antarctic base St. Kliment Ohridski (BAB) is a national scientific facility, located on Livingston Island, South Shetland Islands. A specialised weather forecast of good quality is essential for the people working and living on this base. The purpose of this work is to set up a limited BAB area forecasting system based on the Weather Research and Forecasting (WRF) model and validate its performance. The elevation of the base is 12 to 15 m above sea level, an average of 25 people work there during the austral summer, usually from late November until early March. The weather in the region is mostly influenced by extratropical

cyclones, which form and propagate as Rossby planetary waves. The cyclones move west to east and tend to diffuse over land, due to friction. Thus, the weather is highly variable with intense storms and strong wind events occurring regularly. Several test cases with shifting weather patterns are used to evaluate the model performance.

MODEL CONFIGURATION

The modelling system is based on the Weather Research and Forecasting model, version 4.0, developed by the National Center for Atmospheric Research (NCAR) and the National Centers for Environmental Prediction (NCEP). The numerical model uses a staggered Arakawa C-grid (Skamarock, 2019) and the nesting is performed in a ratio 9:3:1 km. The domain configuration is shown in Figure 1: it is centered over BAB with coordinates 62.64° S and 60.36° W and consists of three nested domains d01, d02 and d03. The outermost domain – d01, with a resolution of 9 km, has horizontal dimensions of 999 km in both directions and covers the northern part of the Antarctic Peninsula. It is a parent domain to the first nested domain – d02, with a horizontal resolution of 3 km and dimensions of 342 km in both directions. The finest domain – d03, is nested in d02, and covers the area of Livingston Island and its neighbouring small islands; the horizontal dimensions of d03 are 129 km in west-east direction and 111 km in south-north direction. The domain configuration is made so that there are no high mountains or complex relief near the domain borders.

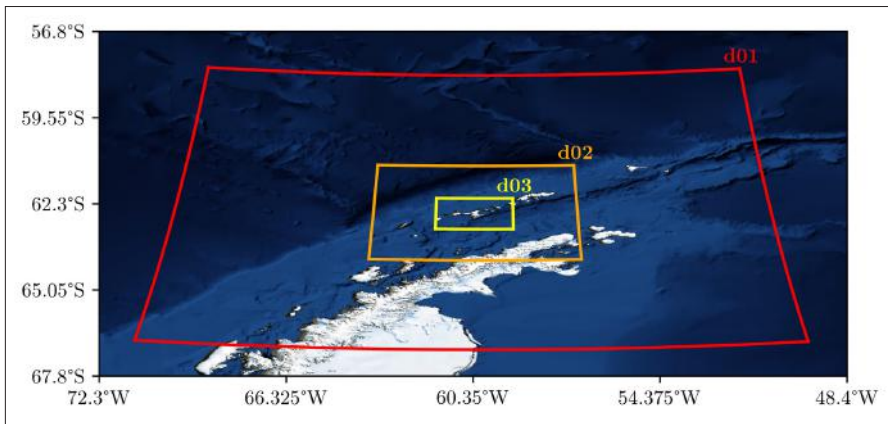


Figure 1. Three domains coverage- d01, d02 and d03. Background image from NASA Visible Earth - Blue Marble.

The land surface boundary condition of the modelling area is assembled via the WRF Preprocessing system program – *geogrid*, which interpolates topography

and land use type data into the model grid. The topography data is taken from the GMTED2010 dataset, developed by the United States Geological Survey (USGS) and the National Geospatial-Intelligence Agency (NGA) and has a horizontal resolution of 225 m. The fitted in the finest domain topography is shown of Figure 2-a. A comparison with regional maps such as the map from Ivanov (2017) show that this dataset does not represent accurately Livingston Island. The mountain range Tangra mountains, reaching heights up to 1700 m, is represented as a flat surface with elevation of ~ 50 m. Figure 2-a represents the topography grid in the finest domain, which has a number of points in the x-direction $i_{\max}=129$ and in the y-direction $j_{\max}=111$, each grid point covers an area of 1 km^2 .

The WRF model can perform mainly with two land use datasets, which cover the entire globe – USGS and MODIS. The USGS data is based on satellite advanced very-high-resolution radiometer (AVHRR) data, collected in the period April 1992 – March 1993. They contain 24 land use types and have a resolution of 1 km. The MODIS data (Moderate resolution imaging spectroradiometer) are gathered by NASA satellite missions in the period 2001-2005. They are made up of 20 land use type categories and their resolution reaches 500 m. A visual comparison between the MODIS and USGS land use type data is given in Figures 2-b and 2-c. According to both datasets, the entire domain area is described with only 2 land use types – snow/ice and water. The land use type is presented in numerical modelling through the following parameters: albedo α [%], soil moisture availability M [%], surface emissivity, ϵ [%], roughness length z_0 [m], thermal inertia λ_T [$\text{Jm}^{-2}\text{K}^{-1}\text{s}^{-1/2}$] and surface heat capacity C [$\text{Jm}^{-3}\text{K}^{-1}$]. The values of these parameters differ throughout the seasons and are used to describe the energy, momentum, water and heat fluxes. They slightly differ between the two datasets, mainly in the parameters z_0 and λ_T , which are slightly higher within the MODIS data, but the difference should not result in large computational differences. Comparing Figures 2-b and 2-c, one can conclude that the coastal line, formed by the USGS data is not as

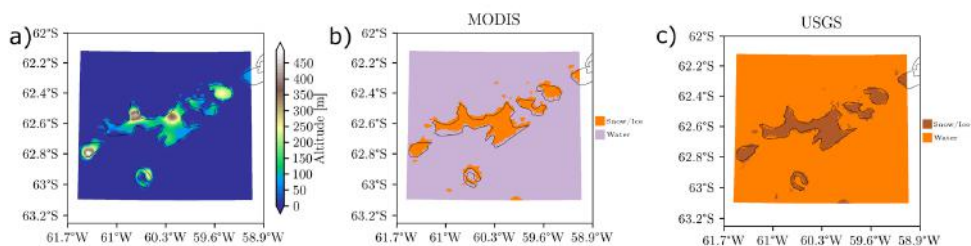


Figure 2. Topography (a) and land use type (b) of the finest domain – d03 with a resolution of 1 km, $i_{\max}=129$, $j_{\max}=111$. The coastlines on the image are taken from the Natural Earth Database (<https://www.naturalearthdata.com/>) and have a horizontal resolution of 10 m.

continuous as the MODIS one. There is a slight displacement of the grid between the two datasets but this problem is eliminated with a manual choice of grid point to represent BAB. Having taken this into account, and the fact the MODIS data is more recently collected, the authors conclude it is better suited for the modelling system. However, the description of the whole Livingston island as covered with snow and ice may not still be accurate in recent years. This problem is addressed further in the text.

For a vertical coordinate in WRF, version 4.0, one can choose a terrain following (TF) coordinate or a hybrid vertical coordinate (HVC). In the present study, hybrid η -levels are used, unevenly distributed from the surface up to isobaric level 50 hPa. In order to determine the optimal number a vertical levels, a sample model run of a 72 hour forecast with a different number of levels has been performed. All WRF experiments in the present study are run on the Sofia University Parallel Computer Center cluster PHYSON. Three different vertical level configurations have been tested – with 35 vertical levels (close to the WRF minimum number), 50 and 70 levels. The η -levels from the three configurations are distributed with equal density near the surface but their distribution difference manifests after certain height. Hence, the description of the atmospheric state near the surface is similar, but the configuration with the least densely distributed levels in height fails to represent adequately high altitude phenomena, such as the polar jet stream. All simulations are performed using the same number of computer cores, 88 in this case, on the PHYSON cluster. Although being a heterogenic HPC, the PHYSON cores operate on similar frequencies and the time difference that arises from the fact that different simulations are run on different CPU types is negligible. The computer time for the simplest simulation with 35 vertical levels is 9 h 22 min, the forecast with 50 vertical levels is computed for 13 h 18 min and the one with 70 levels – 18 h 33 min. For an optimal configuration, performed for a minimal time, the 50 η -levels configuration is chosen.

Even though the high horizontal and vertical resolution of recent numerical models allows us to describe smaller scale phenomena, other physical processes on scales smaller than the model grid still need to be parametrized. The parametrization schemes and their combinations has a profound effect on numerical forecasting, especially in larger time scales and therefore the schemes should be chosen carefully. The subgrid processes that are or may be parametrized in WRF comprise of microphysics, convection, turbulence in the planetary boundary layer (PBL), interactions between the atmosphere and the surface layer and the longwave and shortwave radiation. The choice of parametrization schemes for the present study has been made through a literature review. The Antarctic Mesoscale Prediction System¹ (AMPS) produces numerical forecasts for the Antarctic region, made through a modified PolarWRF (Hines & Bromwich, 2008). The physics parametrization in the present configuration are chosen to be coherent and done in accordance with

AMPS. The following schemes are used:

- Boundary layer: Mellor-Yamada-Janjic (Eta) TKE scheme
- Surface layer: Monin-Obukhov (Janjic Eta) scheme
- Land-surface interactions: Unified Noah Land Surface Model
- Microphysics: WSM 5-class scheme
- Long-wave radiation: RRTMG longwave radiation scheme
- Short-wave radiation: Goddard shortwave radiation scheme
- Convection: Kain-Fritsch (new Eta)

For a more detailed description of each scheme, the reader is referred to Skamarock et. al. (2019) or Chtirkova (2020). The Kain-Fritsch convection parametrization scheme is not used in the finest domain, because its horizontal resolution of 1 km can resolve convective processes.

The regional models need suitable atmospheric initial and lateral boundary conditions. They are taken from the GFS 0.25 Degree Historical Archive (NCEP, NWS, NOAA, U.S. 2015) and the lateral boundary conditions are updated every 3 hours of the simulation. The sea surface temperature is also taken as a time varying surface boundary condition and is updated every 3 hours into the simulation. The GFS model analysis in 0 UTC is taken as an initial condition for each of the three domains, while the lateral boundary conditions are given only to the outermost domain. Two-way nesting is performed, which means that the forecast in the parent domains is affected by the solutions in the finer domains.

MODEL VALIDATION

At latitudes around 60°, two of the general circulation cells are closed – namely the Ferrel and polar cells, enabling the formation of a convective zone with westerly dominating winds. The Rossby waves form and propagate over this low-pressure system, with extratropical cyclones influencing the weather by producing storms and high-speed winds. Three test cases with rapidly changing weather are chosen among the recent years weather records from the GFS model analysis and in-situ observations at BAB: 16-19 December 2016, 26 February-1 March 2020 and 25-28 January 2020. The model configuration has been validated against measurements from an automatic meteorological station at BAB, synoptic measurements in the nearby meteorological stations² and ERA-5 climatic hourly reanalysis data (Copernicus Climate Change Service, 2017). The in-situ measurements come from an automatic meteorological station Davis Vantage Vue for the 2016 and 2017 test cases, and an automatic station assembled by MeteoRocks³ for the 2020 test case. The validated meteorological variables are temperature at 2 m, surface pressure, wind speed and wind direction. The total number of synoptic stations in the largest domain is 18, two of which lie in the finest domain. The synoptic observations from “Base Arturo Prat” with WMO index 890057 and coordinates 62.3° N, -59.41°E, are used in the comparison as indicative of the weather pattern in the

region. They are in agreement with the observations from BAB in all test cases. The validation process is divided into 3 parts – the first one consists of a comparison of model simulations with different horizontal resolution, the second one is a general validation for all test cases and lastly a sensitivity experiment to the surface type is performed.

Comparison of simulations with different horizontal resolution

The “nesting” of domains allows us to significantly decrease the horizontal resolution of WRF, as the finest resolution of the current configuration is down to 1 km. This section aims to compare model results with a different resolution – 9 km, 3 km and 1 km, and the role of the sea is also taken into account. The comparison is conducted for the grid point, where BAB is located, and is manually chosen, as mentioned above. The choice criteria consist of an approximate location in the South Bay of Livingston island, a land surface type and sea borders in two sides. In the outermost domain, the grid coordinates of the point are $x_{d01}=55$, $y_{d01}=55$; in the first nested domain BAB falls into $x_{d02}=55$, $y_{d02}=55$; and in the finest domain it is taken as $x_{d03}=61$, $y_{d03}=53$. The following comparison is conducted only for the test case in 2020 with the meteorological variables, which have been measured at BAB. The comparison is visually presented on Figure 3. The black points mark the values, measured at BAB; brown rectangles mark the ERA-5 reanalysis data; dark red triangles are from the synoptic station “Base Arturo Prat” and are shown as an instance of the weather pattern in the region. The red, orange and yellow curves correspond to model simulations with different resolutions in the BAB point. The blue curve shows the values of the respective meteorological variable in point $x_{d03}=60$, $y_{d03}=53$, which has a surface type of water and represents the sea in front of BAB. The green curve is calculated as the mean of the BAB land point and its neighbouring sea point (i.e. the yellow and blue curves) – this calculation is done, because BAB is located close the edge of the corresponding land point, and the effects of the sea should not be neglected.

The comparison of the 2 m temperature time series on Figure 3-a shows the WRF forecasts lower values than the observed ones. It is possible that this difference is due to the lack of proper calibration of the temperature sensor, but the measurements from “Base Arturo Prat” also suggest warmer air temperature and larger temperature amplitudes. The graph clearly shows that decreasing the horizontal resolution leads to closer to measurement simulated values. The rapid cooling in 10 UTC on 27 January 2020 is also described quite well. The simulations with higher resolution generally show higher temperatures, but they nicely describe the minimum at 0.5°C. The higher temperatures of the sea point next to BAB are explained not only with the thermal flux differences between the two points, but also with the higher sea surface temperature – at this point the cooling is less

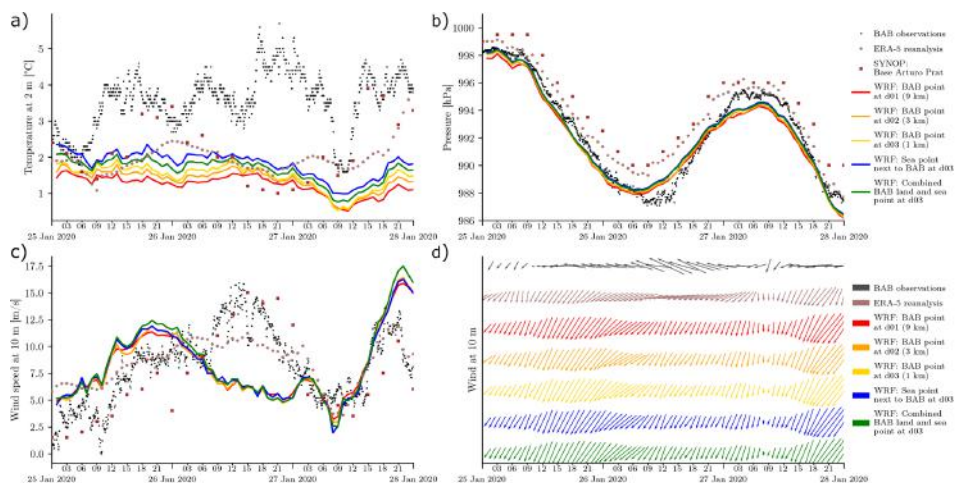


Figure 3. Time series of the meteorological variables 2 m temperature (a), sea level pressure (b), wind speed (c) and wind direction (d) with different horizontal resolution and different methods of accounting for the influence of the sea, compared with observational data and the ERA-5 reanalysis.

pronounced. The combination of the BAB land and its neighbouring sea point, which is comprised by the average value in every time instant, simulate the rapid cooling and the higher temperatures relatively well. In order to give a quantitative measure of the forecast skill, the BIAS, Root mean square error (RMSE) and Mean absolute error (MAE), are calculated as:

$$BIAS = \frac{1}{n} \sum_{i=1}^n M_i - O_i,$$

$$RMSE = \sqrt{\frac{1}{n} \sum_{i=1}^n (M_i - O_i)^2},$$

$$MAE = \frac{1}{n} \sum_{i=1}^n |M_i - O_i|,$$

where n is the number of discrete values, M_i is the model simulated value and O_i – the corresponding (closest in time) observed value. The WRF values are output every hour, therefore for a 3 days forecast $n=72$, in the case of no missing observations. These statistical measures possess the dimensionality of the measured variable and are calculated for each of the model points described above relative to the BAB measurements and to the ERA-5 reanalysis separately. The results are shown in Table 1.

Table 1. Forecast statistics calculated against measurement data and ERA-5 data for simulations with different horizontal resolution and different means of accounting for the influence of the sea.

| | BAB observations | | | ERA-5 reanalysis | | |
|----------------------------------|------------------|--------|--------|------------------|-------|-------|
| | BIAS | RMSE | MAE | BIAS | RMSE | MAE |
| Temperature [°C] | | | | | | |
| BAB in d01 (9 km) | -2.31 | 2.45 | 2.31 | -0.74 | 0.92 | 0.75 |
| BAB in d02 (3 km) | -2.17 | 2.32 | 2.17 | -0.6 | 0.82 | 0.63 |
| BAB in d03 (1 km) – land | -2.07 | 2.23 | 2.07 | -0.5 | 0.75 | 0.57 |
| BAB in d03 (1 km) – sea | -1.73 | 1.93 | 1.73 | -0.16 | 0.56 | 0.44 |
| BAB in d03 (1 km) – land and sea | -1.9 | 2.08 | 1.9 | -0.33 | 0.64 | 0.48 |
| Sea level pressure [hPa] | | | | | | |
| BAB in d01 (9 km) | -0.54 | 0.86 | 0.76 | -1.65 | 1.69 | 1.65 |
| BAB in d02 (3 km) | -0.44 | 0.79 | 0.69 | -1.54 | 1.59 | 1.54 |
| BAB in d03 (1 km) – land | -0.27 | 0.72 | 0.6 | -1.37 | 1.42 | 1.37 |
| BAB in d03 (1 km) – sea | -0.21 | 0.71 | 0.58 | -1.31 | 1.36 | 1.31 |
| BAB in d03 (1 km) – land and sea | -0.27 | 0.72 | 0.6 | -1.37 | 1.42 | 1.37 |
| Wind speed [ms ⁻¹] | | | | | | |
| BAB in d01 (9 km) | -0.12 | 3.68 | 2.84 | -0.38 | 2.73 | 2.23 |
| BAB in d02 (3 km) | -0.2 | 3.79 | 2.91 | -0.45 | 2.86 | 2.33 |
| BAB in d03 (1 km) – land | 0.12 | 3.95 | 3.13 | -0.14 | 3.04 | 2.49 |
| BAB in d03 (1 km) – sea | -0.09 | 3.75 | 2.93 | -0.35 | 2.81 | 2.33 |
| BAB in d03 (1 km) – land and sea | 0.12 | 3.95 | 3.13 | -0.14 | 3.04 | 2.49 |
| Wind direction [deg] | | | | | | |
| BAB in d01 (9 km) | -54.71 | 59.56 | 55.11 | -17.44 | 27.55 | 21.27 |
| BAB in d02 (3 km) | -52.29 | 57.74 | 53.14 | -15.02 | 26.46 | 20.23 |
| BAB in d03 (1 km) – land | -52.9 | 58.27 | 53.68 | -15.63 | 26.76 | 21.16 |
| BAB in d03 (1 km) – sea | -54.34 | -59.71 | -54.94 | -17.07 | 28.36 | 22.83 |
| BAB in d03 (1 km) – land and sea | -52.9 | 58.27 | 53.68 | -15.63 | 26.76 | 21.16 |

The BIAS is a measure for the direction of the deviation. All its values for the temperature at 2 m are negative, which again indicates the tendency for lower temperatures, calculated by the model. The numerical comparison of the simulated 2 m temperature with BAB observations and ERA-5 data shows best results in the sea point next to BAB.

The pressure time series, shown on Figure 3-b, suggest that this field is predicted extremely well by the numerical forecast. The negative BIAS shows that the forecasted values are slightly under the measured ones, the smallest deviations of

RMSE=0.71 hPa against BAB observations and 1.36 hPa against ERA-5 reanalysis are as well observed at the sea point in the finest domain.

The wind speed is simulated quite well, which is seen by the amplitudes of the model curves on Figure 3-c and the close to 0 BIAS. The forecast statistics are similar in the simulations with different resolution, as the largest deviations is RMSE=3.95 ms⁻¹ in the sea point. The wind speed maximum around 21 UTC on 27 January 2020 is described fairly well despite the higher peak in the model with ~ 5ms⁻¹.

In order to calculate the statistics for the wind direction, Δd needs to be introduced as the difference in degrees between the simulated and the observed wind direction, it varies in the interval $\Delta d \in [-180^\circ, 180^\circ]$. This quantity is calculated differently, depending on the difference between M_i and O_i (Jiménez & Dudhia, 2013):

$$\Delta d = \begin{cases} M_i - O_i, & \text{if } M_i - O_i \leq |180^\circ| \\ M_i - O_i - 360^\circ, & \text{if } M_i - O_i > 180^\circ \\ M_i - O_i + 360^\circ, & \text{if } M_i - O_i < -180^\circ \end{cases}$$

In this case M_i and O_i have the dimensionality of degrees, indicating a direction, in which 0° corresponds to North. The statistical characteristics are calculated as follows:

$$\begin{aligned} BIAS(wdir) &= \frac{1}{n} \sum_{i=1}^n \Delta d, \\ RMSE(wdir) &= \sqrt{\frac{1}{n} \sum_{i=1}^n (\Delta d)^2}, \\ MAE(wdir) &= \frac{1}{n} \sum_{i=1}^n |\Delta d|. \end{aligned}$$

The results of the comparison between the forecasted direction and the measured one give RMSE values reaching up to 60°. The comparison of the simulated wind direction with ERA-5 data shows more promising results with RMSE values less than 30°. This difference may be due to various factors, one of them being the inadequate topography data, used by the WRF and ERA-5 simulations. Another possible error may have arisen from an imperfect placement of the mast resulting in a Venturi effect or turbulent eddies at heights below 10 m. According to the forecast statistics and Figure 3-d, the horizontal resolution does not have a profound effect on the wind direction. The wind speed is slightly higher in the sea point, due to the smaller roughness length z_0 over the sea surface. The wind direction is approximately the same in all grid points in the comparison. There is a scarce distinction between the WRF and ERA-5 values in the period from 9 UTC on 26 January until 3 UTC on 27 January 2020.

Validation for all test cases

The results from the numerical forecast validation suggest that the horizontal resolution mainly affects the 2 m temperature field, which is improved by ~0.5°C in

the finest domain. The pressure values are also affected. The sea grid point produces the slightest deviations with observed data, which suggests that the location of BAB is strongly influenced by the sea. The forecast statistics for all covered test cases and their average value are presented in Table 2. The test cases in 2016 and 2020 are described relatively well by the model, whereas the 2017 test case proved to be a numerical challenge and the deviations between simulated and observed values are quite high. The WRF shows an average temperature RMSE of 2.59°C against BAB measurements, the pressure field is forecasted very well with an average RMSE of just 1.34 hPa for the three cases. The wind speed RMSE ranges from 2 to 9 ms⁻¹ for the different test cases, the average value being 5 ms⁻¹. The wind direction is highly biased with RMSE values up to 70°, which could be due to the poor topography representation or flawed in-situ measurements.

Table 2. Forecast statistics calculated against measurement data and ERA-5 data for the three test cases and their average value for each meteorological variable.

| | BAB observations | | | ERA-5 reanalysis | | |
|--------------------------------|------------------|--------|--------|------------------|-------|-------|
| | BIAS | RMSE | MAE | BIAS | RMSE | MAE |
| Temperature [°C] | | | | | | |
| Test case 2016 | -1.44 | 1.69 | 1.44 | -0.17 | 0.98 | 0.62 |
| Test case 2017 | -1.21 | 3.86 | 3.31 | -1.67 | 3.95 | 2.83 |
| Test case 2020 | -2.07 | 2.23 | 2.07 | -0.50 | 0.75 | 0.57 |
| Average for all test cases | -1.57 | 2.59 | 2.27 | -0.78 | 1.89 | 1.34 |
| Sea level pressure [hPa] | | | | | | |
| Test case 2016 | 0.57 | 1.10 | 0.81 | -0.82 | 1.27 | 1.14 |
| Test case 2017 | 0.76 | 2.21 | 1.86 | -1.16 | 2.52 | 1.71 |
| Test case 2020 | -0.27 | 0.72 | 0.60 | -1.37 | 1.42 | 1.37 |
| Average for all test cases | 0.35 | 1.34 | 1.09 | -1.12 | 1.74 | 1.41 |
| Wind speed [ms ⁻¹] | | | | | | |
| Test case 2016 | -0.96 | 2.67 | 2.18 | 0.61 | 1.39 | 1.10 |
| Test case 2017 | -4.70 | 8.36 | 6.51 | -1.36 | 4.61 | 3.36 |
| Test case 2020 | 0.12 | 3.95 | 3.13 | -0.14 | 3.04 | 2.49 |
| Average for all test cases | -1.85 | 4.99 | 3.94 | -0.30 | 3.01 | 2.32 |
| Wind direction [deg] | | | | | | |
| Test case 2016 | -6.15 | 35.14 | 27.48 | -3.60 | 35.61 | 26.76 |
| Test case 2017 | -32.18 | 119.22 | 109.55 | -53.07 | 99.88 | 83.46 |
| Test case 2020 | -52.90 | 58.27 | 53.68 | -15.63 | 26.76 | 21.16 |
| Average for all test cases | -30.41 | 70.88 | 63.57 | -24.10 | 54.08 | 43.79 |

Land cover type sensitivity

The land use type in the BAB grid point, as well as the whole Livingston island, is depicted as snow and ice. The available land use data – MODIS, is assembled in the period 2001-2005, but due to the climate changes and the dynamics of land and sea ice, these data may prove unsuitable for 2020 simulations. Recent Landsat images, as well as some summer photos in the region, indicate the presence of rock fields and even grasslands. The turbulent fluxes over bare rock areas are quite different from those over snow and ice. In order to quantify the effect of the surface parameters only in one grid point, three additional experiments of altering 1 km² of snow area with another land type are performed. Technically, this narrows to altering the WRF variables LU_INDEX and LANDUSEF in the grid point $x_{d03}=60$, $y_{d03}=53$ of the finest domain. The following land use types are used: Grasslands (LU index=10), Barren or Sparcely Vegetated (LU index=16), Barren Tundra (LU index=20). The parameters of these land use types for the summer season are shown in Table 3. It can be seen that the thermal capacity C of the different surfaces differs by a factor of 10²⁰. The differences in the roughness length z_0 are around 6-7 cm.

Table 3. MODIS land use type parameters for the summer, as in LANDUSE.TBL of WRF, v4.0.

| No. | α [%] | M [%] | ϵ [%] | z_0 [10 ⁻² m] | λ_T [4,184.10 ² Jm ⁻² K ⁻¹ s ^{-1/2}] | C [10 ⁵ Jm ⁻³ K ⁻¹] | Name |
|-----|--------------|-------|----------------|----------------------------|-----------------------------------------------------------------------------------------|-------------------------------------------------------|--------------------------------|
| 10 | 19 | 15 | 92 | 7.5 | 2.37 | 20,8.10 ⁵ | "Grasslands" |
| 15 | 55 | 95 | 98 | 1 | 5 | 9.10 ²⁵ | "Snow and Ice" |
| 16 | 25 | 2 | 85 | 6.5 | 0.81 | 12.10 ⁵ | "Barren or Sparcely Vegetated" |
| 17 | 8 | 100 | 98 | 0.01 | 6 | 9.10 ²⁵ | "Water" |
| 20 | 15 | 2 | 90 | 6 | 1.6 | 12.10 ⁵ | "Barren Tundra" |

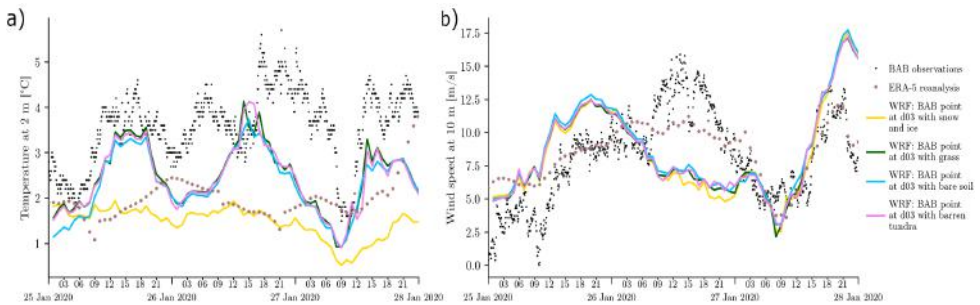


Figure 4. Time series of the meteorological variables 2 m temperature (a) and wind speed (b) corresponding to the different land use type experiments, compared with observational data ant the ERA-5 reanalysis.

The simulation results for the 2020 test case are shown on Figure 4-a for the 2 m temperature and on Figure 4-b for the 10 m wind speed. The BAB measurements and the ERA-5 reanalysis are given as real data representatives. The dark green curve depicts the “Grasslands” experiment, the light blue one represents the “Barren or Sparsely Vegetated” experiment, and the violet one is for the “Barren Tundra” experiment. The yellow curve corresponds to the original simulation with a land use type of “Snow and Ice” and it is the same as in the previous figures.

Table 2. Forecast statistics calculated against measurement data and ERA-5 data and the unmodified model run for the different land use types.

| | BAB observations | | | ERA-5 reanalysis | | | WRF – snow/ice | | |
|--------------------------------|------------------|-------|-------|------------------|-------|-------|----------------|------|------|
| | BIAS | RMSE | MAE | BIAS | RMSE | MAE | BIAS | RMSE | MAE |
| Temperature [°C] | | | | | | | | | |
| Snow/ice | -2.07 | 2.23 | 2.07 | -0.50 | 0.75 | 0.57 | - | - | - |
| Grasslands | -1.07 | 1.30 | 1.10 | 0.50 | 1.01 | 0.79 | 1.01 | 1.18 | 1.02 |
| Barren/Sparsely Vegetated | -1.20 | 1.39 | 1.22 | 0.37 | 0.92 | 0.75 | 0.87 | 1.07 | 0.93 |
| Barren Tundra | -1.10 | 1.34 | 1.15 | 0.47 | 1.01 | 0.79 | 0.97 | 1.15 | 0.99 |
| Sea level pressure [hPa] | | | | | | | | | |
| Snow/ice | -0.27 | 0.72 | 0.60 | -1.37 | 1.42 | 1.37 | - | - | - |
| Grasslands | -0.27 | 0.73 | 0.61 | -1.37 | 1.42 | 1.37 | 0.00 | 0.02 | 0.01 |
| Barren/Sparsely Vegetated | -0.27 | 0.72 | 0.61 | -1.37 | 1.42 | 1.37 | 0.00 | 0.02 | 0.01 |
| Barren Tundra | -0.27 | 0.72 | 0.61 | -1.37 | 1.42 | 1.37 | 0.00 | 0.02 | 0.01 |
| Wind speed [ms ⁻¹] | | | | | | | | | |
| Snow/ice | 0.12 | 3.95 | 3.13 | -0.14 | 3.04 | 2.49 | - | - | - |
| Grasslands | 0.25 | 3.79 | 3.04 | 0.00 | 2.88 | 2.42 | 0.13 | 0.41 | 0.31 |
| Barren/Sparsely Vegetated | 0.49 | 3.85 | 3.14 | 0.23 | 2.96 | 2.47 | 0.37 | 0.53 | 0.43 |
| Barren Tundra | 0.29 | 3.78 | 3.02 | 0.03 | 2.87 | 2.43 | 0.17 | 0.47 | 0.35 |
| Wind direction [deg] | | | | | | | | | |
| Snow/ice | -52.90 | 58.27 | 53.68 | -15.63 | 26.76 | 21.16 | - | - | - |
| Grasslands | -53.93 | 59.00 | 54.41 | -16.66 | 27.05 | 21.19 | -1.03 | 2.97 | 1.72 |
| Barren/Sparsely Vegetated | -53.41 | 58.82 | 54.01 | -16.13 | 27.05 | 21.43 | -0.50 | 2.23 | 1.34 |
| Barren Tundra | -53.91 | 58.93 | 54.41 | -16.64 | 27.02 | 21.40 | -1.01 | 3.18 | 1.89 |

The 2 m temperature is highly sensitive to the land use type. On Figure 4-a, one can see that the diurnal cycle is more pronounced, when the surface is different from snow and ice, thus the thermal capacity is higher. Table 4 presents the forecast statistics for these simulations calculated against BAB measurements, ERA-5 reanalysis and the unmodified model run – the last group is given in order to evaluate the model response to this change. The numerical comparison shows that the 2 m temperature is the highest

with grasslands, slightly lower with barren tundra, even lower with barren or sparsely vegetated soil and the lowest with snow and ice, which corresponds precisely to the respective thermal capacities in Table 3. Accordingly, with higher temperatures, the forecast BIAS approaches 0. The smallest values of RMSE and MAE against BAB measurements are obtained with grasslands, because the temperature in this experiment is the highest. The best results against ERA-5 data are obtained with the original simulation with snow and ice, which suggests that the WRF and ERA-5 models are configured with similar land type data. The atmospheric pressure field is almost unaffected by the change in the land type. The wind speed at 10 m is only slightly altered with values of $\sim 0.5 \text{ ms}^{-1}$ – the results with the least RMSE=3.78 against BAB measurements are obtained with the barren tundra surface type. Figure 4-b shows that the 10 m wind speed timeseries curve is similar in all experiments. The average wind speed is the highest with the barren or sparsely vegetated soil, although its roughness length z_0 is relatively high. Overall, the change in land use type affects all surface meteorological variables, but the largest differences are observed in the 2 m temperature field, which is relatively increased by $\sim 1^\circ\text{C}$ with grasslands, compared to snow and ice. Although the “Grasslands” experiment produces the best results, it does not ideally describe the situation. The experiments are conducted with a change of only 1 km^2 of the land surface, while the Landsat images and summer photos in the region suggest a higher area without snow. The most adequate description of the land surface would be the use of more recent satellite data to alter a larger area in the finest domain, as well as parts of the larger model domains. The barren or sparsely vegetated soil also produces fairly good results. The differences are explained by the values of the surface parameters, indicative for each land type. The lower thermal capacity C , as well as the lower thermal inertia λ_T of the barren soil, in combination with the low albedo α , lead to the absorption of more short-wave radiation and a faster warming from the Sun. The relatively low surface emissivity reduces radiative cooling during the night, which explains the higher night temperatures of barren soil, compared to snow and ice land type in WRF. As a conclusion, the snow and ice land use type does not adequately represent Livingston island in the summer season.

CONCLUSION

A complete configuration of the WRF model for forecasting the weather in the Livingston island area is set up. The GMTED2010 topography data is proven to be flawed in the region, for this reason the authors advise the use of the Reference Elevation Model of Antarctica (REMA) in further simulations, which is a high resolution, time-stamped Digital Surface Model (DSM) of Antarctica at 8-meter spatial resolution (Howat et al., 2019). The model grid is centred over BAB, the length of each simulation is 72 hours and the results are compared with measurements at BAB, nearby synoptic stations and the ERA-5 reanalysis. Various cases with passing cyclones and shift of weather patterns are addressed in our study. The WRF

is found to represent satisfactory the temperature at 2 m, sea level pressure and wind at 10 m in the point of BAB during weather shift events. A comparison of results with different horizontal resolution suggests that the forecast quality increases with the model grid resolution. The BAB point is found to be strongly influenced by the sea and its effect should be considered in the forecast representation. Further details on the influence of sea surface temperature on the forecast skill can be found in Chtirkova (2020) and Chtirkova & Peneva (2020).

A sensitivity experiment with altering the land use type in one grid point (1 km²) in the finest domain is carried out. This grid point corresponds to the location of the base, where the snow melts completely during summer and reveals the rocky soil underneath. A change in the land use type, respectively the thermal capacity of the underlying surface, significantly increases the forecast quality. This experiment shows that MODIS data, collected with satellite missions during 2005, does not adequately represent the current situation on places, affected by climate change, such as Livingston Island. For accurate simulations in these regions, a revision of the land use type is advisory.

ACKNOWLEDGMENTS

The authors would like to express their gratitude to all people and projects, involved in the operation and maintenance of the PHYSON cluster (<http://physon.phys.uni-sofia.bg/about-physon-bg>).

NOTES

1. NCAR, UCAR – The Antarctic Mesoscale Prediction System (AMPS): <https://www2.mmm.ucar.edu/rt/amps/>
2. Synoptic data from the weather information service OGIMET: <https://www.ogimet.com/>
3. The MeteoRocks project: <https://meteo.rocks/page/aboutus>

REFERENCES

- Skamarock, William C. et al. (2019). *A Description of the Advanced Research WRF Model Version 4*, UCAR/NCAR. doi: 10.5065/1DFH-6P97, url:<https://opensky.ucar.edu/islandora/object/opensky:2898> .
- L.L. Ivanov (2017). *Antarctica: Livingston Island and Smith Island. Scale 1:100000 topographic map*, Manfred Wörner Foundation, ISBN 978-619-90008-3-0 .
- Hines, K. M., and D. H. Bromwich (2008). *Development and testing of Polar WRF. Part I. Greenland ice sheet meteorology*. Mon. Wea. Rev., 136, 1971-1989, url: https://polarmet.osu.edu/PolarMet/PMGFulldocs/hines_bromwich_mwr_2008.pdf.

- Chtirkova, B. (2020). *A study on the impact of sea surface temperature on the weather forecast for the Bulgarian Antarctic Base on Livingston Island (Master's Thesis)*. Sofia University "St. Kliment Ohridski", Sofia, Bulgaria.
- National Centers For Environmental Prediction/National Weather Service/NOAA/U.S. Department Of Commerce (2015). *NCEP GFS 0.25 Degree Global Forecast Grids Historical Archive*, doi: 10.5065/D65D8PWK, url: <https://rda.ucar.edu/datasets/ds084.1/> .
- Copernicus Climate Change Service (C3S) (2017). *ERA5: Fifth generation of ECMWF atmospheric reanalyses of the global climate*, url: <https://cds.climate.copernicus.eu/cdsapp#!/home> .
- Jiménez, Pedro A. and Jimmy Dudhia (2013). On the Ability of the WRF Model to Reproduce the Surface Wind Direction over Complex Terrain, *Journal of Applied Meteorology and Climatology* 52.7, p. 1610—1617. doi: 10.1175/jamc-d-12-0266.1, url: <https://doi.org/10.1175/jamc-d-12-0266.1> .
- Howat, I. M., Porter, C., Smith, B. E., Noh, M.-J., and Morin, P. (2019). *The Reference Elevation Model of Antarctica*, *The Cryosphere*, 13, 665-674, <https://doi.org/10.5194/tc-13-665-2019> .
- Chtirkova, B. and Peneva, E (2020). *The impact of SST on the weather forecast quality in the Bulgarian Antarctic Base area on Livingston Island*, EGU General Assembly 2020, Online, 4–8 May 2020, EGU2020-9347, <https://doi.org/10.5194/egusphere-egu2020-9347>

✉ **Boriana Chtirkova**

<https://orcid.org/0000-0001-5743-8511>
Department of Meteorology and Geophysics
Faculty of Physics
“St. Kliment Ohridski” University of Sofia
E-mail: bshtirkova@uni-sofia.bg

✉ **Elisaveta Peneva**

<https://orcid.org/0000-0003-1325-685X>
Department of Meteorology and Geophysics
Faculty of Physics
“St. Kliment Ohridski” University of Sofia
E-mail: elfa@phys.uni-sofia.bg

✉ **Gergana Georgieva**

<https://orcid.org/0000-0003-3515-9524>
Department of Meteorology and Geophysics
Faculty of Physics
“St. Kliment Ohridski” University of Sofia
E-mail: ggeorgieva@phys.uni-sofia.bg

The 1st International Conference on Environmental Protection and Disaster RISKS (<http://envirorisk.bas.bg/>) is based on the scientific topics covered by The National Scientific Program „Environmental Protection and Reduction of the Risk of Adverse Events and Natural Disasters“ (<https://nnpos.wordpress.com/>). The program is approved by Council of Ministers Decision No 577 / 17.08.2018 and funded by the Ministry of Education and Science (Agreement No D01-230/06-12-2018).

The main areas of environmental management covered by the conference are: Natural Hazards and Risks, Air Pollution, Climate and Health, Water resources, human activities and management, Biodiversity, Biotechnology for environmental management, Informatics, Remote sensing, high performance computing and GIS for environmental monitoring.

Co-organizers of the conference are:

– the National Geoinformation Center (NGIC) of the Republic of Bulgaria, Project "NATIONAL GEO-INFORMATION CENTER", financed by the National Road Map for Scientific Infrastructure 2017-2023, Contr. No D01-282 /17.12.2019 (<http://ngic.bg/>);

– the Crisis Management and Disaster Response Centre of Excellence (CMDR COE - <https://www.cmdrcoe.org/>), located in Sofia, the Republic of Bulgaria

– and the Bulgarian Academy of Sciences (<http://www.bas.bg/en/>).